AFAL-TR-76-184

AD-B015 200

# SCANNED LASER ILLUMINATOR/RECEIVER

R. A. Honzik and F. B. Warren
Martin Marietta Corporation
P. O. Box 5837
Orlando, Florida 32805

NOVEMBER 1976

Final Report - December 1975 - July 1976

APPROVED FOR PUBLIC RELEASE; DISTRIBUTION UNLIMITED.

AIR FORCE AVIONICS LABORATORY
AIR FORCE WRIGHT AERONAUTICAL LABORATORIES
AIR FORCE SYSTEMS COMMAND
WRIGHT-PATTERSON AIR FORCE BASE, OHIO 45433

81 11 18 016

ASD 81-1773

# NOTICE

This technical report has been reviewed and is approved for publication.

Dr. Harry M. Dobbins
Project Engineer, Fire Control Technology Group
Fire Control Branch

G. M. Fitzgibbon
Fire Control Technology Group
Fire Control Branch

DEPARTMENT OF DEFENSE
UNITED STATES OF AMERICA

DEPARTMENT OF THE AIR FORCE
AIR FORCE WRIGHT AERONAUTICAL LABORATORIES (AFSC)
WRIGHT-PATTERSON AIR FORCE BASE, OHIO 45433

REPLY TO ATTN OF: TST (G. Doben, 785-5572)

13 Nov 81

SUBJECT: Transmittal of AFAL-TR-76-184

TO: Defense Technical Information Center
Cameron Station
Alexandria, Virginia 22314

The attached report has been delimited and is now approved for public release. However, we have changed page 203. Therefore please make a new microfiche and destroy the previous microfiche for the subject report.

JAMES G. JOHNSON, DIRECTOR
Technical Information Center
Support Services Office

1 Atch
AFAL-TR-76-184
AD-B015200

UNCLASSIFIED
SECURITY CLASSIFICATION OF THIS PAGE (When Data Entered)

## REPORT DOCUMENTATION PAGE

READ INSTRUCTIONS
BEFORE COMPLETING FORM

1. REPORT NUMBER
AFAL-TR-76-184

2. GOVT ACCESSION NO.

3. RECIPIENT'S CATALOG NUMBER

4. TITLE (and Subtitle)
SCANNED LASER ILLUMINATOR/RECEIVER

5. TYPE OF REPORT & PERIOD COVERED
Final Technical Report
Dec 75 - Jul 76

6. PERFORMING ORG. REPORT NUMBER
OR 14,268

7. AUTHOR(s)
R. A. Honzik and F. B. Warren

8. CONTRACT OR GRANT NUMBER(s)
F33615-76-C-1005

9. PERFORMING ORGANIZATION NAME AND ADDRESS
Martin Marietta Aerospace
P. O. Box 5837
Orlando, Florida 32805

10. PROGRAM ELEMENT, PROJECT, TASK AREA & WORK UNIT NUMBERS
317J0798

11. CONTROLLING OFFICE NAME AND ADDRESS
Air Force Avionics Laboratory
Wright-Patterson AFB
Dayton, Ohio 45433

12. REPORT DATE
November 1976

13. NUMBER OF PAGES
204

14. MONITORING AGENCY NAME & ADDRESS(if different from Controlling Office)

15. SECURITY CLASS. (of this report)
UNCLASSIFIED

15a. DECLASSIFICATION DOWNGRADING SCHEDULE

16. DISTRIBUTION STATEMENT (of this Report)

APPROVED FOR PUBLIC RELEASE; DISTRIBUTION UNLIMITED.

17. DISTRIBUTION STATEMENT (of the abstract entered in Block 20, if different from Report)

18. SUPPLEMENTARY NOTES

19. KEY WORDS (Continue on reverse side if necessary and identify by block number)

High Energy Laser (HEL); precision tracking, high resolution imaging; laser illuminators; hybrid CCD receivers; galvonometer scanners

20. ABSTRACT (Continue on reverse side if necessary and identify by block number)

This report summarizes the results of an analytical and investigative study of compatible laser illuminator, high sensitivity receiver, and precision scanner techniques which are applicable to a high resolution, high data rate tracking and imaging sensor intended for airborne HEL applications. This technology survey has subsequently led to the conceptual design of a Scanned Laser Illuminator/Receiver (SLIR) sensor which utilizes a linearly scanned fan-beam laser illuminator and a synchronously scanning linear array receiver

DD FORM 1 JAN 73 1473 EDITION OF 1 NOV 65 IS OBSOLETE

UNCLASSIFIED
SECURITY CLASSIFICATION OF THIS PAGE (When Data Entered)

For performing the primary HEL operational functions of long range target acquisition, precision target tracking, and accurate aimpoint selection.

A detailed description of the preliminary design of a SLIR laboratory breadboard system is also included. This breadboard is configured around a 100 watt (average) Q-switched Nd:YAG laser illuminator, a hybrid CCD receiver employing silicon PIN photodiodes, and a servo-controlled moving-iron galvonometer scanner. Acquisition range performance of this breadboard is predicted to be approximately 8 kilometers for very small missile targets (100 $cm^2$ optical cross-section) to nearly 24 kilometers for large aircraft targets (10 $m^2$ geometric cross-section). An estimate of the labor and cost to develop this SLIR laboratory breadboard is also included.

# PREFACE

This program was conducted under Contract Number F33615-76-C-1005 for the Fire Control Branch of the Avionics Laboratory at Wright-Patterson Air Force Base, Ohio. Dr. Harry M. Dobbins of the Fire Control Technology Group served as contract monitor.

This report covers work performed by the Electro-Optics Department of Martin Marietta Aerospace, Orlando, Florida, from 15 December 1975 through 15 July 1976. Dr. Bob L. Landrum, Manager of the Electro-Optics Department, was the Program Manager, with Richard A. Honzik and Frank B. Warren sharing the responsibility as Task Leader. Significant contributions to this report were also performed by M. Amon, R. M. Clendenin, J. M. Martin, L. B. Peresztegy, and W. G. Zinn.

TABLE OF CONTENTS

TABLE OF CONTENTS (Continued)

## LIST OF ILLUSTRATIONS

## LIST OF TABLES

# SECTION I

## INTRODUCTION AND SUMMARY

The enormous potential of High Energy Lasers as long range, fast reaction weaponry has intrigued all three military services for a number of years and has led to the recent investment of considerable fiscal and manpower resources to realize such a system. The application of High Energy Lasers (HELs), however, has presented many technological difficulties, some of which require sizeable extensions of the present state-of-the-art for their solution. One of these difficulties arises from the need to precisely place and maintain the HEL beam on the target's area of vulnerability particularly when the target exhibits severe line-of-sight dynamics. A precision pointing and tracking system is, therefore, a most necessary adjunct to any HEL application.

Previous analytical and experimental studies have indicated that a passive acquisition and tracking system is often incapable of providing the necessary resolution, signal-to-noise ratio, or dynamic range to ensure long range acquisition and precision tracking. Passive contrast seekers operating in the visible or near-infrared spectral bands suffer from low apparent contrast between the desired target and its background and are limited to daylight operation. Additionally, unpredictable contrast reversals and sun glint, which may readily confuse HEL tracker logic, are frequent occurrences with an airborne target.

Passive FLIR trackers operating in the 3 to 5 μm spectral band also suffer from low apparent contrast since little blackbody emission from the target's skin is radiated at this wavelength. Emission from the target's plume, on the other hand, generally peaks in the 3 to 5 μm region and, therefore, constitutes a strong radiation source. However, plume instabilities give rise to frequent temporal and spatial variation in the magnitude and extent of this source which invariably leads to poor tracking accuracy. Another liability of passive FLIR trackers is their limited dynamic range. "Hot spot interference" due to the interaction between the HEL beam and the target may easily be orders of magnitude higher than the radiant signal from the target itself. This "interference" readily causes image blooming and severely degrades tracking accuracy at precisely the instant it is most important.

Eight to 14 μm passive FLIR trackers are generally superior to their lower wavelength counterparts due to the higher contrasts available at this wavelength when viewing targets against the cold sky background. Ground clutter, when tracking against an earth background, however, presents serious tracking difficulties. Furthermore, their poor spatial resolution capability (due to diffraction limitations) necessitates operation at very high (>100:1) signal-to-noise ratios if reasonable tracking accuracies are to be achieved. This poor resolution capability also increases the difficulty in obtaining precise aimpoint selection since image quality is less than desirable.

An active pointing and tracking system operating in the near-infrared spectral region offers the potential of eliminating most, if not all, of these problems. A recent study(1) conducted for the Air Force Weapons Laboratory by MIT Lincoln Labs has investigated the present state-of-the-art in laser and detector technology which might be applicable to the precision pointing and tracking requirement. This study concluded that two basic system approaches were worthy of further study: a scanned laser illuminator/receiver employing a high average power, high PRF Nd:YAG laser with a high sensitivity 1.06 μm scanning receiver; and a flood laser illuminator/receiver employing a high average power "doubled YAG" laser with an intensified SIT camera tube receiver. Of these two approaches, the scanned system promised the best range and growth potential for the HEL application.

The present study, which this report documents, extends the initial investigation performed by MIT Lincoln Labs by examining in detail the technologies and design concepts appropriate to the development of a Scanned Laser Illuminator/Receiver (SLIR) precision pointing and tracking sensor. Although it is recognized that the SLIR system must interface with an inertially stabilized tracking gimbal, a tracker processor, and the HEL itself, the scope of this study did not permit a detailed analysis of these interfaces. It did permit, however, the analysis and preliminary

---

(1) Dimmock, J. O., and Keyes, R. J., "Active Imaging Study (U)", MIT Linco
Laboratory, Technical Status Report No. 55TSR-0001, 2 August 1974.

design of a SLIR Laboratory Breadboard model with which the performance of the system can be verified and these interfaces investigated.

The SLIR configuration, as described in this report, employs a pulsed fan-beam Nd:YAG laser illuminator which is scanned in one direction to illuminate a 10 mrad square search field. A synchronously scanned linear hybrid CCD receiver, providing 10 μrad resolution during precision track mode operation, is used to detect the target-reflected return and to generate precise tracking signals. This high resolution permits accurate target tracking at moderate signal-to-noise ratios (≈ 10:1) and provides excellent imagery for precise aimpoint selection. Range-gating is provided at the receiver to minimize the effect of atmospheric backscatter and to negate the problem of background clutter (both cloud and earth background) which is prevalent with passive tracking systems. The choice of the 1.06 μm laser wavelength ensures that the effects of plume instabilities and "hot spot interference" will be minimal with the SLIR system and active illumination precludes the possibility of tracker-confusing contrast reversals.

This report begins with a discussion in Section 2.0 of the operational requirements and constraints which drive the design of the SLIR system. This is followed in Section 3.0 by an analysis of the appropriate technologies in the scanner, illuminator, and receiver areas. Predicted signal-to-noise ratio and imaging performance of a full-up SLIR system is analyzed in Section 4.0 which is followed by a detailed description of the proposed SLIR Laboratory Breadboard design in Section 5.0. Estimates of the cost and development planning necessary for the manufacture of this breadboard are given in Section 6.0. The last section of this report, Section 7.0, summarizes the conclusions of this study and proposes recommendations for further development effort. Each of these sections emphasizes that the Scanned Laser Illuminator/Receiver is an attractive solution to the HEL pointing and tracking problem and warrants further development effort.

# SECTION II

# SLIR SYSTEM CONSIDERATIONS

The Scanned Laser Illuminator/Receiver (SLIR) system is intended to provide long range target acquisition and precision tracking capability for airborne High Energy Laser (HEL) applications. Because the effectiveness of an HEL weapon is a function of aimpoint selection as well as precise aimpoint tracking, the SLIR system must also provide high resolution imaging capability. Although the specific method for achieving aimpoint selection, be it manual or automatic, is extremely important to the overall function of the SLIR system, this aspect is beyond the scope of this study and design effort. Likewise, the selection of the proper tracking algorithm and the mechanization of the tracking servo loop are equally important considerations, but they too are beyond the limits of this study. The SLIR system is, in essence, a high resolution imaging sensor whose video output signal is suitable in both signal-to-noise ratio and tracking data rate to effect long range target acquisition, precision target tracking, and precise aimpoint selection.

The design of the SLIR system is driven by its performance requirements, which are in turn driven by the operational demands of the HEL engagement. Because these operational requirements can have a great impact on the feasibility and practicality of the SLIR system design, it is extremely important that they be carefully defined and not over-specified. There is a tendency of human nature to always ask for more than one actually needs just to increase one's confidence in the success of the final outcome, but often this tendency results in unnecessary complication and increased cost as well. As will be apparent later, the operational demands which impact the design of the SLIR system seriously strain the present state-of-the-art in a number of areas and consequently over-specification can easily affect the feasibility of the system in addition to its complexity and cost.

The following subsections present a brief and somewhat qualitative look at the basic HEL system operational requirements, tracking system modes of operation, and system interface requirements and constraints which may impact the SLIR system design. A descriptive and comparative discussion of several generalized SLIR system concepts is presented in a subsequent subsection which is in turn followed by a semi-quantitative analysis of the effect of various system and operational parameters on the acquisition range performance predicted for the SLIR system by the parametric range equation.

## 2.1 Basic Operational Assumptions and Requirements

Targets. The basic operational requirements which the SLIR system must meet are dictated by the apparent optical and dynamic characteristics of the targets which the HEL weapon is likely to engage and by the optical and dynamic environment of the engagement scenario. Two target types are likely to be encountered in an airborne application: missiles and other aircraft. Generally speaking, missiles will be targets of small cross-section and high acceleration dynamics. Aircraft are invariably targets of considerably larger cross-section and significantly lower dynamic capability. For the purpose of this design study, the pertinent characteristics of these two target types have been generalized as listed in Table 1.

TABLE 1

Generalized Target Characteristics

| | Geometric Cross-section (meters$^2$) | Optical Cross-section (meters$^2$) | Closing Velocity (feet/second) |
|---|---|---|---|
| Missile | -- | 0.01 | 1000 or 4000 |
| Aircraft | 10 | -- | 800 |

It is convenient to specify an optical radar cross-section rather than a geometric cross-section for a small target (such as a missile) at long range. This optical cross-section, $A_e$, is a measure of the target's radiant intensity, $J_t$, when illuminated by a laser source and is defined as:

$$A_e = \frac{4\pi J_t}{H_i}$$

where $H_i$ is the incident irradiance at the target due to the laser illuminator. There is a direct, although often non-analytical correspondence between a target's geometric and optical cross-sections. If we generalize the target to be an ideal Lambertian reflector with mean diffuse reflectivity, $\rho$, then this correspondence may be derived for several simple geometries. For example, the correspondence between the geometric cross-section, A, of a diffuse spherical target and its optical radar cross-section may be shown to be

$$A_e = \frac{8}{3} \rho A \qquad \text{(diffuse spherical target)}$$

Similarly, the correspondence between the geometric cross-section of a diffuse flat target and its optical radar cross-section is readily derived as

$$A_e = 4 \rho A \cos^2 \theta \qquad \text{(diffuse flat target)}$$

where $\theta$ is the angle between the normal to the target surface and the line of sight (and illumination). To simplify the subsequent analyses, a generalized correspondence has been assumed for the remainder of this study and has been defined as

$$A_e = 4 \rho A \qquad \text{(generalized target)}$$

This definition will generally result in some optimism in detection range predictions by defining the target's optical cross-section to be somewhat larger than may actually be the case (in the absence of optical augmentation effects, of course). This optimism can be negated, however, by assuming a mean target reflectivity which is somewhat lower than actual. For the SLIR study effort, a diffuse reflectivity of 0.2 at 1.06 μm was assumed.

Operational Environment. The operational scenario for the HEL engagement has not been defined for this study. However, it is reasonable to expect that the engagement could occur at virtually any altitude, from on the deck on up. For the SLIR study effort, minimum and maximum altitude limits of 0.1 and 10 kilometers have been assumed. The effect of altitude on SLIR system performance is most apparent in the areas of atmospheric extinction and atmospheric turbulence. Figures 1 and

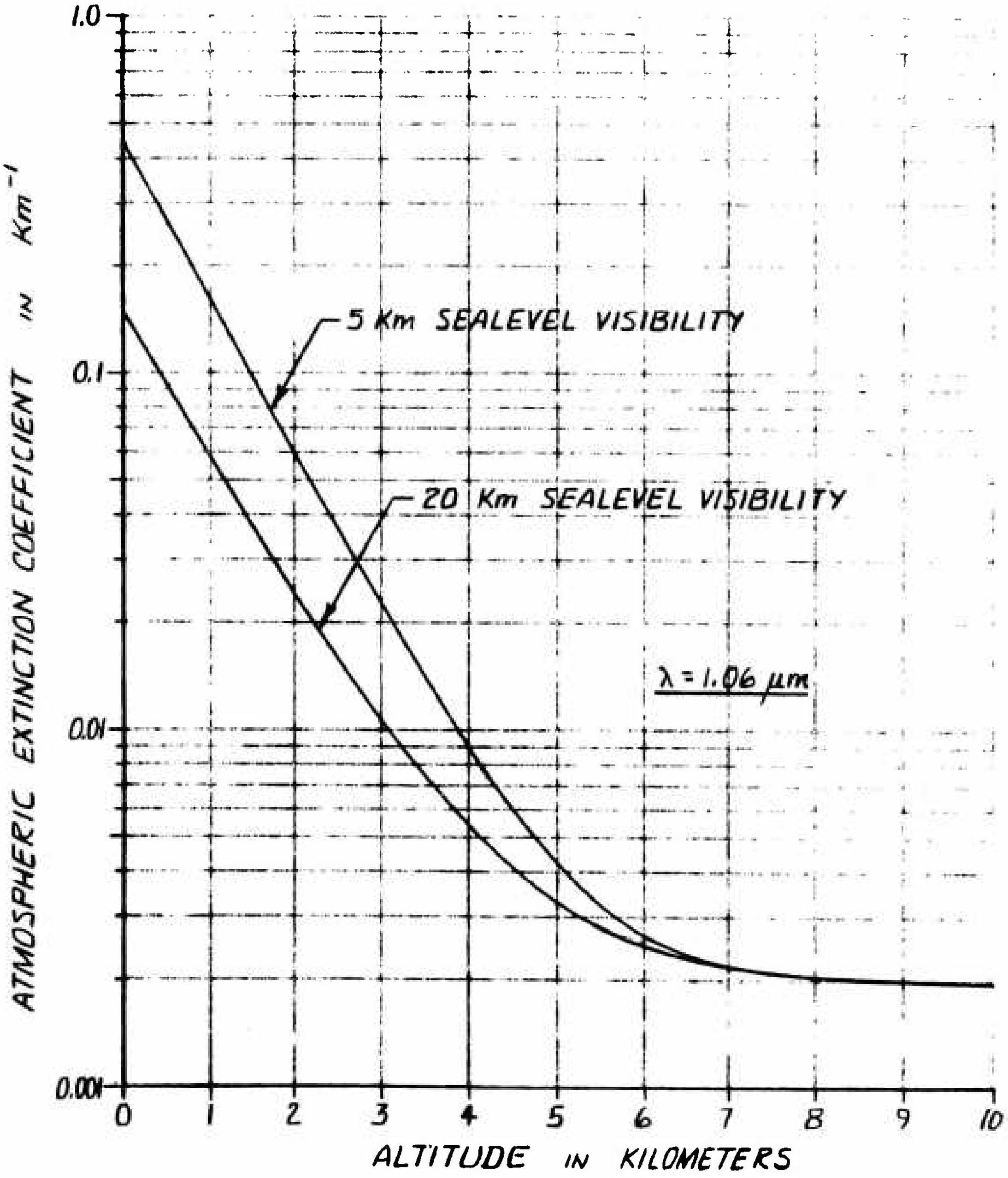

Figure 1. Atmospheric Extinction Dependence on Altitude

2 illustrates this altitude effect on these two optical parameters at a wavelength of 1.06 μm. Note that at altitudes above a few kilometers, both atmospheric extinction and turbulence are low and relatively insensitive to surface conditions (e.g., weather). Throughout much of the SLIR study effort, an atmospheric extinction coefficient of 0.05 $km^{-1}$ was assumed which is representative of operation at the low to middle altitudes.

Search Field. Electro-optical devices are generally unsuited to large area target search. Consequently, it was assumed that initial target search and acquisition is performed by the aircraft's radar system. The characteristics of this radar system have not been defined. Consequently, reasonable estimates of the system's angular hand-over accuracy (± 5 milliradians) and range accuracy (± 15 meters) have been assumed. This hand-over accuracy is assumed to be symmetrical in azimuth and elevation about the radar's pointing command and to be representative of target angular position at a high confidence level (e.g., 2 or 3 sigma). Therefore, a 10 mrad by 10 mrad search field of view is assumed to be adequate for high probability target acquisition. Note that a 10 mrad diameter circular search field would also be adequate. In general, it is desirable to keep the search field as small as possible consistent with a high probability that the target is within this search field.

Acquisition Range. It is always preferable to acquire targets at the longest range possible since this facilitates any ensuing response. As a minimum, targets should be acquired at ranges in excess of the nominal effective range of the HEL weapon so that the full combat space available can be utilized. An acquisition range goal of 10 nautical miles was assumed for large targets, such as the 10 $meter^2$ aircraft target; a shorter range goal of 5 nautical miles was assumed for small targets, such as the previously defined missile target, since their smaller cross-section compounds the acquisition problem.

Acquisition Search Rate. With a scanning system, such as the SLIR, the size of the search field is not the only parameter of significance affecting acquisition probability. Due to possible target angular motion relative to inertial space, the time in which the field is searched is also of importance. If the search time is too long, the target may have

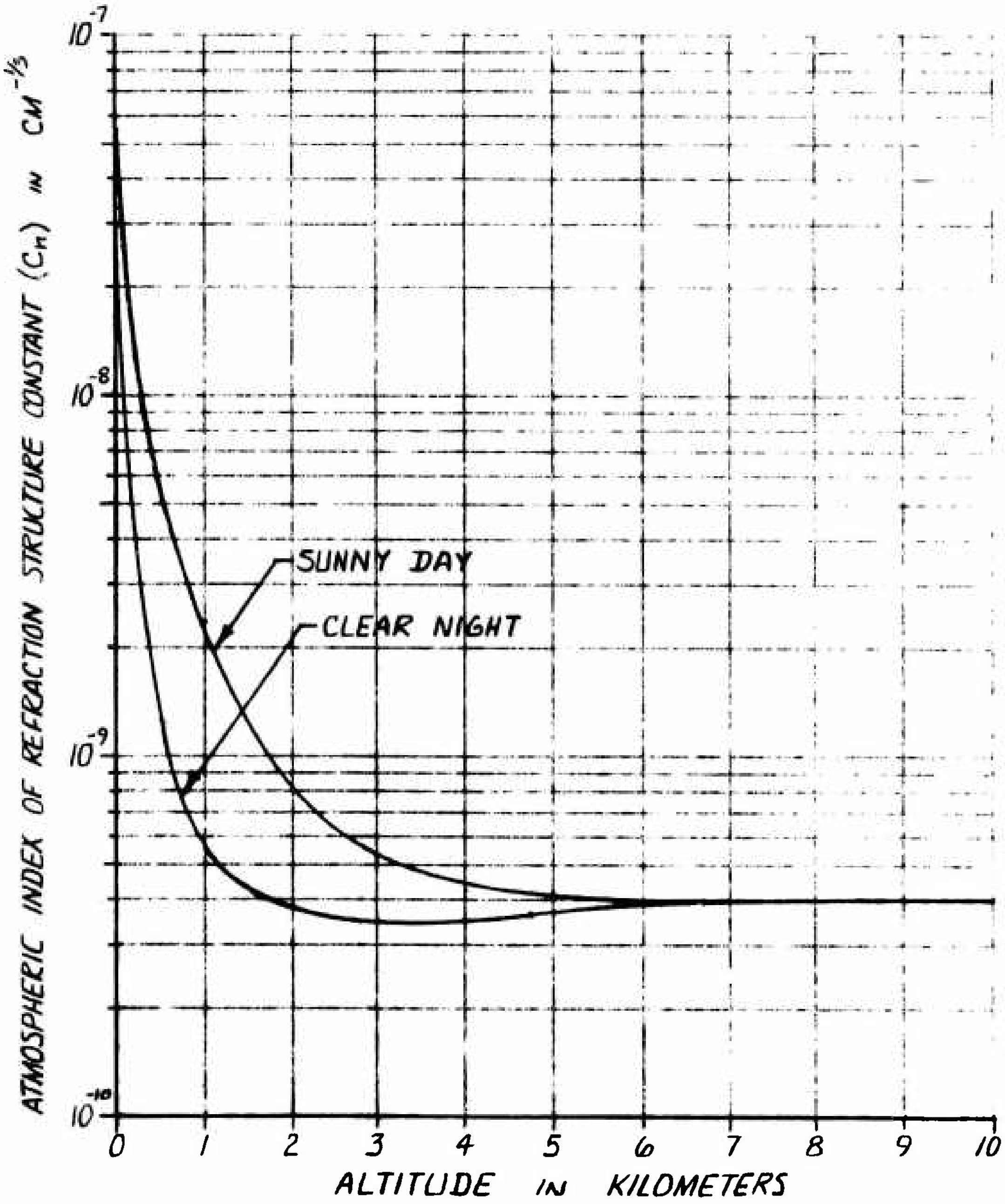

Figure 2. Atmospheric Turbulence Dependence on Altitude

the opportunity to move out of the search field before it is detected and acquired. The probability of this occurring is a function of the target's line-of-sight (LOS) rate which, in turn, is a function of the relative flight dynamics between the target and the SLIR system. Although the specific LOS rate is determined by the specifics of the relative flight dynamics, a reasonable estimate of the range of LOS rates likely to be observed during a typical encounter can be made by assuming simplified engagement dynamics.

If the target flies an ideal intercept trajectory with the SLIR aircraft, the LOS rate between the two will be exactly zero. If, on the other hand, the target flies a trajectory which results in an intercept miss, a non-zero LOS rate will result which increases dramatically with decreasing range. If this miss is fairly large and intentional, this latter trajectory may be thought of as an aircraft fly-by. If the miss is fairly small and unintentional, this trajectory is representative of an attacking missile. Simple geometry will show that for such a simplified engagement, the LOS rate, $\dot{\sigma}$, may be determined from

$$\dot{\sigma} = \frac{R\dot{M} - M\dot{R}}{R^2 + M^2}$$

where R is the range and $\dot{R}$ the range rate between the target and the SLIR aircraft and M is the miss distance and $\dot{M}$ the rate of change in miss distance at the point of closest encounter. If we further simplify this relation by assuming a constant miss distance (i.e., $\dot{M} = 0$) and a constant closing velocity (i.e., $\dot{R} = -V_C$). then the LOS rate becomes:

$$\dot{\sigma} = \frac{MV_C}{R^2 + M^2}$$

This equation is plotted as a function of range in Figure 3 for an aircraft fly-by at one kilometer and for a missile attack assuming a 10 meter guidance miss. Constant closing velocities of 800 feet/second for the aircraft and 1000 to 4000 feet/second for the missile were assumed. Note that the fly-by trajectory results in the higher LOS rate, but that at the acquisition ranges desired this LOS rate is typically less than 10 mrad/second. If we arbitrarily require that the target move not more

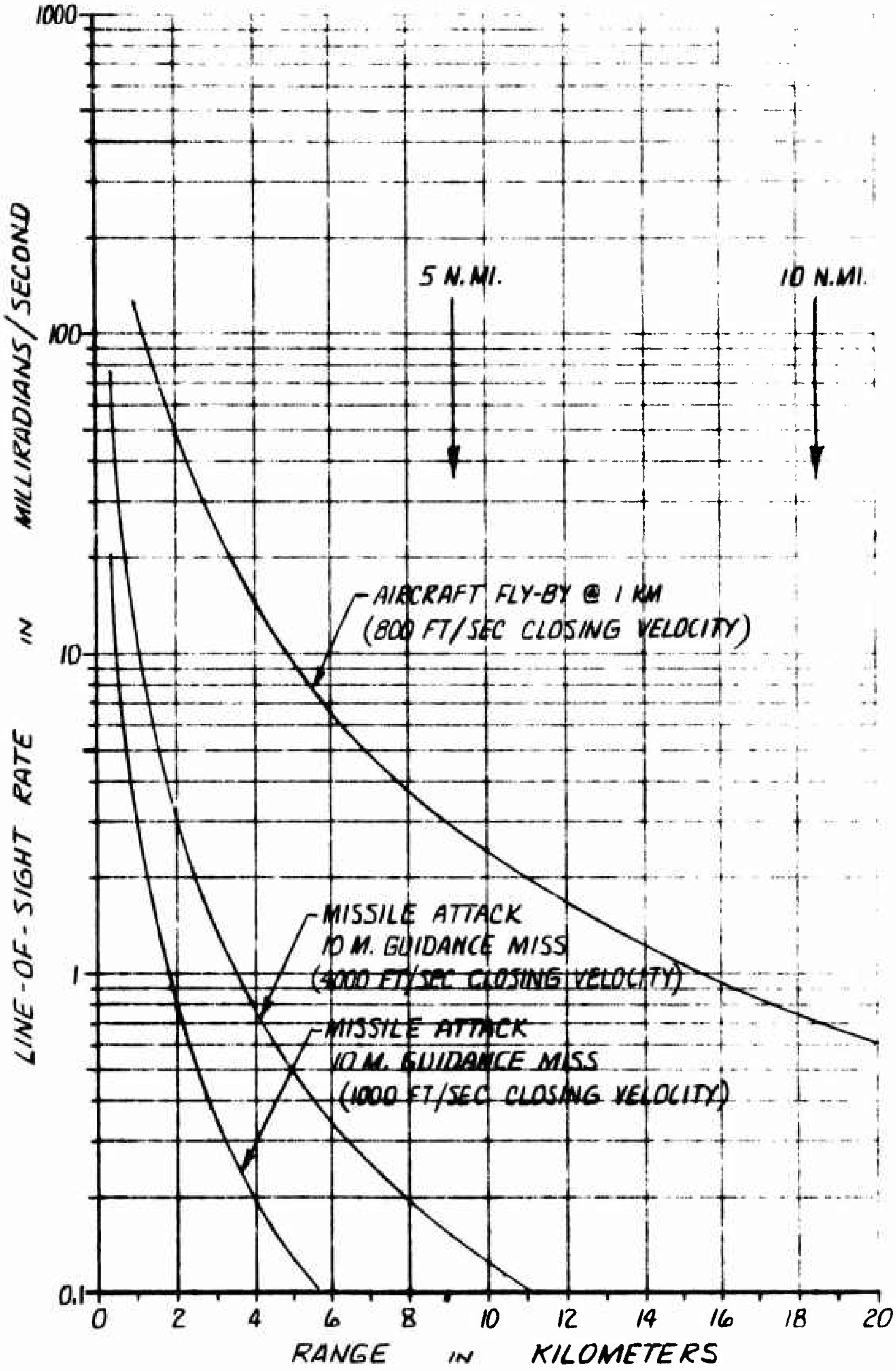

Figure 3. Typical LOS Rates during HEL Engagements

than one-tenth of the search field of view per search frame, then the minimum frame rate which the SLIR system may have during acquisition is 10 frames/second.

Track Accuracy. Once the target has been acquired and track has been initiated, the primary purpose of the SLIR system is to boresight the HEL weapon on the target. Because the effectiveness of the HEL weapon is a direct function of the energy density at the target, it is extremely important that the HEL beam is focused on the target with the smallest spot size diffraction and atmospheric turbulence will allow and that the beam is maintained fixed on the selected aimpoint for the duration of the "zap". The latter requirement places stringent demands on SLIR system track accuracy.

For a uniformly illuminated aperture, the unaberrated static intensity distribution of the HEL beam would be the familiar Airy disc. This distribution is generally approximated by a Gaussian form such that the intensity distribution in the focal (target) plane may be written as (assuming no aberrations):

$$I_s(r) = I_o \exp\left(-2 \frac{r^2}{W_o^2}\right)$$

where $I_o$ is the peak intensity and $W_o$ is the $1/e^2$ radius of the diffraction limited beam cross-section at the focal plane, i.e.,

$$W_o = 1.22 \frac{\lambda R}{D}$$

where D is the HEL aperture diameter and R is the distance to the target.

If we assume for simplicity that all tracking errors are uncorrelated and that their combined probability distribution is Gaussian with zero mean and non-zero variance, $\sigma^2$, then convolving this distribution with the static HEL beam intensity distribution yields the time-averaged dynamic intensity distribution(2), i.e.,

$$\bar{I}_d(r) = \frac{W_o^2 I_o}{W_o^2 + 4\sigma^2} \exp\left(-2 \left[\frac{r^2}{W_o^2 + 4\sigma^2}\right]\right)$$

---

(2) J. E. Negro, "Pointing Variance and Beam Degradation Calculations", Laser Digest, AFWL-TR-74-100, Spring 1974.

Note that the effect of tracking jitter is to reduce the on-axis intensity and to increase the $1/e^2$ beam radius at the target plane from $W_o$ to $\sqrt{W_o^2 + 4\sigma^2}$.

Since the energy density at the target is inversely proportional to beam cross-section, tracking jitter will reduce the time-averaged energy density by a factor, $\xi$, given by

$$\xi = \frac{W_o^2}{W_o^2 + 4\sigma^2}$$

If we now define the RMS angular tracking accuracy of the SLIR system as

$$\theta_t = \frac{\sigma}{R}$$

some simple algebraic manipulation will yield

$$\theta_t = \frac{1.22\ \lambda}{2D} \sqrt{\frac{1 - \xi}{\xi}}$$

This equation is plotted in Figure 4 for both a $CO_2$ and a CO HEL weapon. Note that to maintain a high energy density on the target, the RMS tracking jitter must be less than 5 or 10 μrad. This requirement drives both the data rate and sensor resolution requirements of the SLIR system.

Tracking Data Rate. Once the target has been acquired and track has been initiated, the primary effect of sensor frame rate is on track accuracy. Because the scanned sensor constitutes a sample data system, delays proportional to the sample rate may be introduced into the tracking loop. The specific effect of these data delays on tracking accuracy is a function of the tracker algorithm employed. Most tracker algorithms measure the LOS angles on two successive frames, use this data to estimate the LOS rate, and then predict the LOS angle for the following frame. If the LOS acceleration is zero, this procedure results in perfect prediction and essentially ideal tracking. Unless a perfect intercept trajectory is flown, however, there will always be some LOS acceleration, although it may be negligibly small except at very short range. Milton(3) indicates that if one knows (or measures) the LOS rate, $\dot{\sigma}$, but does nothing to compensate for LOS acceleration, $\ddot{\sigma}$, then the frame rate, $F_R$, must

---

(3) A. F. Milton, "Active Illuminator and Receiver Options for Aimpoint Selection and Precision Tracking (U)", NRL MR2558, March 1973.

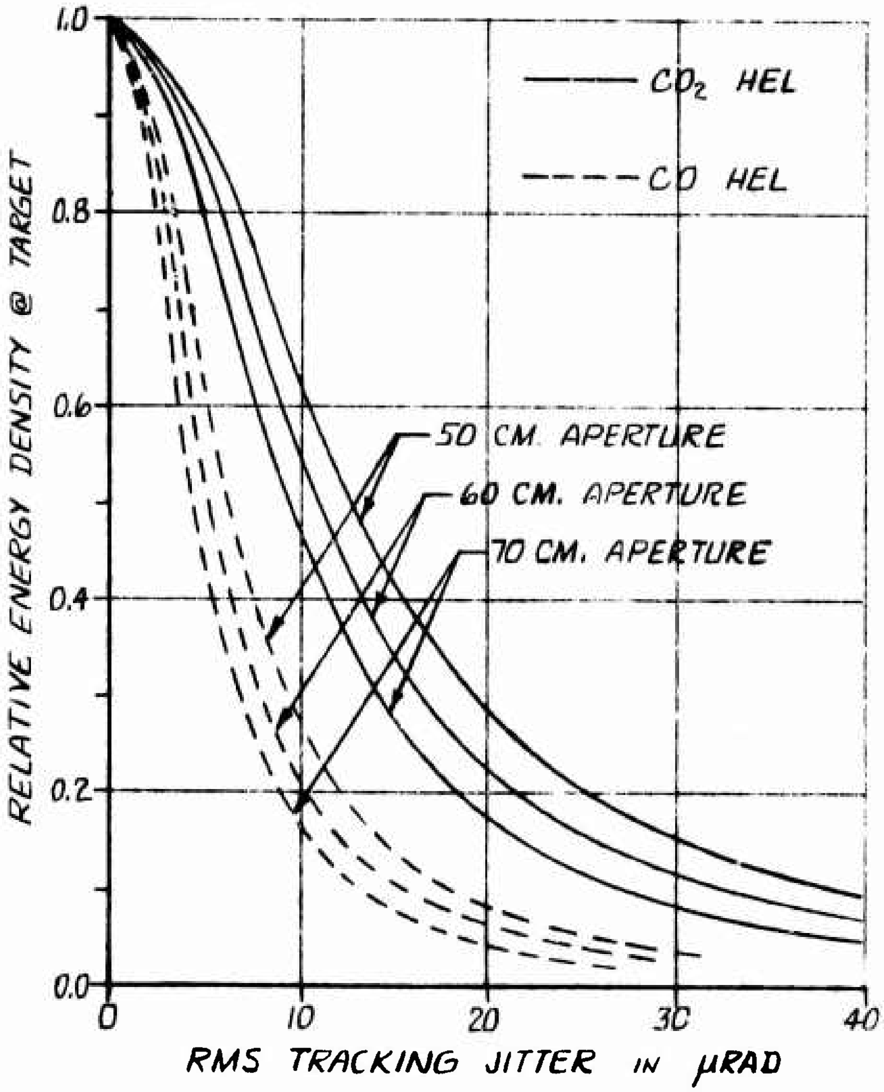

Figure 4. Effect of Tracking Jitter on HEL Effectiveness

satisfy the inequality

$$F_R \geq \sqrt{\frac{\ddot{\sigma}}{2\delta}}$$

for the desired track accuracy, $\delta$, to be realizable. (Other factors such as signal-to-noise ratio and detector quantization also affect track accuracy but these effects are ignored here.)

Although LOS acceleration, as was LOS rate, is determined by the specifics of the relative flight dynamics between the target and the SLIR aircraft, an estimate of the magnitudes involved can again be made by assuming a simplified engagement. Differentiating the LOS rate as modeled before and imposing the same conditions of a fixed miss distance, M, and a constant closing velocity, $V_c$, yields the following

$$\ddot{\sigma} = \frac{2MRV_c^{\,2}}{(R^2+M^2)^2}$$

This equation is plotted as a function of range in Figure 5 again for an aircraft fly-by at one kilometer and a missile attack with a 10 meter guidance miss. Note that over the engagement volume of 20 to 1 kilometers in range, the LOS acceleration may be expected to be less than 100 mrad/second$^2$. For a desired track accuracy in the one microradian range, this translates to a maximum frame rate requirement of about 225 Hertz. Because the expected LOS acceleration is less, lower frame rates are permissible at longer ranges as illustrated in Figure 6. The significant point to note is that high frame rates are necessary only at very short range even if the desired track accuracy is extremely demanding.

Track Resolution. In addition to data rate, sensor resolution will also affect the attainable track accuracy of the SLIR system. If we have a sensor with discrete detector elements, this resolution will be quantized. This quantization will result in an edge or centroid position sensing error during target track.

It is well known that the RMS (angular) edge position error due to equi-spaced quantization is given by

$$\theta_{q_e} = \frac{\theta_d}{2\sqrt{3}} \qquad \text{(edge tracking)}$$

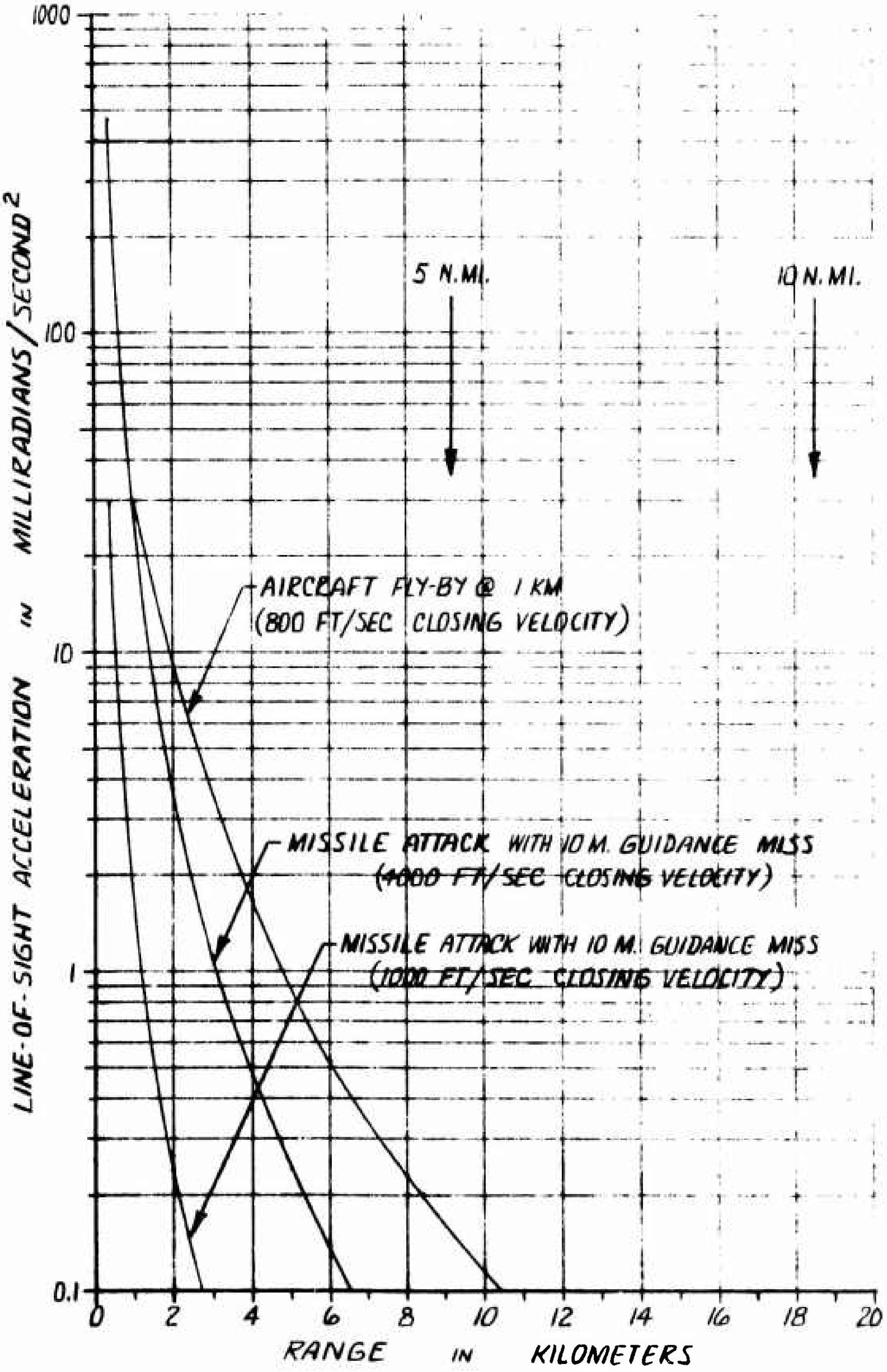

Figure 5. Typical LOS Accelerations during HEL Engagements

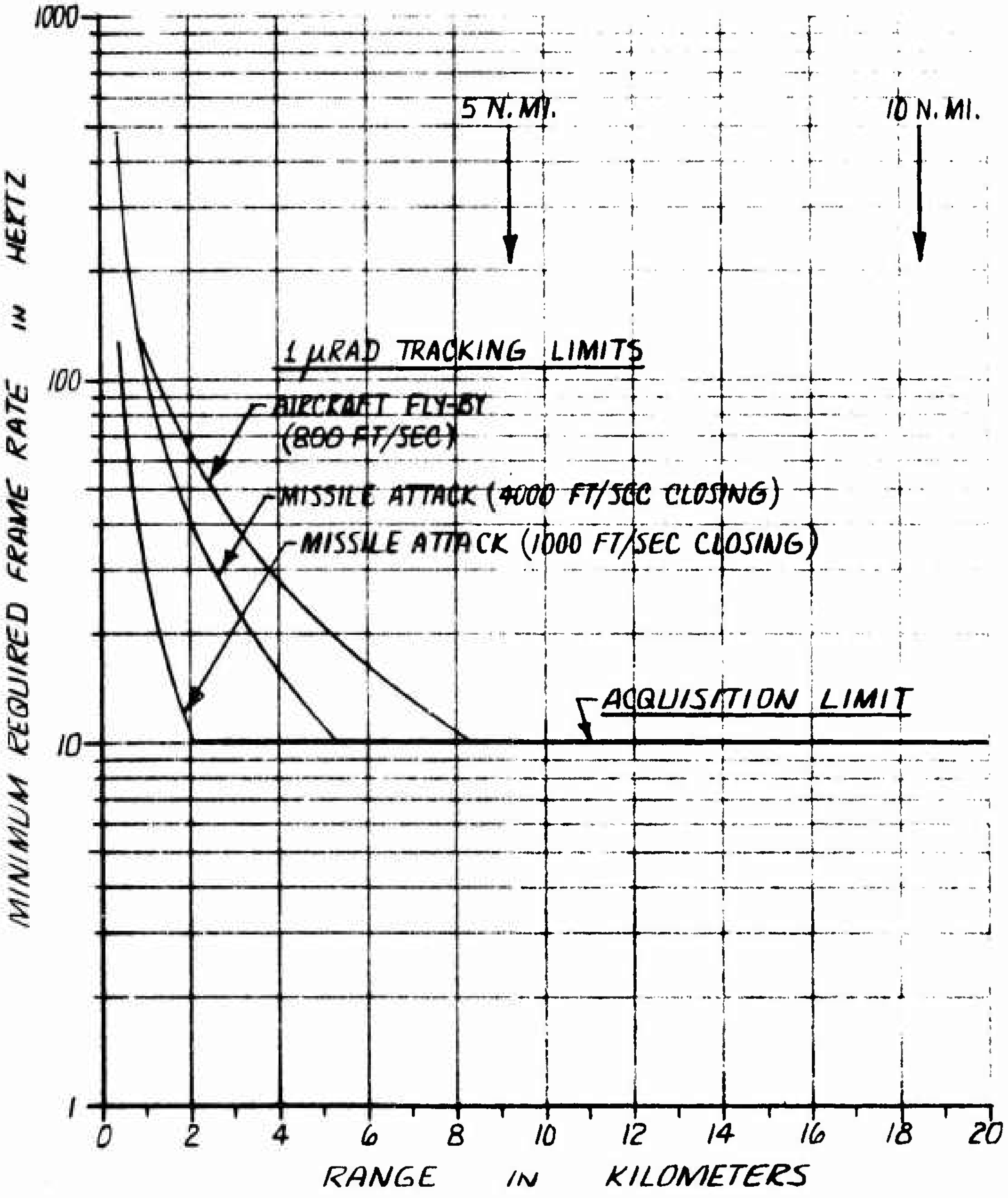

Figure 6. Minimum Frame Rate Requirements for SLIR Operation

where $\theta_d$ is the quantization (angular) resolution. With centroid tracking this RMS position error is improved because two edges are used to obtain the track point. The RMS error is then

$$\theta_{qc} = \frac{\theta_{qe}}{\sqrt{2}} = \frac{\theta_d}{2\sqrt{6}} \qquad \text{(centroid tracking)}$$

If we desire a tracking accuracy capability of less than 2 μrad, the above equation indicates that approximately 10 μrad sensor resolution is required when centroid tracking is employed.

## 2.2 Modes of Operation

Three modes of operation have been defined for the SLIR system: an acquisition mode providing a field of view sufficient to encompass the target with high probability when coarsely pointed by a cueing device such as radar, a track mode providing angular track error data permitting closed-loop tracking of the target after acquisition, and a precision track mode providing angular track error data of sufficient precision and currency to perform the HEL engagement. The track and precision track modes also provide target imaging capability sufficient to permit accurate aimpoint selection for the HEL weapon.

Specific system parameter values for each of these three modes of operation have been suggested in the Statement of Work and these are repeated again in Table 2. These values were based upon an assumed desirability to maintain the scan sweep rate in object space at a constant, fixed value. Although a SLIR system capable of this suggested operational capability might be a highly flexible instrument for test and evaluation purposes, it probably would also be extremely complex as well. Furthermore, the operational versatility indicated by Table 2 often entails significant compromise in operational performance and consequently the need for this versatility must be properly evaluated.

TABLE 2

SOW Suggested Operational Modes

| | | | |
|---|---|---|---|
| Acquisition Mode: FOV (10.24 by 13.65 mrad) | | | |
| Frame Rate | 30, | 60, | 120 Hertz |
| Resolution | 20, | 40, | 80 μrad |
| # Lines | 512, | 256, | 128 |
| Track Mode: FOV (5.12 by 6.83 mrad) | | | |
| Frame Rate | 60, | 120, | 240 Hertz |
| Resolution | 10, | 20, | 40 μrad |
| # Lines | 512, | 256, | 128 |
| Precision Track Mode: FOV (2.56 by 3.41 mrad) | | | |
| Frame Rate | 120, | 240, | 480 Hertz |
| Resolution | 5, | 10, | 20 μrad |
| # Lines | 512, | 256, | 128 |

From the previous discussion on basic SLIR system operational requirements, it appears as though the SOW suggested operational modes may be over-specified. The rectangular shape of the suggested field of views appears to be totally unnecessary. Although the 4:3 aspect ratio is common to conventional television systems, this format was chosen for purely aesthetic reasons when viewing terrestrial scenes and has little bearing, if any, on an air-to-air application. Since the required FOV should reflect the uncertainty with which the position of the target is known, a symmetrical (square or circular) FOV would be a more reasonable choice for the SLIR system. Furthermore, a smaller FOV will permit higher tracking data rates since there are fewer data points to be addressed.

The previous discussion also indicated that high frame rates are required only at short range when one is likely to be in the precision track mode of operation. Hence, it does not appear necessary to have high frame rate capability during acquisition. In fact, an ideal SLIR system would be one which increased its frame rate with decreasing range.

During acquisition 10 to 20 Hertz frame rates appear adequate; while during precision track, the frame rate requirement will gradually increase to over 100 Hertz at fairly short range.

Tracking accuracy (as well as imaging capability) dictates that the sensor resolution be at least 10 μrad during precision track. It may, however, be poorer than this during the acquisition mode. Although it would appear that 5 μrad sensor resolution would be even better, diffraction effects necessitate a very large receiver aperture (e.g., approximately 20 inches diameter at 1.06 μm) if this is to be attainable. Consequently, 10 μrad resolution during precision track appears to be a practical SLIR system goal.

Consideration of all of these operational aspects leads to the recommended SLIR operational modes as listed in Table 3. This simplification results in a system which can meet all basic operational requirements with a minimum of complexity and cost.

TABLE 3

Recommended SLIR Operational Modes

| | Acquisition Mode | Track Mode | Precision Track Mode |
|---|---|---|---|
| FOV | 10 by 10 mrad | 5 by 5 mrad | 2.5 by 2.5 mrad |
| Resolution | 40 rad | 20 rad | 10 rad |
| No. of Lines | 250 | 250 | 250 |
| Frame Rate | 10 to 20 Hertz | 10 to 80 Hertz | 10 to 160 Hertz |

## 2.3 System Interface Requirements and Constraints

Specific SLIR system interface requirements and constraints have not been definitized at this stage of development. However, it is recognized that an airworthy brassboard configuration must be compatible with the Airborne Pointing and Tracking (APT) System illustrated in Figure 7 and, therefore, must be designed for minimum size and weight. No such restrictions have been placed on the laboratory breadboard SLIR system.

Although specific weight, volume, and form factor requirements have not been identified, an aperture constraint, based upon available frontal area on the APT inner gimbal, has been specified in the SOW. It is assumed that the area originally delegated to the Tracker-Imager and to the Wide and Narrow Field TV (see Figure 7) will be available to the SLIR system. Consequently, the diameter of the receiver aperture must not exceed 9 inches and that of the illuminator aperture must not exceed 6 inches.

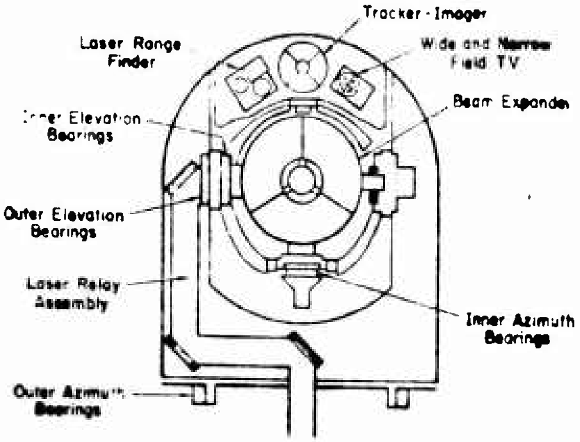

Figure 7. Schematic Diagram of the APT System

## 2.4 Basic SLIR System Concepts

Two basic system design approaches are applicable to the Scanned Laser Illuminator/Receiver: a scanning illuminator with a staring receiver and a scanning illuminator with a scanning receiver. (Although a flood illuminator approach is recognized as a viable alternative to the scanned approach, it is also a solution which is non-responsive to the intent of the SOW.) A staring receiver implies an instantaneous field of view (IFOV) which is wide and which completely covers the scan field of interest. A scanning receiver, on the other hand, implies a narrow IFOV which must be scanned to completely cover the scan field of interest. Within these two basic approaches, however, are at least two variations, each with their own separate and distinctive characteristics. For example, an optical receiver, be it either staring or scanning, may employ either a single detector element or an array of detector elements.

If the latter, this array may be of either linear or areal geometry. Careful consideration must be given to each of these alternatives, not only on theoretic grounds, but on practical grounds as well. It does little good to propose a configuration which is theoretically optimal if it cannot be realized in practice. Each of the basic alternatives appropriate to the Scanned Laser Illuminator/Receiver is illustrated in Figure 8, and is discussed in the following paragraphs.

Single Detector Staring Receiver. The resolution of a staring receiver employing a single detector is defined solely by the beamwidth of the scanning laser beam. Therefore, the illuminator beam must be "pencil-shaped" and must exhibit a constant and well-defined beamwidth over its entire scan field. For a desired system "resolution" on the order of 5 or 10 microradians, the performance requirements which the laser illuminator and its scanner must meet are exceedingly stringent. Furthermore, the single detector staring receiver is highly susceptible to background and backscatter radiation since the entire FOV is focused on the single detector and range-gating of the detector is not functionally practical. Consequently, the single detector staring receiver is an unattractive approach for the Scanned Laser Illuminator/Receiver.

Multiple Detector Staring Receiver. The viability of a staring receiver with a multiple detector array is considerably more favorable. System resolution is now defined by the resolution characteristic of the detector array. Hence, the performance requirements placed on the laser illuminator and its scanner can be greatly relaxed. Furthermore, the area array staring receiver is less susceptible to background and backscatter radiation and can be range-gated if a pulsed illuminator is used. Note, however, that a pencil-beam pulsed illuminator requires a PRF so high that range-gating of the receiver is virtually ineffective.

Single Detector Scanning Receiver. The third concept, which employs a single detector scanning receiver, is an attractive solution in that it provides an excellent match between the illuminator beam and the receiver IFOV and is negligibly sensitive to background and backscatter radiation. Although this concept utilizes a simple single-detector receiver, the scanning and synchronization of the illuminator beam and the

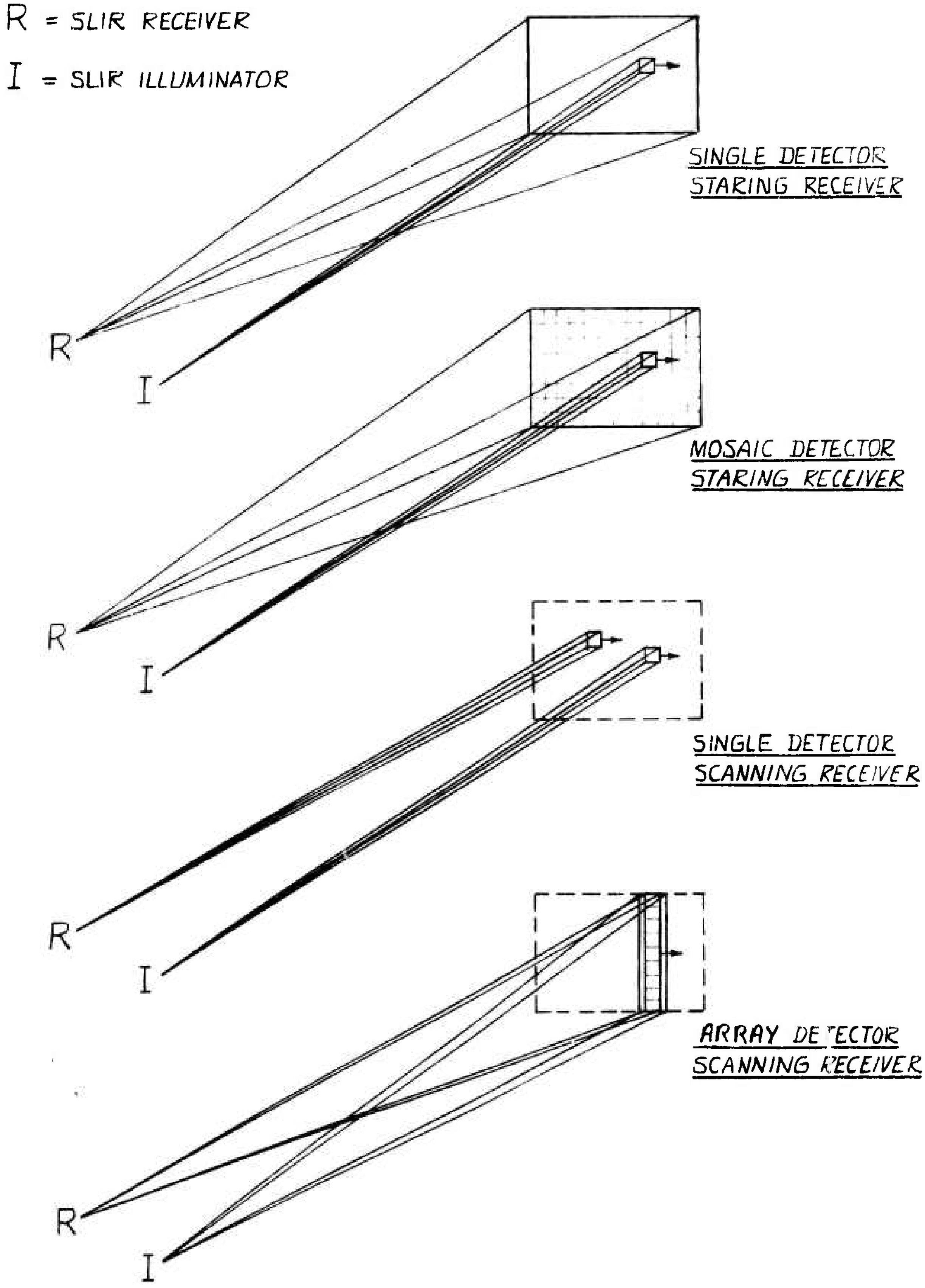

Figure 8. Alternative SLIR System Concepts

receiver IFOV is extremely difficult to achieve if resolution on the order of 10 microradians is to be achieved. Not only is two-axis, high-speed scanning required for both the illuminator and the receiver, but precise angle-of-arrival compensation between the two is required to offset the round-trip propagation delay due to the finite velocity of light.

Multiple Detector Scanning Receiver. The last concept, which employs a multiple detector scanning receiver, is in essence a hybrid between the second and third concepts which accrues many of their advantages while minimizing their disadvantages. Although this concept is slightly susceptible to background and backscatter radiation, it also provides a good match between the illuminator beam and the receiver IFOV while requiring only single axis, low speed scanning which greatly reduces the problems of scan synchronization and angle-of-arrival compensation.

System Concept Summary. A summary of the basic characteristics of each of the four general concepts just described is given in Table 4. Although each presents its own distinct advantages and disadvantages, the last appears to offer the best compromise in that it promises good performance with minimal complexity. This baseline SLIR system concept is schematically illustrated in Figure 9.

The basic system requirements of long range target acquisition and high resolution target tracking and imaging dictate the use of a laser illuminator providing high average beam power in a low order mode together with a matching high sensitivity, high resolution receiver. A CW-pumped Nd:YAG laser operated in a pulsed mode and providing a fan-shaped illumination beam through the use of anamorphic beam expansion is a prime candidate for the illuminator. Similarly, a line array of high 1.06 μm quantum efficiency photodiodes which are multiplexed by a charge-coupled device (CCD) shift register is a prime candidate for the receiver. To minimize the effects of backscatter radiation, the receiver must be range-gated in delayed synchronism with the pulsed illuminator.

## TABLE 4

### Alternate SLIR System Concepts Summary

- Single Detector, Staring Receiver
  - Wide IFOV
  - Resolution defined by illuminator beamwidth
  - Highly susceptible to background and backscatter
  - Range-gating not practical
- Multiple Detector, Staring Receiver
  - Wide IFOV
  - Resolution defined by detector array
  - Moderately susceptible to background and backscatter
  - Range-gating practical with fan or flood beam illuminator only
- Single Detector, Scanning Receiver
  - Narrow IFOV
  - Resolution defined by detector
  - Virtually insensitive to background and backscatter
  - Requires two-axis scanning
  - Requires precise range accuracy for dynamic angle compensation
- Multiple Detector, Scanning Receiver
  - Intermediate IFOV
  - Resolution defined by detector array
  - Moderately susceptible to background and backscatter
  - Range-gating practical with fan beam illuminator
  - Requires one-axis scanning only
  - Does not require precise range accuracy or dynamic angle compensation

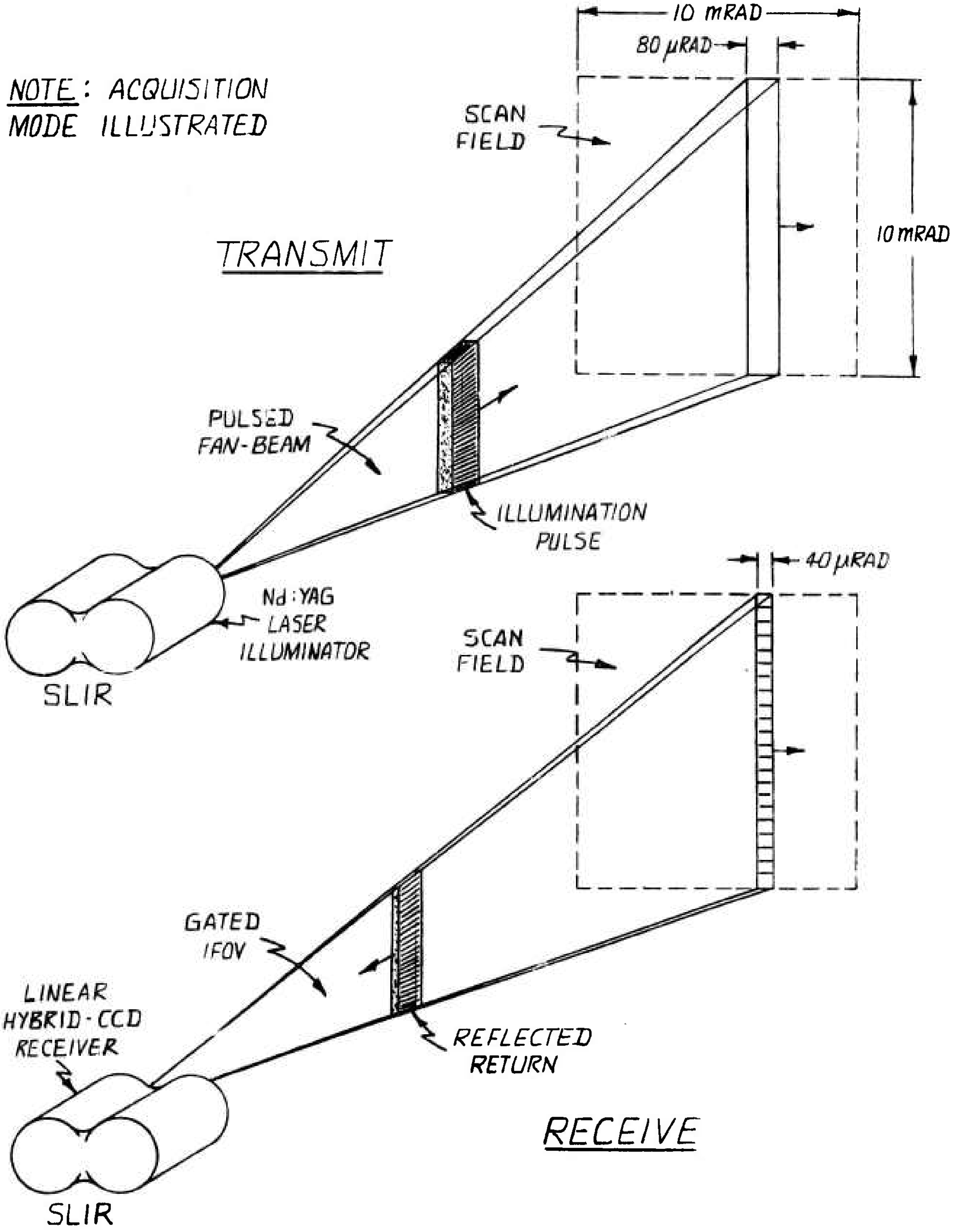

Figure 9. Baseline SLIR System Concept

The operation of the selected SLIR concept may be best described by dividing the operational sequence into a transmit period and a receive period. During the transmit period a fan-shaped illumination pulse is generated by the laser illuminator and subsequently propagates toward the search field containing the target. After reflection by the target, this illumination pulse propagates back during the receive period and is detected by the receiver. The receiver's IFOV is gated open only during the time that a return from the target is expected. The synchronism between the generation of the illumination pulse and the opening of the receiver's gate is determined by simultaneously measuring the range to the target (e.g., by means of search radar or a laser rangefinder). Some overlap between the illumination beam profile and the receiver IFOV, as illustrated, is probably desirable to account for any misregistration between the two.

## 2.5 Range Equation Fundamentals

The impact of the previously described SLIR system requirements on the SLIR system design can be clearly dramatized by an examination of the appropriate range equation which predicts system performance. This range equation is derived briefly in what follows.

Suppose we have a laser which is capable of a time-averaged radiant output beam power of $P_L$ watts. If this laser is Q-switched to generate output pulses of duration $t_p$ and at a repetition rate of PRF, then the peak radiant output beam power (per pulse) will be

$$P_p = \frac{P_L}{t_p\,(PRF)}$$

Similarly, the peak radiant output beam energy (per pulse) will be

$$E_p = P_p\, t_p = \frac{P_L}{PRF}$$

Now, if this radiant energy from the laser is collected by illuminator optics with efficiency $\tau_I$ and uniformly projected into a solid angle $\Omega_B$, then the illuminator beam radiant intensity (per pulse) will be

$$J_B = \frac{P_p \tau_I}{\Omega_B} = \frac{P_L \tau_I}{t_p (PRF)\ \Omega_B}$$

After propagating a distance R through an atmosphere of transmittance $\tau_A$, the irradiance (per pulse) at this distance will be

$$H_I = \frac{J_B \tau_A}{R^2}$$

$$= \frac{P_L \tau_I \tau_A}{t_p (PRF)\ \Omega_B\ R^2}$$

A target at the distance R which is irradiated by the illumination beam will reflect a portion of the incident energy back in the direction from which it came. The amount of energy returned will depend upon the size and directionally reflective properties of the target itself. For a target at long range, it is usually convenient to define an effective optical cross-section, $A_e$, such that the target's apparent radiant intensity $J_t$, will satisfy the following relation:

$$J_T = \frac{A_e}{4\pi}\ H_I \qquad \text{(unresolved target)}$$

At short range, where the target's angular subtense is much larger than the IFOV of a single detector element and the target may be considered to be resolved or imaged, it is more convenient to define the target's radiant intensity in terms of its reflectivity, $\rho$, and its apparent size, $A_T$, i.e.,

$$J_T = \frac{\rho A_T}{\pi} H_I \qquad \text{(fully resolved target)}$$

After reflection from the target and again propagating a distance R through an atmosphere of transmittance $\tau_A$, the illuminator beam radiant energy will produce an irradiance (per pulse) at the receiver of

$$H_R = \frac{J_T \tau_A}{R^2}$$

This energy will be collected by the receiver aperture of diameter D and focused by imaging optics with effective focal length F and effective transmittance $\tau_R$ onto a detector element of area $A_D$. The radiant power incident on each detector is then

$$P_D = \zeta \frac{\pi D^2}{4} \tau_R H_R$$

where $\zeta$ is the fractional part of the object's image in the focal plane received by that detector. If none of the image falls on a particular detector, then $\zeta = 0$ for that detector. Conversely, if all of the image falls on a particular detector (such as would be the case when the object is unresolved), then $\zeta = 1$. Also, if only a portion of the image falls on a particular detector, then for that detector

$$\zeta \simeq \frac{A_D}{A_I}$$

$$= \frac{\theta_D^2 R^2}{A_T}$$

where $A_I$ is the area of the image and $\theta_D^2$ is the instantaneous field of view of a single detector in object space.

The radiant energy (per pulse) incident upon a detector element may then be written as

$$E_D = P_D \, t_p$$

$$= \frac{P_L \, \tau_I \, \tau_R \, \tau_A^2 \, A_e \, D^2}{16 \, (PRF) \, \Omega_B \, R^4} \qquad \text{for unresolved target at long range}$$

$$= \frac{P_L \, \tau_I \, \tau_R \, \tau_A^2 \, \rho \, \theta_D^2 \, D^2}{4 \, (PRF) \, \Omega_B \, R^2} \qquad \text{for fully resolved target at short range}$$

The receiver signal-to-noise ratio produced by this radiant signal energy is dependent upon the noise characteristics of the receiver itself. When the predominant source of noise is due to the detector (and its subsequent signal processing electronics), it is convenient to characterize the receiver by its noise equivalent energy (NEE) or its noise equivalent power per root bandwidth (NEP). The signal-to-noise ratio at the receiver output may then be written as

$$SNR = \frac{E_D \, \xi_p}{(NEE)}$$

or

$$SNR = \frac{E_D \, \xi_p}{t_p \, (NEP) \sqrt{B}}$$

where $\xi_p$ is the relative pulse responsivity of the detector/preamplifier combination and B is the receiver noise bandwidth.

For the ideal case in which both detector and background noise are negligible with respect to signal shot noise, we have the ultimate receiver performance. It is well known that under these conditions, Poisson statistics apply and the signal-to-noise ratio is given by the square root of the number of signal electrons generated; i.e.,

$$SNR = \sqrt{\left(\frac{\eta}{h\nu}\right) E_D \, \xi_p}$$

where $\eta$ is the detector's quantum conversion efficiency, h is Planck's constant ($6.626 \times 10^{-34}$ joule-sec) and $\nu$ is the frequency of the detected electro-magnetic radiation ($2.83 \times 10^{14}$ Hertz for 1.06 μm radiation).

Using the above equations and solving for range R then yields the following range equations

$$R_V = \frac{R}{\sqrt{\tau_A}} = \left[\frac{1}{16} \, (A_e) \left(\frac{P_L \, \tau_I}{(PRF) \, \Omega_B}\right) \left(\frac{\tau_R \, \xi_p \, D^2}{(SNR) \, (NEE)}\right)\right]^{1/4} \qquad \text{Unresolved Target}$$

or

$$R_V = \frac{R}{\sqrt{\tau_A}} = \left[ \frac{1}{16} (A_e) \left( \frac{P_L \; \tau_I}{t_p \; (PRF) \, \Omega_B} \right) \left( \frac{\tau_R \; \xi_p \; D^2}{(SNR) \; (NEP) \sqrt{B}} \right) \right]^{\frac{1}{4}} \quad \text{Unresolved target}$$

$$\left. \begin{aligned} R_V &= \frac{R}{\tau_A} = \left[ \frac{1}{4} (\rho) \left( \frac{P_L \; \tau_I}{(PRF) \; \Omega_B} \right) \left( \frac{\tau_R \xi_p \; \theta_D{}^2 \; D^2}{(SNR) \, (NEE)} \right) \right]^{\frac{1}{2}} \\ &\text{or} \\ R_V &= \frac{R}{\tau_A} = \left[ \frac{1}{4} (\rho) \left( \frac{P_L \; \tau_I}{t_p \; (PRF) \; \Omega B} \right) \left( \frac{\tau_R \; \xi_p \; \theta_D{}^2 \; D^2}{(SNR) \, (NEP) \sqrt{B}} \right) \right]^{\frac{1}{2}} \end{aligned} \right\} \text{Resolved target}$$

where the term in the first parentheses represents target parameters, the term in the second parantheses represents illuminator parameters, and the term in the third parentheses represents receiver parameters. Note that because atmospheric transmittance, $\tau_A$, is a function of range, these equations have been written in terms of a hypothetical "vacuum range", $R_V$. The important thing to note from these equations is that range performance increases with the fourth-root of the system parameters when the target is unresolved, but with the square-root of the system parameters when it is fully resolved. The transition from the unresolved to fully resolved situation occurs at a range dependent upon both target size and receiver IFOV. This transition range may be readily shown to be

$$R_{trans} \approx \sqrt{\frac{A_e}{4 \rho \theta_D{}^2}}$$

for a diffusely reflecting target of reflectivity $\rho$ and effective optical cross-section $A_e$.

For the ideal case of a signal shot noise limited receiver, the appropriate range equations are:

$$R_V = \frac{R}{\sqrt{\tau_A}} = \left[ \frac{1}{16} (A_e) \left( \frac{P_L \; \tau_I}{(PRF) \; \Omega_B} \right) \left( \frac{\tau_R \xi_p \; \eta \; D^2}{h\nu \; (SNR)^2} \right) \right]^{\frac{1}{4}} \quad \text{unresolved target}$$

$$R_V = \frac{R}{\tau_A} = \left[ \frac{1}{4}(\rho) \left(\frac{P_L\ \tau_I}{(\mathrm{PRF})\ \Omega_B}\right) \left(\frac{\tau_R\ \xi_p\ \eta\ \theta_D{}^2\ D^2}{h\nu\ \mathrm{SNR})^2}\right)\right]^{\frac{1}{2}} \qquad \text{fully resolved target}$$

These last two equations are plotted in Figure 10 for a small missile target of 100 $\mathrm{cm}^2$ optical cross-section and 0.2 reflectivity. A Nd:YAG laser capable of 100 watts average output beam power and an ideal signal shot-noise-limited detector having unity quantum efficiency at 1.06 μm were assumed as representative of the best illuminator and receiver performance that can be expected in the near future. Typical SLIR system parameters, as defined in previous subsections, have also been assumed. The curves in Figure 10 indicate that acquisition of the small missile target at a 5 nautical mile (9.26 kilometer) range is possible with such a SLIR system if the illuminator PRF is 10 kilohertz or less. A signal-to-noise ratio approaching 10 to 1 is predicted under these conditions. It should be noted that a receiver which is not signal shot-noise-limited will exhibit a correspondingly lower signal-to-noise ratio. Hence Figure 10 represents the upper performance limit that can be expected for a small missile target of 100 $\mathrm{cm}^2$ optical cross-section.

Aircraft targets will provide substantially higher signal-to-noise ratios at longer ranges due to their correspondingly larger optical cross-sections. A typical value for the optical cross-section of an aircraft target might be on the order of 10 $\mathrm{m}^2$, or three orders of magnitude higher than this missile target. Assuming that this value is representative, the upper performance limits that can be expected with a SLIR system when engaging an aircraft target are as shown in Figure 11. These curves indicate that acquisition of aircraft targets at a 10 nautical mile (18.52 kilometer) range is possible with such a SLIR system if the illuminator PRF is in the 10 kilohertz range. As before, these curves represent upper performance limits for a SLIR system. A system which exhibits non-unity detector quantum efficiency or non-signal shot-noise-limited receiver operation will also exhibit a correspondingly lower signal-to-noise ratio performance. Also, since the curve shown in Figures 10 and 11 are plotted in terms of "vacuum range", the actual range will be somewhat less depending upon

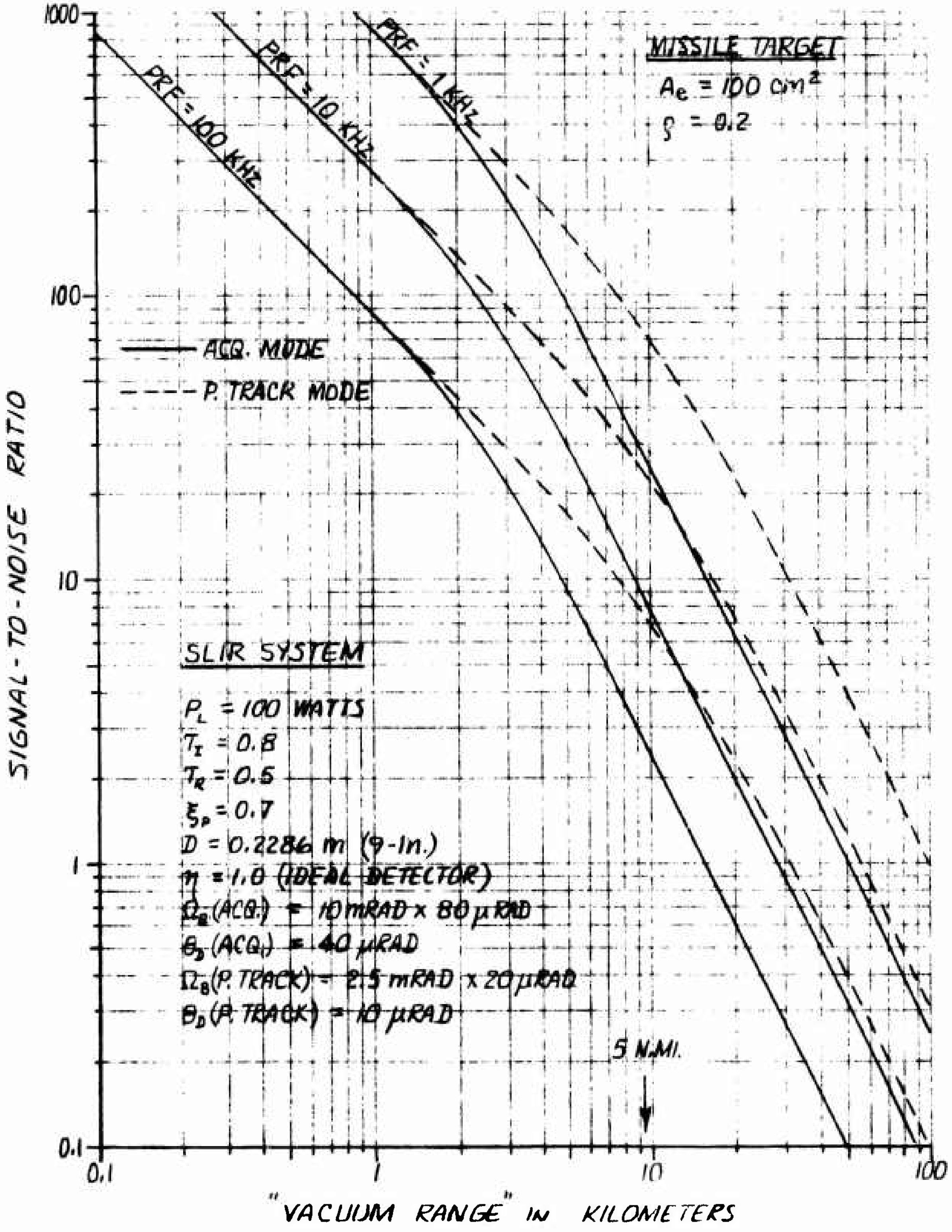

Figure 10. Limiting Performance of Ideal SLIR System for Missile Target

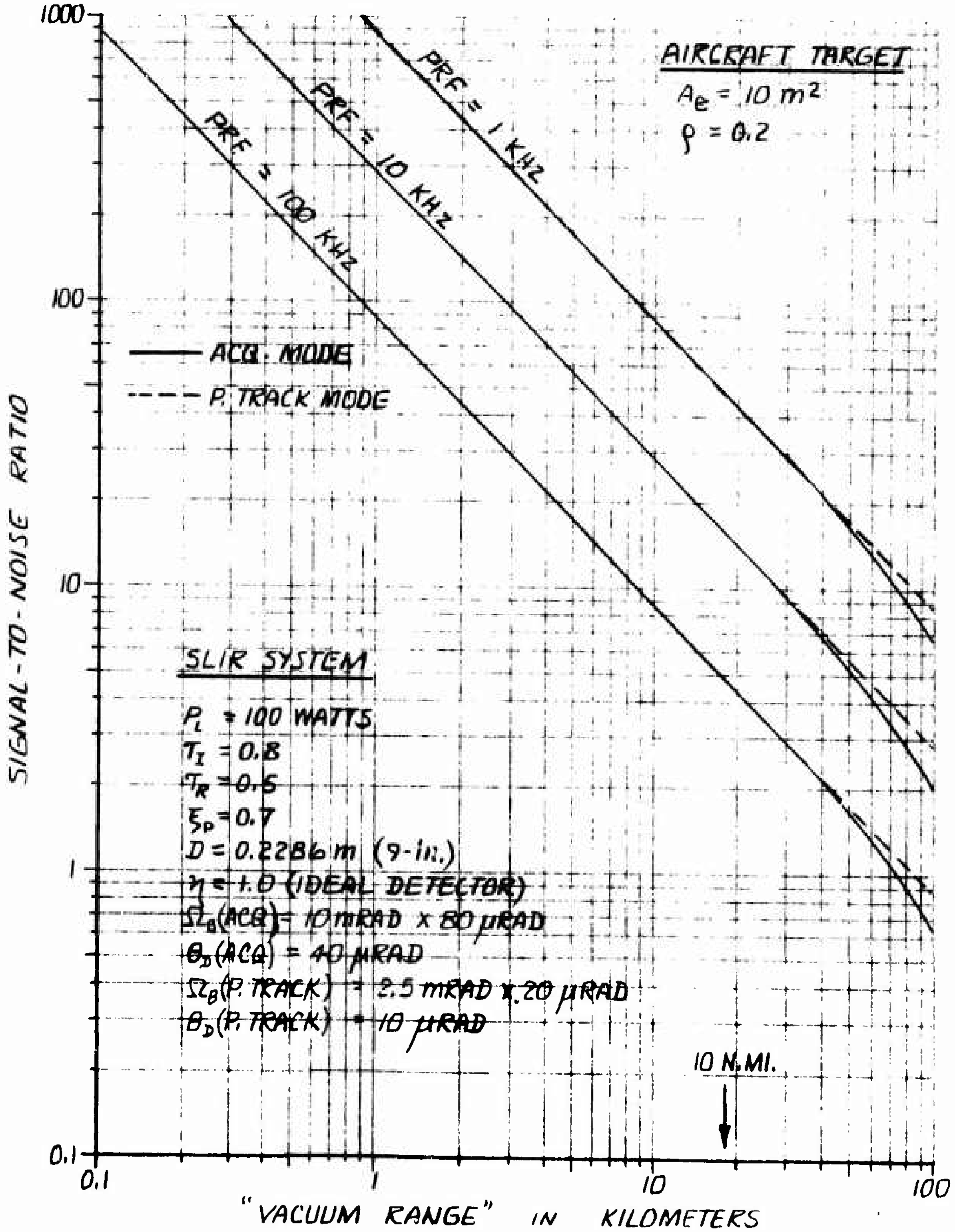

Figure 11. Limiting Performance of Ideal SLIR System for Aircraft Target

atmospheric extinction due to weather. At high altitudes (above 5 kilometers), this extinction is nearly negligible except for ranges in excess of 20 kilometers.

It is apparent from Figures 10 and 11 that signal-to-noise ratio or range performance is enhanced by either lower illuminator PRF or tighter illuminator beam spread. One cannot arbitrarily reduce these two parameters, however, since they both have a direct impact of the system frame rate, $F_R$. Simple logic will show that the frame rate is related to illuminator PRF by

$$F_R = \xi_I \frac{(\mathrm{PRF})\ \Omega_B}{\phi_F^2}$$

where $\xi_I$ is the illuminator scan efficiency which includes beam overlap and dead time, and $\phi_F$ is the angular subtense of an assumed square search field. This equation is plotted in Figure 12 for a scan efficiency of 0.5 and a search field of 10 by 10 mrad (acquisition mode). A fan-beam illuminator which completely covers the search field by a linear one-dimensional sweep is assumed. Note that at a one kilohertz illuminator PRF, the frame rate is limited to less than 10 Hertz. A 10 kilohertz PRF, on the other hand, permits frame rates in the 10 to 100 Hertz range. Higher frame rates require correspondingly higher illuminator PRF. This observation emphasizes the need to maintain low frame rates and, therefore, low illuminator PRF during long range target acquisition when signal-to-noise ratio is paramount. Once track is established and range closure occurs, higher frame rates and illuminator PRF can be used to trade excess signal-to-noise ratio for increased data rate which becomes increasingly important at the short ranges where target dynamics become significant.

The illuminator PRF requirements for a comparable pencil-beam SLIR system are also indicated in Figure 12. Note that such a system would require illuminator PRFs in the megahertz range which is clearly far beyond the present state-of-the-art. Consequently, a pencil-beam system configuration is a totally impractical solution to the SLIR operational requirements.

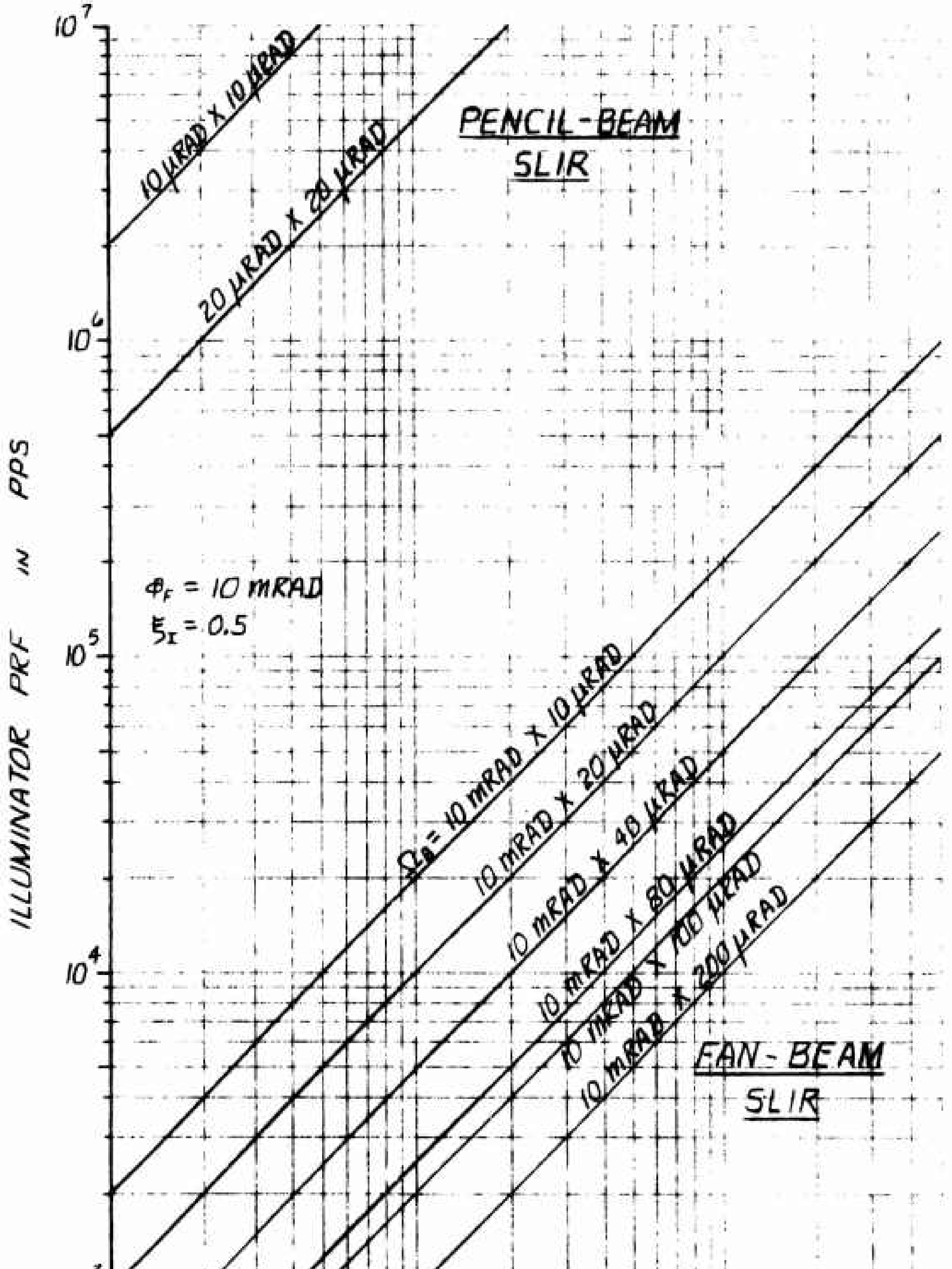

Figure 12. Illuminator PRF Requirements

# SECTION III

# TECHNOLOGY CONSIDERATIONS

As emphasized in the previous section, the SLIR system performance goals are quite demanding. The realization of this performance with actual hardware will necessarily require judicious component selection and specification and careful system design so as to minimize unnecessary compromise. In some areas, particularly those of the high power laser and the high sensitivity receiver, the required performance exceeds the present state-of-the-art. In most cases, however, the technology for achieving these performance levels already exists but has not been applied in either the manner or to the level required by the SLIR system.

In the following subsections, this technology is examined in some detail with specific emphasis on its direct applicability to the fan-beam SLIR system concept previously described. Operational limitations which influence the achievement of performance goals by these technological solutions are also discussed. Although a technology survey and evaluation of this sort should be extensive and thorough, the level of effort allocated to this study did not permit such an ambitious undertaking. Nevertheless, every effort has been made to cover, at least qualitatively, every area of technical importance relating to the scanner, the illuminator, and the receiver of the selected SLIR system concept.

## 3.1 Illuminator/Receiver Scanning Technology

Laser scanning techniques can, in a practical sense, be divided into two basic types: those capable of providing "large" angular excursions of the laser beam, and those limited to providing only small angular excursions. These scanner types can be further subdivided into those giving precise, repeatable excursions and those which preclude exact geometric registration from scan to scan or from frame to frame. A final subdivision may be made by separating those techniques which are capable of the laser scanning rates required by the system configuration from those which are not. Mechanical, electro-optical, and acousto-optical laser scanning techniques may be similarly subdivided among these classes to facilitate the selection of the best technique for the Scanned Laser Illuminator/Receiver.

The possible laser illuminator/receiver concepts range from the simple flood laser/staring receiver concept, as exemplified by conventional active TV systems, to the complex scanned pencil-beam laser/synchronously scanned receiver system, as exemplified by reconnaissance laser linescanners. Intermediate to these two extremes are a class of concepts which use a one-dimensionally scanned fan-beam laser.

The flood beam laser concept is attractive because of its relative simplicity. Because it minimizes laser beam manipulation, it avoids any geometric registration problems which might otherwise exist. Conversely, the scanned pencil-beam concept presents potentially severe problems in laser beam manipulation (at video rates), geometric registration (including angle of arrival effects due to propagation delay), and beam shaping (small beam divergence). The fan-beam concept reduces the laser beam manipulation and registration problems to a one-dimensional situation in which field (or frame) rates rather than line rates are involved. Consequently, implementation of the fan-beam concept is considerably more straight forward than implementation of a pencil-beam configuration.

In considering a particular scanning technique which requires geometric registration between the laser illuminator and a scanning receiver, it is important to realize that geometric fidelity is enhanced if both laser and receiver use the same type of scanning technique or, better yet, if they both use the same scanning element on a time or area shared basis. This is particularly important when implementing the scanned pencil-beam concept in a high resolution system and is highly desirable when implementing the scanned fan-beam concept since it effectively circumvents any problems which may occur due to slaving accuracy or random jitter. This desired commonality between laser and receiver scanner, however, restricts the number of scanning techniques to only a few possibilities. Of these, electro-optic, acousto-optic, and mechanical scanners are the most viable candidates.

### 3.1.1 Electro-Optic Effect Scanners

The electro-optic effect may be utilized to deflect a laser beam and thereby generate a scan of the field-of-view. With reference to Figure 13, the operation of such a laser beam deflector may be described as follows.

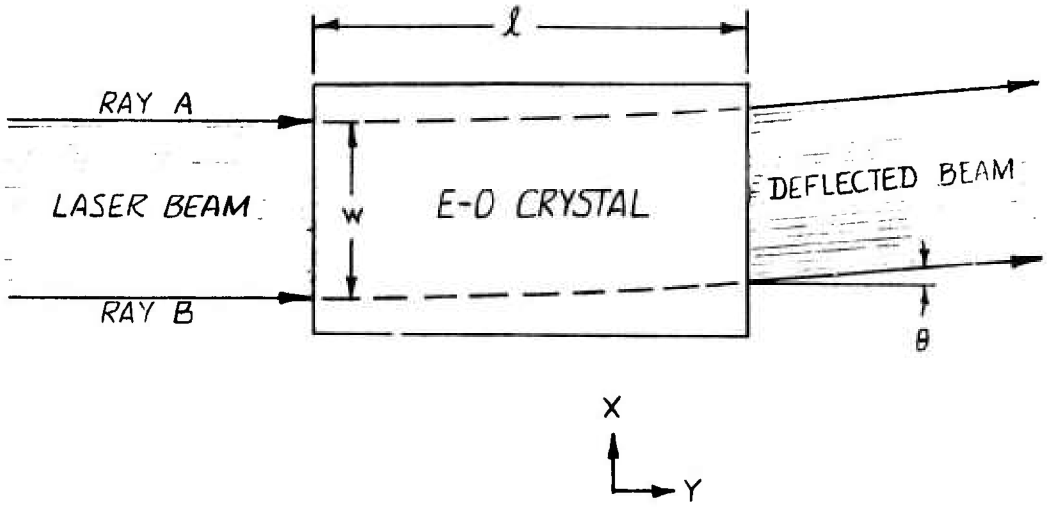

Figure 13. Electro-Optic Deflection

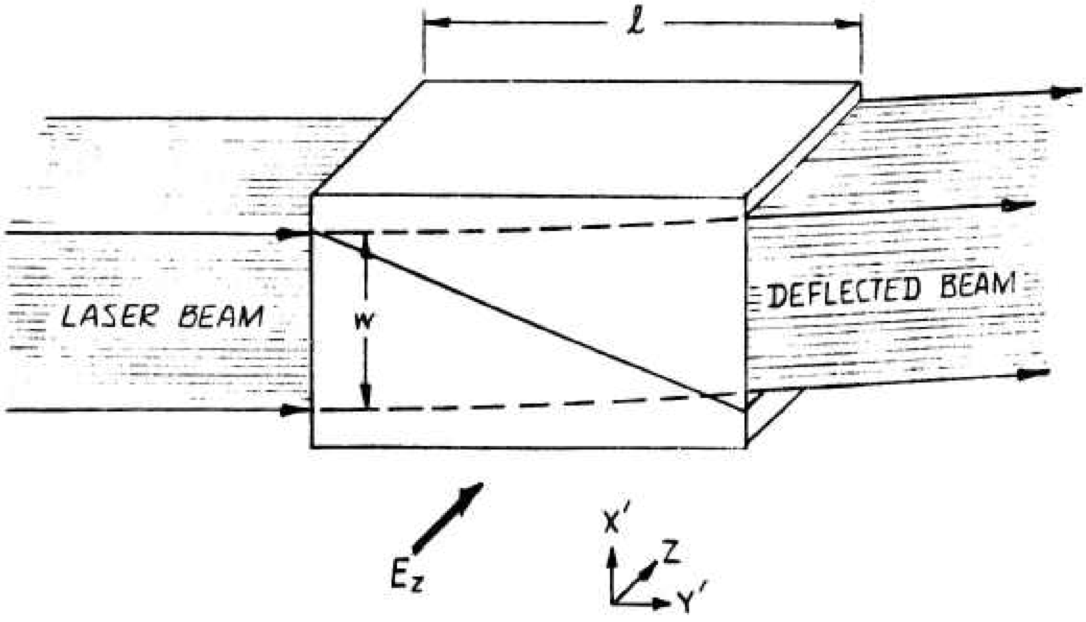

Figure 14. Double Prism KDP Beam Deflector

A collimated laser beam is incident on a crystal which exhibits the electro-optic effect; i.e., one in which the index of refraction, $\eta$, can be made a linear function of the transverse direction (e.g., $\eta(x)=\eta_o + ax$) by the application of an electric field across the crystal. If the indices of refraction for rays A and B, as shown in Figure 13, differ by $\Delta\eta$, then the upper ray (A) will lag the lower ray (B) at the exit plane (just inside the crystal) by

$$\Delta y = \ell \frac{\Delta\eta}{\eta}$$

This results in a deflection, $\theta$, of the output beam of

$$\theta = \eta\,\theta_{\text{internal}} = -\frac{\ell}{W}\Delta\eta = -\ell\frac{d\eta}{dx}$$

At 1.06 μm an electro-optic beam deflector using two KDP prisms as shown in Figure 14 can be fabricated. The z-axes of each of the two prisms are oriented parallel but opposite to each other and an electric field is applied in the z-direction. A polarized laser beam propagates through the crystal in the y' direction with its plane of polarization oriented in the x' direction. A ray propagating entirely in the upper prism will then encounter an index of refraction given by

$$\eta_A = \eta_o - \frac{\eta_o^3}{2} r_{63} E_z$$

where $r_{63}$ is the 6, 3 electro-optic tensor coefficient characteristic of the crystal. Similarly a ray propagating entirely in the lower prism sees an index of refraction given by

$$\eta_B = \eta_o + \frac{\eta_o^3}{2} r_{63} E_z$$

The deflection angle may then be written as

$$\theta = \frac{\ell}{W}\eta_o^3 r_{63} E_z$$

For KDP crystals, the ordinary index of refraction, $\eta_o$, is approximately 1.51 and the electro-optic tensor coefficient, $r_{63}$, is approximately $10.6 \times 10^{-12}$ m/volt. For an electric field, $E_z$, of $10^5$ volts/m and an $\ell/W$ ratio of 10, the beam deflection that can be achieved is then

$$\theta = 37\ \mu\text{rad}$$

The use of KD*P material instead of KDP can increase this deflection angle by a factor of 2.1 due to its larger electro-optic tensor coefficient; but in any event, the deflection that can be achieved by the electro-optic effect with reasonable parameter values is small. Although optical magnification of this deflection is possible, it is only at the expense of increased beam divergence. Consequently, the use of the electro-optic effect as a scanning technique for the Scanned Laser Illuminator/Receiver is not favorable and may be summarily eliminated from further consideration.

### 3.1.2 Acousto-Optic Effect Scanners

The acousto-optic effect may also be used to deflect a laser beam and thereby generate a scan of the field-of-view. When a light wave and an acoustic wave interact within an acoustic deflector, the light wave is directed to a Bragg angle that may be varied by the frequency of the acoustic wave. Hence, a laser beam may be deflected through an angle which is proportional to the acoustic drive frequency. The operation of such a scanner is illustrated in Figure 15 and described as follows.

A collimated laser beam propagating in the y-direction is incident on a crystal in which an acoustic wave is propagating in the orthogonal x-direction. The A-O deflector may operate in one of two modes: in the first, the laser beam diameter is small with respect to the acoustic wavelength; in the second, the beam diameter is large. In the first case, beam deflection is achieved by refraction of the incident beam by the acoustic wave. In the second case, the short acoustic wavelength produces in effect a diffraction grating within the crystal and beam deflection is achieved through interference effects. In both cases, the acoustic wave is usually generated by a piezoelectric transducer affixed to the acousto-optic crystal. However, the first case of refractive deflection is useful only if a sinusoidal scan of the laser beam is desired since it is sinusoidally deflected by the passing acoustic wave. The second case of diffractive deflection is considerably more versatile and is therefore considered in more detail in what follows.

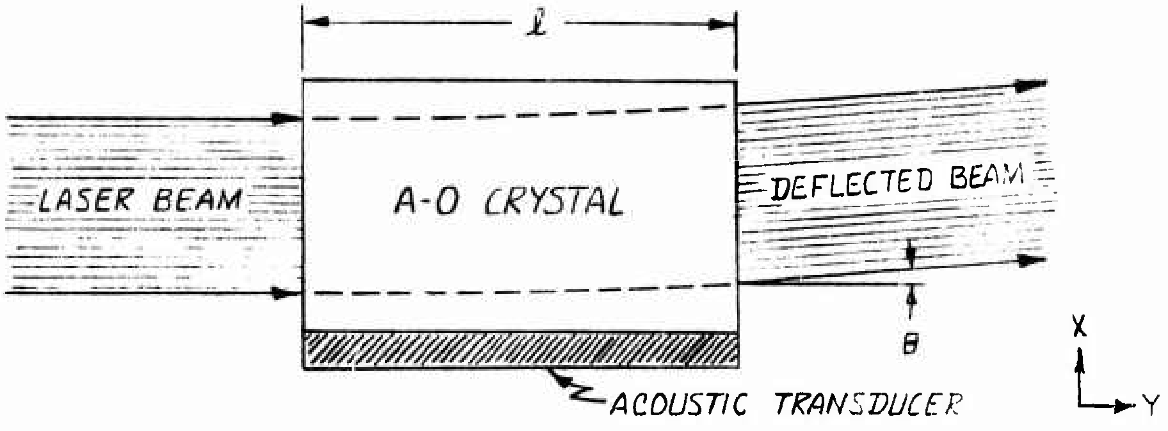

Figure 15. Acousto-Optic Deflection

The deflection angle, θ, produced by an acousto-optic deflector operated in the diffraction mode is given by

$$\theta = \sin^{-1} (\pm N \frac{\lambda}{\Lambda})$$

where N is an integer indicating the order of the diffracted wave, and $\lambda$ and $\Lambda$ are the wavelengths of the laser and the acoustic wave in the A-O crystal, respectively.

Not all of the incident laser energy will undergo deflection in an acousto-optic deflector, however. An important parameter for acousto-optic deflectors is the fraction of the total laser intensity that is deflected. This fraction, $I/I_o$, is given by

$$\frac{I}{I_o} = \sin^2 \frac{\Delta\phi}{2}$$

where

$$\Delta\phi = \pi\sqrt{\frac{2}{\lambda^2} (\frac{L}{H}) M_2 P_{AC}}$$

and L and H are the interaction length and height, respectively, $P_{AC}$ is the acoustic power, and $M_2$ is the A-O crystal figure of merit. A widely used A-O material is fused quartz which has an index of refraction of 1.45, an acoustic velocity of $5.96 \times 10^5$ cm/sec, and an acoustic figure of merit ($M_2$) of $1.51 \times 10^{-18}$ $sec^3/gm$.

If we consider a fused quartz A-O deflector operating at 1.06 μm with an interaction length to height ratio (L/H) of 5:1, an acoustic power ($P_{AC}$) of 20 watts, and an acoustic wavelength of $5.96 \times 10^{-3}$ cm, which corresponds to 100 megahertz, the deflection angle in the first order (N=1) is

$$\theta = 12 \text{ mrad}$$

and the deflector efficiency is

$$\frac{I}{I_o} \simeq 0.5$$

This example is illustrative of the reasonable deflection angles (approximately one degree) that can be achieved with A-O deflectors. Other materials, superior to quartz in terms of their figure of merit, higher drive frequencies, and higher acoustic drive powers can also be used to increase the deflection capability to values significantly higher than that indicated by this example.

Because acousto-optic deflectors are capable of 1000 to 2000 elements per scan resolution and multi-megahertz bandwidths, they have been effectively applied in scanning high resolution images at commercial TV video rates. A pencil-beam SLIR system based on this technique would be feasible especially if used with a staring receiver. Registration and synchronization between the pencil beam and a simultaneously scanning receiver, however, would require that the receiver employ acousto-optic scanning as well. For precise registration and synchronization, use of the same scanner for both the illuminator and the receiver would probably be necessary--a requirement which the acousto-optic scanner is not likely to meet.

### 3.1.3 Mechanical Scanners

Mechanical scanning allows the greatest freedom of selection among the techniques available for manipulating a laser beam over angular excursions of one degree or more. Both reflective and refractive elements can be used. However, mechanical scanning is generally limited to low to moderate scanning rates and is often sensitive to vibration-induced scanning jitter. Consequently, mechanical scanning techniques are not well suited to two-dimensional pencil-beam scanning because they are incapable of attaining video scan rates and give rise to insurmountable geometric and temporal registration problems between the transmitter and the receiver.

However, if a fan-beam illuminator is used, the limitations and weaknesses of mechanical scanning virtually disappear. Required scan rates are now at field or frame frequencies which are normally well within the capabilities of a mechanical scanner. Furthermore, geometric and temporal registration is now required in one axis only and typically with a more forgiving tolerance.

Scan synchronization of the receiver with the illuminator requires that non-linearities in the illuminator scan be faithfully tracked by the receiver and vice-versa. The ideal way to insure this tracking fidelity is to have both the illuminator and the receiver share the same scanner and the same optics. The next best approach is to share either the optics (so that magnification is common over all field of view options) or the scanner (so that vibration-induced scanning jitter is common and hence differentially removed). Because a common optics configuration is exceedingly difficult to design, the common scanner approach is the most attractive alternative for the SLIR system.

Although a common scanner configuration will in principle eliminate all scan jitter between illuminator and receiver, it will not eliminate the scan jitter between the receiver and some absolute reference such as the line of sight to the target. This uncompensated jitter can result in track inaccuracies. Because this jitter cannot be completely eliminated (or compensated), the best one can do is to minimize its effect. This is done by providing sufficient optical magnification between object space and the scanner such that any existing scanner jitter will be de-magnified in object space. Hence a gimballed mirror in front of the illuminator/receiver optical systems is a poor scanner choice because no de-magnification of scanner jitter occurs. However, a scanning element placed behind high power (e.g., at least 10X) illuminator/receiver afocal telescopes is an excellent scanner choice since not only is the effect of scanner jitter minimized but the physical size of the scanner is reduced as well, thereby permitting higher scan rates. In many scanner systems, it is not practical to place the scan element in this optimal position due to a requirement for wide field-of-view scan coverage. This is not a problem for the SLIR system, however, since the maximum scan requirement in object space is only ± 5 milliradians.

There are several generic classes of mechanical scanners. Of these, those with the most applicability to the SLIR system are high inertia mirror scanners, low inertia mirror scanners, and prism scanners. Each of these is discussed in some detail in the following.

High Inertia Mirror Scanners. The rotational mirror drum scanner is unchallenged in its ability to provide a combination of high resolution, excellent linearity, and high scan rate capability over moderate to large scan fields. Because of its high inertia, this type of scanner can scan with very high accuracy and high stability. The prime constraint of high inertia scanners is that they are limited to relatively rigid scan formats.

Scanner fabrication is the principle difficulty with rotational mirror scanners due to the need for a multitude of precisely positioned and aligned mirror facets. Unless the facets are all positioned exactly the same with respect to the axis of the spinner and with respect to each other, unacceptable scan-to-scan variations result. Thus repeatability is a significant problem in fabricating systems employing rotational scanners. These difficulties can be alleviated by use of "holographic facets" which can be created by applying holograms to the surface of an otherwise smooth scanner drum. Their location, size, and shape can vary considerably and still function in a manner similar to their conventionally faceted counterparts. Although such an approach may be attractive in a laser beam scanning application, it would be of questionable effectiveness in a receiver scanning role since it depends upon a high degree of wavefront coherence for its operation.

The important design parameters of a rotating multi-faceted mirror scanner are the number of facets, the drum size (diameter), and the scan efficiency. Because the mirror drum can provide a highly linear scan with virtually instantaneous fly-back, proper selection of the number and size of the individual mirror facets can result in a scanner with nearly 100 percent scan efficiency. Practical constraints on mirror drum diameter, however, may significantly reduce scanner efficiency below this optimum.

The geometry of a typical multi-faceted mirror scanner is illustrated in Figure 16. For simplicity this scanner has been drawn with only eight facets but in practice any number of facets may be used. It may be readily seen that for the generalized scanner with n facets, the apex angle subtended by each facet is simply $2\pi/n$. Rotation of the scanner drum about its geometric axis will then cause an optical ray striking a single mirror facet to be periodically deflected through an angle of twice the apex angle or $4\pi/n$. If we desire an optical deflection of this magnitude, then the effective scan efficiency will be exactly unity. If, however, we desire an optical deflection $\phi$ which is less than $4\pi/n$, then the rotating mirror drum will over-scan resulting in an effective scan efficiency of less than unity. Simple geometry shows that for an optical ray of negligible cross-section, the effective scan efficiency of a multi-faceted mirror scanner is

$$\xi_s = \frac{n\phi}{4\pi}$$

With an optical beam (either laser beam or collimated optical bundle) of finite cross-section, the beam will be periodically deflected by two adjacent mirror facets simultaneously as the edge between the two facets intersects the beam. When this occurs the beam will be deflected in two directions rather than the one unique and desired direction resulting in a loss in effective scan efficiency. For an optical beam of large cross-section, this loss in scan efficiency can be extremely significant. Referring to Figure 17, which depicts a single mirror facet at the two extremes of its useful scan rotation, we see that the maximum useful optical deflection is

$$\begin{aligned}\phi &= \frac{4\pi}{n} - 4\,\theta \\ &= \frac{4\pi}{n} - 4\sin^{-1}\left(\sqrt{2}\,\frac{D_b}{D_s}\right)\end{aligned}$$

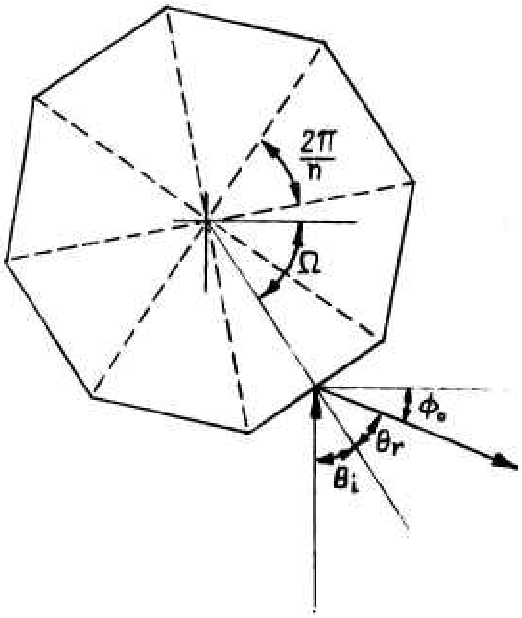

Figure 16. Rotating Multifaceted Mirror Geometry

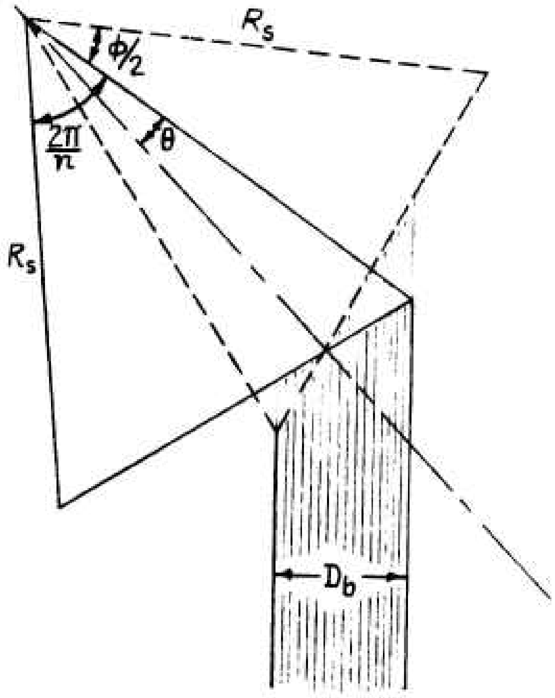

Figure 17. Single Facet Rotational Extremes with Finite Beam Cross-Section

Where $D_b$ is the diameter of the optical beam and $D_s = 2R_s$ is the diameter of the mirror drum. The effective scan efficiency is then

$$\xi_s = \frac{n\phi}{4\pi}$$

$$= 1 - \frac{n}{\pi} \sin \left( \sqrt{2}\,\frac{D_b}{D_s} \right)$$

This equation is plotted as a function of the scanner to beam diameter ratio in Figure 18 with the number of facets as a parameter. Note that the effective scan efficiency may also be written as

$$\xi_s = \frac{\phi}{\phi + 4\theta}$$

$$= \phi \left[ \phi + 4 \sin^{-1} \left( \sqrt{2}\,\frac{D_b}{D_s} \right) \right]^{-1}$$

This equation is also plotted in Figure 18 with the desired optical deflection as a parameter. Note from the figure that for fairly small deflection angle (e.g., 10 mrad), high scan efficiency requires a very large number of facets and a large ratio of scanner to optical beam diameter. If the optical beam diameter is of any appreciable size at all, the size of the scan drum is so large as to make it impractical. Consequently the rotating multi-faceted mirror scanner is not, by itself, an attractive solution for small angle scan applications such as the SLIR system.

This conclusion can be alleviated, however, by the use of optical magnification to magnify small field angles in object space to considerably larger scan angles at the scanner. As mentioned previously, this magnification also reduces the size of the optical bundle at the scanner face and minifies the effect of scanner jitter in object space as well. An afocal telescope of magnification M and entrance aperture D will magnify a desired field angle $\phi_f$ (i.e., $\phi = M\phi_f$) and will minify the optical bundle (i.e., $D_b = D/M$). The scanner efficiency for this desired field angle in object space may then be written as

$$\xi_s = \frac{M\phi_f}{M\phi_f + 4\theta}$$

$$= M\phi_f \left[ M\phi_f + 4 \sin^{-1} \left( \sqrt{2}\,\frac{D}{MD_s} \right) \right]^{-1}$$

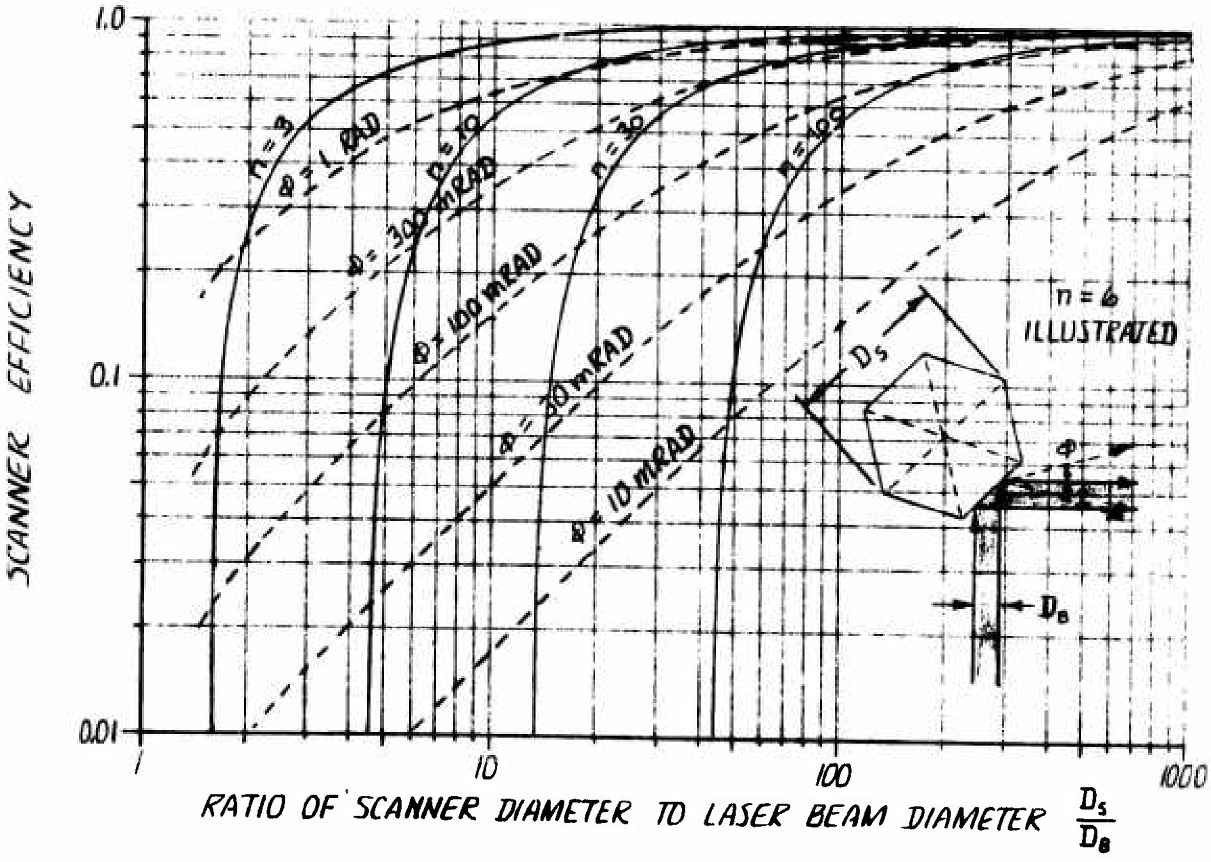

Figure 18. Scan Efficiency of Rotating Multi-faceted Mirror Scanners

Solving for the required scanner diameter then yields

$$D_s = \sqrt{2}\,D \left\{ M \sin \left[ \frac{M\phi f}{4} \left( \frac{1-\xi_s}{\xi_s} \right) \right] \right\}^{-1}$$

An alternate expression which explicitly illustrates the dependence of scanner diameter on facet number may also be derived as

$$D_s = \sqrt{2}\,D \left\{ M \sin \left[ \frac{4\pi - nM\phi f}{4n} \right] \right\}^{-1}$$

Both of these equations are plotted as a function of optical magnification in Figure 19 for a SLIR receiver aperture of 9 inches and a scan field of 10 mrad (acquisition mode). Note that for a particular number of facets, a minimum drum diameter is obtained when the scanner is designed for a 50 percent scan efficiency. Note also that increasing the number of facets will increase this minimum drum diameter but will reduce the required optical power of the telescope. If we desire a drum diameter no larger than 8 or 9 inches, Figure 19 indicates that a scanner with 25 facets coupled with a 25 to 30 power afocal telescope will provide a 10 milliradian scan of object space at an efficiency of 50 to 60 percent. This appears to be the optimum situation for a SLIR system employing a rotating multi-faceted mirror.

For scanning high power laser beams, the rotating multi-faceted mirror scanner offers significant advantages over competing techniques in terms of thermal management. The large thermal mass of the mirror drum effectively precludes large thermal gradients which might otherwise cause distortion of the mirror surface. Furthermore, since a number of facets sequentially scan the beam, any laser energy which is absorbed is efficiently distributed around the drum. Hence, each facet sees a considerably lower time-averaged laser beam power than would a single mirror scanner. These advantages must be weighed, however, against the size and cost of the mirror drum and the design difficulties which a 25 to 30 power afocal telescope presents.

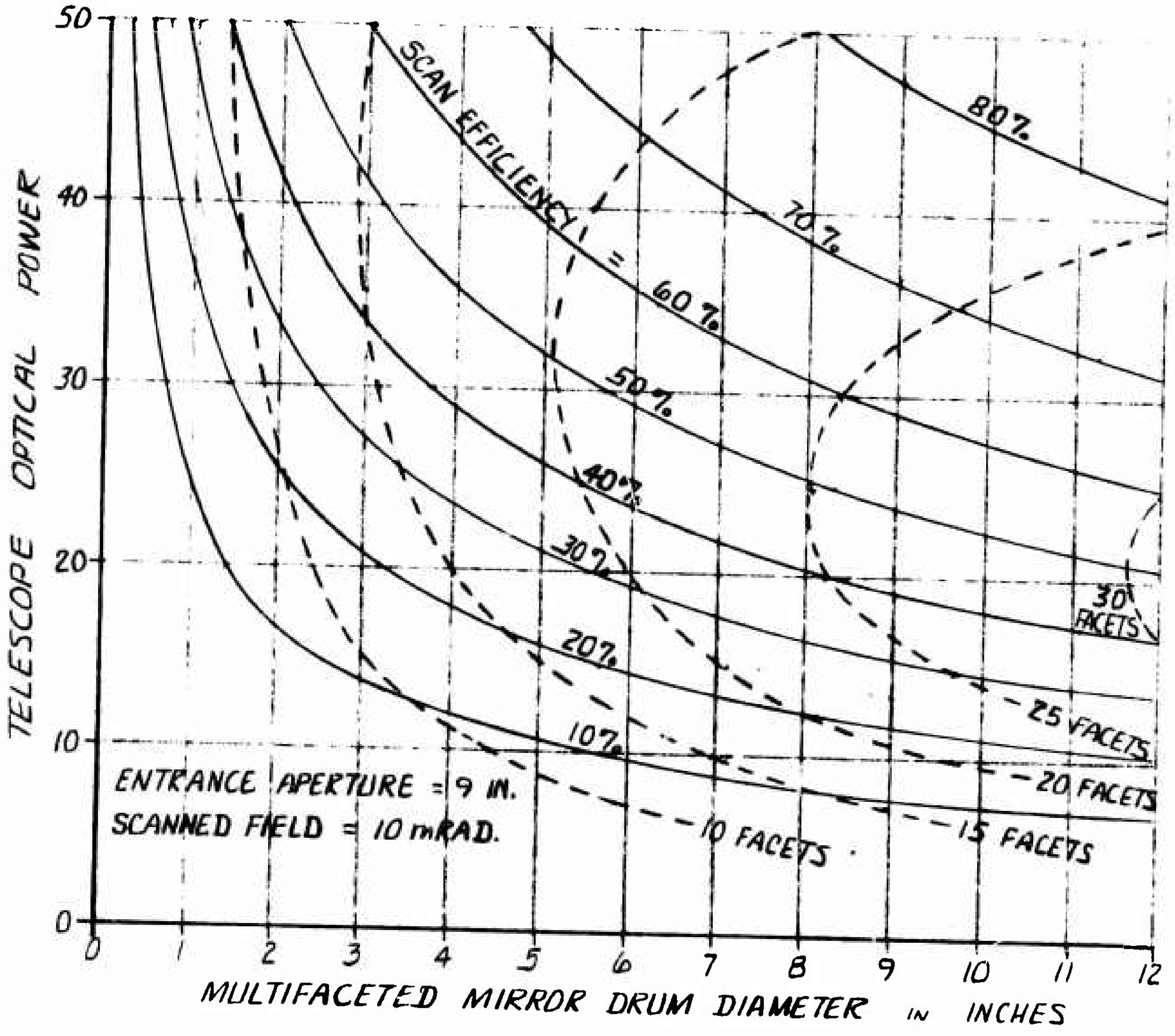

Figure 19. Compatibility of Rotating Multi-faceted Mirror Scanner with SLIR System Requirements

Low Inertia Mirror Scanners. Whereas high inertia scanners are multifaceted and rotational, low inertia scanners are single-mirrored and oscillatory. Low inertia scanners typically are incapable of the wide angle, high rate scan dynamics characteristic of rotational scanners; they also do not exhibit the same high degree of scan linearity. Nevertheless, they are often adequate for moderate angle, moderate rate scan applications where their smaller size and reduced cost are significant factors. Furthermore, because low inertia scanners employ a single mirror rather than multiple mirror facets, their scan-to-scan repeatability can be superior to their high inertia competitor. This single mirror characteristic, however, also makes low inertia scanners more susceptible to dynamic and thermal distortion, the latter of which is particularly significant for applications requiring high power laser beam scanning.

Two general types of low inertia mirror scanners are common, the tuned resonant or torsional scanner, and the galvonometer scanner. The principle difference between these two is their scan pattern, which results from their basic mechanization. The mirror of a tuned resonant scanner is suspended by a taut band or supported by a torsion bar and is caused to oscillate at a resonant frequency. Consequently, the scan pattern is sinusoidal in angle at a fixed scan frequency. With small mirrors and at small deflection angles, resonant scanners can operate at scan frequencies in excess of 10 kilohertz.

In contrast, galvonometer scanners are primarily non-resonant and produce scan patterns whose angular deflection is directly proportional to the magnitude of an electrical drive signal. Consequently with a sawtooth or triangular wave driving signal applied to their input, galvonometer scanners can provide a linear uni-directional or bi-directional angular scan but typically at scan rates far below that of its resonant counterpart. By means of angular position feedback, a galvonometer scanner can also be operated in a closed servo loop which can greatly improve the linearity of the scan. Furthermore, because a servo-controlled galvonometer scanner is basically non-resonant, it can be operated at variable scan frequencies and, therefore, exhibits considerably more operational flexibility than the tuned resonant scanner. For the SLIR system application where both scan linearity and operational flexibility are important, the galvonometer scanner is the obvious choice among the low inertia mirror scanner alternatives.

Galvonometer scanners may be of either the moving-coil or the moving-iron type. The two outstanding characteristics of the moving-iron galvonometer are its high torque-to-inertia ratio and its good linearity. Consequently, moving-iron galvonometers are suitable for the linear deflection of fairly large scan mirrors whereas moving-coil galvonometers are not. General Scanning, Inc., of Watertown, Mass., manufactures a series of moving-iron galvonometer scanners which appear to be applicable to the SLIR system. These scanners are also available with built-in position transducers which permit closed-loop servo control for greater scan linearity and accuracy. This position transducer operates by detection of capacitance variation between the rotating armature and a set of stationary electrodes. The transducer linearity exceeds ± 0.15 percent of peak-to-peak deflection, the servo-loop signal-to-noise ratio affords a resolution (repeatability) of one second of arc (4.85 $\mu$rad), and the signal response lag is only 10 microseconds. Shaft wobble of the General Scanning type G-300PDT galvonometer, which has been specifically designed for servo-controlled deflection of large (up to 100 by 100 millimeter) scan mirrors, is typically below 5 arc-seconds and, therefore is compatible with the precision tracking requirements of the SLIR system if optical magnification of object space is employed. Other characteristics of the G-300PDT galvonometer are listed in Table 5.

The maximum scan rate of a galvonometer scanner is limited by the maximum angular acceleration, a, which can be produced by the scanner's torque motor. This angular acceleration is given by the ratio of the available torque, T, to the total galvonometer rotor inertia, J; i.e.,

$$a = \frac{T}{J}$$

The total rotor inertia is, in turn, the sum of the armature inertia, $J_a$, and the mirror inertia, $J_m$; consequently, large mirrors which exhibit large inertia can severely limit the angular acceleration and, therefore, scan rate capability of a galvonometer scanner.

The inertia of a rectangular and an elliptical scan mirror may be easily calculated from the equations given in Figure 20. If we assume that the length of the mirror is $\sqrt{2}$ times larger than the width of the mirror such that it is capable of accepting a circularly symmetric optical bundle at a 45 degree angle to its normal, then the mirror inertia can be shown to increase

## TABLE 5

## Servo-Controlled Galvonometer Scanner Characteristics
(General Scanning G-300PDT)

| | |
|---|---|
| Torque (approx.) | 1000 gm-cm |
| Armature Inertia | 3.7 gm-$cm^2$ |
| Deflection Range | 0 to 25° peak-to-peak |
| Linearity | ± 0.15% of peak-to-peak |
| Repeatability | 1 arc second |
| Shaft Wobble | < 5 arc second |
| Signal Response Time | 10 μsec |
| Zero Drift Stability | < 0.2 arc minute* |
| Gain Drift Stability | < 0.03%* |
| Life | $10^{10}$ cycles |

*with temperature regulation

### RECTANGULAR MIRROR

$$J_m = \frac{1}{12}\sigma \ell w t\,(\ell^2 + t^2)$$

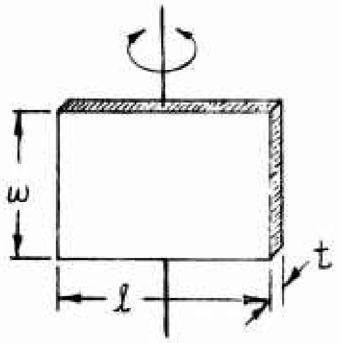

### ELLIPTICAL MIRROR

$$J_m = \frac{\pi}{48}\sigma \ell w t\left(\frac{3}{4}\ell^2 + t^2\right)$$

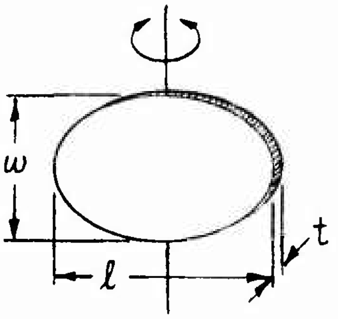

NOTE: $\sigma$ = MIRROR DENSITY

Figure 20. Moment of Inertia for Typical Scan Mirrors

as the fourth-power of the mirror width as illustrated in Figure 21. In general, the elliptical mirror will exhibit an inertia which is only 55 percent that of a rectangular mirror of the same size due to its lower mass. Consequently, an elliptical mirror, or at worst a rectangular mirror with its corners cut off, is best if scan rate capability is important.

If we assume a sinusoidal scan motion with a peak-to-peak mirror deflection of $\phi$, then simple analysis will show that the maximum scan frequency is given by

$$f_{max} = \frac{1}{2\pi}\sqrt{\frac{2a}{\phi}}$$

$$= \frac{1}{2\pi}\sqrt{\frac{2T}{\phi J}}$$

$$= \frac{1}{2\pi}\sqrt{\frac{2T}{\phi(J_a+J_m)}}$$

where substitution has been made for the scanner's maximum angular acceleration capability. A non-sinusoidal (e.g., sawtooth or triangular) scan motion will be limited to lower scan frequencies. It has been found that a servo-controlled galvonometer scanner which is griven by a sawtooth waveform will be limited to scan frequencies (frame rates) given by

$$f_{saw} = (1 - \xi^2)\ f_{max}$$

$$= \frac{1 - \xi^2}{2\pi}\sqrt{\frac{2T}{\phi(J_a+J_m)}}$$

where $\xi$ is the scan efficiency, the ratio of the linear rise portion of the sawtooth to the total sawtooth period. Note that a sawtooth scan requires that $\xi > 0.5$ since when $\xi = 0.5$ we have essentially a triangular scan motion.

Note from the above equation that for a galvonometer scanner of fixed torque capability, the scan rate may be optimized by minimizing the product of the angular deflection and the total rotor inertia. Optical magnification of object space by an afocal telescope can be used to optimize this capability while minimizing scanner jitter since the required scan deflection increases directly with magnification while mirror inertia is proportional to the fourth power of mirror size which decreases with increasing magnification. With optical magnification of power M, the maximum sawtooth frame rate capability of a galvonometer scanner may be written as

$$f_{saw} = \frac{1 - \xi^2}{2\pi}\sqrt{\frac{4T}{M\ \theta_F\left[J_a+J_m(M)\right]}}$$

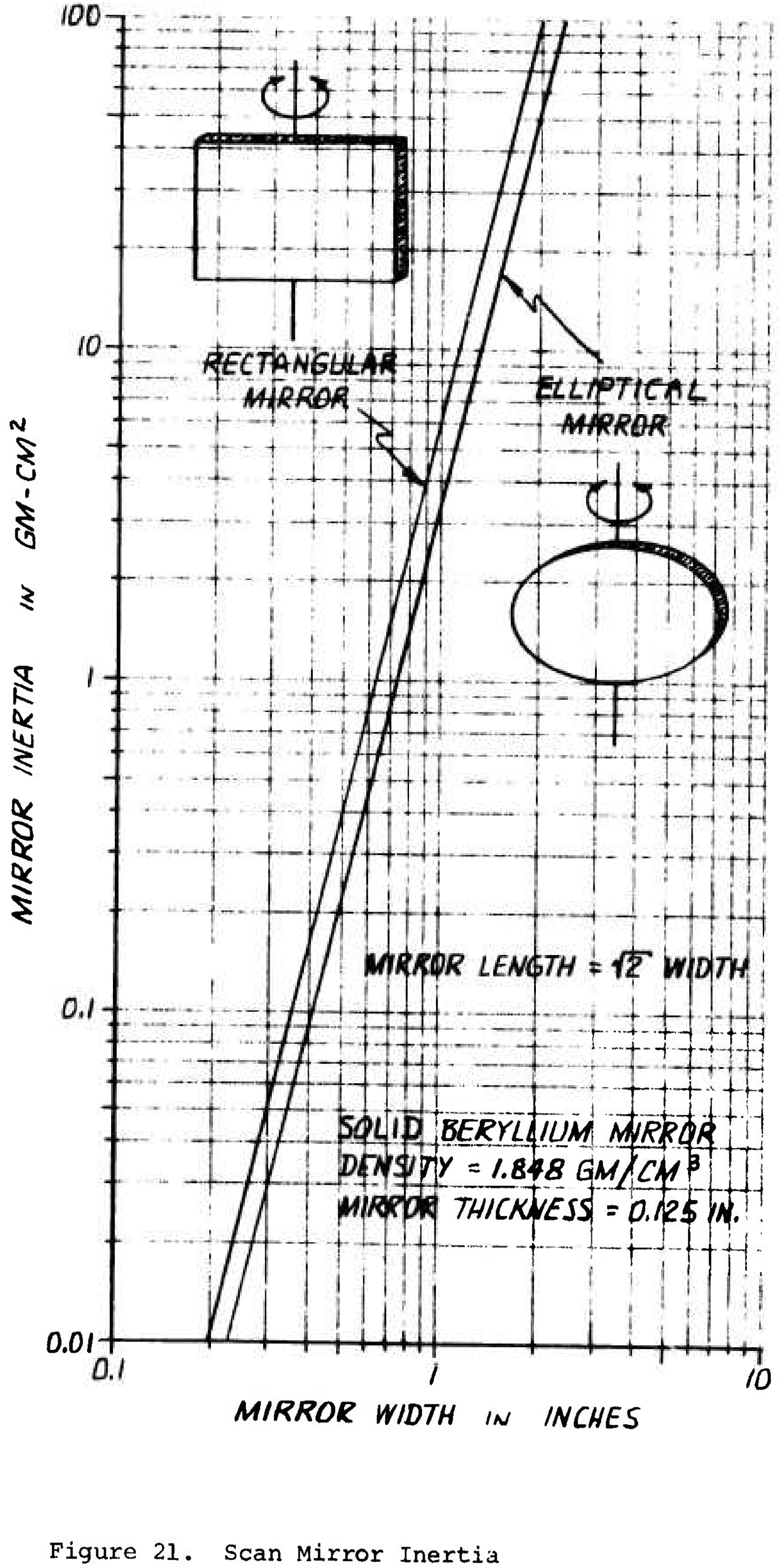

Figure 21. Scan Mirror Inertia

Where $\theta_F$ is the desired optical scan angle in object space and $J_m(M)$ for an elliptical mirror is given by

$$J_m(M) = \frac{\sqrt{2}\pi}{48} \sigma t \left(\frac{D}{M}\right)^2 \left[\frac{3}{2}\left(\frac{D}{M}\right)^2 + t^2\right]$$

where D is the diameter of the optical bundle prior to minification; i.e., the diameter of the afocal telescope's entrance aperture.

The sawtooth frame rate capability of a galvonometer scanner exhibiting 1000 gm-cm of torque with an armature inertia of 3.7 gm-cm$^2$ (e.g., General Scanning's series G-300PDT scanners) is plotted as a function of optical magnification in Figure 22 for a 10 mrad scan field and a 9-inch entrance aperture. Note that the maximum frame rate capability of the galvonometer scanner is achieved if the telescope power is 10 to 15. Lower magnification requires a large scan mirror with high inertia. Conversely, higher magnification requires increased mirror deflection magnitude. A 10 to 15 power afocal telescope provides the optimal magnification for the scan of a 10 mrad field with a 9-inch entrance aperture and consequently is optimum for a SLIR configuration employing a galvonometer scanner. At this magnification, frame rates of up to 200 Hertz should be possible with a scan efficiency of no less than 60 percent. Note that higher scan efficiencies are possible at lower frame rates. The galvonometer scanner's capability of achieving fairly high scan efficiency with moderate optical magnification requirements is a significant advantage over the rotating multi-faceted mirror drum approach which enhances its candidacy as the best scan technique for the SLIR system.

The galvonometer scanner can also be driven with a triangular waveform which can effectively double its frame rate capability if field interlace is not employed. The triangular waveform, however, results in a bi-directional scan format which not only complicates the design of the system's video and tracker electronics but also complicates the mechanization of angle-of-arrival compensation between the illuminator beam and the receiver IFOV. Hence, the bi-directional scan format is an attractive alternative only if the maximum possible frame rate capability is mandatory.

Prism Scanners. Several prism configurations, when rotated about their optical axis, cause the image passing through them to rotate at twice the prism's angular rate. The Dove, Pechan, and "K" prisms are typical examples of such prism scanners which are commonly used in image derotation applications. Another derotation prism, which has unfortunately received little

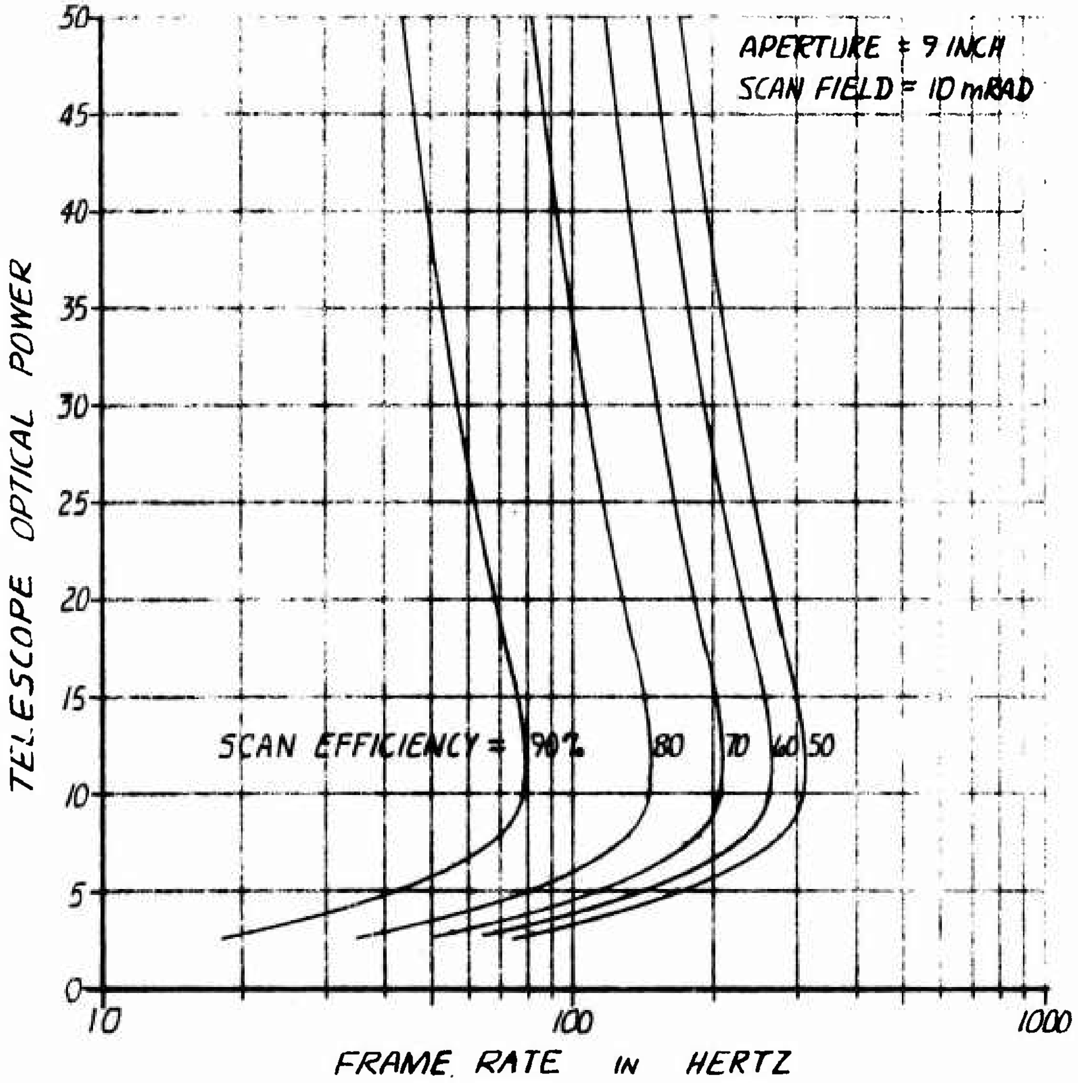

Figure 22. Compatibility of Galvonometer Scanner with SLIR System Requirements

attention in the past, is the delta prism. This prism scanner, however, offers significant advantages over its more familiar counterparts, particularly in an illuminator/receiver application such as the SLIR system. Unlike the Pechan and "K" prisms, the delta prism is a single element device and, therefore, is more compatible with operation in a dynamic environment. The possibility of prism face misalignment due to rotational stress is, therefore, eliminated. Because the delta prism is a single element device, it also requires no cementing of component parts. The absence of optical cement makes the delta prism more compatible with high power laser use since thermal expansion problems between the prism surface and the cement are avoided.

The use of a delta prism as an image rotator is illustrated in Figure 23. Since three reflections are involved, the delta prism will either invert or revert the image depending on its orientation. In orientation (a), the image is inverted. Rotating the prism about the line of sight by 90° results in a rotation of the image by 180° to produce the reverted image as shown in orientation (b). Further rotation of the prism by 90° to orientation (c) results in an additional rotation of the image by 180° producing an inverted image identical to that produced by orientation (a). Consequently, one complete revolution of the delta prism about the line of sight results in two complete revolutions of the image.

When the delta prism is used in front of an imaging lens having a linear array of photodetectors at its image plane, rotation of the prism results in a circular scan of object space. Similarly, when another delta prism is rotated in front of a fan-beam laser illuminator, the illumination beam is caused to sweep out a circular area in object space in a con-scan fashion. Phase synchronization of the two delta prisms results in a Scanned Laser Illuminator/Receiver configuration which affords a unity scan efficiency (i.e., no retrace dead time) with a simple rotational scan motion. Because the rotation is unidirectional and continuous, possible backlash between the two scan mechanisms is of no significance. Also, because the scan motion is non-reciprocating, no mechanical resonances are encountered which would preclude or hinder operation with a variable scan rate.

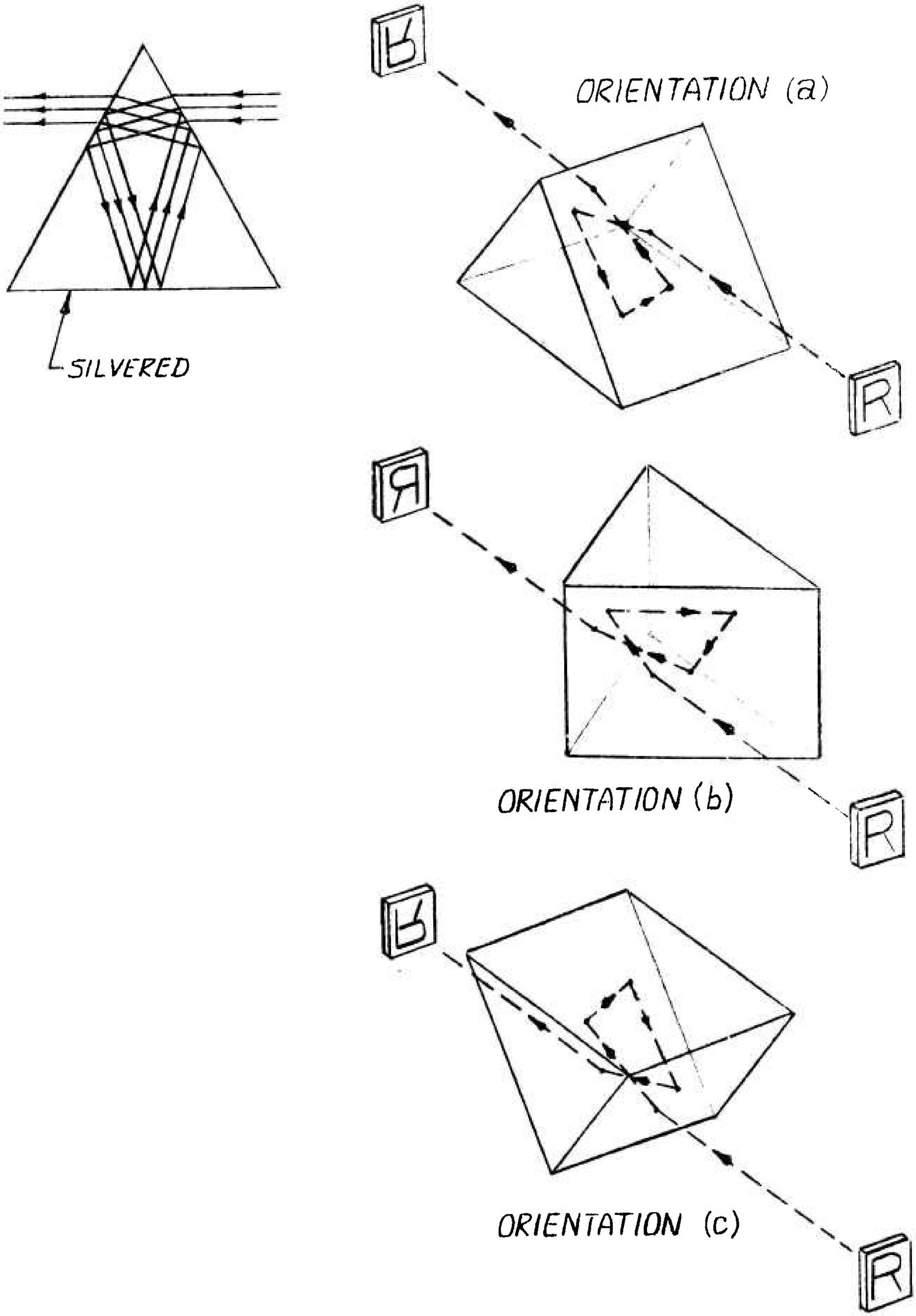

Figure 23. Delta Prism Scanner

### 3.1.4 Angle-of-Arrival Compensation

Due to the finite propagation velocity of electromagnetic radiation, a light pulse, emitted by an illuminator and reflected back to an adjacent receiver from a target at a distance R will be subject to a finite propagation delay. If the illuminator is dynamically scanning an area in space and the receiver is similarly scanning in synchronism, this finite propagation delay will result in an angle-of-arrival lag, $\psi_p$, between the illuminator's projection angle $\psi_s$, and the receiver's look angle $\psi_R$; i.e.,

$$\psi_p = \psi_s - \psi_R$$

$$= \frac{2R\,\omega_s}{c}$$

where c is the velocity of light ($3 \times 10^8$ meters/second) and $\omega_s$ is the angular scan rate of the illuminator beam in object space.

If we assume an illumination beam with angular cross-section $\phi_B$ by $\beta\phi_B$, where $\beta \geq 1$ and denotes the beam aspect ratio, and require this beam to uniformly cover a projection field of $\phi_F$ by $\alpha\phi_F$, where $\alpha \geq 1$ and similarly denotes the projection field aspect ratio, then the necessary angular scan rate of the illuminator beam may be written as

$$\omega_s = \frac{F_R}{\xi_s}\left(\frac{\alpha\phi_F^2}{\beta\ \phi_B}\right)$$

where the beam is assumed to scan in the direction orthogonal to its $\beta\phi_B$ dimension, $\xi_s$ is the illuminator scan efficiency which accounts for all dead time, overlap, or boundary effects, and $F_R$ is the desired frame rate.

Substition of this equation into the previous one for the angle-of-arrival lag yields

$$\psi_p = \frac{2R\ F_R}{c\ \xi_s}\left(\frac{\alpha\phi_F^2}{\beta\ \phi_B}\right)$$

Note that $\psi_p$ is a function of range R, and therefore may change with range closure. Differentiating this last equation with respect to time then yields the rate at which this angle-of-arrival lag changes; i.e.,

$$\omega_p = \frac{d\psi_p}{dt}$$

$$= \frac{2}{c\ \xi_s}\left(\frac{\alpha\ \phi_F^2}{\beta\ \ \phi_B}\right)\left[F_R\frac{dR}{dt} + R\frac{dF_R}{dt}\right]$$

where the possibility of the frame period changing with time has been explicitly allowed. Note that $\omega_p$ will equal zero and, therefore, $\psi_p$ will be constant if

$$\frac{dF_R}{dt} = -\frac{F_R}{R}\left(\frac{dR}{dt}\right)$$

Dynamic compensation for this angle-of-arrival lag can be effected in either of two ways. If it is desirable to hold the frame rate constant, then angular compensation which is a function of range must be provided to correct for this range-dependent angle-of-arrival lag. If this angle-of-arrival lag is always a small fraction of the scan width, angular compensation can be relatively straight-forward since compensation is required in one direction (the scan direction) only. If, however, the angle-of-arrival lag is of-the-order-of or larger than the scan width, angular compensation must be two-dimensional if large scan inefficiencies are to be avoided.

The second method of dynamic compensation is to hold the angle-of-arrival lag constant and independent of range by increasing the frame rate linearly with decreasing range at a rate which is proportional to the target's rate of closure, dR/dt, as indicated by the previous equation. If we require that $\psi_p$ be maintained at a constant value $\psi$, then the frame rate must satisfy the following relation

$$F_R = \frac{c}{2R}\left[\xi_s\left(\frac{\psi}{\alpha\phi_F}\right)\left(\frac{\beta\phi_B}{\phi_F}\right)\right]$$

Note that the ratio $(\psi/\alpha\phi_F)$ is a normalized angle-of-arrival lag which relates the actual angle-of-arrival lag to a fractional part of the scan width.

Because it is desirable for high scan efficiency to maintain the angle-of-arrival lag at a value which is a small fraction of the scan width, the normalized angle-of-arrival lag should be less than $10^{-1}$ or preferrably less than $10^{-2}$.

It is worth noting that if the angle-of-arrival lag is always less than a pixel width, no dynamic compensation may be necessary. For a receiver having 250 pixels (resolution elements) per scan width, this corresponds to a normalized angle-of-arrival lag of $4 \times 10^{-3}$ or less. For this situation to hold, the frame rate must satisfy the following inequality

$$F_R < 4 \times 10^{-3} \frac{c}{2R} \left[\xi_s \left(\frac{\beta\phi_B}{\phi_F}\right)\right]$$

For a fan-beam illuminator, the ratio $\beta\phi_B/\phi_F$ will be nearly unity. Hence the frame rate which obviates angle-of-arrival compensation for a fan-beam SLIR system is

$$F_R < 600 \frac{\xi_s}{R(km)} \text{ Hertz}$$

where the range R is in kilometers. Assuming unity scan efficiency, this last inequality states that the frame rate must be less than 60 Hertz at 10 kilometer range or less than 600 Hertz at 1 kilometer range for the angle-of-arrival lag to be negligible. With a scan efficiency of less than unity, these frame rate limits would be correspondingly reduced. A reasonable design goal for the SLIR system which both meets the data rate requirements imposed by target dynamics and the desired track accuracy and also obviates the need for angle-of-arrival compensation would be a 20 Hertz frame rate at 10 kilometer range and a 200 Hertz frame rate at 1 kilometer range.

## 3.2 Laser Illuminator Technology

The acquisition of small missile targets (100 $cm^2$ optical cross-section) at long range (5 nautical miles or more) will require a laser illuminator capable of at least 100 watts average radiant power. This follows directly from the range equation derived previously when the SLIR acquisition mode parameter requirements are substituted. For a scanning illuminator configuration, such as is explicitly specified by the SLIR Statement-of-Work, this high power must be obtainable concurrently with small (at least in one dimension) illuminator beam divergence. Furthermore, the presence of backscattered radiation from the propagating illumination beam suggests the use of a pulsed illuminator output such that the effect of backscatter can be minimized through range-gating of the receiver. For a fan-beam illuminator which is scanned in one direction only, laser illuminator pulse repetition frequencies (PRFs) in the 5 to 50 kilohertz range would be required to permit frame rates in the 20 to 200 Hertz range. A pencil beam illuminator, on the other hand, would require laser PRFs in the megahertz range.

### 3.2.1 Illuminator Constraints

The design of a laser illuminator suitable for use in the SLIR system is subject to several constraints. The maximum allowable exit aperture (6 inches) of the illuminator optics places severe limitations on laser source beam divergence and beam diameter when very low (20 to 80 µrad) far field beam divergence is desired. As a direct consequence of the second law of thermodynamics, the output radiance of the illuminator cannot exceed the radiance of its internal laser source. The optical law which embodies this principal is the LaGrange Invariant, which states:

$$(nD \sin \theta)_{out} \geq (nD \sin \theta)_{in}$$

where n is the refractive index of the medium, D is the diameter of the radiant beam, and θ is the half-angle beam divergence.

Since both $n_{out}$ and $n_{in}$ are typically near unity (for an air medium) and since for small beam divergence the sine of an angle is approximately equal to that angle in radians, an equivalent relation to the LaGrange Invariant is

$$D \alpha_{out} \geq d \alpha_{in}$$

where D is the diameter of the output radiant beam with $\alpha_{out}$ its full beam divergence and d is the diameter of the radiant beam at the laser source with $\alpha_{in}$ its raw beam divergence.

For the SLIR system, both D and $\alpha_{out}$ are constrained by system requirements. Practical limitations require that D be no larger than 6 inches (152.4 mm). System performance goals require that $\alpha_{out}$ be matched to the receiver IFOV in both the scan and ortho-scan directions. Hence we can write that the divergence-diameter product of the laser source is constrained by the following inequality

$$d\alpha \leq (152.4\text{mm})\ \phi$$

where $\phi$ is the desired far-field beam divergence. This equation is plotted in Figure 24 for far-field beam divergence in the 10 μrad to 80 μrad range. Note that the most severe constraint on laser raw beam parameters results during precision track mode operation ($\phi$ = 20 μrad), which specifies that the laser beam divergence-diameter product can be no larger than 3.048 mrad-mm. As will be apparent later, the impact of this constraint is most significant when high laser beam power is required.

### 3.2.2 Laser Scaling Laws

In designing a suitable laser source for the SLIR system, several scaling laws were adopted. These laws allow extrapolation from demonstrated laser performance to required laser performance without exceeding state-of-the-art technology. Specifically laws for output beam power and beam divergence are given. Pulse repetition rate and pulsewidth capability are treated separately. Output power scaling is based upon the allowable intensity of the average circulating power in a laser resonator. Power output from the oscillator is assumed to scale linearly with cross-sectional area of the mode volume; i.e.,

$$P_o = \delta I_o A$$

where $\delta$ is the coupling fraction of the output mirror, A is the active mode cross-section, and $I_o$ is state-of-the-art circulating intensity. For the stable resonator, it is advantageous to minimize A for stability; thus, for high output power capability, a high value for $I_o$ is essential. $\delta$ is optimized from consideration of medium gain and resonator losses to give the most efficient operation of the laser.

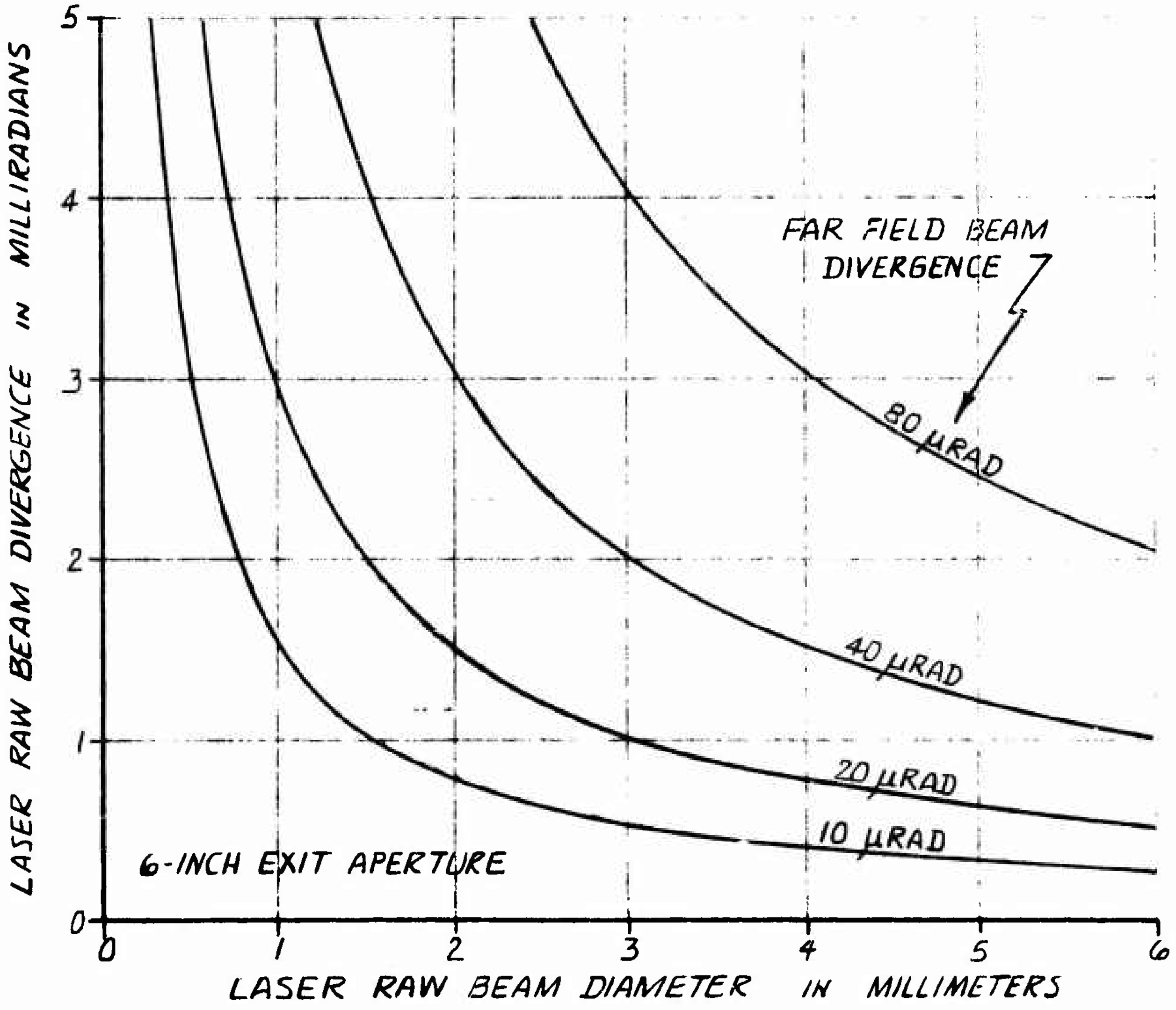

Figure 24. SLIR Illuminator Constraints

The beam divergence scaling law depends upon the type of resonator used, either stable or unstable. The divergence law for a stable resonator states that when a given resonant cavity design is operated multimode to obtain higher output power in accordance with the output power law above, the beam divergence scales as the ratio of beam diameters or radii

$$\alpha_{\text{multimode}} = \alpha_o \ (W/W_o)$$

where W is the beam radius of a multimode beam within which 90 percent of the beam power is contained, $W_o$ is the fundamental mode or $TEM_{oo}$ beam radius which is determined by the resonator design, and $\alpha_o$ is the fundamental mode full beam divergence; i.e.,

$$\alpha_o = 2\lambda/\pi W_o$$

$\alpha_o$ is, therefore, the limiting cone which contains 90 percent of the beam power. These beam divergence relationships follow directly from stable resonator mode theory and this relationship holds for any distance from a resonator's minimum beam waist position.

Scaling laws for beam divergence of unstable resonators follow to a close approximation the behavior of the Cassegrain telescope. For constant single mode operation, the beam divergence varies with beam diameter as follows:

$$\alpha = \beta\lambda/d$$

where $\lambda$ is the wavelength of the laser, d is the secondary mirror diameter or the rod diameter, whichever is smaller and $\beta$ is a factor dependent upon the ratio of secondary to primary mirror diameters and the intensity distribution of the incident electromagnetic wave.

### 3.2.3 Laser Selection

The laser scaling laws were used to examine candidate laser devices for the SLIR system. Low order mode operation is dictated by the illuminator output aperture and beam divergence requirements. Nominally, a six-inch diameter aperture is available and a minimum 20 microradian beam divergence is needed. The beam divergence scaling law shows that the product of beam divergence and beam diameter is proportional to wavelength.

$$\alpha_o(2W_o) = 4\lambda/\pi$$

This product is constant through the optical system. Thus, the above requirements indicate that laser wavelength must satisfy the following inequality:

$$\lambda \leq (\frac{\pi}{4}) D\phi$$

Where D is the output diameter and $\phi$ is the beam divergence. With the $D\phi$ product limited to 3.048 mrad-mm as shown before, we have that

$$\lambda \leq 2.36 \text{ micrometers}$$

Laser sources included in the acceptable wavelength range are, therefore, Nd:YAG lasers at 1.064 micrometers, cryogenic GaAs lasers at 0.86 micrometers, ruby lasers at 0.6943 micrometers, and a wide range of visible transition lasers including copper vapor lasers at 0.5106 and 0.5782 micrometers. Also included in this range are frequency doubled lasers such as Nd:YAG at 0.532 micrometers and ruby at 0.347 micrometers and various dye lasers. Typical performance characteristics of several of these laser sources which might be suitable for illuminator applications are given in Table 6.

Of the potential laser sources listed in Table 6, only the Nd:YAG laser and possibly the copper vapor laser are viable candidates for the SLIR system. The frequency doubled Nd:YAG laser is incompatible with high PRF operation due to low doubling efficiency at the low peak powers which result. Even narrow pulsewidth techniques cannot raise the peak power sufficiently for efficient frequency doubling. Although the ruby laser is capable of very high beam power output, it, too, is not a viable candidate for the SLIR system. Thermal considerations limit ruby laser operation to very low PRFs. The cryogenic GaAs PN junction laser is capable of fairly high power at high PRF and with an attractively high power conversion efficiency. But GaAs lasers also exhibit a very wide beam divergence and, therefore, are also unsuitable for SLIR application. Each of these three laser sources, with the possible exception of ruby, are more compatible with a flood-beam illuminator approach.

### 3.2.4 Laser Design Approaches

A preliminary laser illuminator design has been developed using Nd:YAG. This design has been driven by the required illuminator performance demanded by the SLIR system.

The required divergence-diameter product (3.048 mrad-mm) for the illuminator calls for a low order mode laser resonator. This can be seen by considering the power scaling law and using a state-of-the-art intensity,

## TABLE 6

## Typical High Power, Pulsed Laser Sources

| | Copper Vapor | Doubled Nd:YAG | Ruby | Cryogenic GaAs | Nd:YAG | Nd:YAG |
|---|---|---|---|---|---|---|
| Emission Wavelength (μm) | 0.5106 | 0.53 | 0.6943 | 0.86 | 1.064 | 1.064 |
| Mode | | Multi-mode | Multi-mode | Multi-mode | Multi-mode | $TEM_{oo}$ |
| Max. Pulse Repetition Freq. (PRF) | 10 KHz | 30 Hz | 2 Hz | 15 KHz | 50 KHz | 50 KHz |
| Typical Pulse Width (nsec) | 10 | 20 | 20 | 2000 | 200 | 200 |
| Max. Laser Beam Power (watts avg.) | 12 | 10 | 120 | 20 | 100 | 20 |
| Typical Raw Beam Divergence (mrad) | 4 | 4 | 4 | 800 | 10 | 1.2 |
| Typical Raw Beam Diameter (mm) | | 10 | 12 | | | 1.1 |
| Typical Power Conversion Efficiency | 0.1% | 1% | 0.1% | 25% | 2% | 0.4% |

$I_o$, of 20,000 W/cm$^2$. A near optimum coupling fraction for Nd:YAG lasers is 10 percent. Thus, the required cross-section for 100 watt operation would be

$$A = P_o/\delta I_o$$

$$A = 0.05 \text{ cm}^2$$

Assuming a circular beam cross-section, the beam diameter would be

$$d = 2.5 \text{ mm}$$

However, a fundamental mode resonator with this spot size would be extremely sensitive to alignment drift as can be seen from the sensitivity parameter

$$S = \frac{1}{4}\left(\frac{d}{d_o}\right)^4$$

where $d_o$ is the confocal resonator spot size (i.e., $d_o = 2\sqrt{\lambda\ell/2\pi}$ where $\ell$ is the resonator optical length). With a typical resonator length of 40 cm, $d_o$ = 0.5 mm and the sensitivity parameter becomes S = 134. Typically $S \simeq 1$ for high stability commercial lasers. Thus, the stability parameter limits d to about one millimeter which, in turn, limits the stable laser power of a fundamental mode oscillator to about 20 watts. This can be seen using a beam diameter of about 1.0 mm in the power scaling formula.

Unstable Resonator Design. Although an amplifier can be used to increase this 20 watts up to the 100 watt level, it would be desirable to use a laser oscillator alone. For this reason, an unstable resonator design was considered since the fundamental mode of this resonator can be achieved with any cross-section and, therefore, is not subject to the power limitation of the stable resonator.

The basic design equation of an unstable resonator is the tube Fresnel number, $N_T$(4)

$$N_T = D^2/4\ell\lambda$$

---

(4) A. E. Siegman, "Stabilizing Output with Unstable Resonators", Laser Focus, May, 1971.

where these terms have been defined previously. The tube Fresnel number is related to the so-called equivalent Fresnel number, $N_{Eq}$, by

$$N_T = \frac{2M^2}{M-1} N_{Eq}$$

where M is the magnification of the resonator and $N_{Eq}$ derives from unstable resonator mode theory. In particular,

$$N_{Eq} = 0.5, 1.5, 2.5, \ldots$$

represent fundamental mode resonators. The magnification determines the output coupling of the resonator and is given approximately by

$$\delta = \left(\frac{M^2-1}{M}\right)^2$$

It is seen that the principle quantity which minimizes the beam divergence-diameter product is maximum $\delta$. Essentially the secondary mirror is an obscuration to the primary mirror. The output coupling increases as the primary mirror to secondary mirror diameter increases. This ratio is equal to the geometric magnification, M. Clearly unstable resonators are best suited to high gain lasers. Nd:YAG is a high to moderate gain laser. A reasonable output coupling falls within the 10 to 20 percent range. Using the largest value in this range yields M = 1.36. The value of $\beta$ in the unstable resonator scaling formula for beam divergence is found from considering a curve of magnification vs $\beta$, as given in Figure 25, for circularly obscured apertures. With M = 1.36, this curve gives $\beta = 8.8$ yielding a divergence-diameter product of 9.2 mrad-mm at 1.064 micrometers. Thus, the unstable resonator does not appear to be compatible with SLIR requirements since it is unable to meet the 3.048 mrad-mm laser source requirement.

Oscillator-Amplifier Design. A 20 watt $TEM_{00}$ mode Nd:YAG laser oscillator is within current technical capability. To achieve 100 watts of fundamental mode output power, an amplifier stage of 7 dB gain is needed.

Table 7 lists the key parameters of the proposed oscillator.

The Q-switch performance of this oscillator is shown in Figure 26. This performance was obtained using cw pumping with krypton arc lamps. It can be seen that over the range of 5 KHz to 50 KHz the pulse energy

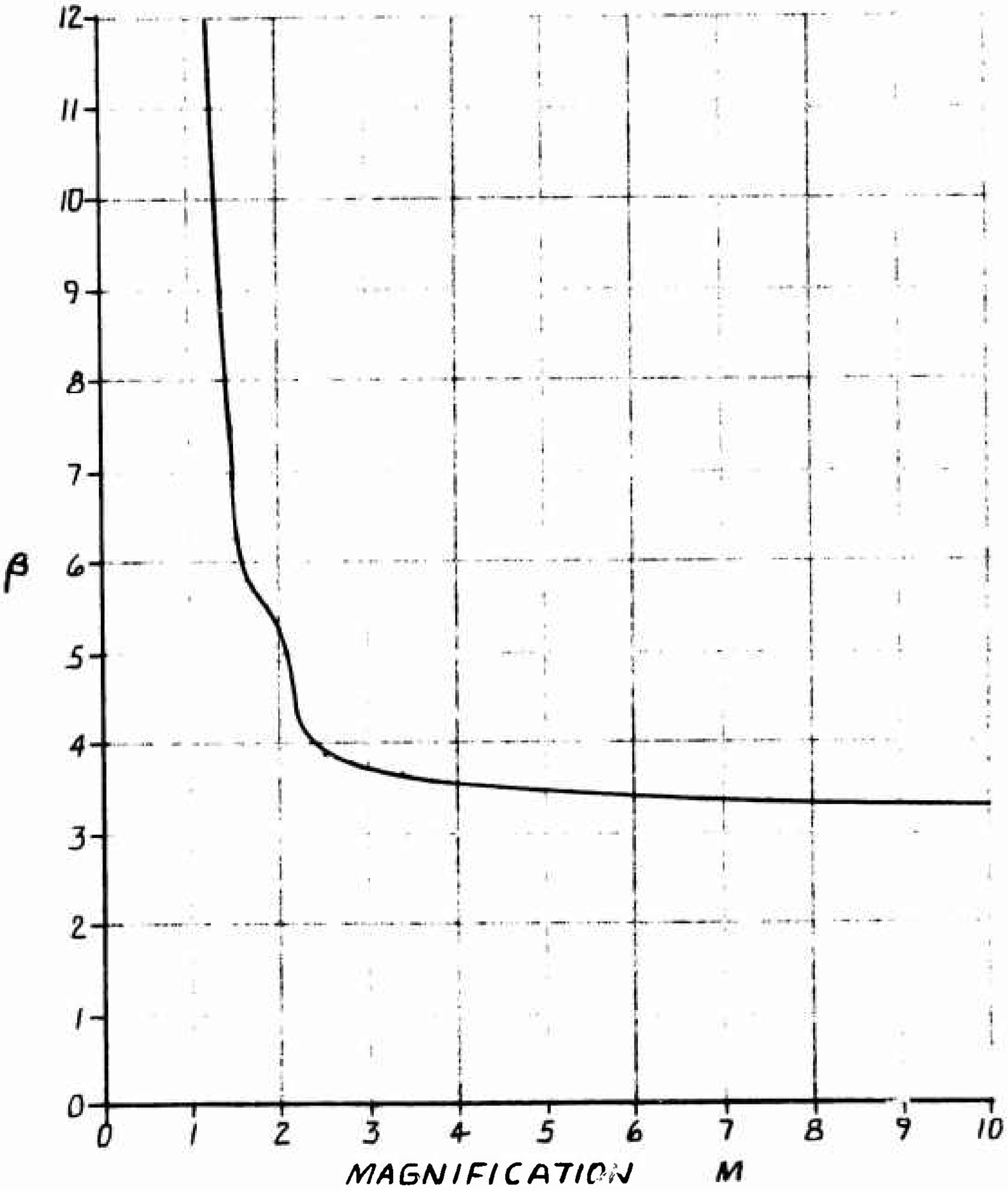

Figure 25. Unstable Resonator β Curve

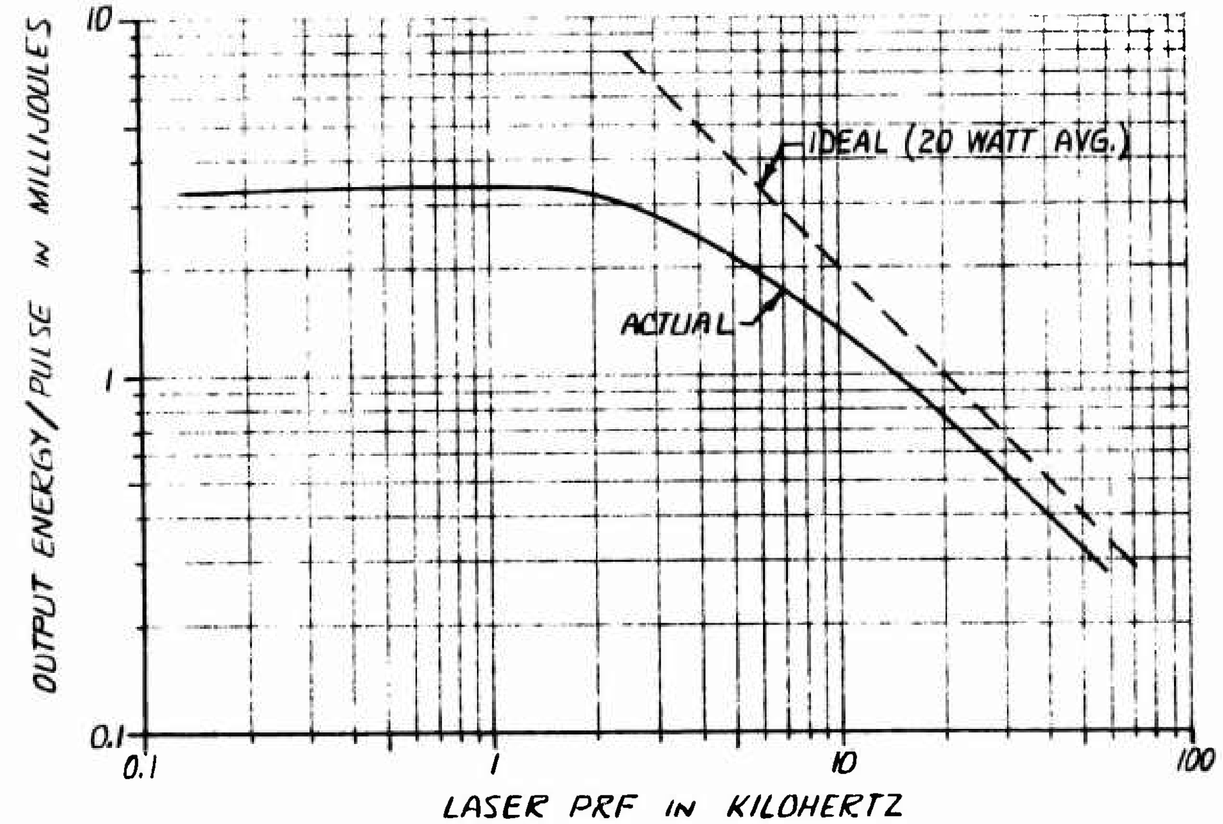

Figure 26. Output Pulse Energy of Q-Switched Oscillator

TABLE 7

Oscillator Parameters*

| | |
|---|---|
| Optical Length | 50 cm |
| Beam diameter | 1.06 mm |
| Beam divergence | 1.26 mr |
| Cavity | Half symmetric |
| Mirror radius | 200 cm |
| Laser rod | 3 mm diameter x 76 mm length |
| Output power | 20 watts cw ($TEM_{00}$) |
| Input power | 5 kW to 7 kW |

*Extrapolated from Quantronix Model 116-1

increases with decreasing pulse repetition frequency, which is a desirable feature for long range target acquisition. The pulse energy changes with PRF because the pumping time between pulses also varies with PRF. This can be understood by considering the rate equation for pumping

$$\frac{dN}{dt} = -N/\tau + W$$

where $\tau$ is the fluorescence decay time, W is the pumping rate, and N is the inversion density. Solving for N then yields

$$N = \tau W \left(1 - e^{-t/\tau}\right)$$

Thus, as pulse repetition rate decreases the inversion builds to a maximum, $\tau W$. Considering the decay time for Nd:YAG of 200 microseconds, the pulse energy will level off below 2 kHz as shown in Figure 26. Similar performance using pulsed pumping would require varying the energy to the lamp. Pulse pumping is not practical at high repetition rates due to the long recovery times of the lamp gas.

Figure 27 illustrates the beam divergence-diameter performance required of the laser illuminator for the acquisition, track, and precision track modes of operation. The desired laser performance is indicated by the cross-hatched areas shown. Also shown is the performance that can be

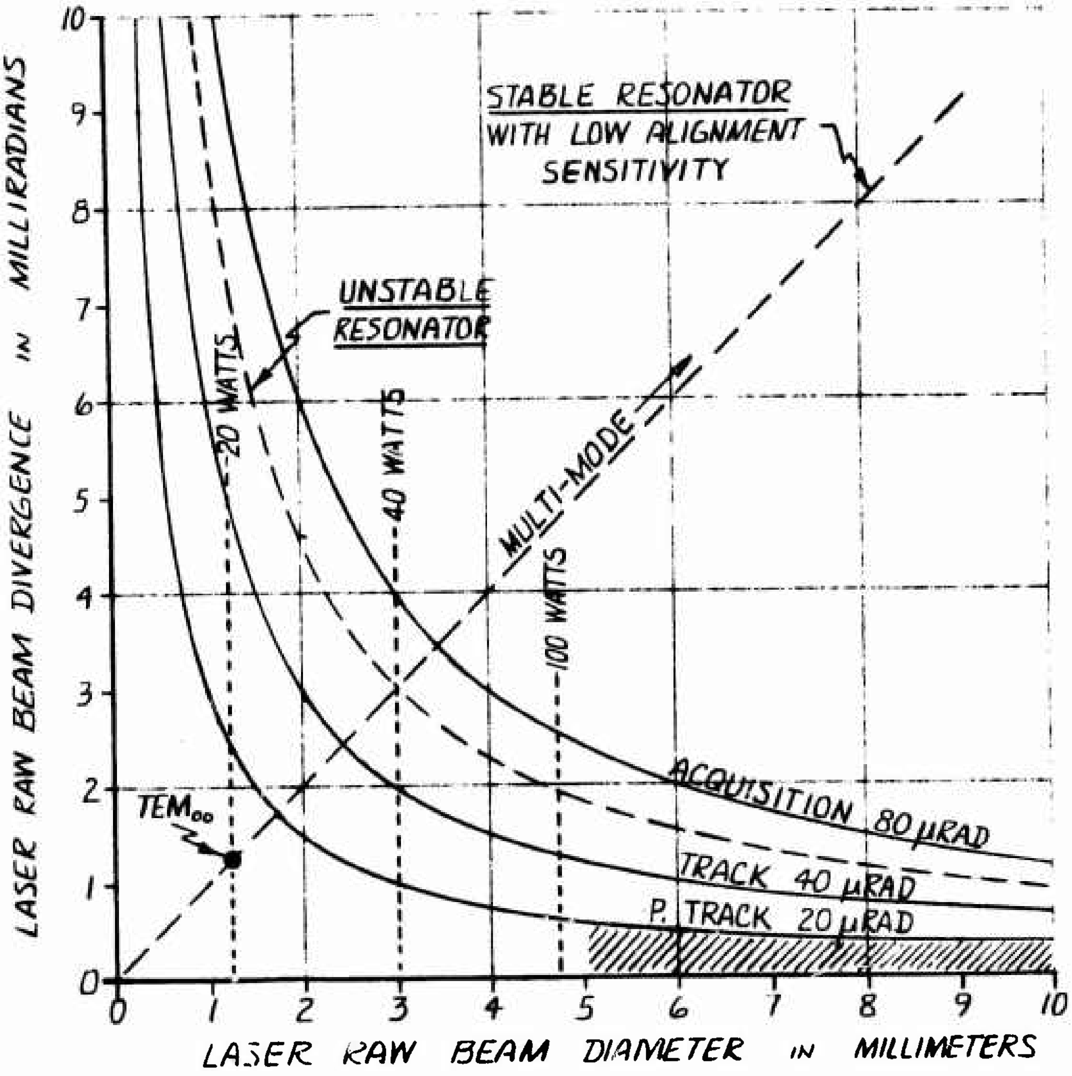

Figure 27. Laser Performance Requirements

expected of both $\mathrm{TEM}_{00}$ mode stable and unstable resonators. The large divergence-diameter product of the unstable resonator makes it clearly unacceptable. The small divergence-diameter product of the $\mathrm{TEM}_{00}$ mode stable oscillator is acceptable, however. Nevertheless, due to alignment sensitivity, it is not reasonable to allow the mode diameter to grow beyond about 1.0 mm. Based on state-of-the-art circulating intensities, vertical lines which indicate the average power obtainable at different mode diameters are also shown in the figure. 20 watts is obtainable at 1.0 mm, but 100 watts requires a mode diameter of nearly 5 mm.

By expanding the oscillator beam from 1 mm to about 5 mm and using an amplifier stage with a 5 mm rod diameter, the average beam power may be raised to the 100 watt level assuming no beam distortion is introduced by the amplifier.

The amplifier design will be most efficient when saturated. The key parameters of the proposed amplifier design are listed in Table 8.

TABLE 8

Amplifier Parameters

| | |
|---|---|
| Laser Rod | 5.0 mm diameter x 76 mm length |
| Saturated Gain | 0.21/cm |
| Optical Power input | 20 Watts |
| Optical Power output | 100 Watts |
| Input Power | 10 kW |

The oscillator/amplifier arrangement has a number of advantages over an oscillator alone and some disadvantages. The disadvantages are possibly reduced efficiency and a larger head size. The advantages are considerable, however. First, the oscillator is operated at moderate power, thereby reducing the thermal problems associated with producing the Q-switched output. Furthermore, the amplifier sections allow power conservation by varying their cw pump rates. For close range tracking, reduced power from the illuminator may be achieved by reducing the amplifier pumping rather than varying the oscillator output. This is especially important since thermal focusing in solid state laser rods limits the power range of a given cavity configuration for acceptable performance.

### 3.2.5 Laser PRF Limitations due to Range-Gating Requirements

Consider the laser illuminator, reflected return, and receiver gating waveforms as shown in Figure 28, where $t_p$ is the illuminator pulsewidth, PRF is the illuminator pulse repetition frequency, $t_d$ is the receiver gate delay, $t_g$ is the receiver gate width, $t_{m1}$ is the time between the trailing edge of the preceding illuminator pulse and the leading edge of the receiver gate, and $t_{m2}$ is the time between the trailing edge of the receiver gate and the leading edge of the succeeding illuminator pulse.

Note that the reflected return arrives back at the receiver after a round trip propagation time of $2R/c$ where R is the range to the target and c is the velocity of light. Because the range to the target may be known (i.e., measured) only to an accuracy of $\pm \Delta R$, the receiver gate width must be wide enough to allow for this uncertainty in arrival time.

Note also that n is the number of in-flight pulses existing when the receiver is gated on (the waveforms of Figure 28 illustrate the situation for $n = 2$).

The following relations may be readily deduced from the waveforms shown:

$$t_p \leq \frac{1}{PRF}$$

$$\frac{4\Delta R}{c} + t_p \leq t_g \leq \frac{1}{PRF}$$

$$t_d \leq \frac{2(R-\Delta R)}{c}$$

$$t_{m1} \geq t_m + \frac{2\,R_{min}}{c}$$

$$t_{m2} \geq t_m$$

where $t_m$ is the minimum allowable time between the trailing edge of the preceding illuminator pulse and the leading edge of the receiver gate or the minimum allowable time between the trailing edge of the receiver gate and the leading edge of the succeeding illuminator pulse, and $R_{min}$ is the minimum range from the illuminator/receiver for which it is absolutely necessary to gate out illumination pulse backscatter.

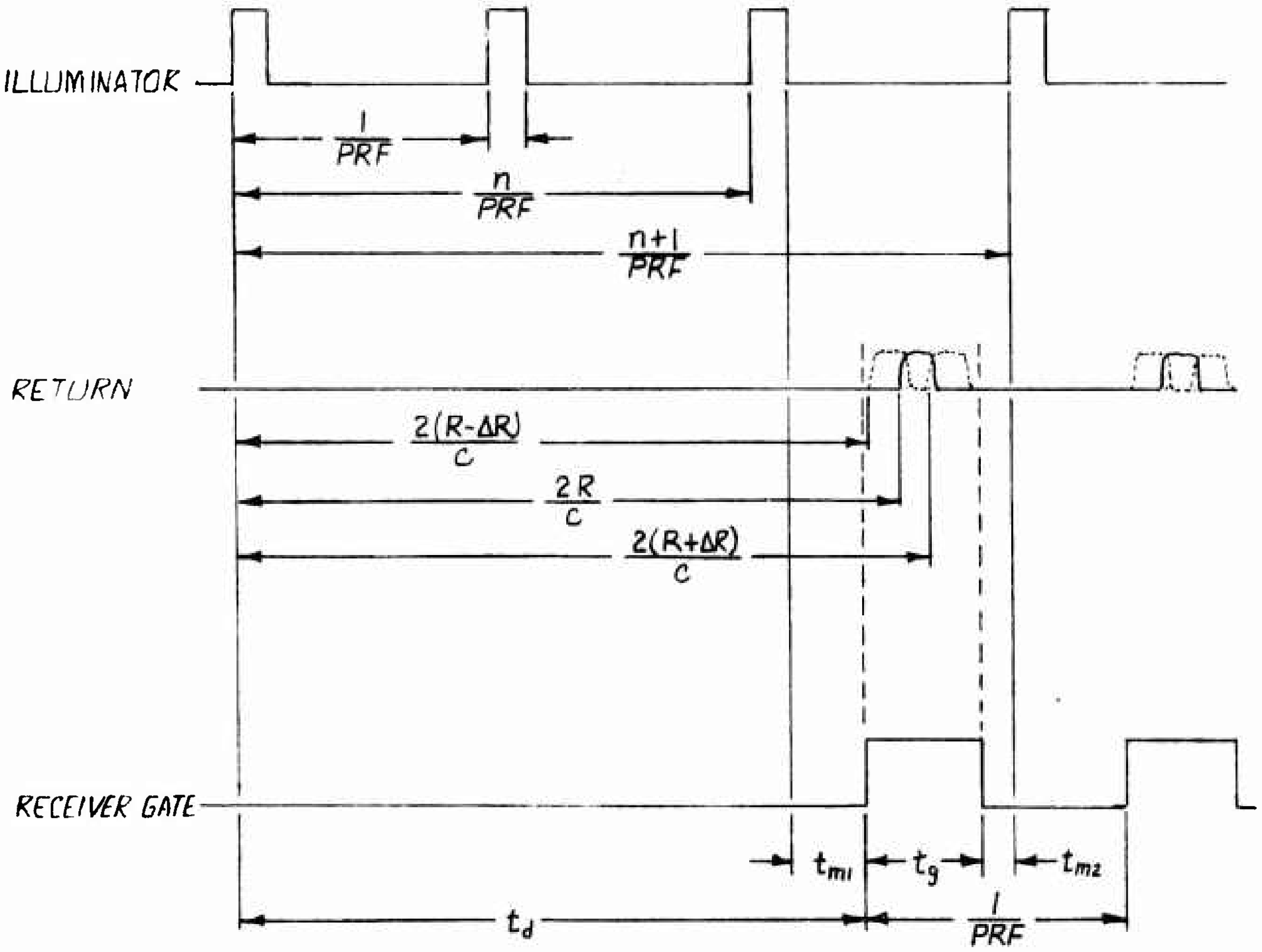

Figure 28. Range-Gate Timing

Using the above relations, we can now generate limits on PRF as

$$\frac{n}{PRF} = t_d - t_p - t_{m1}$$

$$PRF = \frac{n}{t_d - t_p - t_{m1}}$$

But the above relations show that

$$t_d - t_p - t_{m1} \leq \frac{2(R-\Delta R-R_{min})}{c} - t_p - t_m$$

so the lower bound on PRF is given by

$$PRF \geq \frac{n}{\frac{2\ (R-\Delta R-R_{min})}{c} - t_p - t_m} \qquad \underline{\text{lower bound}}$$

For the upper bound we begin by assuming that the receiver gate is centered about the expected position in time of the reflected return and write that

$$\frac{n+1}{PRF} = \frac{2R}{c} + \frac{t_p}{2} + \frac{t_g}{2} + t_{m2}$$

$$PRF = \frac{n+1}{\frac{2R}{c} + \frac{t_p}{2} + \frac{t_g}{2} + t_{m2}}$$

But again using the above relations, we have that

$$\frac{2R}{c} + \frac{t_p}{2} + \frac{t_g}{2} + t_{m2} \geq \frac{2(R+\Delta R)}{c} + t_p + t_m$$

So, the upper bound on PRF is given by

$$PRF \leq \frac{n+1}{\frac{2\ (R+\Delta R)}{c} + t_p + t_m} \qquad \underline{\text{Upper bound}}$$

An absolute upper bound on PRF is provided by the sum of the illuminator pulsewidth, the receiver gate width, the minimum backscatter blanking period, and the two minimum "guard periods" between illuminator pulses and receiver gates; i.e.,

$$PRF \leq \frac{1}{t_p + t_g + \frac{2R_{min}}{c} + 2t_m}$$

$$\leq \frac{1}{\frac{2\ (R_{min} + 2\Delta R)}{c} + 2t_p + 2t_m} \qquad \underline{\text{Absolute upper bound}}$$

These PRF bounds or limits are plotted in Figure 29 for the typical conditions listed below and for n ranging from 0 to 10.

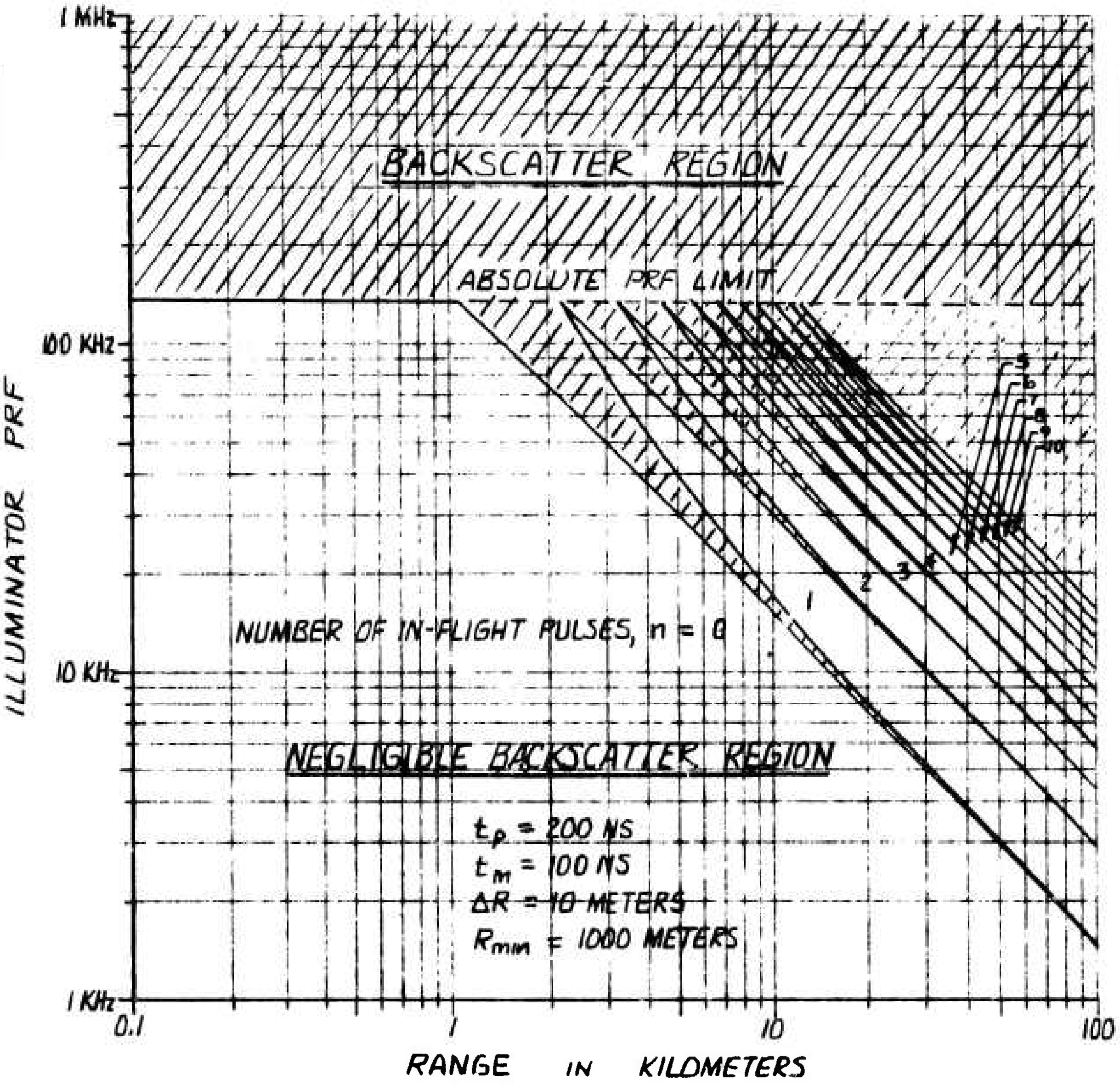

Figure 29. Illuminator PRF Limitations due to Backscatter

$t_p = 200$ ns

$t_m = 100$ ns

$\Delta R = 10$ meters

$R_{min} = 1000$ meters

Note from the figure that it is possible to use PRFs higher than the simple relation

$$PRF_{max} = \frac{c}{2R}$$

would indicate provided that the absolute upper limit is not exceeded. However, if these higher PRFs are used at long range, brief backscatter regions will be encountered periodically as the range decreases.

To prevent ever entering a backscatter region, either the PRF can be abruptly switched to a different value as these regions are approached or the PRF can be increased linearly with decreasing range so as to keep it always within a region of negligible backscatter.

## 3.3 Receiver Technology

While laser technology at 1.06 µm has become highly developed over the past few years, imaging receiver technology has not. Near-infrared imaging systems have been hampered in the past by the generally poor performance of imaging sensors at the 1.06 µm wavelength. For example, the venerable S-1 photocathode exhibits a quantum efficiency of only 0.05 to 0.1 percent at this wavelength. Special III-V alloy photocathodes, which are presently receiving considerable development emphasis, have to date exhibited 1.06 µm quantum efficiencies in the one percent range, although high performance has been predicted. This detective capability is far from the 10 to 50 percent quantum efficiencies readily obtainable with visible spectrum imaging sensors.

To meet the target acquisition range performance desired, the SLIR system requires a high sensitivity 1.06 µm imaging receiver. Such a receiver requires a detector which exhibits sufficiently high 1.06 µm 1.06 µm quantum efficiency, very low leakage current, and extremely low output capacitance such that it can be mated to a preamplifier in which the amplifier's input noise does not swamp out the signal. With the advent of charge coupled device (CCD) technology, such a receiver is possible.

A CCD is an inherently low noise imaging device, particularly if it is of the buried-channel variety. Because conventional CCDs employ silicon-based MOS construction, they also exhibit some photo response at 1.06 µm. This sensitivity is fairly low, however, due to silicon's characteristically small absorption coefficient at this wavelength. However, aside from its obvious capabilities as a monolithic image sensor, the CCD may also be used as an analog shift register to multiplex a separate array of photodetectors specifically designed for high quantum efficiency at 1.06 µm. Such a hybrid approach retains the low-noise signal processing attributes of the CCD while enhancing its detectivity at 1.06 µm. Technology considerations which affect this hybrid CCD approach are discussed in detail in the following subsections.

### 3.3.1 Hybrid CCD Technology and Signal-to-Noise Considerations

Technology and Application. Earlier sections of this report have established the need for a large linear array of perhaps 250 elements to provide the necessary field-of-view and resolution for a scanning system. The detector elements required are very small and essentially contiguous. Although a real-time system consisting of 250 separate amplifier channels is possible in principle, it presents severe problems in practice. Disregarding the physical problem of securing 250 conduction paths to an array of small total area, the problem of providing initial amplification very close to the detector elements remains. Conduction paths of significant length would degrade the high performance possible with small, low capacitance elements. Providing 250 preamplifiers in close proximity obviously requires high density circuits, and integrated circuits generally give poorer noise performance than that obtainable from a well-designed discrete circuit. Even assuming that an acceptable integrated circuit amplifier array could be fabricated within a sufficiently small area, one is still faced with the problem of dealing with 250 signal leads and 250 discrete processing stages at some point unless a large portion of the entire electronics is an integrated or hybrid circuit. While the nature of this discussion is very intuitive, it seems apparent that a parallel-in, serial-out CCD shift register approach requiring only a few amplifier systems is very desirable if this approach can provide adequate performance. In fact, a real-time system cannot equal the noise performance of an integrating CCD system unless the illuminator pulsewidth is narrower than is generally practical for a high PRF 1.06 μm laser.

The term hybrid CCD as used here refers to a photosensor array connected to a CCD array of equivalent dimension. Although the CCD alone can provide photodetection, there are no presently available CCD's which have sufficient quantum efficiency at the wavelength of interest to meet the ultimate tracker system sensitivity requirements. Figure 30 illustrates the hybrid CCD concept. A three-phase CCD clock is shown for purposes of illustration. The photodiodes feed signal current into the CCD in parallel

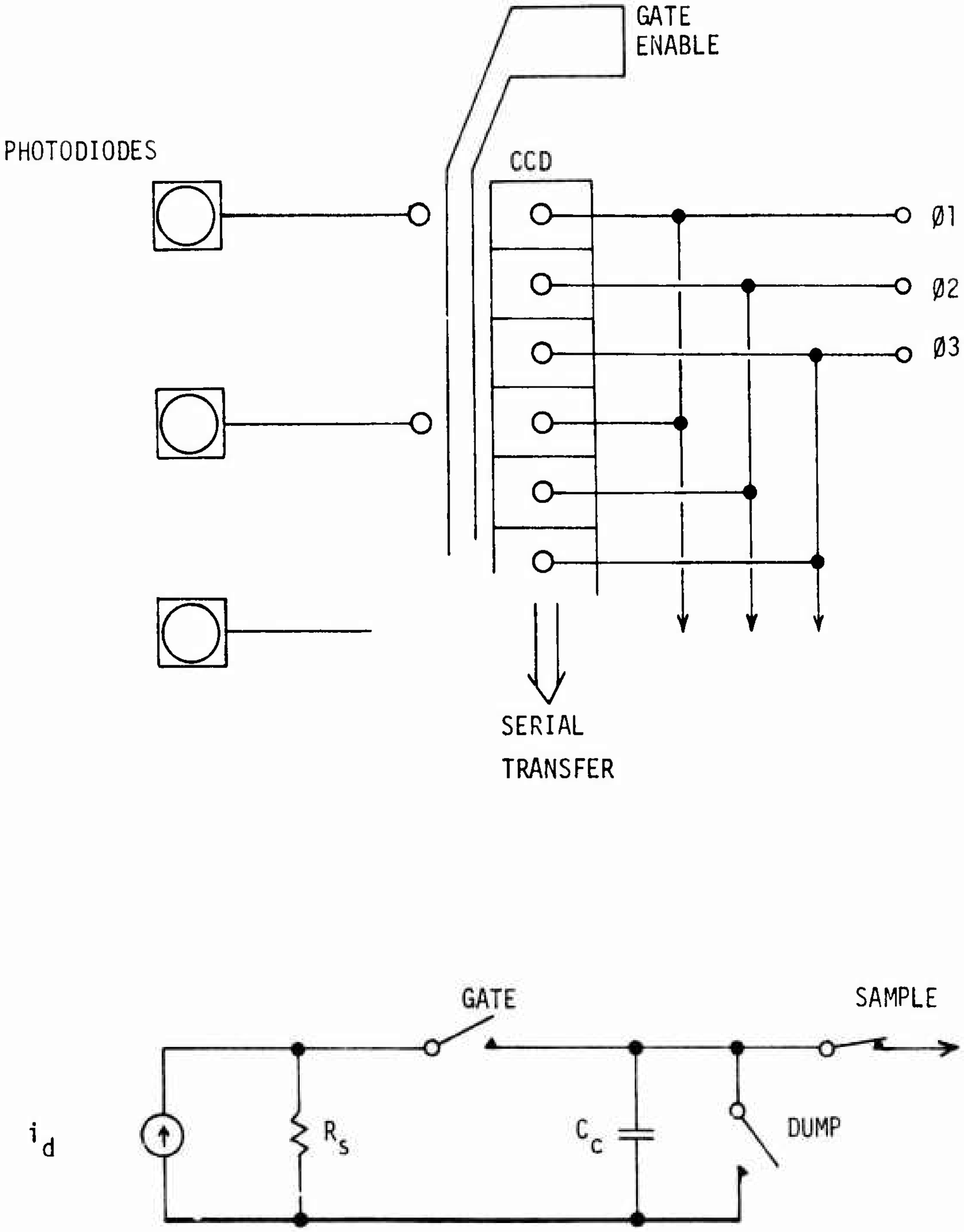

Figure 30. Photodiode-CCD Array: Physical Representation and Simplified Electrical Equivalent for One Stage

fashion, and signal can be serially clocked out. The figure does not deal specifically with the photodiode-CCD interface; this will be discussed in the following sub-topic. The lower portion of Figure 30 shows a simplified electrical equivalent of a single photodiode-CCD stage. In addition to the gating property, this schematic indicates an ability to dump and hold dumped the CCD storage--which is available in some CCD's (e.g., Fairchild's CCILID1728).

The marriage of photodiode arrays with CCD's has already been accomplished for some applications. References (5) and (6) discuss design considerations and test results for far-infrared sensors directly bonded to CCD arrays. This technique is called 'direct injection' and is discussed more fully in the next sub-topic. The analyses in these references are not completely applicable to a SLIR system, because the IR photodiodes and sensors used exhibited significantly greater cell capacitance and shunt conductance than would detectors commensurate with SLIR requirements, and the temporal operating frequencies are somewhat different. The IR sensors also operated at lower voltages than those normally associated with the PIN diodes and avalanche photodiodes (APD's) discussed later in this report. This is a potential problem in that high photodiode reverse bias voltages can place a voltage across the CCD input which destroys the input circuit, particularly if the photodiode receives large signal irradiation. The solutions to this problem are examined in the next sub-section, which deals specifically with the photodiode parameters.

Signal-to-Noise Considerations. The following work will primarily address the derivation of signal-to-noise (S/N) performance when a sampled integrating device (CCD) is used to receive signal from a real-time sensor. The analysis will be influenced by the fact that incident signal is returned from a reflected laser pulse with half-amplitude width of about 200 nano-seconds. It is assumed that approximate target range even at maximum acquisition distance is known from radar data, so that range gating may be used at all times. Since the hybrid CCD is a sampled nonlinear system, it is convenient to first consider the noise accumulated during CCD signal storage, and then account for noise due to subsequent

---

(5) Hess, et al, "The MOSART (Monolithic Signal Processor and Detector Array Integration Technology) Program (U)," Proceedings, IRIS, Vol. 19, Sept 1974.

(6) A. J. Steckl, "Injection Efficiency in Hybrid IR CCDs," Proceedings, 1975 Conference on the Applications of CCDs, San Diego, Calif., 29-31 October 1975.

sampling and amplification. The initial storage in itself constitutes a linear system, as does amplification after sampling of the serial output.

Photodiode and Direct Injection Noise. The simplified circuit of Figure 30 will be used to derive the general noise variance for initial storage. This figure neglects photodiode capacitance which, in an integrated array, should be small in comparison to the CCD input capacitance. The current into capacitor $C_c$ is then defined by a simple transfer function as:

$$i_c = \frac{R_s C_c S}{R_s C_c S + 1}\, i_d$$

In a representative hybrid CCD configuration, a typical $C_c$ value of 1 pf and the shunt resistance $R_s$ for a small, low-leakage diode give a corner frequency $f_c = \frac{1}{2\pi R_s C_c}$ in the range of several hundred hertz, or lower. For $f >> f_c$, almost all signal current flows into $C_c$; while for $f < f_c$, most of the current flows through the resistor. This implies that almost all signal current from a 200 nsec pulse is integrated by $C_c$, and that sensor 1/f noise tends not to influence the final charge on $C_c$. Restating the above transfer function in terms of steady-state frequencies:

$$|H(f)| = \frac{f}{\sqrt{f^2+f_c^{\,2}}}$$

For a mean square noise current which has constant power density $\eta$ in the spectrally flat region beyond a 1/f knee at $f_k$, the frequency dependent power spectral density below $f_k$ is well approximated by

$$p(f) = \eta \frac{f_k}{f}$$

Ignoring the 1/f noise contribution above the 1/f knee $f_k$, the mean square noise current due to 1/f noise is:

$$\overline{i_f^{\,2}} = \int_0^{f_k} p(f)\, |H(f)|^2\, df$$

Using the results developed just above,

$$\overline{i_f{}^2} = \eta f_k \int_0^{f_k} \frac{f}{f^2+f_c{}^2}\, df.$$

This integral is easily evaluated and gives:

$$\overline{i_f{}^2} = \frac{\eta}{2} f_k \, \ell n \left[ \frac{f_k{}^2+f_c{}^2}{f_c{}^2} \right] \tag{1}$$

Since the $\overline{i_f{}^2}$ in Equation (1) is constant in time, the rms noise charge accumulated by CCD storage capacitance during a gate period $\tau_g$ is

$$\sigma_f = \int_0^{T_g} \sqrt{\overline{i_f{}^2}}\, dt = \sqrt{\overline{i_f{}^2}}\, T_g, \text{ or,}$$

$$\sigma_f = \sqrt{\frac{\eta}{2} f_n \;\; \ell n \left[ \frac{f_k{}^2+f_c{}^2}{f_c{}^2} \right]} \;\; (T_g) \tag{2}$$

In the absence of 1/f noise, receiver noise can be considered spectrally flat, and the CCD essentially integrates the output diode current $i_d(t)$ over almost the entire frequency range of interest. The charge available at time t is then:

$$Q = CV = \int_o^t i_d(t)\, dt$$

Under the assumption of perfect integration, the noise charge variance is easily derived. An integrator with no initial storage which integrates input over a gate period $T_g$ and is later sampled can be represented by the linear transfer function:

$$H(S) = \frac{1}{S} - \frac{e^{-sT_g}}{s} ,$$

where the $\frac{e^{-sTg}}{s}$ term represents a negative integration which begins to add to the output at the end of the gate time, causing the resultant output to remain the value present at $t = T_g$. For the steady-state spectral noise components, this transfer function becomes:

$$H(w) = \frac{1 - e^{-j\omega T_g}}{j\omega} .$$

The output noise variance $\sigma_N^2$ due to white input noise of one-sided power spectral density $\eta$ (in Amps$^2$/hz) is:

$$\sigma_N^2 = \eta \int_o^\infty |H(f)|^2 \, df$$

H(f) corresponding to the H(w) for a sampled integrator gives:

$$\sigma_N^2 = \frac{\eta}{2} T_g \qquad (3)$$

The rms noise $\sigma_N$ (with units of coulombs) is therefore proportional to the square root of the gate time. It is interesting to note that when $T_g$ is equal to and coincident with the signal pulsewidth, an integrator following a real-time sensor is actually a matched filter, giving optimum S/N. An intuitive explanation is that the integrator tends to zero-average high frequency noise components while collecting all pulse energy.

Table 9 illustrates the relative magnitude of the two rms charge values $\sigma_f$ and $\sigma_N$ for a representative range of $f_c$ and $f_k$ values, and a conservative gate period $\tau_g$ = 1 microsecond. The table brackets the $R_sC_c$ corner frequency at 1000 and 100 Hz. $R_s$ for a small, low-leakage sensor will be several hundred meg-ohms or greater. The channel resistance of the MOSFET CCD input circuit is also several hundred meg-ohms at low-level acquisition range currents. Although consideration of the entire sensor and input structure

TABLE 9

Relative Contribution of 1/f and Spectrally Flat Noise for Various Corner Frequencies and 1/f Knees

| $f_c$ | $f_k$ | $\sigma_f/\sigma_N$ |
|---|---|---|
| 1000 Hz | 100 Hz | .001 |
| | 1000 Hz | .026 |
| | 10000 Hz | .215 |
| | 100000 Hz | .960 |
| 100 Hz | 100 Hz | .008 |
| | 1000 Hz | .068 |
| | 10000 Hz | .304 |
| | 100000 Hz | 1.175 |

is slightly more complicated than the development here, the results are approximately the same for large resistances and small $C_c$. The CCD input capacitance $C_c$ can reasonably be expected to be about 1 pf or less. This leads to an $f_c$ perhaps greater than 1000 Hz, but the 100 Hz entries are shown to represent a worst-case condition. The most severe 1/f consideration for the "direct injection" hybrid interface technique will likely be the input MOSFET 1/f knee location. MOSFET 1/f characteristics can vary widely, but securing 1/f knees below 100 kHz is common and certainly could be done for a specifically fabricated hybrid CCD. The table shows that the noise charge due to 1/f noise current becomes important only for knee frequencies around 100 kHz or greater. This result would seem to make unnecessary any evaluation of circuit values which is more specific than the discussion above.

It is now necessary to determine the power spectral density $\eta$. Noise current will originate from three major sources: 1) photodiode shot noise; 2) the real photodiode shunt resistance; and 3) the photodiode-CCD interface or CCD input circuit. Evaluation of the first two is a standard procedure. The interface will constitute a noise mechanism no matter how it is implemented. The most common and practical implementation is the direct injection method illustrated in Figure 31. The photodiode is connected directly to a p-type diffusion area in an n-type substrate. When the gate voltage $V_g$ is not sufficiently large to enable the conduction of charge into the potential well storage (under $V_s$), this input p-n junction is a reverse-biased diode, and both diodes are held reverse biased by the potential difference between the bias supply and substrate potential. The electrode potentials create a depletion area indicated by the dashed line which can behave as a p-channel MOSFET, controlled by the insulated gate voltage $V_g$. The p-type diffusion acts as the source and the inverted region under $V_g$ and $V_s$ acts as the drain. The correct $V_g$ potential will turn this MOSFET completely on, but the photodiode current generator in series with the MOSFET source limits current to that produced by the photodiode. The capacitance of the CCD input structure is composed of several parallel capacitances, with the MOSFET gate-to-source capacitance dominating. If photodiode capacitance is of significant size in comparison with CCD input capacitance, the signal sharing between these capacitors will necessitate consideration of injection efficiency. The condition $|V_s|>|V_g|$ is required so that charge stored in input capacitance will accumulate in the storage well under $V_s$. Transfer voltage $V_T$ and the first phase clock $\phi_1$ are applied at the proper times to move the signal charge down the CCD in normal fashion.

Since the CCD input circuit operates as a grounded gate MOSFET, the major input noise will be due to the MOSFET channel resistance $R_n$. $R_n$ can be roughly approximated as $R_n \simeq 1/g_m$. For very low average current $I_d$, MOSFET transconductance $g_m$ is approximately:

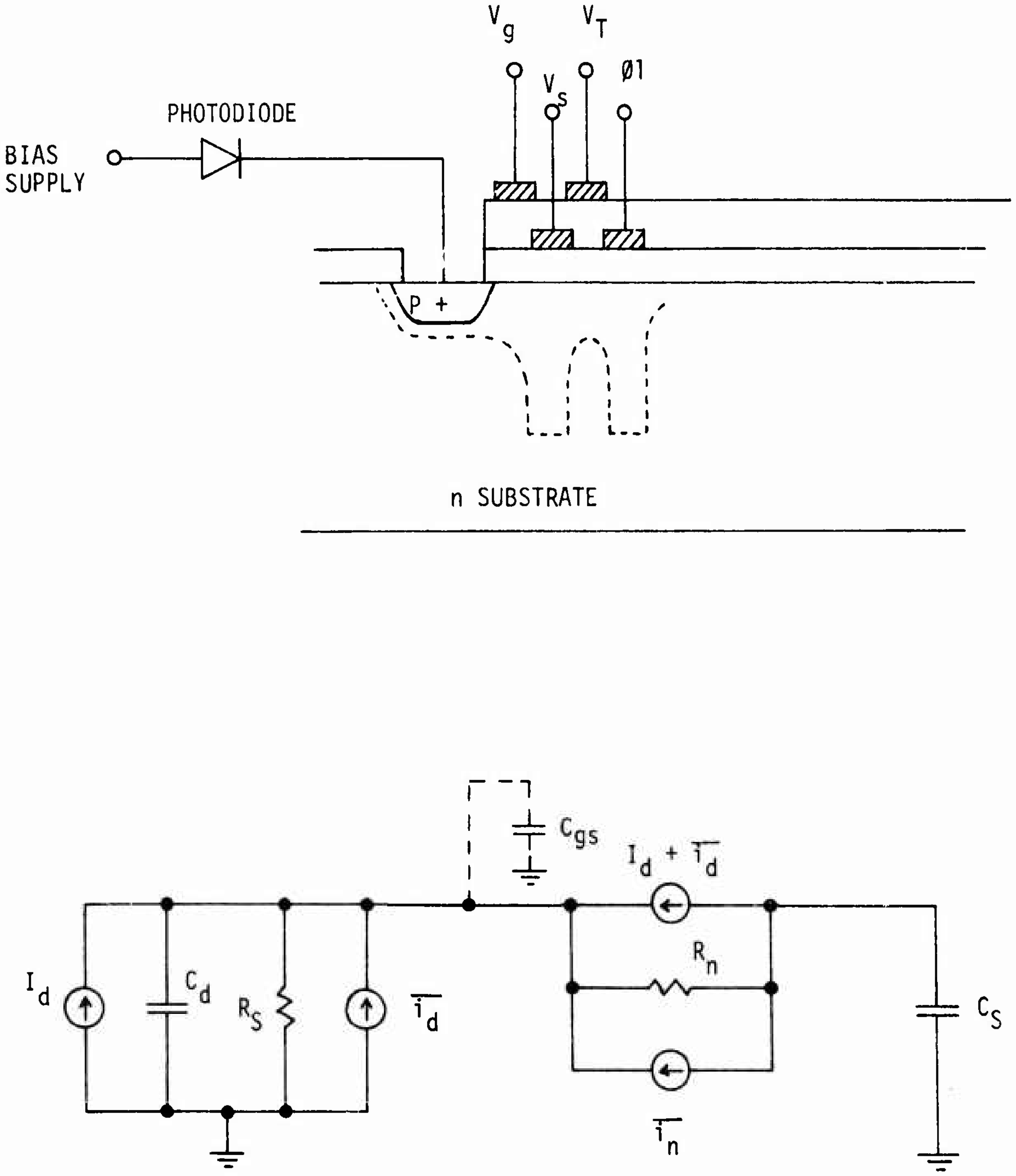

Figure 31. Physical and Electrical Representation of Direct Injection Interface Technique.

$$g_m \approx \frac{q}{kT} I_d,$$

where: $q$ = electron charge

$k$ = Boltzmann's constant

$T$ = absolute temperature ($^{o}$K).

Then the mean square noise current due to $R_n$ is:

$$\overline{i_n^2} = 4kT\ (1/R_n)\ \Delta f \approx 4kT\ g_m\ \Delta f = 4qI_d\ \Delta f. \tag{4}$$

It is now possible to derive the total noise power spectral density $\eta$ by evaluating the mean square noise current due to the photodiode. To provide the most general analysis, APD parameters will be used. The analysis will be valid for other photodiodes if a gain of 1 is assigned. The most accurate expression for APD noise current makes use of excess noise factors for photocurrent and bulk leakage. However, the excess noise factors are difficult to assess without specific data and are usually approximated. This situation is often dealt with by approximating the noise as:

$$\overline{i_d^2} = \{\ 2q\ \left[\ I_{SL} + (P_d\rho + I_{BL})\ G^{\alpha}\right] + \frac{4kT}{R_S}\ \}\ \Delta f, \tag{5}$$

where:

$I_{SL}$ = surface leakage current

$I_{BL}$ = bulk leakage current

$P_d$ = average power (due to background and signal) incident on the detector during the gate time

$G$ = gain of the APD

$\rho$ = detector responsivity in amps/watt

$R_S$ = shunt resistance

The $G^{\alpha}$ term is a method of accounting for the fact that APD gain is not noiseless, by assigning $\alpha > 2$. The average diode current of equation (4) is:

$$I_d = I_{SL} + (P_d\rho + I_{BL})G$$

If a charge variance $\sigma_c^2$ is designated to account for subsequent CCD processing and amplification (after initial storage), equations (3), (4) and (5), together with the above expression for $I_d$, give the following total charge variance:

$$\sigma_N{}^2 = \{ q \left[ 3I_{SL} + (P_d\rho + I_{BL}) (G^\alpha + 2G) \right] + \frac{2kT}{R_s} \} T_g + \sigma_c{}^2 \qquad (6)$$

For a signal of time-varying power $P_{ds}(t)$ incident on the detector from time $t_1$ to $t_2$ within the gate time, the signal charge stored in a CCD element during gate integration time is:

$$S = \int_o^{T_g} G\, \rho P_{ds}(t)\, dt = G\rho \int_{t_1}^{t_2} P_{ds}(t)\, dt.$$

For average signal power $P_{ds}$ and pulsewidth $T_W$, the stored signal charge is:

$$S = G\, \rho\, P_{ds}\, T_W \qquad (7)$$

From equations (6) and (7), the signal-to-rms noise ratio is:

$$S/_N = \frac{\rho\, P_{ds}\, T_W\, G}{\sqrt{\{ q \left[3I_{SL} + (P_d\rho + I_{BL}) (G^\alpha + 2G)\right] + \frac{2kT}{R_s} \} T_g + \sigma_c{}^2}} \qquad (8)$$

This assumes that pulse and D.C. responsivities are about equal for pulsewidths of several hundred nsec. The optimum APD gain $G_o$ can be determined by setting the derivative of the above expression with respect to G equal 0. This is not directly solvable for a general gain penalty $G^\alpha$, but is the G value which satisfies the equation:

$$\left[q\, (P_d\rho + I_{BL})\, T_g\, (\alpha-2)\right] G^\alpha - \left[ 2q(P_d\rho + I_{BL})\, T_g\right] G - \left[(6q\, I_{SL} + \frac{4kT}{R_s})\, T_g + 2\sigma_c{}^2 \right] = 0 \qquad (9)$$

The $(G^\alpha + 2G)$ term in equation (8) will be dominated by $G^\alpha$ for appreciable gain. If the 2G portion of this term is neglected, a useful approximation results which can be used to estimate optimum gain or to aid in iteratively solving equation (9):

$$G_o \simeq \left[\frac{(6q\, I_{SL} + \frac{4kT}{R_s})\, T_g + 2\, \sigma_c{}^2}{q\, (P_d\rho + I_{BL})\, T_g\, (\alpha-2)}\right]^{1/\alpha} \qquad (10)$$

If subsequent CCD processing noise is assumed small compared to initial storage noise, a simpler relation results which depends only on APD parameters:

$$G_o \simeq \left[\frac{6q\, I_{SL} + \frac{4kT}{R_s}}{q\, (P_d\rho + I_{BL})(\alpha-2)}\right]^{1/\alpha} \qquad (11)$$

CCD and Processing Noise ($\sigma_C$). CCD noise performance will be assessed in terms of noise incurred from CCD input to the final post video amplifier output, with the understanding that noise due to sensors preceding the CCD (if present) is not included. Noise due to signal amplification after the serial CCD output is commonly referred back into the CCD cell as a charge variance, and this method of noise evaluation will be used here. Also, CCD noise is most conveniently discussed in terms of rms electrons per output signal. A theoretical calculation of CCD noise is quite lengthy, and some theoretical models are not fully developed. For this reason, it is advantageous to cite test results with measured noise values. At typical clocking frequencies, CCD noise depends mainly on the quality and type of CCD device and on the type of output circuit employed. Of the several basic types of CCD's available, buried channel devices offer the best signal transfer efficiency and noise performance, and the highest permissible clock frequencies (100 Mhz). The output circuits commonly used are conventional MOSFET amplifiers and floating gate amplifiers (FGA), both on-chip; and correlated double sampling techniques can be used with a conventional amplifier structure to greatly improve CCD noise performance. Correlated double sampling takes advantage of the long RC time constant which results when the signal voltage of the CCD output capacitance appears on the high impedance gate of a MOSFET preamplifier. Since this capacitance is necessarily reset through a low resistance prior to the transfer of each new signal packet, the reset noise voltage present at the end of the reset period will persist relatively unchanged for an appreciable interval. Then subtracting the voltage sampled just before the end of the reset pulse from the voltage sampled afterwards will remove the reset noise component from the output voltage. Broderson and Emmons report in Reference 7 that a theoretical noise of 25 rms electrons was predicted and 27 rms electrons measured for a standard buried channel 150 stage linear CCD clocked at .5 MHz. This includes the noise contribution of the output amplifier, which consisted of ordinary MOSFET transistors.

The FGA offers some noise advantage over conventional amplifiers and also reduces or eliminates practical problems such as clock and

---

(7) Brodersen, R. W., and Emmons, S. P., "Noise in Buried Channel Charge Coupled Devices," IEEE Transactions on Electron Devices, Vol. ED-23, No. 2, February 1976.

reset pulse feedthrough in the signal. Wen reports in Reference 8 that present FGA performance gives 150 to 180 rms noise electrons with an expected improvement by a factor of 3 to 4 in the future as device geometry is optimized. This is for a 28 Mhz amplifier bandwidth and includes amplifier noise. The nominal SLIR clock frequency of 10 Mhz would decrease this bandwidth and decrease the noise accordingly. Extensive CCD noise measurements for conventional output amplifiers have been accomplished at Martin Marietta. In a formal test report (Reference 9), S. Buchanan and D. Schmieder give 188 rms noise electrons for a standard randomly selected CCD (Fairchild CCD121-1728) clocked at 16 Mhz. Buchanan states that almost half of the rms electrons were due to the use of a non-optimum commercial integrated circuit video amplifier.

Based on definite measured values, it is reasonable to assume that the CCD noise contribution is nominally in a range from 30 to 100 rms electrons for the SLIR application, giving a charge standard deviation of: $30\,q \leq \sigma_c \leq 100\,q$.

Receiver Noise Equivalency. Receiver noise equivalent power (NEP) can be determined from equation (8), optical parameters, and the laser pulsewidth. Noise equivalent charge (NEC) is found directly from equation (8) by setting NEC equal to the rms charge noise, which is the denominator of this equation. It should be noted that the average power $P_d$ incident on the detector during the gate time is due to background power $P_{db}$ and the signal power $P_{ds}$ averaged over the gate time. Substituting $P_d = P_{db} + P_{ds} \left(\frac{T_w}{T_g}\right)$ from equation (8):

$$\mathrm{NEC} = \sqrt{\left\{q\left[3I_{SL} + \left(\left[P_{db} + P_{ds}\left(\frac{T_w}{T_g}\right)\right]\rho + I_{BL}\right)\left(G^{\alpha} + 2G\right)\right] + \frac{2kT}{R_s}\right\}T_g + \sigma_c{}^2} \qquad (12)$$

The units of NEC are coulombs.

---

(8) D. D. Wen, "Design and Operation of a Floating Gate Amplifier" IEEE Journal of Solid State Circuits, Vol. SC-9, No. 6, December 1974.

(9) Buchanan, S., and Schmieder, D., "CCD121 Performance Data," Doc. No. TRP01300000-001, internal Martin Marietta Test Report, June 1976.

Since NEC (and consequently NEP) depends on the signal power $P_{ds}$, equation (12) as it appears above must be solved iteratively to find NEC. However, $P_d$ is relatively small, especially since signal power must be averaged over the gate time and the gate period $T_g$ is likely several times as large as the signal pulsewidth. Therefore, neglecting $P_{ds}$ should provide a reasonable approximation, and using such a first approximation for NEC to develop $P_{ds}$ should provide a very accurate answer on the second iteration. Detector NEP is found by setting the signal charge of equation (7) equal to NEC and solving for the $P_{ds}$ value consistent with this condition. This gives:

$$NEP_d = \frac{NEC}{G\rho T_w}, \text{ or}$$

$$NEP_d = \frac{1}{G\rho T_w} \sqrt{\left\{q \left[ 3I_{SL} + \left(\left[P_{db} + P_{ds} \left(\frac{T_w}{T_g}\right)\right] \rho + I_{BL}\right)(G^{\alpha} + 2G)\right] + \frac{2kT}{R_s} \right\} T_g + \sigma_c^2}, \qquad (13)$$

where NEP is given in watts incident on the detector. Of more interest is the receiver NEP and noise equivalent irradiance, which will be designated $NEP_r$ and $NEI_r$. For an unresolved long-range target, it follows straightforwardly that:

$$NEP_r = \frac{1}{\tau_o} NEP_d, \text{ and} \qquad (14)$$

$$NEI_r = \frac{NEP_d}{\tau_o A_o}, \qquad (15)$$

where $\tau_o$ is effective optical transmission and $A_o$ is the area of the optical aperture. This assumes that the optical blur spot is small enough to place most of the signal energy within a single detector area. If significantly less than all signal energy falls within the detector area, this factor can be taken into account by adjusting $\tau_o$.

Because of the integration provided by the CCD, it will often be convenient to work with the receiver noise equivalent energy, $NEE_r$. For a sensor with quantum efficiency $\varepsilon$, the $NEE_r$ in terms of photons per signal pulse is:

$$NEE_{rp} = \frac{NEC}{\tau_o \varepsilon q G} \text{ , or}$$

$$NEE_{rp} = \frac{1}{\tau_o \varepsilon q G} \sqrt{\left\{ q \left[ 3I_{SL} + \left( \left[ P_{db} + P_{ds} \left( \frac{T_w}{T_g} \right) \right] \rho + I_{BL} \right) \left( G^{\alpha} + 2G \right) \right] + \frac{2kT}{R_s} \right\} T_g + \sigma_c^{2}} \tag{16}$$

Although equation (16) is in terms of photons/pulse, it is an energy rather than power relation, because the result is relatively independent of signal pulsewidth so long as the pulse is short enough to allow storage capacitance to integrate nearly all pulse power. From the relation energy/photon = $\frac{hc}{\lambda}$, equation (16) can be rewritten in terms of joules. h is Planck's constant, c the velocity of light, and $\lambda$ the wavelength of interest. Then,

$$NEE_{rj} = \frac{hc}{\lambda} \left( NEE_{rp} \right). \tag{17}$$

### 3.3.2 Receiver Optics and Detector Constraints

Detector size is not only important to the physical fabrication of hardware, but strongly influences receiver noise performance because of size dependent noise sources. The primary physical factors which determine detector size are the effective focal length, the optical diffraction limit, and the desired angular resolution in object space (detector angular subtense). The nominal diffraction limit in radians ($\theta$), according to a standard equation, is:

$$\theta = \frac{2.44\ \lambda}{D_o} ,$$

where $\lambda$ is the wavelength of interest and $D_o$ is the optical aperture diameter. Since $D_o$ is constrained by specification to $\leq 9$ inches and $\lambda = 1.06$ micron has been chosen, a diffraction limit of about 11 microradians is a fixed parameter. A linear resolution of about 10 microrad detector angular subtense has also been derived in prior sections as necessary for close-range tracking. This leaves two degrees of freedom in configuring the detector and optics: physical detector size and effective focal length. The linear angle $\phi$ subtended by a square detector of side length d for a focal length L is:

$$\phi = d/L.$$

Figure 32 is a plot of this function for d = .5, 1, 2, and 3 mil. The primary consideration for choosing among these values is the resulting effective focal length. A 1 mil detector gives about 100 inches versus an almost 200 inch effective focal length for 2 mils. The main factor here is the need to limit effective focal length to a value short enough to provide good optical baseline stability and reasonable ease of design. The actual optical path length is, of course, shorter than the effective focal length because of optical magnification. While there is no compelling criterion for selecting a specific detector size, the figure shows that a 1 mil detector is a reasonable choice. Detectors smaller than this are difficult to fabricate, and larger detectors give excessive focal length requirements.

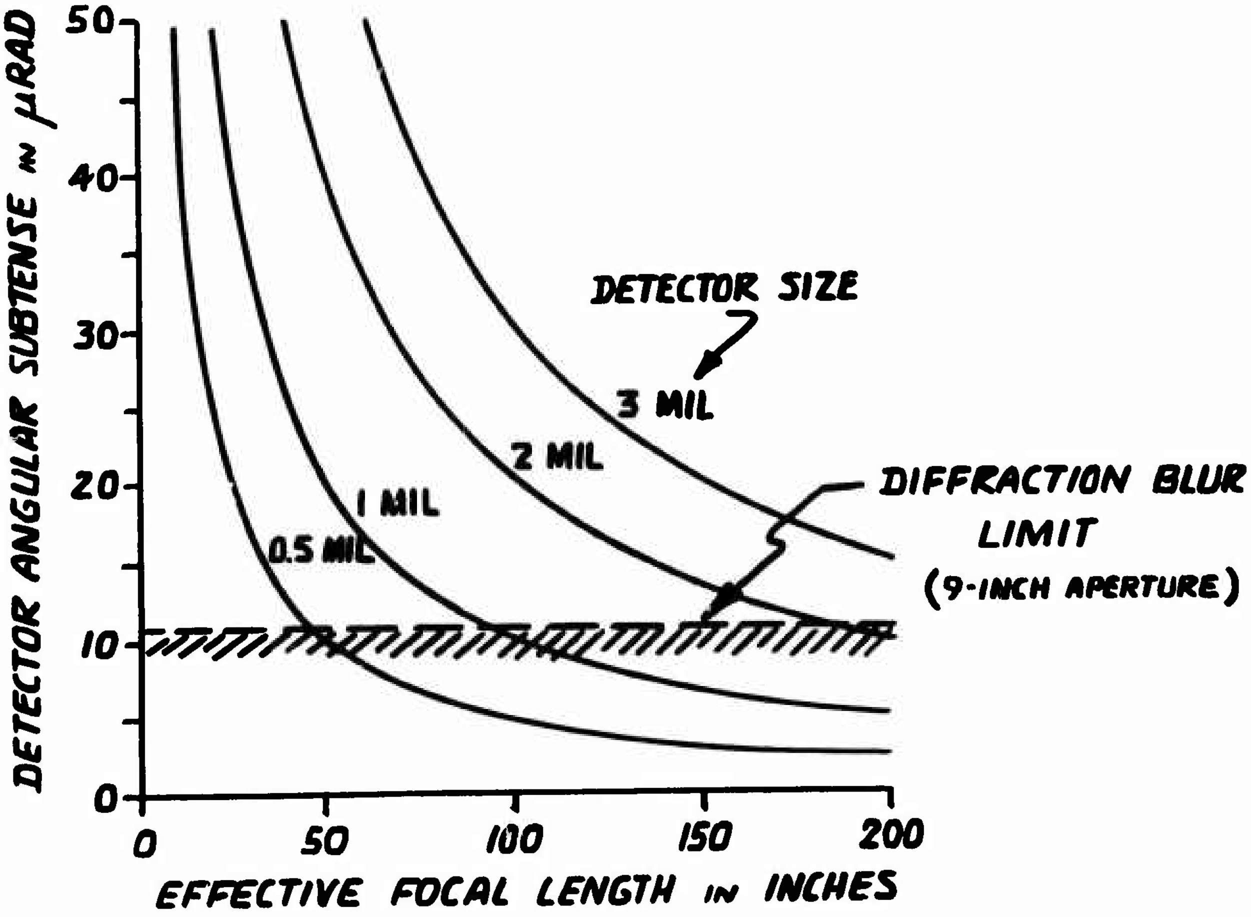

Figure 32. Detector Size Constraints

### 3.3.3 High Performance 1.06 Micron Detectors

There are two primary candidate detectors which have been studied in detail: a GaAsSb avalanche photodiode (APD), and the silicon PIN diode. The APD is a high quantum efficiency, low leakage device, while the PIN has moderate quantum efficiency and very low leakage. This subsection addresses the characteristics of these photodiodes. Section 4.0 will develop the signal-to-noise and range performance attainable with the parameters derived here.

**GaAsSb APD**. This is an APD developed by Dr. Richard Eden of Rockwell International Science Center. References 10 through 12 are papers and reports regarding this device. Information on the device has been obtained from these references and from direct contact with Dr. Eden. There have been several versions of this APD and similar APD's, exhibiting unity gain for reverse bias voltages between 60V and 80V, and lower. The latest device is a 3 mil diameter APD for which Eden reports a noise equivalent energy (NEE) of 375 photons/pulse when used at unity gain in a real-time system with narrow signal pulses (Reference 10).

A physically smaller device would present less leakage current and cell capacitance, and consequently, greater sensitivity. For the 3 mil device, Eden gives cell capacitance as .1 pf and bulk and surface leakages ($I_{BL}$ and $I_{SL}$) at 60V reverse bias as:

$$I_{BL} = 300 \text{ pA}, \; I_{SL} = 3 \text{ nA}.$$

These currents increase approximately proportional to APD gain at higher reverse bias. Bulk leakage scales with area and surface leakage with perimeter. Extrapolating these figures to a 1 mil square APD gives approximately:

$$I_{BL} = 50 \text{ pA}, \; I_{SL} = 1 \text{ nA}.$$

---

(10) R. C. Eden, et al, "High Sensitivity Gigabit Data Rate GaAs$_{1-x}$ Sb$_x$ Avalanche Photodiode 1.06μ Optical Receivers," Proceedings 1975 International Electron Devices Meeting, Washington, D. C., Dec. 1975.

(11) R. C. Eden, "Heterojunction III-V Alloy Photodetectors for High-Sensitivity 1.06 μm Optical Receivers," Proceedings of the IEEE, Vol. 63, No. 1, January 1975

(12) R. C. Eden, "1.06 Micron Avalanche Photodiode," Tech. Rep. AFAL-TR-72-343, January 1973.

According to Eden, the gain penalty of this APD is similar to that of silicon APD's. Although he has made no measurements specifically regarding 1/f noise characteristics because his application is for narrow real-time pulse amplification, Eden is sure from knowledge of other test measurements that the 1/f knee is significantly below 100 kHz.

Shunt resistance, even with gain, is on the order of 1000 MΩ or greater. Table 10 summarizes APD parameters for an APD commensurate with SLIR requirements. These parameters are for room temperature and some can be improved by cooling the device.

TABLE 10

GaAsSb Characteristics at Unity Gain

| | |
|---|---|
| size | 1 mil x 1 mil |
| capacitance | $\leq$ .1 pf |
| bulk leakage | 50 pA |
| surface leakage | 1 nA |
| shunt resistance | $> 10^9\ \Omega$ |

PIN Diode. While the silicon PIN diode is usually thought of as a low quantum efficiency device at 1.06 micron, efficiency can be increased by trading off transit time. Since the present SLIR configuration uses an integrating hybrid sensor and a nominal 200 nanosecond laser pulsewidth, PIN frequency response can be relatively poor compared to the usual optimization for 10 or 20 nanosecond real-time pulse applications. It is also desirable to develop a low voltage PIN which is fully depleted at reverse bias of 50V or less because of CCD interface considerations. Martin Marietta designs and fabricates PIN's and PIN arrays in-house at the Orlando plant.

The quantum efficiency of a silicon PIN diode with light incident upon the N surface and the intrinsic material of high resistivity P type and a reflector on the $P^+$ surface can be treated as the sum of components from the depletion region and the nondepleted region of the detectors. These expressions are shown below.

$$QE = QE_{DEPLETION} + QE_{NONDEPLETION}$$

where

$$QE_{DEPLETION} = 1-e^{-\alpha W} + R_1 \{\exp[-a(W + 2X)] - \exp[-2\alpha (W+X)]\}$$

$$QE_{NONDEPLETION} = e^{-\alpha W}\left\{\frac{\alpha L}{\alpha^2 L^2 - 1}\left[\frac{(s-(XD)\,e^{-\alpha X} + \left(\alpha Ls - \frac{D}{L}\right)\sinh\left(\frac{X}{L}\right) + (\alpha D - s)\cosh\left(\frac{X}{L}\right)}{\frac{D}{L}\cosh\left(\frac{X}{L}\right) + s\,\sinh\left(\frac{X}{L}\right)}\right]\right\}$$

$$+ R_1 e^{-\alpha(W+X)}\left\{\frac{\alpha L}{\alpha^2 L^2 - 1}\left[\frac{\left(s + \alpha D\right)e^{-\alpha X} \quad \left(s + \alpha D\right)\cosh\left(\frac{X}{L}\right) + \left(\frac{D}{L} + s\,L\right)\sinh\left(\frac{X}{L}\right)}{\frac{D}{L}\cosh\left(\frac{X}{L}\right) + s\,\sinh\left(\frac{X}{L}\right)}\right]\right\}$$

and where

$\alpha$ = absorption coefficient

$W$ = depletion layer width

$X$ = nondepletion layer width

$R_1$ = reflection of back metal

$L$ = diffusion length of minority carrier

$s$ = surface recombination velocity of back surface

$D$ = diffusion coefficient.

Martin Marietta devices are typically designed such that the surface recombination velocity is zero and the diffusion length of minority carriers is typically .03 cm. With allowances for AR coatings, devices with a 50 percent quantum efficiency at 1.06 microns at room temperature can be easily achieved. A slight modification of the equations would be required for P side incident devices.

Given the internal quantum efficiency, the DC responsivity of the device can be calculated from

$$\text{Responsivity (A/W)} = .8\ QE\ \lambda$$

where

$QE$ = decimal quantum efficiency

$\lambda$ = wavelength in microns.

DC responsivities of .4 A/W are expected from a device operating at 50 volts bias.

The pulse responsivity of a device is governed by the time constants of the depletion and nondepletion regions of the silicon. The nondepletion region has a time constant related to the minority carrier lifetime and since this is generally in the microsecond range, that portion of responsivity can be ignored when considering the response of a detector to a 200 nsec pulse. The response times within the depletion region of a partially depleted device are governed by the capacitance and load resistance as well as the dielectric relaxation time. These response times are generally in the 20 nsec range and essentially all electrons generated within the depletion region contribute to pulse responsivity. The depletion region for 10,000 Ω-cm material biased at 50 volts can be found by the abrupt junction model of a diode junction and is approximately 200 microns. Assuming an absorption coefficient of 10 $cm^{-1}$ for 1.06 microns, radiation quantum efficiencies in the depletion region of 25-30 percent can be expected. For a 200 nsec pulse, this would correspond to responsivities of .21 to .25 amperes/watt.

Leakage Current. The leakage current of a photodiode is given by the sum of three currents. The most important of these is due to currents created within the depletion region of device. These currents are caused by alternate emission of electrons and holes from centers whose energy level is near the intrinsic Fermi level. This current can be described by

$$I_{dep} = 1/2\, q \frac{n_i W A}{\tau}$$

where

$q$ = electronic charge

$n_i$ = intrinsic carrier concentration

$\tau$ = lifetime within the depletion region

W = depletion later width

A = area of depletion region

For a nominal 25 microsecond lifetime, the leakage currents for an electrically active area of 6 mils by 2 mils would be .07 namp at the 90 percent yield point. These values are well within the capability of device processing with currents of .003 namps typical for the depletion region volume considered.

The second current contribution is due to the thermally generated currents which diffuse to the depletion region and are swept out by the field of depletion region. This current is generally small in comparison to the depletion region current.

The third current contribution comes from surface contributions to device leakage. Below is a list of some of the factors influencing surface current:

1 Conduction from surface films on device insulator

2 Conduction through inversion channels

3 Generation from surface states in device depletion areas on surface

4 Ionic conduction in insulator layers.

The surface currents are generally negligible when a guard ring structure is used.

The capacitance of the device can be adequately modeled as an abrupt junction and this is given by

$$C = \left(\frac{K_s \varepsilon_o}{2(V_r + \phi_b)\rho\mu}\right)^{1/2} A$$

where

$K_s$ = dielectric constant

$\varepsilon_o$ = permitivity of free space

$V_r$ = reverse bias

$\phi_b$ = built in field of diode

$\rho$ = resistivity of material

$\mu$ = mobility of majority carrier

$A$ = area of device

Conservatively estimating the electrically active area as 2 mil x 6 mil, the device capacitance per element would be typically $4.2 \times 10^{-15}$ farads. Clearly lead and stray capacitances would predominate.

The value for the shunt resistance for the device for small signals can be obtained from the equation for the leakage current. Thus,

$$\frac{1}{R_{shunt}} = \frac{dI}{dv} = \frac{1}{2} q \frac{\nu}{\tau} A \frac{dW}{dv}$$

where

$$w = [2 \varepsilon\varepsilon_o (v_r + \phi_b)\rho\mu]^{1/2}.$$

Thus, it can be shown that

$$R_{shunt} \approx \frac{2v}{I} \approx 1.4 \times 10^{12} \text{ ohms}.$$

The following problem areas should also be considered when investigating a monolithic linear array for 1.06 micron radiation when using silicon:

1 Channel resistance between elements

2 Optical crosstalk between elements related to angle of incidence of incident radiation and detector structure.

In summary, an electrical area of 2 mil x 6 mil has been designed for an optical 1 mil square PIN. Device capacitance is negligible and dominated by stray capacitance (which should itself be unimportant in an array for the application described in Section IV and 3.3.1 of this report). Typical leakage current is .003 nanoamp with perhaps .01 nanoamp being a conservative value. Shunt resistance of a single cell is too large to be a significant factor.

### 3.3.4 Background Radiation

At the visible and near-infrared wavelengths, the primary source of background radiation is solar illumination during daylight hours or lunar and starlight illumination during the nighttime hours. Of these, solar illumination is obviously the most severe source of background radiation as in emphasized by the spectral distributions shown in Figure 33. At a wavelength of 1.06 μm, this figure indicates that the spectral irradiance of solar illumination is about $4 \times 10^{-2}$ watts/cm$^2$-μm whereas that of lunar illumination is more than six orders of magnitude lower.

As a worst case situation, we will consider the background radiation due to the direct solar illumination of clouds with mean diffuse reflectivity (at 1.06 μm) of 0.8. The spectral radiance of such clouds would then be

$$\begin{aligned} N_{B\lambda} &= \frac{\rho}{\pi} H_{S\lambda} \\ &= 10^{-2} \text{ watts/cm}^2\text{-ster-}\mu\text{m} \end{aligned}$$

The spectral radiant background power received by each detector in the focal plane of the receiver may then be determined from

$$P_{B\lambda} = \tau_a \, \tau_r \left(\frac{\pi D^2}{4}\right) \theta_d{}^2 \, N_{B\lambda}$$

where $\tau_a$ and $\tau_r$ are the effective transmittance of the atmosphere and the receiver optics respectively, D is the diameter of the receiver's entrance aperture, and $\theta_d$ is the angular subtense in object space of a single detector element (assumed to be square in geometry). If we assume $\tau_a = 1.0$ for conservatism, $\tau_r = 0.5$, D = 9 inches, and $\theta_d = 40$ μrad (acquisition mode), then the worst case spectral radiant background power at each detector element would be

$$P_{B\lambda} = 3.28 \times 10^{-9} \text{ watts/ } \mu\text{m}$$

A spectral passband filter may be used to limit the radiant background power which actually reaches each detector. A filter with a 100Å passband centered at 1.06 μm would be a likely candidate. The worst case radiant background power at the detector would then be

$$P_B = 3.28 \times 10^{-11} \text{ watts}$$

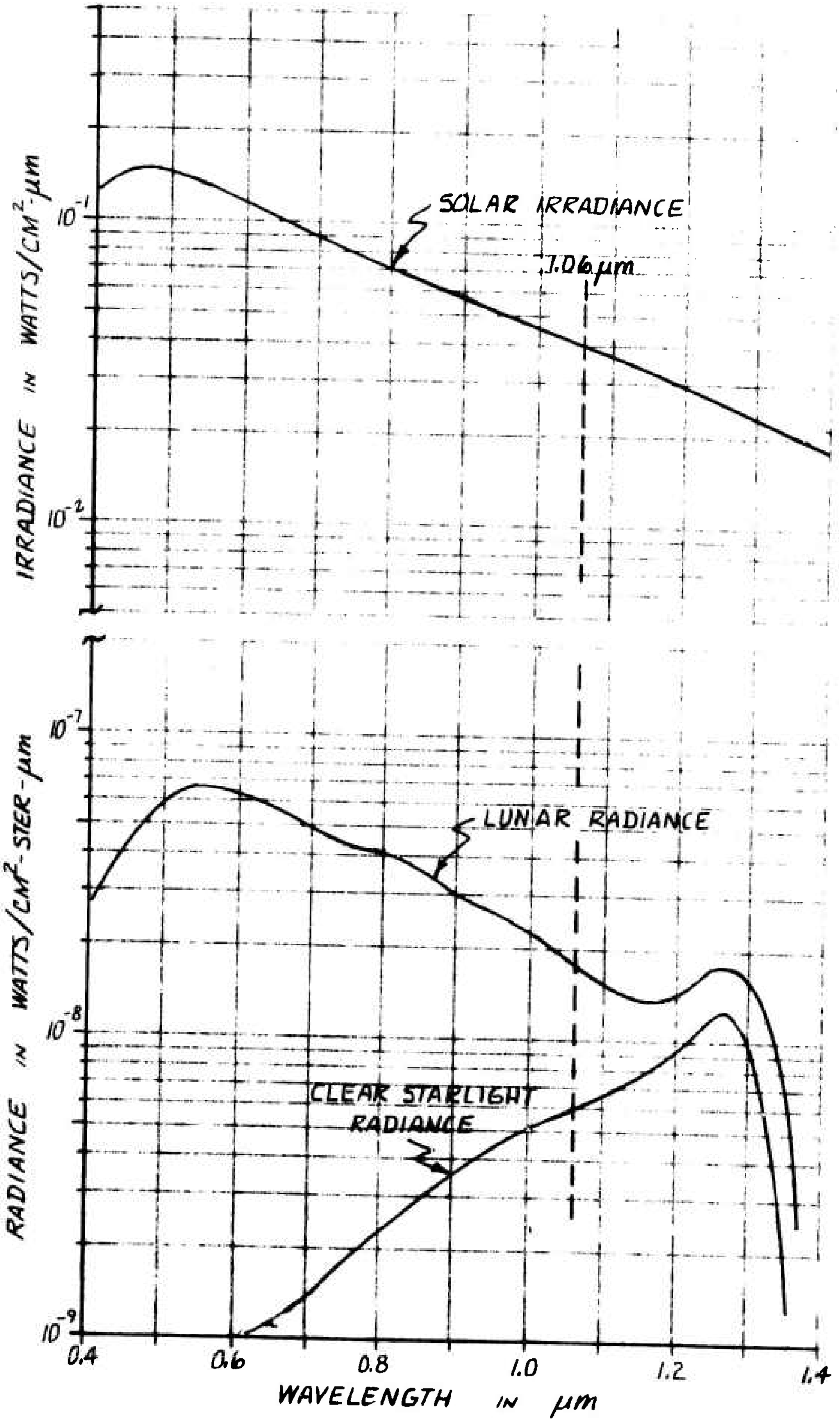

Figure 33. Background Radiation Levels

Since the energy per photon at 1.06 μm is $1.875 \times 10^{-19}$ joules, this background power corresponds to a photon rate of $1.75 \times 10^{8}$ photons/second. Although this photon rate is large, the number of background photons which contribute to background noise can be quite low if the receiver is range-gated. For example, during a one microsecond gate period each detector element will experience only 175 photons under worst case conditions. This level is sufficiently low such that background radiation will not constitute a significant noise source for a range-gated SLIR system.

### 3.3.5 Backscatter Radiation

Consider a pulsed laser illuminator consisting of a laser capable of average output beam power $P_L$ and a beam expander optical system characterized by an optical transmittance (to the laser beam) of $\tau_I$. Then peak illuminator beam power, $P_B$, occuring during a single pulse of duration $t_p$ is

$$P_B = \frac{P_L \ \tau_I}{t_p \ (PRF)}$$

where PRF is the laser pulse repetition frequency. If we now assume a rectangular cross-section illumination beam of total divergence $\phi_B$ in one direction and $\beta\phi_B$ in the other, where $\beta \geq 1$, then the peak illuminator beam intensity is

$$\begin{aligned} J_B &= \frac{P_B}{\beta \ \phi_B^2} \\ &= \frac{P_L \ \tau_I}{\beta \ \phi_B^2 \ t_p \ (PRF)} \end{aligned}$$

The peak irradiance at a distance r produced by this illumination beam is then

$$\begin{aligned} H_r &= \frac{J_B \ \tau_{A(r)}}{r^2} \\ &= \frac{P_L \ \tau_I}{\beta \ \phi_B^2 \ t_p \ (PRF) \ r^2} \quad \exp(-\sigma r) \end{aligned}$$

where $\tau_A(r)$ is the atmospheric transmittance over the distance r and $\sigma$ is the atmospheric attenuation (extinction) coefficient.

By analogy, the peak irradiance at a distance (r+dr) produced by this same illumination beam is

$$H(r+dr) = \frac{J_B \; \tau_A \; (r+dr)}{(r+dr)^2}$$

$$= \frac{P_L \; \tau_I}{\beta \; \phi_B^2 \; t_p \; (PRF)(r+dr)^2} \; \exp\left[-\sigma(r+dr)\right]$$

The differential change in peak irradiance occurring while the pulse propagates from r to (r+dr) is then

$$dH = H_r - H_{(r+dr)}$$

$$= J_B \left\{ \frac{\exp\left[-\sigma r\right]}{r^2} - \frac{\exp\left[-\sigma(r+dr)\right]}{(r+rd)^2} \right\}$$

$$= \frac{J_B}{r^2} \exp\left[-\sigma r\right] \left\{1-\exp\left[-\sigma dr\right]\right\}$$

where a convenient approximation has been made by assuming that dr<<r for all r of interest.

Now the attenuation coefficient, $\sigma$, is representative of both absorption and scattering processes in the atmosphere. We can separate these two attenuation processes by writing

$$\sigma = \sigma_A + \sigma_S$$

where $\sigma_A$ is the atmospheric absorption coefficient and $\sigma_S$ is the atmospheric scattering coefficient. The differential change in peak irradiance occurring while the pulse propagates from r to (r+dr) can then be written as

$$dH = \frac{J_B}{r^2} \exp\left[-(\sigma_A + \sigma_S) r\right] \left\{ 1-\exp\left[-(\sigma_A + \sigma_S) \; dr\right] \right\}$$

The differential change in peak irradiance due solely to scattering during propagation of the pulse from r to (r+dr) may then be written as

$$dH_S = \frac{J_B}{r^2} \exp\left[-(\sigma_A+\sigma_S) r\right] \left\{1-\exp\left[-(\sigma_A+\sigma_S) dr\right] -1 + \exp\left[-\sigma_A \; dr\right]\right\}$$

$$= \frac{J_B}{r^2} \exp\left[-(\sigma_A+\sigma_S) r\right] \exp\left[-\sigma_A \; dr\right] \left\{1-\exp\left[-\sigma_S dr\right]\right\}$$

If we now assume that dr is very small such that $\exp\left[-\sigma_A dr\right] \simeq 1$ and $\left\{ 1 - \exp\left[-\sigma_S dr\right] \right\} \simeq \sigma_S dr$, then the differential change in peak irradiance due to scattering may be approximated as

$$dH_S \approx \frac{J_B \sigma_S}{r^2} \exp\left[-(\sigma_A + \sigma_S) r\right] dr$$

While Rayleigh (i.e., molecular) scattering can be treated as isotropic, Mie scattering from aerosols in the atmosphere is highly angle dependent. Therefore, the scattering coefficient, $\sigma_S$, is not isotropic and must be considered as a function of the scattering angle, $\theta$. It is customary to define an angular scattering coefficient per unit solid angle, $\beta_S(\theta)$, which when integrated over $4\pi$ steradians equals the total scattering coefficient; i.e.,

$$\sigma_S = \int_{4\pi} \beta_S(\theta)\, d\Omega$$

Only the scattering represented by $\beta_S(\pi)$ contributes to the backscattered radiation seen by the receiver. Consequently the differential change in peak backscatter radiance during propagation of the illuminator pulse from r to (r+dr) is given by

$$\begin{aligned} dN_{bs} &= dH_S \left(\frac{\beta_S(\pi)}{\sigma_S}\right) \\ &= \frac{J_B}{r^2} \beta_S(\pi) \exp\left[-(\sigma_A + \sigma_S) r\right] dr \end{aligned}$$

Now the receiver focal plane irradiance produced by a surface of radiance N at a distance r is given by the familiar equation

$$H = \frac{\pi N}{4T^2\ (1+m)^2} \exp\left[-(\sigma_A + \sigma_S) r\right]$$

Where T is the T-number of the optical system and m is the magnification of the image (note that for most cases of interest; i.e., at long range, $m \ll 1$).

The radiant power on a detector of area $A_d$ produced by this radiance is then

$$\begin{aligned} P_D &= HA_d \\ &= H\ \{\ F^2 (1+m)^2\ \gamma \theta_D^{\ 2}\ \} \\ &= \frac{\pi \tau_R\ \gamma\ \theta_D^{\ 2}\ D^2 N}{4} \exp\left[-(\sigma_A + \sigma_S) r\right] \end{aligned}$$

where F is the effective focal length of the optical system, D is the diameter of the entrance aperture, $\tau_R$ is the receiver's optical transmittance at the wavelength of interest, and $\theta_D$ is the detector angular subtense in object space (i.e., the detector IFOV) with $\gamma \geq 1$ the detector aspect ratio.

The differential peak radiant power at the detector produced by the differential peak backscatter radiance is then

$$dP_{bs} = \frac{\pi\tau_R\ \gamma\theta_D^2 D^2}{4}\ dN_{bs}\ \exp\left[\ -(\sigma_A+\sigma_S)\,r\ \right]$$

$$= \frac{\pi J_B\ \tau_B\ \gamma\theta_D^2 D^2}{4\ r^2}\ \beta_S(\pi)\ \exp\left[\ -2\ (\sigma_A+\sigma_S)\,r\right]\ dr$$

With a range-gated receiver, this differential radiant power must be integrated over the gate period, $t_g$. Figure 34 illustrates the timing relationships between the illuminator pulses, the desired target return, the receiver gate, and the zeroth and nth pulse backscatter returns. Note that if there are one or more in-flight illumination pulses during the receiver gate period, the received backscatter radiant power is the sum of the backscatter contributions of each. Therefore, the peak radiant backscatter power received by the detector is

$$P_{bs} = K \sum_{n\ =\ 0}^{N} \left\{ \int_{R_{1n}}^{R_{2n}} \left(\frac{r-R_{1n}}{R_{2n}-R_{1n}}\right) \frac{\exp\left[-2\sigma r\right]}{r^2}\ dr + \int_{R_{2n}}^{R_{3n}} \frac{\exp\left[-2\sigma r\right]}{r^2}\ dr \right.$$

$$\left. + \int_{R_{3n}}^{R_{4n}} \left(\frac{R_{4n}-r}{R_{4n}-R_{3n}}\right) \frac{\exp\left[\ -2\sigma r\right]}{r^2}\ dr \right\}$$

where we have lumped all of the range-independent parameters into a constant defined by

$$K = \frac{\pi J_B\ \tau_R\ \gamma\theta_D^2\ D^2}{4}\ \ \beta_s(\pi)$$

The indicated integrals unfortunately cannot be evaluated in closed form, but they can be easily evaluated by computer. They can also be evaluated by table look-up if they are rewritten in a more familiar form. Since the mth order exponential integral is defined as(13)

$$E_m(Z) = \int_1^{\infty} \frac{\exp\ (-Zt)}{t^m}\ dt$$

use of the substitutions $t = r\ R$ and $Z = 2\sigma R$ allows us to write

$$\int_R^{\infty} \frac{\exp\ (-2\ \sigma r)}{r}\ dr = E_1(2\sigma R)$$ and

---

(13) See M. Abramowitz and I. A. Stegun (ed.), "Handbook of Mathematical Functions", National Bureau of Standards Applied Mathematics Series 55, March 1965, p. 228.

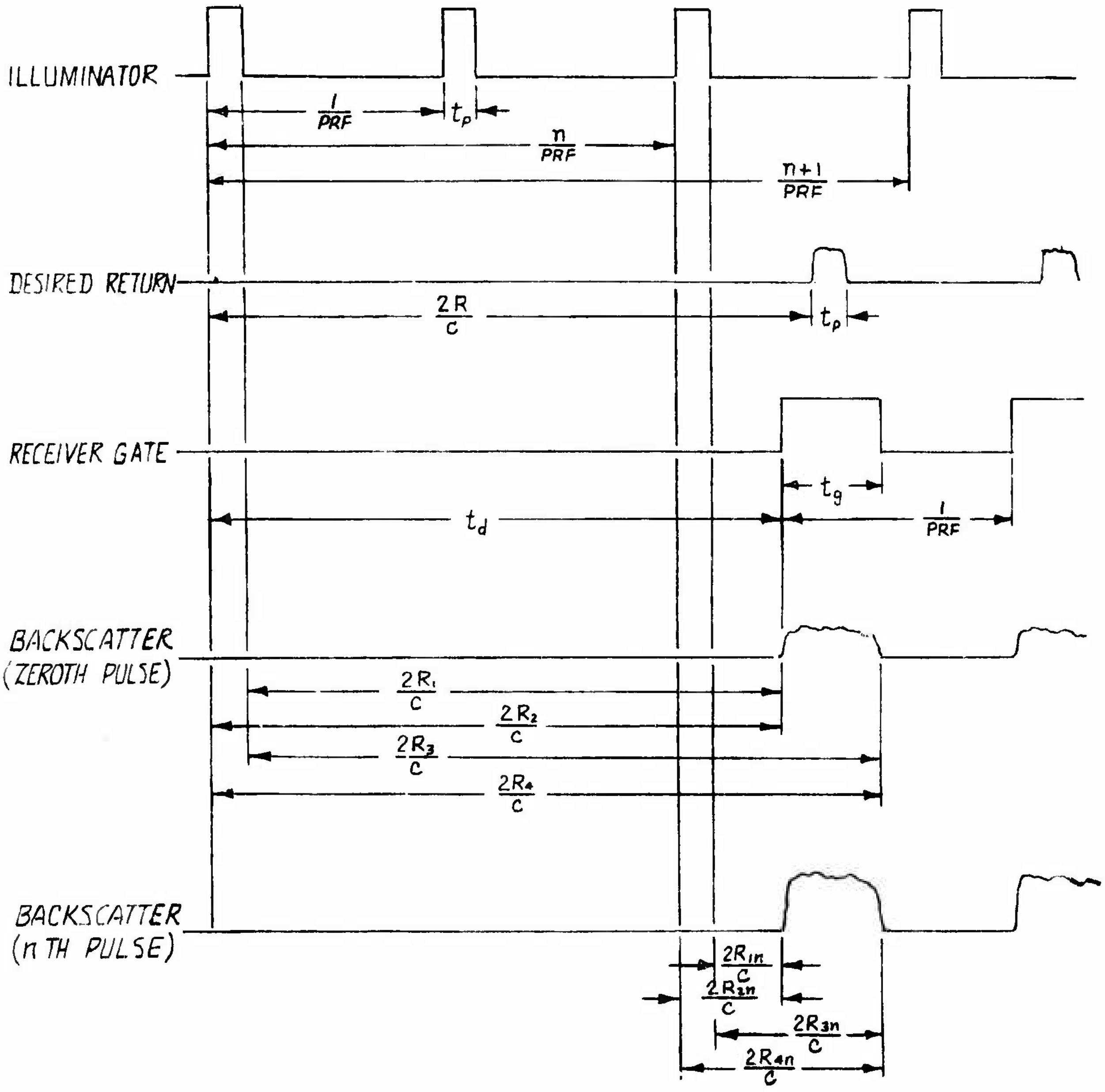

$$R_{1n} = \frac{c}{2}\left(t_d - t_p - \frac{n}{PRF}\right) \qquad R_{3n} = R_{1n} + \frac{c t_g}{2}$$

$$R_{2n} = R_{1n} + \frac{c t_p}{2} \qquad R_{4n} = R_{1n} + \frac{c t_g}{2} + \frac{c t_p}{2}$$

Figure 34. Range-Gate Timing Relationships

$$R\int_{R}^{\infty}\frac{\exp\,(-2\sigma r)}{r^2}\,dr = E_2(2\sigma R)$$

Noting that $(R_{2n} - R_{1n}) = (R_{4n} - R_{3n}) = ct_p/2$ and that for any $f(x)$

$$\int_{X_1}^{X_2} f(x)\,dx = \int_{X_1}^{\infty} f(x)\,dx - \int_{X_2}^{\infty} f(x)\,dx$$

We may then rewrite the equation for the peak backscatter power as

$$P_{bs} = K\,\frac{2}{ct_p}\sum_{n=0}^{N}\Bigg\{E_1(2\sigma R_{1n}) - E_1(2\sigma R_{2n}) - E_2(2\sigma R_{1n}) + \frac{2R_{1n}+ct_p}{2R_{2n}}\,E_2\,(2\sigma R_{2n})$$

$$+\ \frac{2R_{4n}-ct_p}{2R_{3n}}\ E_2(2\sigma R_{3n}) - E_2(2\sigma R_{4n}) - E_1(2\sigma R_{3n}) + E_1(2\sigma R_{4n})\Bigg\}$$

Due to the interrelationship between $R_{1n}$, $R_{2n}$, $R_{3n}$, and $R_{4n}$, this equation can be rewritten solely in terms of $R_n = R_{1n}$, the minimum distance between the $n^{th}$ in-flight pulse and the receiver.

$$P_{bs} = \frac{2K}{ct_p}\sum_{n=0}^{N}\Bigg\{E_1(2\sigma R_n) - E_1(2\sigma R_n + \sigma ct_p) - E_2(2\sigma R_n) + E_2(2\sigma R_n + \sigma ct_p)$$

$$+\ E_2(2\sigma R_n + \sigma ct_g) - E_2(2\sigma R_n + \sigma ct_p + \sigma ct_g) - E_1(2\sigma R_n + \sigma ct_g)$$

$$+\ E_1(2\sigma R_n + \sigma ct_p + \sigma ct_g)\Bigg\}$$

This equation can be evaluated by table look-up of the functions $E_1(z)$ and $E_2(z)$. It has been plotted in Figure 35 as a function of the minimum range gate distance, R, for the situation with no in-flight pulses (i.e., for N=0). Typical systems parameters have been assumed as listed in the figure. A backscatter coefficient, $\beta_s(\pi)$, of $1.5\text{x}10^{-3}$/km-ster, which corresponds to a total scattering coefficient of 0.05 $\text{km}^{-1}$, was also assumed for this figure. The number of backscatter photons received by each detector during the one microsecond gate period is also given in the figure.

For backscatter to be a negligible contributor to receiver noise, the number of received backscatter photons must be no greater than a few hundred per gate period. Figure 35 indicates that with a 100 watt illuminator

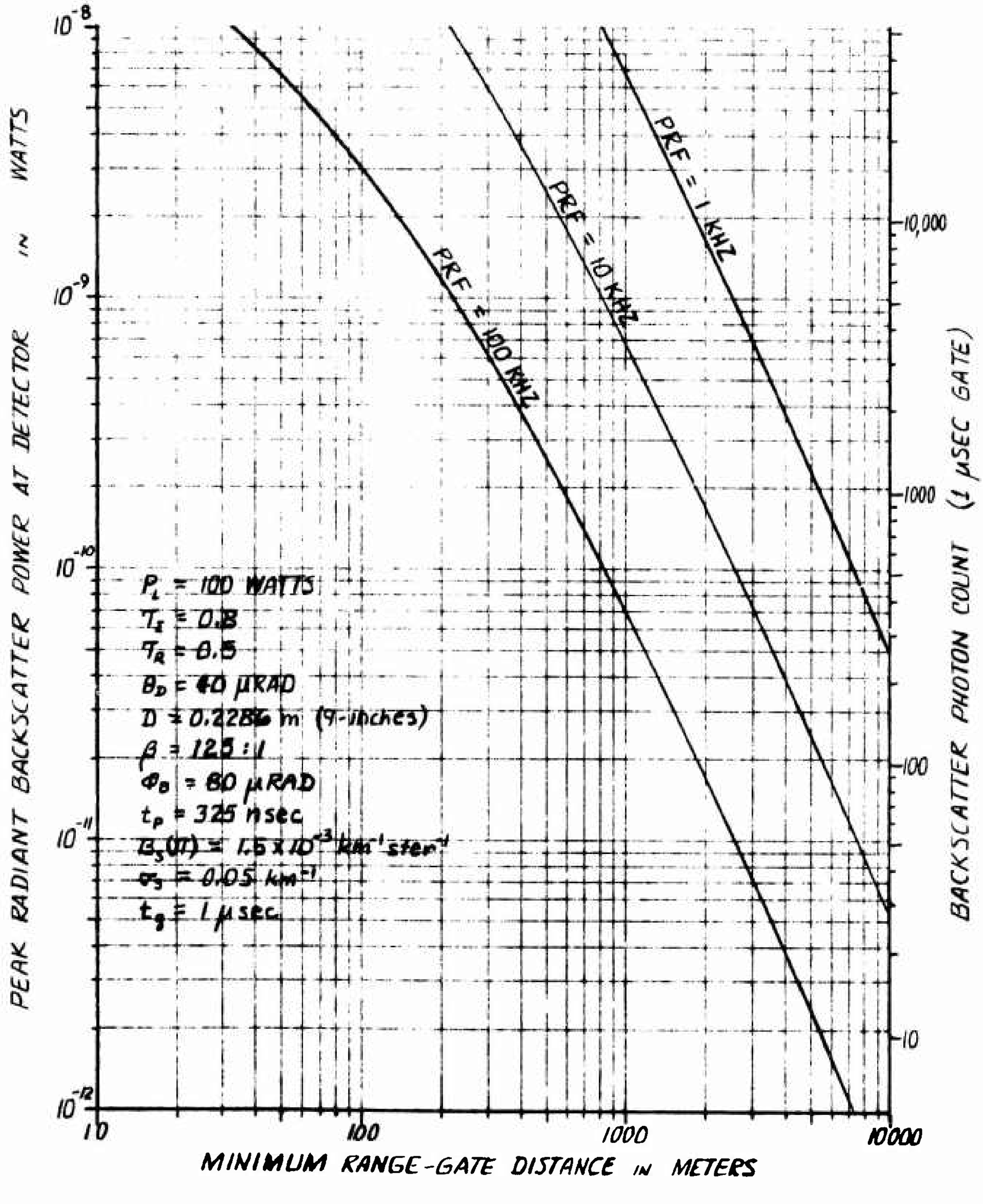

Figure 35. Backscatter Radiation Levels

operating at a PRF of 10 kilohertz, the photon count due to backscatter from a range-gated volume at a range of 10 kilometers will be on the order of 30 photons. At shorter ranges the photon count will increase unless the illuminator PRF is increased also since increasing the PRF reduces the illuminator peak power. Gradually increasing the illuminator PRF (and therefore the SLIR system frame rate as well) with decreasing range will then serve to maintain the backscattered radiation at an insignificant level since what increase that does occur will be offset by the increased signal return from the target itself.

### 3.3.6 Receiver Noise Equivalent Energy (NEE)

For an integrating sensor, signal-to-noise performance is conveniently evaluated by consideration of receiver noise equivalent energy (NEE). Receiver NEE in terms of photons per signal pulse was developed in equation (16) of sub-section 3.3.1. This equation, along with a list of parameters, is repeated below:

$$NEE_{rp} = \frac{1}{\tau_o \varepsilon q G} \sqrt{\left\{ q \left[3I_{SL} + \left(\left[P_{db}+P_{ds}\left(\frac{T_w}{T_g}\right]\rho+I_{BL}\right)(G^{\alpha}+2G)\right] + \frac{2kT}{R_s} \right\} T_g+\sigma_c^2} \tag{18}$$

| Symbol | Definition | Typical Value | Units |
|---|---|---|---|
| $\tau_o$ | effective optical transmission | .63 | none |
| $\varepsilon$ | sensor quantum efficiency | $< 1$ | none |
| $I_{SL}$ | sensor surface leakage | $1 \times 10^{-9}$ | amps |
| $I_{BL}$ | sensor bulk leakage | $.05 \times 10^{-9}$ | amps |
| $\rho$ | sensor responsivity | .85 | amps/W |
| $G$ | sensor gain | $\geq 1$ | none |
| $\alpha$ | sensor gain penalty exponent | 2.3 | none |
| $T_W$ | signal pulse width | $200 \times 10^{-9}$ | sec |
| $T_g$ | receiver gate time | $.5 < T_g < 1$ | μsec |
| $R_s$ | sensor shunt resistance | $\geq 10^8$ | ohm |
| $\sigma_c^2$ | charge variance for CCD processing and amplification | $\leq 10^4 q^2$ | coulomb$^2$ |
| $P_{db}$ | total background power incident on detector | $3 \times 10^{-9} (\Delta\lambda)$ | w |
| $P_{ds}$ | total average signal power incident on detector during signal pulse | -- | W |

Although this equation was developed for an APD, it remains valid for other types of photodiodes if a gain G=1 is assigned. As mentioned previously, the equation requires an iterative solution in its present form because signal strength influences both sides of the equation. If sensor pulse responsivity is significantly lower than d.c. responsivity, NEE must be increased accordingly.

Some discussion of the typical values shown in the list is in order. The background power of $3 \times 10^{-9}$W/micron is a worst-case value derived from the work of section 3.3.4. $P_{db}$ can be made very small by use of a 100 or 200Å filter. A noise charge variance $\sigma_c^2$ incurred after initial CCD storage equivalent to 100 rms electrons or less is considered feasible, and 30 rms electrons are possible with CCD correlated double sampling. Sensor-related values in the list are for the high quantum efficiency 1.06 μm GaAsSb APD developed by Richard Eden of Rockwell International Science Center. These values were developed in sub-section 3.3.3. The leakage currents shown are for low gain and will increase at higher gains and bias voltages. A conservative value for inherent optical bandpass of this APD (.1 micron) will be used, giving a worst-case result of $3\times10^{-10}$ W of background power. Since the .96 quantum efficiency of this APD is near unity, $\varepsilon=1$ will be used, which gives P=.85A/W at 1.06 μm. The gate time $T_g$ is dependent on the accuracy of radar ranging data and limits of .5 μsec and 1 μsec have been assumed reasonable. $R_s$ = 100 MΩ will be used as a conservative value. These values give the results shown in Table 11.

TABLE 11

Receiver NEE Values for GaAsSb APD with Unity Gain

| $T_g$(sec) | $\sigma_c$ | $NEE_r$(photons) for gain = 1 |
|---|---|---|
| $.5\times10^{-6}$ | 30q | 190 |
| $.5\times10^{-6}$ | 100q | 250 |
| $1.0\times10^{-6}$ | 30q | 270 |
| 1.0x10-6 | 100q | 310 |

This APD can give significantly lower NEE values when operated with gain. Figure 36 shows receiver NEE as a function of gain, for the numerical parameters used in deriving Table 11. Because background noise is amplified by the APD, it is advantageous to insert a 200Å filter of .8 transmission, and the NEE plot takes this into account. The APD leakage currents were also increased as a function of gain, according to plots in reference 12. The figure shows that an NEE ≤ 100 photons can be maintained through a gain range from approximately 2 to 15. However, it may be difficult to dependably operate a large array uniformly within such gain limits. The APDs themselves will exhibit different gains at a specific voltage, which causes gain variation even when all sensors experience the same bias potential. Even if all APD gains can be made nearly uniform for a specific potential, the direct injection interface technique hinders attainment of uniform bias potential. This is because the high impedance CCD input circuits will capacitively divide bias voltage with the series APD, and uniform APD bias can be obtained

---

(12) R. C. Eden, "1.06 Micron Avalanche Photodiode", Tech. Rep. AFAL-TR-72-343, January 1973.

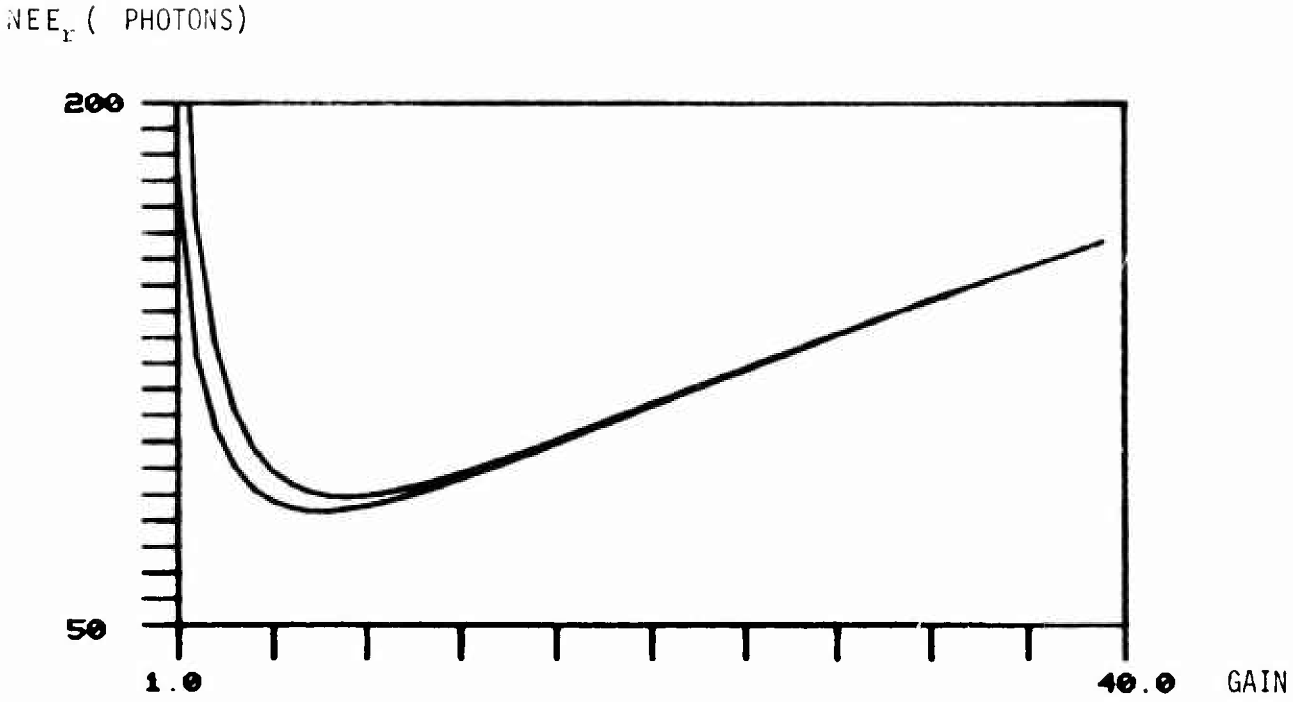

CURVES FOR 30 & 100 CCD RMS ELECTRONS

RECEIVER GATE TIME = 5.00E-07 SEC

Figure 36. Receiver NEE as a Function of GaAsSb APD Gain

only if the input MOSFETs have uniform characteristics. It would be possible to effect a closed-loop gain control by providing independently controlled bias voltages to all APDs and automatically adjusting bias by observing output from a calibration signal pulse, but this adds significant complexity and it may not be practical to access all of several hundred APD bias leads. This leaves two possible conditions under which a high performance APD could be used with gain: 1) the APD array and CCD input circuits can be manufactured with sufficiently uniform characteristics; 2) a large shunt resistor is placed from each APD-CCD interface point to ground. Condition 1 requires further investigation and perhaps development work to be evaluated. Condition 2 is straightforward but has the disadvantage of more complexity in the hybrid array. Given low leakage current in the nano-amp region, a very large shunt resistor can maintain almost the entire bias supply across the APD while contributing insignificant noise current. Since a receiver NEE of 100 photons is achievable through a gain range from about 2 or 3 to 15, relatively independent of CCD noise, 100 photons is a reasonable estimate of receiver NEE for the GaAsSb APD with gain. For large deviations from nominal gain, uniform imagery could still be attained by gain normalization.

Small, high-quality PIN silicon diodes can give receiver NEE performance that rivals that of the high quantum efficiency GaAsSb APD with unity gain. This is primarily due to their very low leakage current, although PINs can be made to exhibit d.c. quantum efficiencies on the order of 50 percent to 60 percent, and pulse quantum efficiencies from 25 percent to 30 percent for 200 nano-second pulses (at 1.06 micron). Denoting $\varepsilon_s$ as the effective quantum efficiency for a 200 nsec pulse, $I_L$ as total leakage current, and $\rho_{dc}$ as d.c. responsivity (A/W); equation (18) can be rewritten for the PIN as:

$$\mathrm{NEE}_{rp} = \frac{1}{\tau_o \varepsilon_s q} \sqrt{\left\{ 3q \left[ I_L + \left(P_{db} + P_{ds} \left[\frac{T_w}{T_g}\right]\right) \rho_{dc} \right] + \frac{2kT}{R_s} \right\} T_g + \sigma_c^2} \quad (19)$$

All other parameters are as listed under equation (18), except that an optical bandpass filter nominally 200Å wide with an .8 transmission must be incorporated, giving a $\tau_o$ of .5. This gives a worst-case background power $P_{db} = 1.3 \times 10^{-11}$W incident on the detector. According to the values derived for small PIN diodes in sub-section 3.3.3, 0.003 nano-amp leakage current is typical. A leakage of $I_L$=.01 nano-amp will be used here as a pessimistic value. Noise current from the large shunt resistance $R_s$ is negligible compared to leakage and background current shot noise and shot noise on the signal. For a 200 nsec pulse responsivity of .25 A/W, $\epsilon_s$=.3; d.c. responsivity is .4 A/W. For the gate width $T_g$ and CCD rms noise $\sigma_c$ indicated, Table 12 shows the receiver NEE performance obtainable with PIN diodes. Note that performance is thoroughly dominated by CCD noise. The table shows that a receiver NEE of 300 photons or better might reasonably be expected with silicon PIN diodes.

TABLE 12

Receiver NEE Values for PIN Diode, at Room Temperature

| $T_g$ (sec) | $\sigma_c$ | $NEE_r$ (photons) |
|---|---|---|
| $.5 \times 10^{-6}$ | 30q | 240 |
| $.5 \times 10^{-6}$ | 100q | 680 |
| $1.0 \times 10^{-6}$ | 30q | 250 |
| $1.0 \times 10^{-6}$ | 100q | 690 |

In summary, the following approximate receiver NEE values can be expected with the devices discussed:

| | |
|---|---|
| GaAsSb APD with gain > 1 . . . . . . . | 100 photons |
| GaAsSb APD with unity gain . . . . . . . | 200 photons |
| Silicon PIN diode . . . . . . . . . . . | 300 photons. |

## 3.4 SLIR System Design Concepts

The basic operational requirements dictated by the HEL application and described in Section 2.0 are the forces which drive the design of the SLIR system. The scanner, illuminator, and receiver technologies just discussed in the previous subsections, however, are the considerations which guide the design. This combination of requirements and constraints quickly limits the SLIR design to only a few viable concepts each presenting their own unique assets and liabilities. Selection of the optimum concept is often difficult since such selection must be based on qualitative as well as quantitative grounds. It is often impossible to reduce each concept to the same common denominator which permits quantitative one-to-one evaluation criteria.

### 3.4.1 Basic Design Considerations

Three basic SLIR system concepts have evolved during this study, each concept configured around one of the three scanning techniques identified in the previous section. Each of these system concepts has the potential for meeting the primary SLIR functions of long range airborne target acquisition and precision short range target tracking and imaging. These concepts evolved from consideration of a set of basic design principles which reflect the fundamental system performance capabilities necessary to perform these primary functions. A number of these design considerations are as follows:

1 For an air-to-air encounter, the required acquisition field of view (FOV) must be large enough to encompass with high probability any handoff error from the primary acquisition device (e.g., radar). Because this handoff error is likely to be symmetrical in azimuth and elevation, the required acquisition FOV may likewise be symmetrical in azimuth and elevation even to the point of being circular as opposed to square or rectangular. The track and precision track FOV's may likewise be symmetrical.

2 During long range target acquisition, illuminator beam energy requirements are at their greatest, but data rate (frame rate) requirements are at their least. Since average illuminator beam power is equal to the product of the illuminator beam energy per pulse and the illuminator

PRF, a reduction in PRF results in a reduction in laser output power requirements. This is permissible at long range since low data rate requirements permit lower illuminator PRF.

3 High data rates are required only during target tracking and then only at short ranges where target dynamics may result in large line-of-sight rates and accelerations.

4 Similarly high resolution is required only during target tracking or imaging and then only in the central portion of the scanned FOV within which the target will be held by the tracking loop.

5 An illuminator/receiver design employing a fan-shaped illumination beam of sufficiently narrow width and oriented parallel with, but displaced from, the receiver instantaneous FOV (IFOV) will require dynamic boresight compensation to account for parallax but may not require range-gating to eliminate backscatter radiation at the detector. Conversely, a design employing an illumination beam which is coaxial with the receiver IFOV will not require dynamic boresight compensation but will require range-gating.

6 High precision synchronization of the scanning illuminator beam and the receiver IFOV is best achieved by using a common surface of a single scan mechanism; opposite surfaces of a single scan mechanism is a next best alternative. An inferior but perhaps acceptable third choice is the use of two separate but identical scan mechanisms which are mechanically (or electronically) coupled.

7 Minimization of the effect of scan mechanism jitter in the far field requires substantial optical magnification of far field angular space prior to introduction of the scan mechanism in the optical train.

8 To insure precise tracking of illuminator beam and receiver IFOV in the far field, the optical magnification (in the direction of scan) between object space and the scan mechanism must be identical for both the illuminator and the receiver.

9 The illuminator optical train must use beam expanders of a Galilean form so as to avoid focusing of the high power laser beam.

10 If a power change is employed in either the receiver or the illuminator optical train, the high power train should be designed with all fixed components so as to minimize jitter and misregistration possibilities; change to lower power operation should be accomplished by the introduction of additional elements into the high power optical train and then only at points which provide substantial magnification of object space.

11 The need for a power change can be eliminated if acquisition FOV coverage can be provided by a detector/scan mechanism combination which also provides the high resolution, high data rate capability in the central portion of the FOV necessary for precision track and imaging.

### 3.4.2 Candidate System Configurations

Three basic SLIR system concepts were investigated and evaluated during the study. Although there is an infinite number of variations among these concepts, it is felt that these three are representative of the three types of scan mechanisms, high-inertia mirror scanners, low-inertia mirror scanners, and rotating prism scanners, which are appropriate for SLIR system development. Each of these basic system concepts is described in the following paragraphs.

Concept No. 1. The first concept employs a high-inertia rotating multi-faceted mirror drum scanner and is illustrated schematically in Figure 37. By means of a pair of anamorphic Galilean telescopes, the output beam from a high power, high PRF Nd:YAG laser is expanded and shaped into a fan beam of 2.5 milliradian divergence in elevation by 10 microradian divergence in azimuth (250:1 aspect ratio). This fan beam sweeps through a 2.5 mrad square precision track scan field in object space by means of the rotating multi-faceted mirror drum. A power change of 1/2X or 1/4X may be inserted into the optical path, as shown, to spoil the beam, thereby increasing the scan field to 5 mrad square for the track mode or to 10 mrad square for the acquisition mode, respectively. Note that when in the precision track mode, the illuminator optical train contains no moveable elements (except the scan mirror and the boresight compensation mirror) and that considerable optical power is

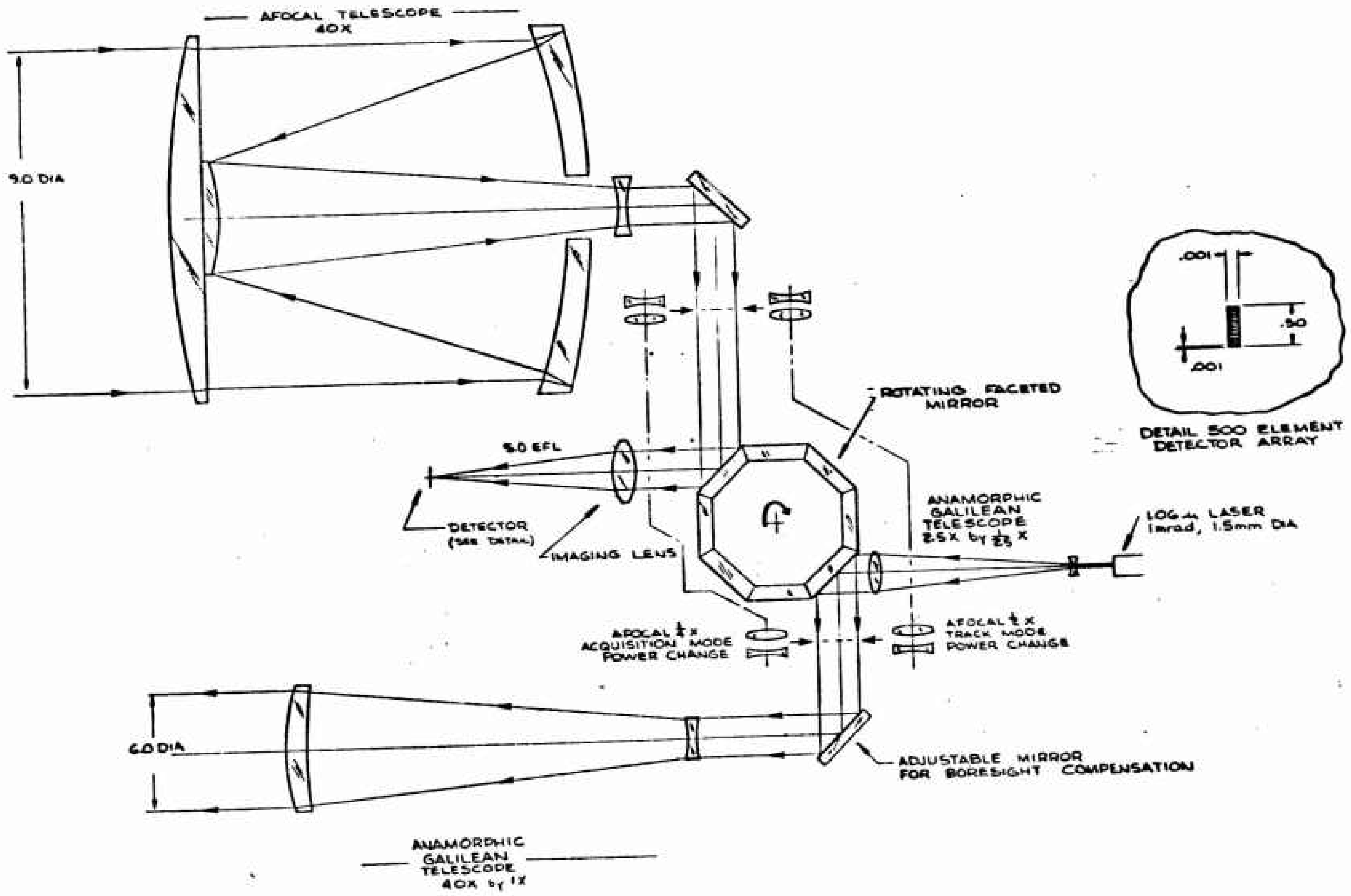

Figure 37. SLIR System Concept No. 1

provided between object space and the scan mirror. The effect of mirror jitter on tracking accuracy with such a configuration should be minimal.

The receiver optical train is similar. An afocal telescope, having identical optical power in the scan direction with its counterpart in the illuminator optical train, relays the minified entrance pupil to an imaging lens which focuses the received energy on the 500 element detector array. The rotating multi-faceted mirror scans the image across the detector array in exact synchronism with the illuminator beam. A power change of 1/2X or 1/4X may be inserted into the optical path to reduce the effective focal length of the receiver optical train so as to change its field of view from 2.5 mrad square (precision track mode) to 5 mrad square (track mode) or 10 mrad square (acquisition mode), respectively, thereby matching the scan fields of the illuminator. The IFOV of each detector in the 500 element linear array is 5 μrad square, 10 μrad square, or 20 μrad square, correspondingly.

The primary disadvantage of this concept is that it is difficult to obtain high scan efficiency with the rotating drum approach. High scan efficiency requires a large number of facets but the minimize size of each facet is determined by the size of the receiver train optical bundle. During the acquisition mode, this optical bundle is on the order of one inch at the scan mirror, with the telescope optical magnification shown (i.e., 40X during precision track but only 10X during acquisition). The scan efficiency of a 4-inch diameter octagonal mirror drum as illustrated would be only 6 percent. A larger diameter mirror drum having more facets would exhibit a somewhat higher scan efficiency( e.g., 25 percent with a 30 facet, 18-inch diameter drum) but this is a very unattractive solution particularly in view of the gyroscopic forces such a massive rotating drum would generate. The best solution is to provide higher telescope magnification to reduce the size of the optical bundle. For example, if 25X magnification were provided for the acquisition mode, an 8-inch diameter drum having 25 facets could be used with a resulting scan efficiency of about 50 percent. The optical magnification required for precision track mode operation would then be 100X, however, which presents serious optical design problems. Since low scan efficiencies translate into low frame rate capabilities, this first concept does not appear as an attractive configuration for the SLIR system.

Concept No. 2. The second concept is a variation on the first, wherein the low scan efficiency multi-faceted mirror drum has been replaced by a two-sided oscillating galvonometer mirror as shown in Figure 38. The scan efficiency of the galvonometer mirror can approach 100 percent but does so at the expense of scan linearity, particularly near the limits of the scan excursion. This second concept also eliminates the requirement for dynamic boresight compensation by providing a fan-shaped illumination beam which is coaxial with the receiver FOV. As a further simplification, the power change in the receiver optical train was eliminated altogether, resulting in a fixed focal length receiver.

The generation of the scanning fan-shaped illumination beam is essentially the same as that for the previous concept except that a 125:1 rather than a 250:1 beam aspect ratio is provided. The scan, however, is bi-directional due to the oscillating mirror. Again, considerable optical magnification is provided between object space and the scan mirror to minimize the effect of scan jitter on tracking accuracy. Also, the precision track mode utilizes no moveable optical elements except the scan mirror, of course.

Due to the absence of a power change, the receiver optical train is somewhat different from that of concept No. 1. A 1000 element linear array of detectors, each having a 4:1 aspect ratio as shown, is now required to completely cover the 10 mrad square acquisition FOV. Since no power change is employed, each detector's IFOV in the elevation direction is constant at 10 μrad. The IFOV of each detector element in the azimuth direction, however, is variable from 40 μrad (acquisition mode), to 20 μrad (track mode), to 10 μrad (precision track mode) by means of a mechanical, variable-width field stop. The effect of this stop is to reduce the 4:1 aspect ratio of each detector element to 2:1 or 1:1 in accordance with the mode of operation desired.

Note that because there is no aperturing in the elevation direction, the overall receiver FOV in this direction is always 10 mrad. Illumination is provided, however, only in the central 2.5 mrad, 5 mrad, or the full 10 mrad field, depending upon the mode of operation, as a result of the power

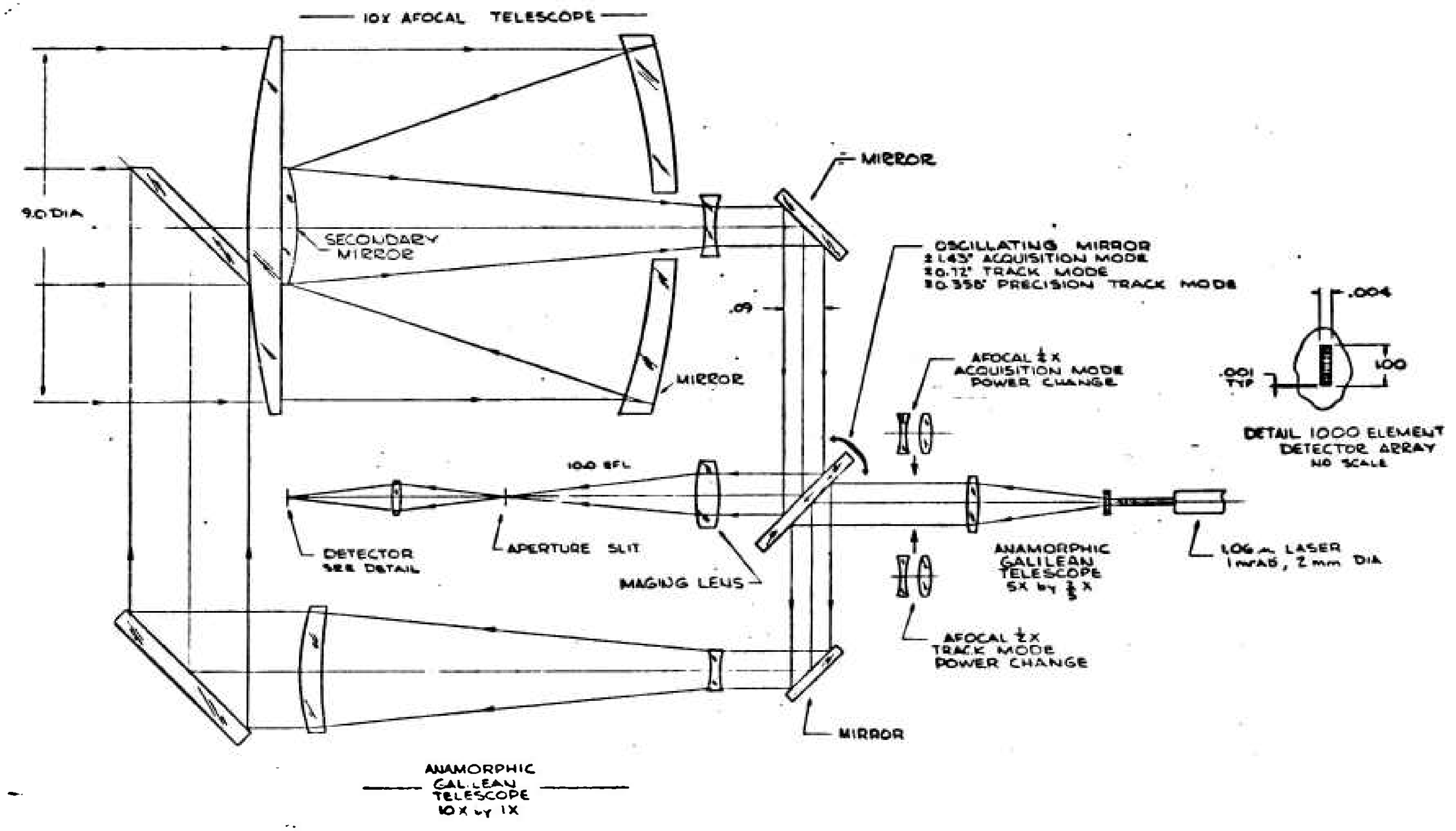

Figure 38. SLIR System Concept No. 2

change in the illuminator optical train. The receiver (and illuminator) FOV in the azimuth direction, conversely, is determined by the magnitude of deflection of the oscillating mirror which may be adjusted to correspond to 2.5 mrad, 5 mrad, or 10 mrad in object space in accordance with the mode of operation.

Although this second concept eliminates some of the difficulties of the previous concept, it introduces others particularly in the area of detector technology since a 1000 element linear array is required. Furthermore, range-gating of this array is mandatory due to the coaxial illuminator/receiver apertures. And, although the power change in the receiver optical train has been eliminated, it still exists in the illuminator train. However, the high scan efficiency of the galvonometer mirror permits frame rates compatible with short range precision tracking and, therefore, this concept represents an improvement in performance capability over the previous concept.

An alternative to this concept which would alleviate some of the difficulties introduced by the 1000 element detector array would be to reinstate the receiver power change which was eliminated in going from Concept No. 1 to Concept No. 2. Although this complicates the optical system somewhat, it also permits the use of a linear detector array having only 250 elements each with a more conventional 1:1 aspect ratio. The variable width aperture stop, together with its attendant re-imaging optics, would also be eliminated by this alternative. Furthermore, the noise performance of the detector array will improve since fewer detector elements, each of smaller physical size, can be employed. Hence, the detection range performance of this alternative to Concept No. 2 should also improve.

Concept No. 3. This concept, which is shown schematically in Figure 39, is radically different from the previous concepts in that it provides a circular rather than a raster scan of object space. The circular scan is attractive in that it is likely to provide a best match to the target position uncertainty resulting from target handoff from the primary acquisition device (e.g., radar) and is also likely to simplify tracker logic since radial error signals are generated directly.

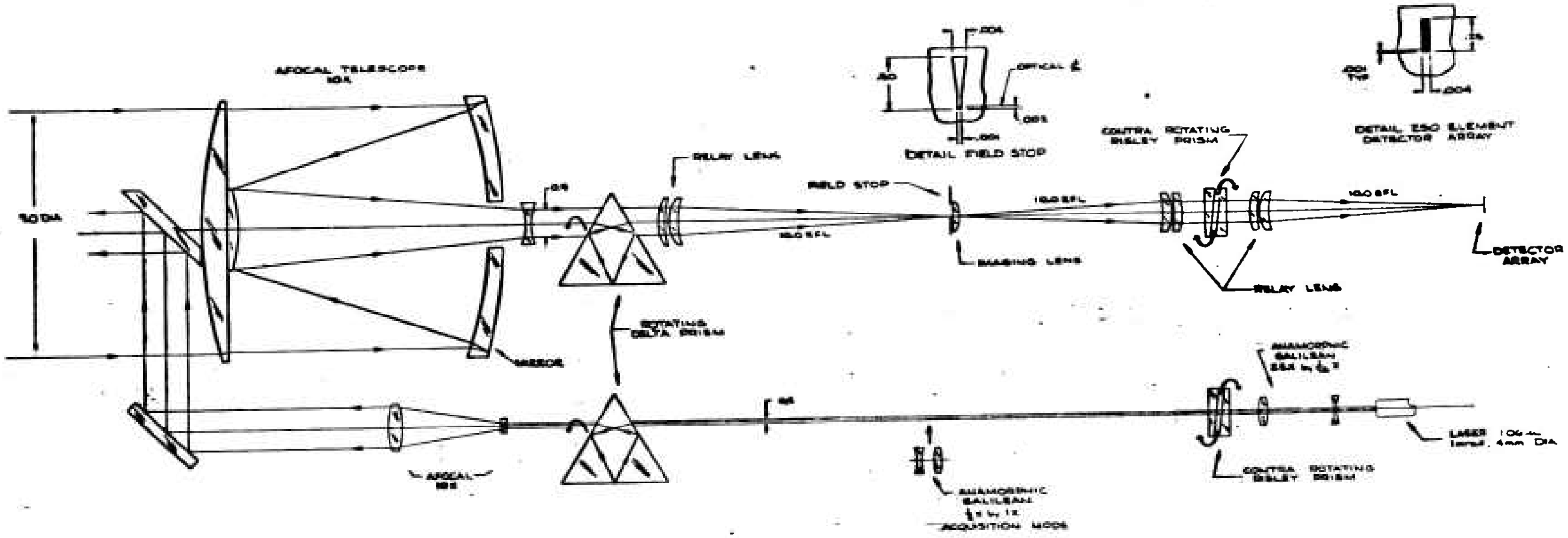

Figure 39. SLIR System Concept No. 3

A fan-shaped illumination beam is generated by the combination of anamorphic and spherical Galilean telescopes as shown. The resulting divergence of the illumination beam in the far field is 40 μrad by 2.5 mrad. A single power change is provided by insertion of an additional anamorphic telescope having 1/2 power in one direction and no power in the other to convert from the precision track mode to an acquisition mode beam divergence of 80 μrad by 2.5 mrad. There is no intermediate track mode with this concept.

Beam scanning is performed by the combination of a two-step contra-rotating risley prism and a continuously rotating delta prism. With the risley prism in one of its two positions, a 2.5 mrad wide annulus of 10 mrad overall diameter is scanned in object space by the delta prism. With the risley prism in the position shown, in which its effect on the optical path is negated, the "hole" of the annulus is scanned by the delta prism. This two-step scan operation is utilized during the acquisition mode when the full 10 mrad search field must be covered. Once target track is established, only the "hole" is scanned by the delta prism. Although a two-step scan procedure is indicated, a gradually collapsing spiral scan is an attractive alternative which warrants further study.

The receiver optical train is similar to that of the illuminator except that no power change is provided. Be means of an identical second set of risley and delta prisms, a 250 detector linear array is caused to scan the same annulus or "hole" in object space. The IFOV of each detector is everwhere 10 μrad in the radial direction, but is variable in the tangential direction increasing from 10 μrad to 40 μrad with increasing radial distance from boresight. This "variable tangential resolution" is provided by a wedge-shaped field stop, as shown, and is compatible with the basic system requirement which specifies that high resolution is needed only for target imaging and tracking which always occurs around boresight.

Aside from the attractiveness of a circular scan for tracking reasons, the primary advantages presented by this concept are unity scan efficiency, the elimination of nearly all power change in the optical path, and the use of a small (250 element) linear detector array. A disadvantage is that obtaining a good match between the illuminator beam far field cross-section and the receiver IFOV is more difficult due to receiver's variable

IFOV in the tangential direction. A poor match results in inefficient use of the illuminator's radiant beam power. An additional disadvantage is that separate, although identical, scan mechanisms are used for the illuminator and the receiver, thereby creating the possibility of scan synchronization loss.

# SECTION IV

# SLIR SYSTEM PERFORMANCE

## 4.1 SLIR System Range Performance

Range is primarily dependent on laser energy per pulse, receiver sensitivity, atmospheric transmission, and the nature of the target. These are two targets of interest: A small unresolved target of .01m$^2$ optical cross-section, and a large resolved target of worst-case reflectivity large relative to a scene resolution element (pixel) that a few pixels should resolve favorable geometry. Since the range obtainable for a single pixel is being examined, the large target will be simplified by assuming a resolved Lambertian plate. Range equations for these targets will be developed below, and computer range plots shown afterward.

Range Equations. Since the hybrid CCD is an integrating sensor and prior work has dealt with receiver noise equivalent energy (NEE), range equations are most easily derived in terms of signal energy. The laser output energy per pulse is

$$E_L = \frac{P_L}{PRF}$$

where $P_L$ is average laser power. Average laser power is somewhat dependent on PRF in that the laser becomes peak power limited at low PRFs. For a uniform beam spread, the energy density (J/m$^2$) incident on the target is

$$H_{ti} = \frac{E_L}{R^2 B\theta_1\theta_2} \tau_{ot} \tau_a$$

where R is range, $\theta_1$ is the horizontal beam width in radians, $\theta_2$ is the vertical beam width in radians, and B is a beam overlap factor. (For example, B=2 for $\theta_1$ twice the receiver IFOV). $\tau_{ot}$ is the effective optical transmission of transmitter optics, and $\tau_a$ is one-way atmospheric transmission. For an unresolved target of optical cross-section $\sigma_t$, the energy reflected from the target is

$$E_t = \frac{\sigma_t}{4\pi} H_{ti}$$

For a resolved Lambertian reflector of reflectivity $\gamma$,

$$E_t = \frac{\gamma\theta_1{}^2 R^2}{\pi} H_{ti}$$

This is for square picture elements of angular subtense $\theta_1$.

The energy density incident on receiver optics is

$$H_{ri} = \frac{E_t}{R^2} \tau_a$$

and the total energy collected by the receiver is

$$E_r = \pi r_o^2 H_{ri}$$

where $r_o$ is the radius of the receiver optical aperture. The number of photons collected by the receiver is

$$N = \frac{\lambda}{hc} E_r$$

where $\lambda$ is the wavelength of interest, h is Planck's constant, and c is the velocity of light. These relations give the following expressions for N

UNRESOLVED TARGET:

$$N = \frac{\lambda}{hc} \cdot \frac{P_L r_o^2 \sigma_t}{4R^4 B\theta_1\theta_2 (PRF)} \tau_{ot} \tau_a^2$$

RESOLVED TARGET:

$$N = \frac{\lambda}{hc} \cdot \frac{\gamma P_L r_o^2 \theta_1}{R^2 B \theta_2 (PRF)} \tau_{ot} \tau_a^2$$

The range at which a given receiver signal-to-noise (S/N) is obtained is found by setting $N = S/N \cdot NEE_r$ and solving for R. Table 13 shows the resulting range equations and a summary of parameters. A uniform beam spread through angles $\theta_1$ and $\theta_2$ has been assumed, althouth this cannot occur in practice. The beam shape will be a gradual Gaussian function which places more energy in the center of the receiver field-of-view (FOV) than at the top and bottom edges. This will result in the SLIR system being somewhat more sensitive in the center of the receiver FOV than indicated by the range equations, and a little less sensitive at top and bottom. However, range varies as the 4th root (unresolved target) or square root (resolved target) of the beam spread variation, and the range equations shown with Table 13 provide a good estimate of SLIR range performance.

Range Performance. A computer program has been written which plots range as a function of altitude according to the range equations of Table 13. The plots assume horizontal paths, or equal SLIR and target altitudes. Atmospheric transmission is obtained from a $9^{th}$ order curve fit to data compiled by Cambridge Air Force Laboratories and listed in

## TABLE 13

## RANGE EQUATIONS AND PARAMETER DEFINITIONS

UNRESOLVED TARGET:

$$R = \left[ \frac{\lambda}{hc} \cdot \frac{P_L \, r_o^2 \, \sigma_t}{4 \; (S/N \cdot NEE_r) \, (B \; \theta_1) \; \theta_2 \; (PRF)} \quad \tau_{ot} \; \tau_a^{2} \right]^{\frac{1}{4}}$$

RESOLVED TARGET:

$$R = \left[ \frac{\lambda}{hc} \cdot \frac{P_L \, r_o^2 \, \gamma \, \theta_1}{B \; \theta_2 \; (PRF) \, (S/N \cdot NEE_r)} \quad \tau_{ot} \; \tau_a^{2} \right]^{\frac{1}{2}}$$

| Symbol | Definition |
|---|---|
| $R$ | range |
| $\lambda$ | signal wavelength |
| $h$ | Planck's constant |
| $c$ | velocity of light |
| $P_L$ | average laser power |
| $r_o$ | radius of optical aperture |
| $\sigma_t$ | target cross-section |
| $S/N$ | desired signal-to-rms noise |
| $NEE_r$ | receiver noise equivalent energy in photons/pulse |
| $\theta_1$ | horizontal laser beam width in radians |
| $B$ | overlap factor for $\theta_1$ |
| $\theta_2$ | vertical laser beam width in radians |
| $PRF$ | laser pulse repetition frequency |
| $\tau_{ot}$ | effective optical transmission of transmitter |
| $\tau_a$ | one-way atmospheric transmission |

reference (14). This data considers all major transmission factors. The curve fit is better than 1 percent accurate at 5 km and 23 km visibility, and is useful only between these visibility limits. This curve fit has ~~been used~~ by Martin Marietta for several recent Air Force programs, such as Compass Hammer.

Range dependence on atmospheric transmission is illustrated by Figure 40. This figure shows the atmospheric extinction coefficient as a function of altitude for 5 km and 20 km sea level visibilities. For altitudes above 5 km, transmission is almost totally independent of sea level visibility. For an extinction coefficient $\alpha$, atmospheric transmission $\tau_o$ over range R is:

$$\tau_o = e^{-\alpha R}$$

Therefore, Figure 40 indicates almost unity transmission for altitudes above a few kilometers, even for ranges as great as 20 km.

A number of computer range plots are shown in Figures 41 through 49. These are primarily intended to illustrate acquisition range performance. This is because the most difficult SLIR requirements to meet are the 9.3 km (5 n.miles) acquisition range for the unresolved cross-section and the 18.5 km (10 n.miles) acquisition specified for the large target. Since S/N increases rapidly with decreasing range, ample S/N should exist at precision track range regardless of the acquisition S/N. A nominal acquisition S/N is difficult to assess without detailed analysis of the entire tracker system, which is beyond the scope of this report. However, since accurate tracking is not necessary at long range and since an 1.06 micron system has better than 10 times the resolution of a FLIR system of equal aperture, a typical acquisition S/N in the interval from 3 to 10 is reasonable. This is roughly equivalent to S/N varying from 30 to 100 with an equivalent FLIR system, so far as tracking precision is concerned. The small unresolved target presents the more difficult acquisition problem and will be investigated first. The plots are for the nominal receiver NEEs developed in sub-section 3.3; where 100 photons is the nominal value for the GaAsSb APD with gain, 200 photons for this device with unity gain, and 300 photons for the silicon PIN diode. All plots are for a 100W

---

(14) R. A. McClatchey, et al, "Optical Properties of the Atmosphere (Third Edition)," Air Force Cambridge Research Laboratories, Tech. Rep. AFCRL-72-0497, August 1972.

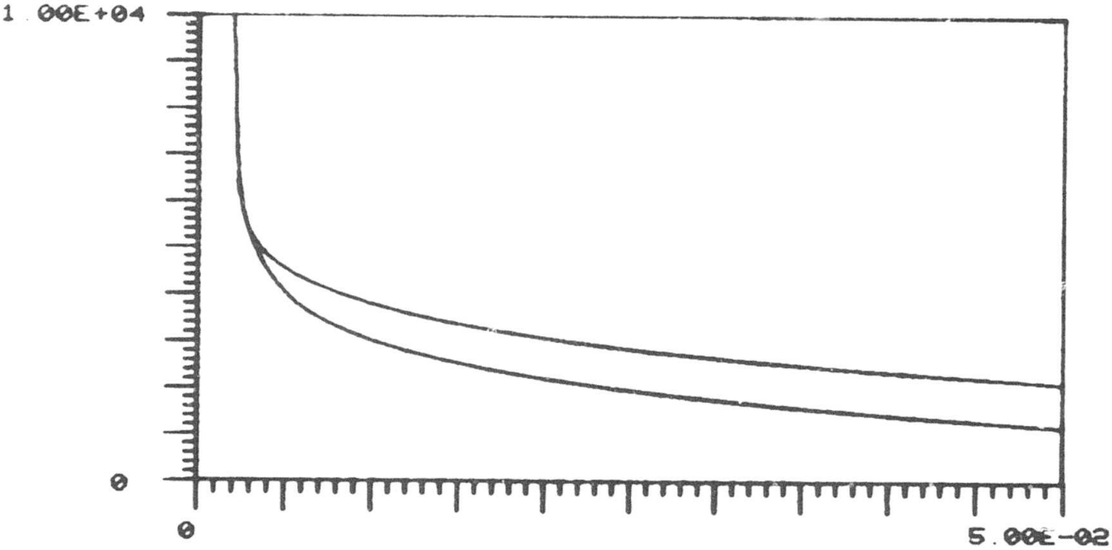

ALTITUDE VS EXTC. COEFF. FOR FIXED VISIBILITIES

CURVES FOR 5.00E+03 & 2.00E+04 METER VISIBILITY

Figure 40. Atmospheric Extinction Coefficient as a Function of Altitude

(average power) laser and a 20 Hz acquisition frame rate, and all distances are in meters.

Run 1 shows the .01 $m^2$ unresolved cross-section for the APF with gain and S/N=3. Run 2 repeats these circumstances for S/N of 10. Runs 1 and 2 indicate that the 9.3 km acquisition range requirement is easily met for typical acquisition S/N values. Runs 3 and 4 repeat the previous sequence for the APD with unity gain, with the same result regarding acquisition range. Runs 5 and 6 are for the PIN diode, and show that this sensor is close to meeting acquisition requirements with the nominal NEE assigned to it. Runs 7 and 8 are for a large resolved target of .1 reflectivity. These runs use the mose pessimistic NEE value of 300 photons because the range requirements are satisfied even for this value at significant altitude. Since range varies inversely as the square root of NEE, very good performance is attained for NEEs of 200 and 100. Run 9 is included to show the extremely long range obtainable for a high reflectivity target.

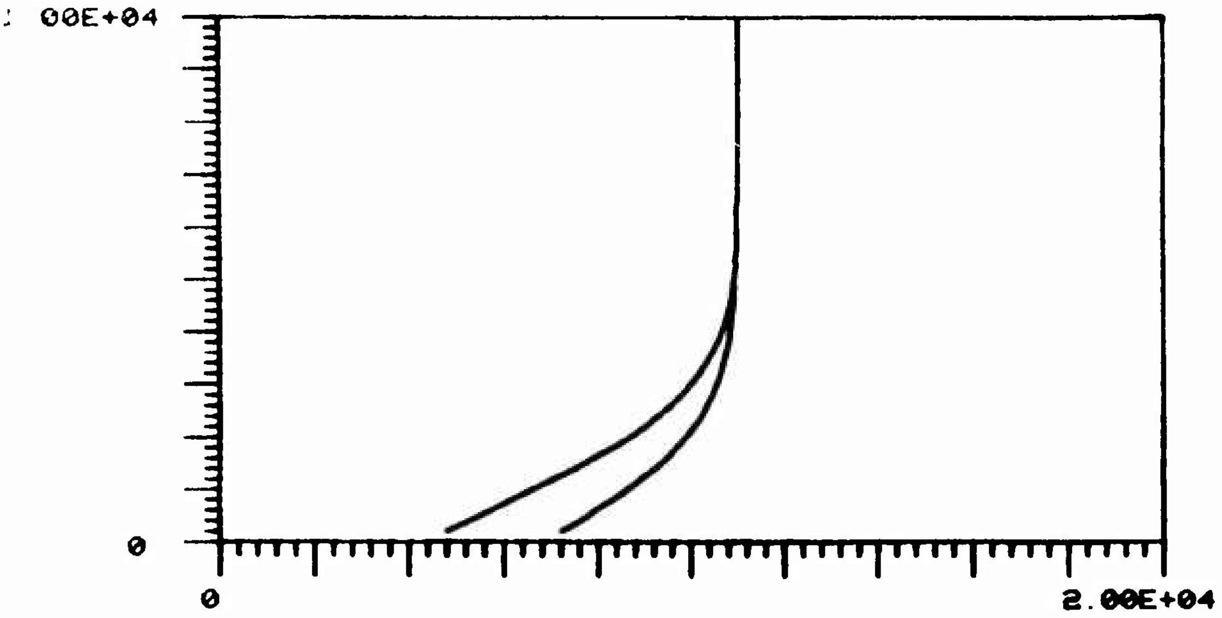

```
ALTITUDE VS RANGE FOR FIXED VISIBILITIES

CURVES FOR  5.00E+03 &  2.00E+04 METER VISIBILITY

PARAMETERS  AVG LASER POWER (W) =  100.0
            SIGNAL-TO-NOISE   =     3.0
            RECEIVER NEE (PHOTONS/PULSE) =   100.0
            FRAME RATE (HZ)  =      20.
            250  ELEMENT ARRAY OF 40.  URAD IFOV

           TARGET CROSS-SECTION = 0.010 SQ M
```

Figure 41. Run No. 1

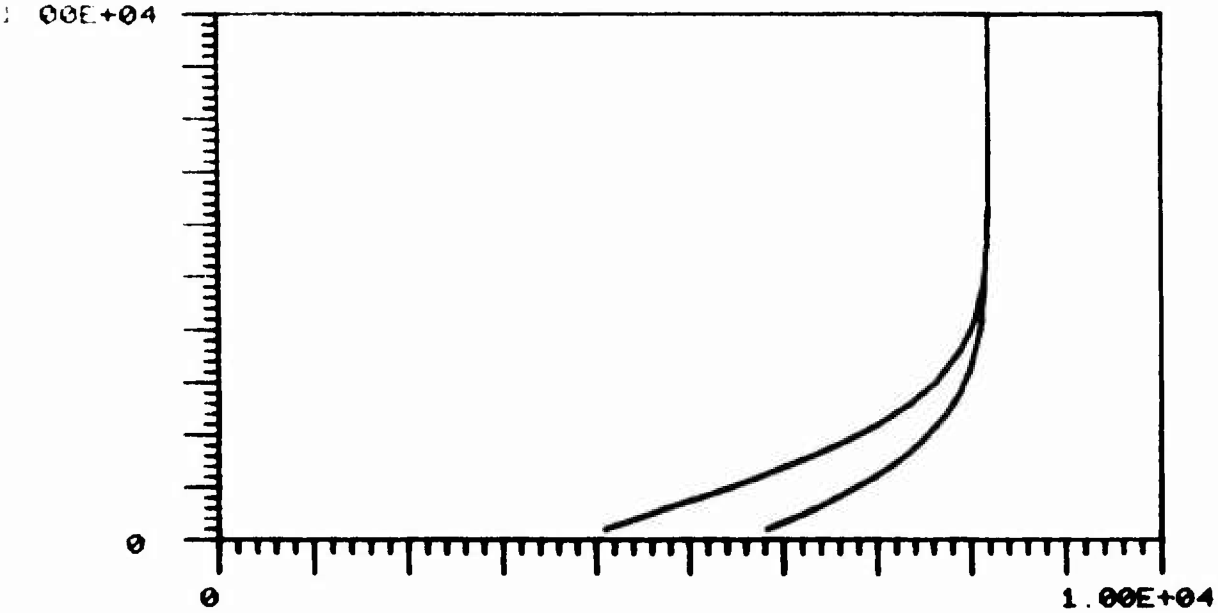

ALTITUDE VS RANGE FOR FIXED VISIBILITIES

CURVES FOR 5.00E+03 & 2.00E+04 METER VISIBILITY

PARAMETERS: AVG LASER POWER (W) = 100.0
SIGNAL-TO-NOISE = 10.0
RECEIVER NEE (PHOTONS/PULSE) = 100.0
FRAME RATE (HZ) = 20.
250 ELEMENT ARRAY OF 40. URAD IFOV

TARGET CROSS-SECTION = 0.010 SQ M

Figure 42. Run No. 2

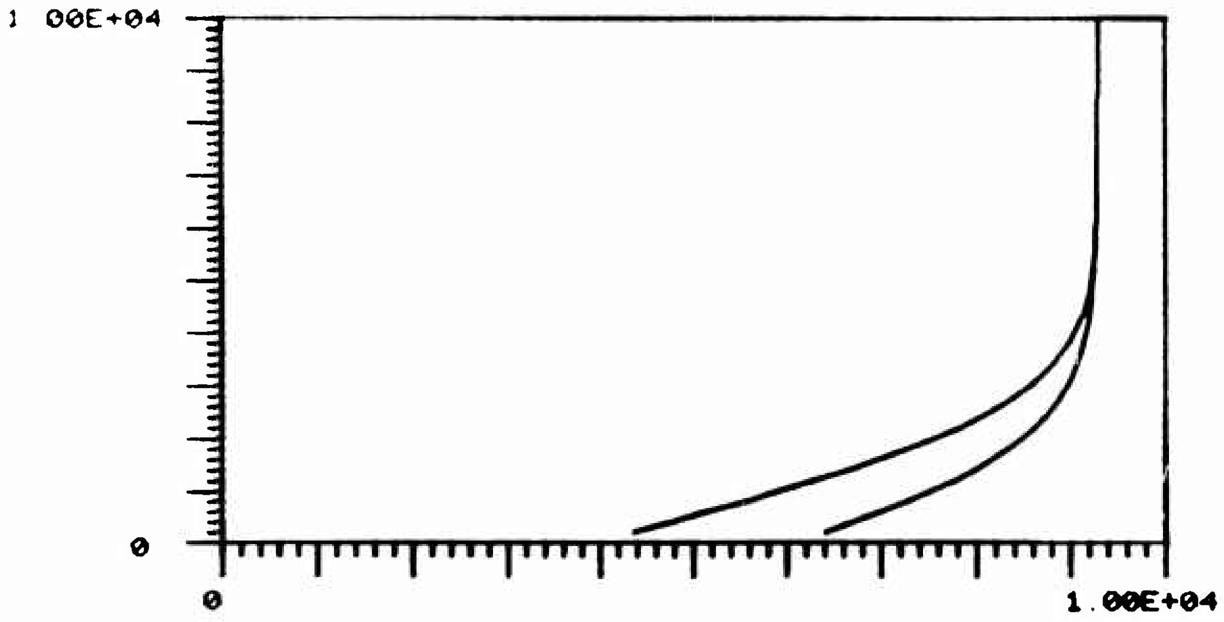

ALTITUDE VS RANGE FOR FIXED VISIBILITIES

CURVES FOR 5.00E+03 & 2.00E+04 METER VISIBILITY

PARAMETERS: AVG LASER POWER (W) = 100.0
SIGNAL-TO-NOISE = 3.0
RECEIVER NEE (PHOTONS/PULSE) = 200.0
FRAME RATE (HZ) = 20.
250 ELEMENT ARRAY OF 40. URAD IFOV

TARGET CROSS-SECTION = 0.010 SQ M

Figure 43. Run No. 3

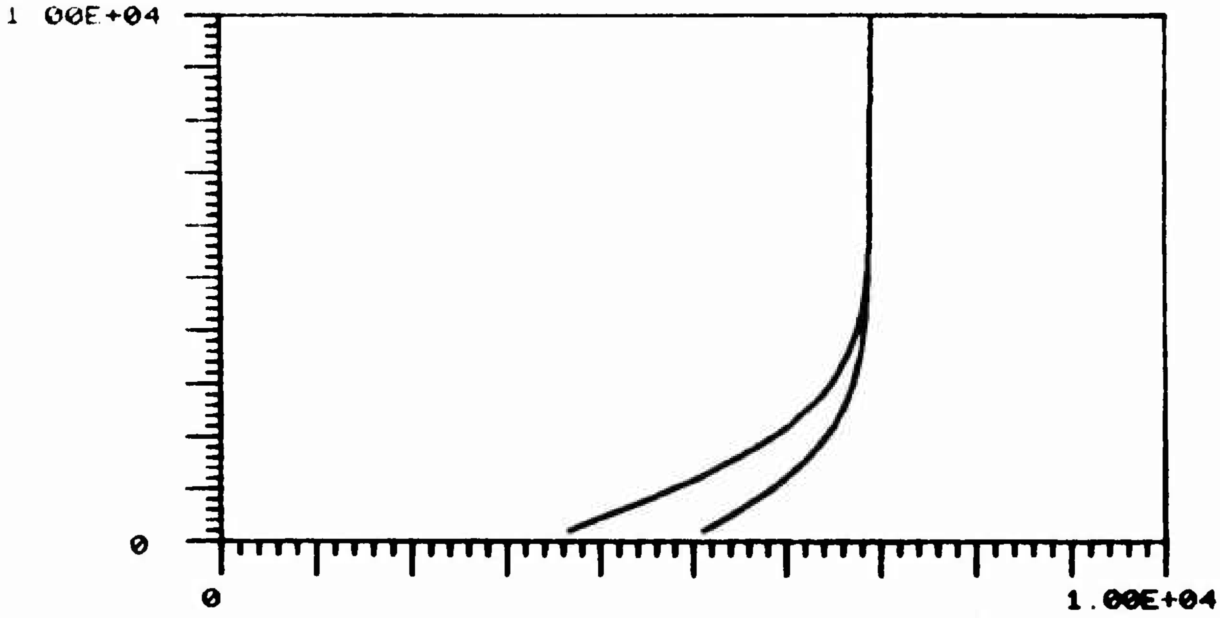

ALTITUDE VS RANGE FOR FIXED VISIBILITIES

CURVES FOR 5.00E+03 & 2.00E+04 METER VISIBILITY

PARAMETERS: AVG LASER POWER (W) = 100.0
SIGNAL-TO-NOISE = 10.0
RECEIVER NEE (PHOTONS/PULSE) = 200.0
FRAME RATE (HZ) = 20.
250 ELEMENT ARRAY OF 40. URAD IFOV

TARGET CROSS-SECTION = 0.010 SQ M

Figure 44. Run No. 4

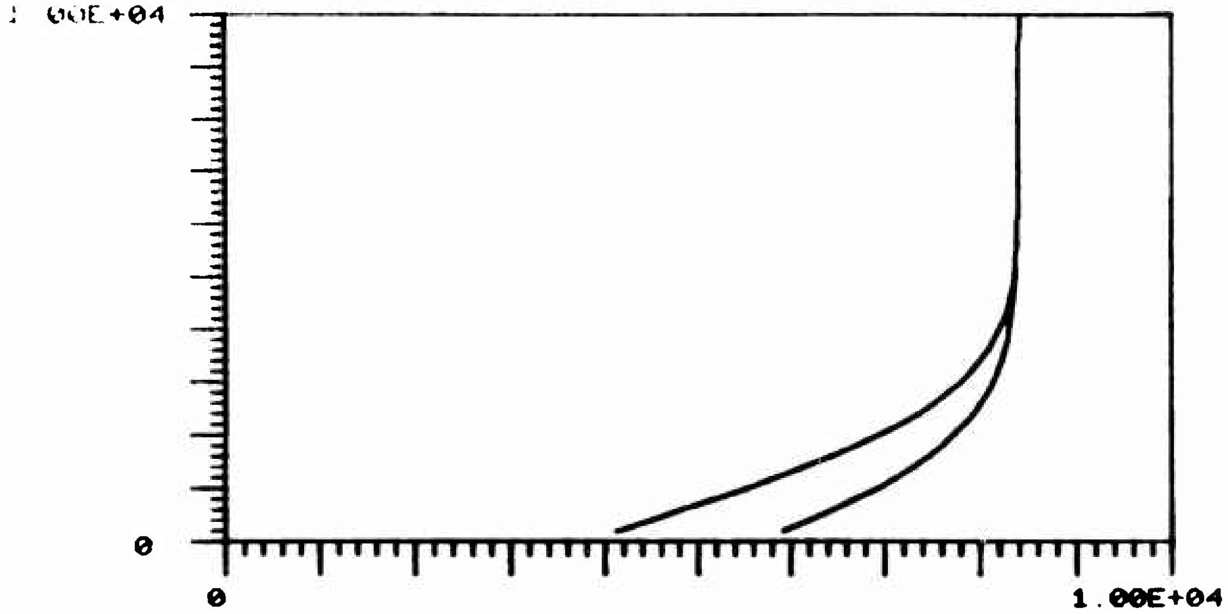

ALTITUDE VS RANGE FOR FIXED VISIBILITIES

CURVES FOR 5.00E+03 & 2.00E+04 METER VISIBILITY

PARAMETERS: AVG LASER POWER (W) = 100.0
SIGNAL-TO-NOISE = 3.0
RECEIVER NEE (PHOTONS/PULSE) = 300.0
FRAME RATE (HZ) = 20.
250 ELEMENT ARRAY OF 40. URAD IFOV

TARGET CROSS-SECTION = 0.010 SQ M

Figure 45. Run No. 5

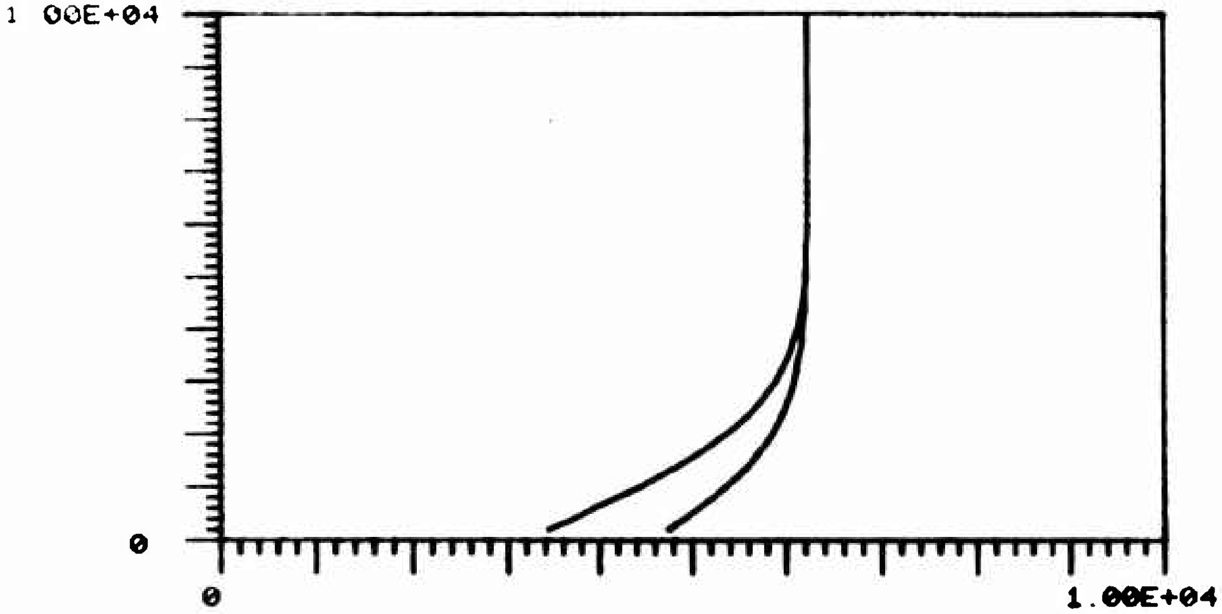

ALTITUDE VS RANGE FOR FIXED VISIBILITIES

CURVES FOR 5.00E+03 & 2.00E+04 METER VISIBILITY

PARAMETERS: AVG LASER POWER (W) = 100.0
SIGNAL-TO-NOISE = 10.0
RECEIVER NEE (PHOTONS/PULSE) = 300.0
FRAME RATE (HZ) = 20.
250 ELEMENT ARRAY OF 40. URAD IFOV

TARGET CROSS-SECTION = 0.010 SQ M

Figure 46. Run No. 6

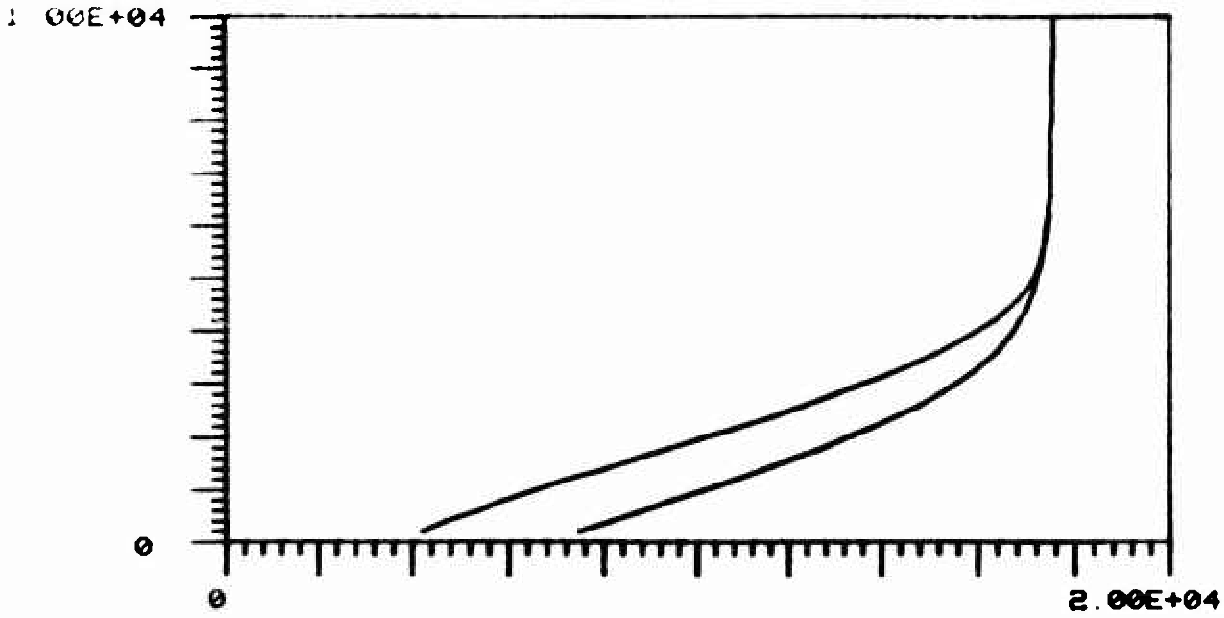

ALTITUDE VS RANGE FOR FIXED VISIBILITIES

CURVES FOR 5 00E+03 & 2.00E+04 METER VISIBILITY

PARAMETERS: AVG LASER POWER (W) = 100.0
SIGNAL-TO-NOISE = 3.0
RECEIVER NEE (PHOTONS/PULSE) = 300.0
FRAME RATE (HZ) = 20.
250 ELEMENT ARRAY OF 40. URAD IFOV

RESOLVED TARGET OF REFLECTIVITY = 0.10

Figure 47. Run No. 7

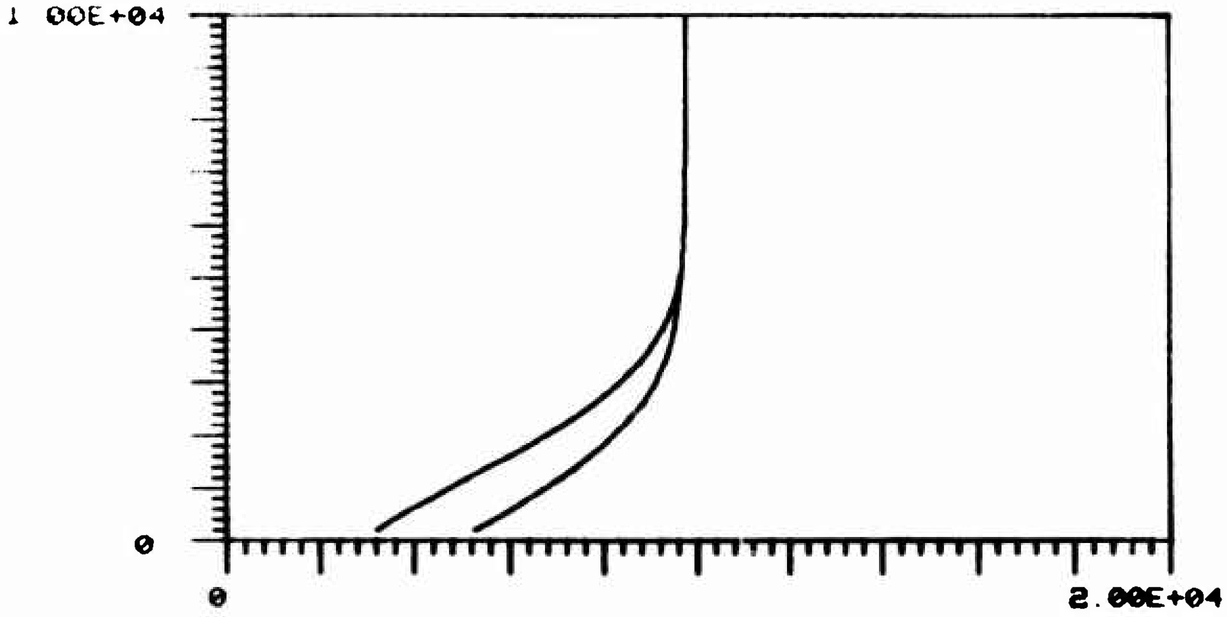

ALTITUDE VS RANGE FOR FIXED VISIBILITIES

CURVES FOR 5.00E+03 & 2.00E+04 METER VISIBILITY

PARAMETERS: AVG LASER POWER (W) = 100.0
SIGNAL-TO-NOISE = 10.0
RECEIVER NEE (PHOTONS/PULSE) = 300.0
FRAME RATE (HZ) = 20.
250 ELEMENT ARRAY OF 40. URAD IFOV

RESOLVED TARGET OF REFLECTIVITY = 0.10

Figure 48. Run No. 8

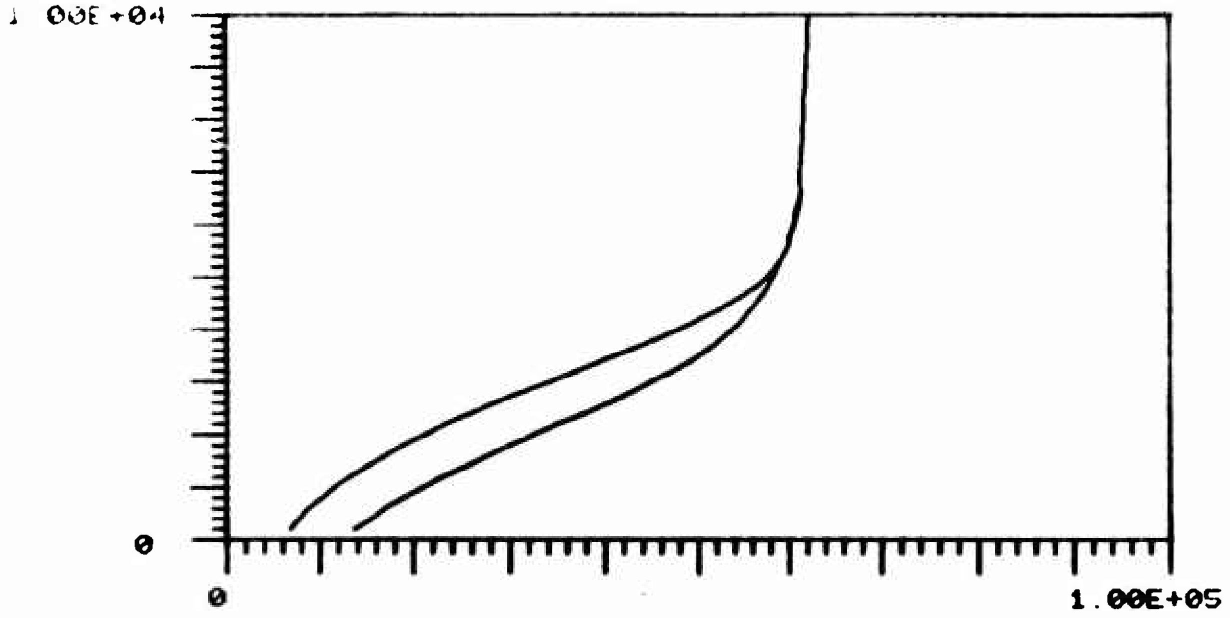

ALTITUDE VS RANGE FOR FIXED VISIBILITIES

CURVES FOR 5.00E+03 & 2.00E+04 METER VISIBILITY

PARAMETERS: AVG LASER POWER (W) = 100.0
SIGNAL-TO-NOISE = 3.0
RECEIVER NEE (PHOTONS/PULSE) = 200.0
FRAME RATE (HZ) = 20.
250 ELEMENT ARRAY OF 40. URAD IFOV

RESOLVED TARGET OF REFLECTIVITY = 1.00

Figure 49. Run No. 9

## 4.2 Imaging Performance

The imaging performance of a sensor system is customarily evaluated in terms of a modulation transfer function (MTF). MTF is a normalized response function with scene spatial frequency being the independent variable. The spatial frequency for which MTF $\approx 0$ is usually assumed to define the limiting resolution of the system. The three main determiners of overall MTF for the SLIR system are: 1) MTF of the sampled detector array; 2) motional MTF due to scan jitter; and 3) MTF of the optics. These three factors will be assessed below, and overall MTF computed. Although MTF is a two-dimensional function over a coordinate plane, MTFs in the scan and ortho-scan directions should be reasonably independent, which allows separate and independent calculation of these MTFs. Since scan jitter occurs primarily in the scan direction, MTF along the scan axis will be evaluated as a worst-case condition. Because the array has many contiguous square detectors and is sampled in the scan direction for contiguous dwell intervals, the scan and ortho-scan MTFs are similar except for jitter.

Detector MTF. MTF in the scan (x) direction will be independent of the array extent in the ortho-scan (y) direction. It is well known that a continuously scanning detector of width d has:

$$\text{MTF} = \mathfrak{F}\left[D(X)\right] = \frac{\text{Sin}\ \pi\, d\, \nu}{\pi\, d\, \nu}$$

where $\nu$ is spatial frequency in units such as cycles/distance or line pairs/rad, and $\mathfrak{F}[D(X)]$ is the Fourier transform of the spatial detector function. The central lobe of this function will end where $\nu = 1/d$, and it is not normally useful to consider frequencies beyond this value. For convenience, the work here will be for unity detector width $d = 1$, and $\nu$ will be expressed in (cycles)/(detector width). Detector width can have units of distance or angle.

The fact that the detector output is sampled at contiguous dwell intervals will, on average, degrade imaging performance from that indicated by the MTF above. It is necessary to qualify this statement because the contiguous sampling constitutes a sampling spatial filter which can enhance or degrade spatial intensity functions at certain frequencies, depending on the phase relationship between the scene intensity function and the detector dwell location. Figure 50 illustrates this. The (a) part of the figure shows the detector perfectly in phase with a sinusoidal scene intensity variation of $\nu = 1/2$ cycles/(detector width). The x-axis can represent either distance or angular travel in the scene. (Although real scenes do not have negative intensities, the average or centerline of the sinusoid has been assigned as 0 here since this will have no effect on the amplitude of Fourier components beyond $\nu = 0$). When the detector is positioned to view the scene interval from 0 to 1, its output is proportional to the integral of the intensity function $I(x)$ in the interval, which is $2/\pi$. Since detector output is sampled once per dwell location, sensor processing (discregarding other factors influencing MTF) will represent the scene as having a constant intensity $2/\pi$ in the interval from 0 to 1. Contiguous samples along the x-axis will result in the steady-state square wave of which one period is shown in (a). Since this square wave is actually the idealized response for the situation described, the response to a sinusoidal variation $I(x) = \sin \pi X$ at frequency $\nu = 1/2$ is the first harmonic of the square wave. The square wave fundamental has a peak amplitude of:

$$4/\pi \cdot \frac{2}{\pi} = .81$$

Part (c) of the figure shows a worst-case phase relationship where all samples have 0 value (they would actually have a value equal to the average scene intensity). Part (b) shows a case where the phase is exactly halfway between the extremes of (a) and (c), and by the process just discussed the response at $\nu = 1/2$ is .57 for this phase relationship. The response of a continuously scanning detector characterized by the $\frac{\sin \pi X}{X \pi}$ function would be .637. It is therefore apparent that a sampled detector can exhibit responses superior or inferior to a continuously scanning detector, depending on the spatial frequency and phase. This result is not general for all spatial frequencies; the lower spatial frequencies give slightly poorer response when sampled regardless of phase, although there is some phase-dependent variation in response. However, sampling does not produce a large change in low frequency response since the relatively short detector width begins to behave as a continuously moving impulse sampler.

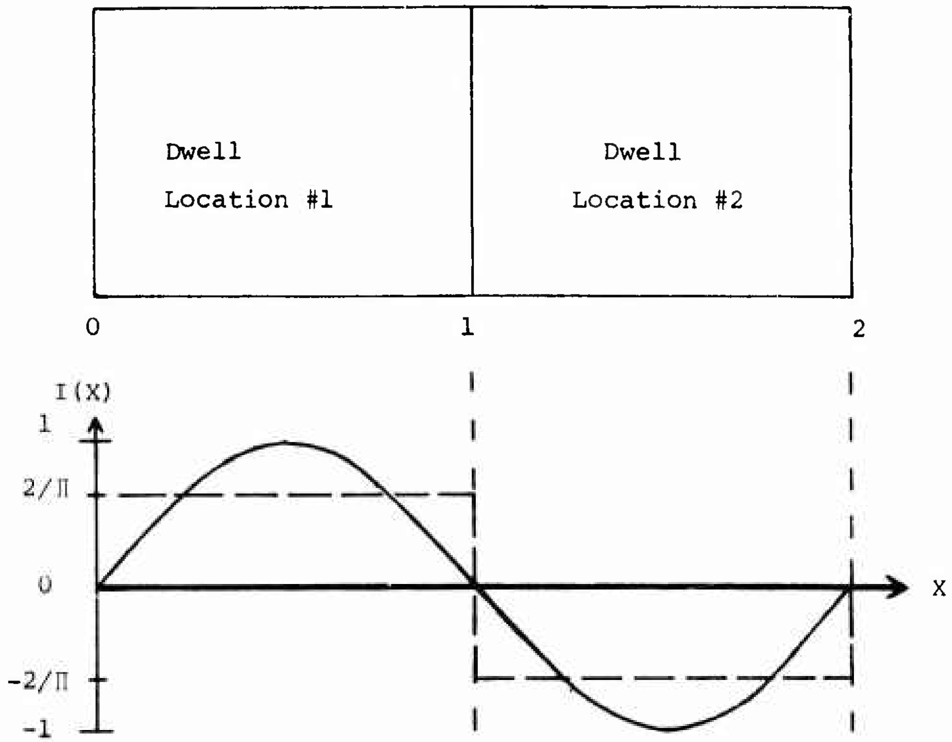

(a) In phase

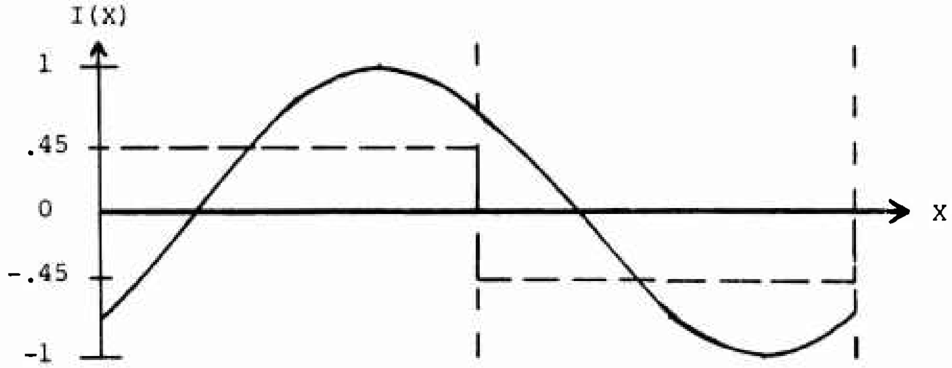

(b) 45° Out of Phase

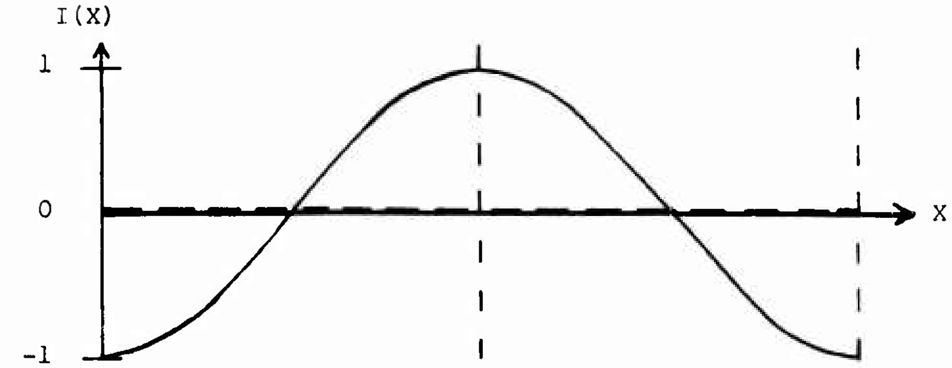

(c) 90° Out of Phase

Figure 50. Detector Response for Various Phase Relationships at Spatial Frequency $\nu$ = 1/2 cycles/(detector width)

The results just developed show that it is necessary to define a phase relationship before a sampled MTF can be assessed. It appears obvious that the phase will be random, but the probability density function describing the random distribution is perhaps subject to argument. A complex scene will have independent phase variations for different objects regardless of the indexing of detector with scene. The scene of interest to a SLIR system, however, is an artificial target with relatively simple and fixed phase relationship between components. This makes the indexing of detector with scene important and tends to influence phase towards being distributed in a flat random manner, although certainly a real phase distribution will not be exactly uniform. In the absence of precise knowledge, the scene/detector phase relationship must be assumed to be intermediate between the possible extremes as indicated in Figure 50. The MTF for a given sinusoidal component will then be assigned as approximately the average between MTF for the best-case phase and MTF for the worst-case phase. Figure 51 shows the detector MTF curve based on this assumption, where MTF for various sinusoidal components was computed as for Figure 50. It should be noted that, since the sampled detector is non-linear, superposition does not hold. Sampled MTF is a transfer function whose form depends on the input, and response to a general scene intensity variation cannot in principal be inferred from the addition of responses to the Fourier components of the variation. However, this is the only convenient analytical method to determine response to a general scene, and in practice gives acceptable results for ordinary scene objects.

Motional MTF. Imagery degradation due to scan jitter can be accounted for by calculating the motional MTF due to jitter. It is first necessary to establish the behavior of jitter. Jitter is most often characterized as a random Gaussian motion. The fourier transform of this motion in the spatial frequency domain is

$$\mathrm{MTF} = e^{-2\left[\pi \sigma \nu\right]^2} \tag{20}$$

where $\sigma$ is the rms jitter excursion and $\nu$ is spatial frequency in units compatible with those of $\sigma$. The scan jitter specified by the General Scanning Company for the scanner evaluated by this study is 10 arc-sec rms.

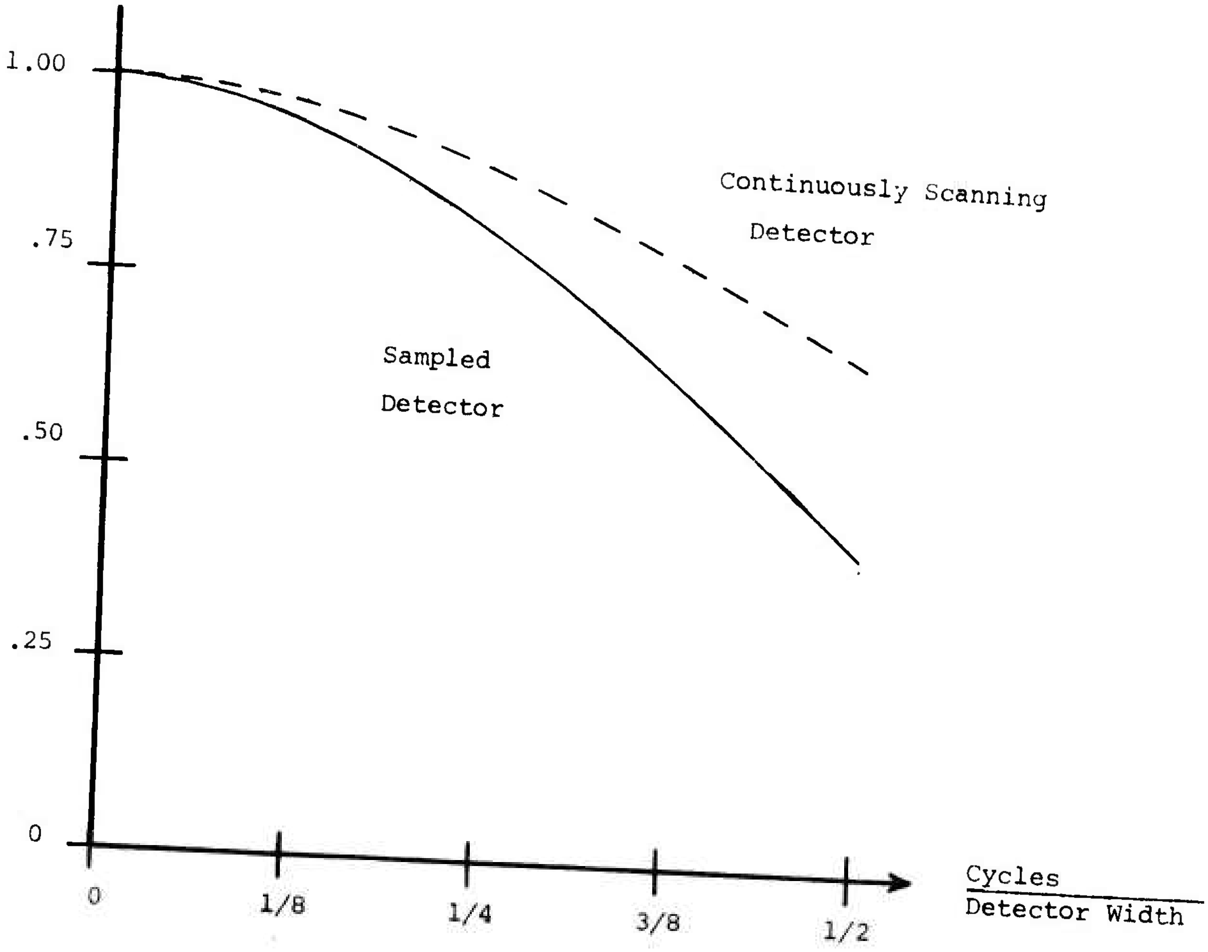

Figure 51. Approximate MTF for Sampled Detector

It is assumed that this is the dominant source of jitter. There is a 10X optical magnification between the scan mirror and object space for all track modes, reducing the effective jitter to 1 arc-sec rms. Designating $\nu$ as cycles/mrad and converting $\sigma$ to mrad:

$$\mathrm{MTF} = e^{-4.64 \times 10^{-4} \nu^2} \qquad (21)$$

This MTF is plotted in Figure 52.

Optics MTF. A complete preliminary optical design has been accomplished for a prototype system and is discussed in Section V. The receiver optics design should be very similar for a breadboard prototype or a fully developed system. MTF curves have been obtained from standard optical design computer programs and are shown in Figure 53. These curves show nearly diffraction limited performance. On-axis MTF is plotted in the curves; off-axis MTF within the receiver total FOV is virtually identical because of the small total FOV. The curves are for the three SLIR operational modes of "Acquisition", "Track" and "Precision Track". Effective focal length (EFL) changes for these modes because of power changes in the receiver optics.

Overall Receiver MTF. The overall MTF is the product of the individual MTFs previously derived. In order to display overall MTF in the convenient units of cycles/mrad, it is necessary to convert the detector and optics MTFs. The detector width for the Acquisition, Track, and Precision Track modes is 40 μrad, 20 μrad, and 10 μrad respectively. This gives 12.5, 25, and 50 cycle/mrad as the desired minimum resolution limits of the three modes for the limiting case of 1/2 cycle (or 1 line in terms of line pairs) per detector width. Detector MTF in units of cycles/(detector width) is converted to cycles/mrad by multiplying the spatial frequency axis values by 1/d, for the detector widths d in mrad as mentioned above. This gives multipliers of 25, 50, and 100 respectively for the Acquisition, Track, and Precision Track modes. The optics MTF in terms of cycles/mm is converted to cycles/mrad by deriving a conversion factor of mm/mrad. The number of mrad $\beta$ subtended by 1 mm in the focal plane is

$$\beta = \frac{d}{\mathrm{EFL}} \times 10^3 .$$

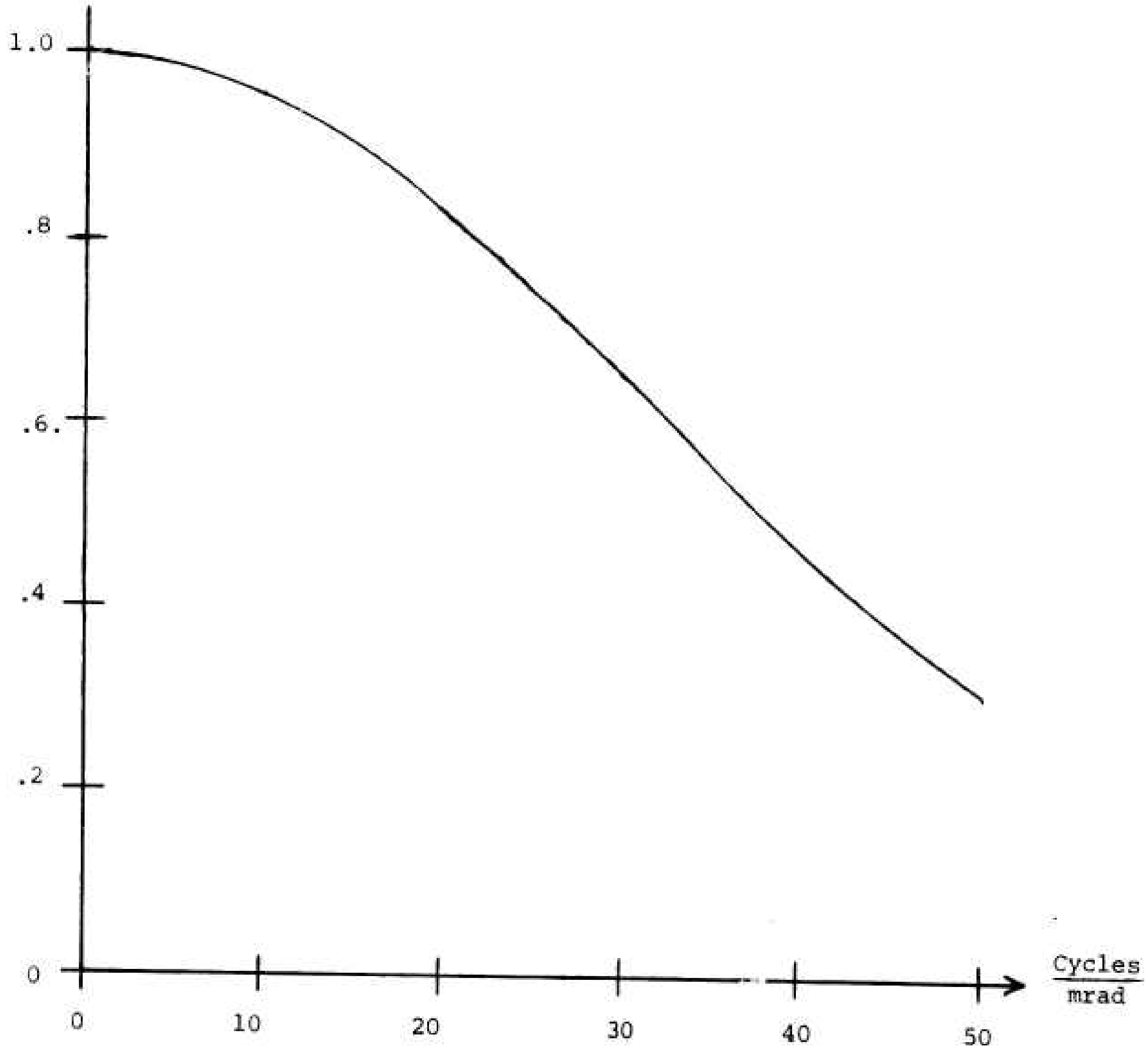

Figure 52. Motional MTF Due to Scan Jitter

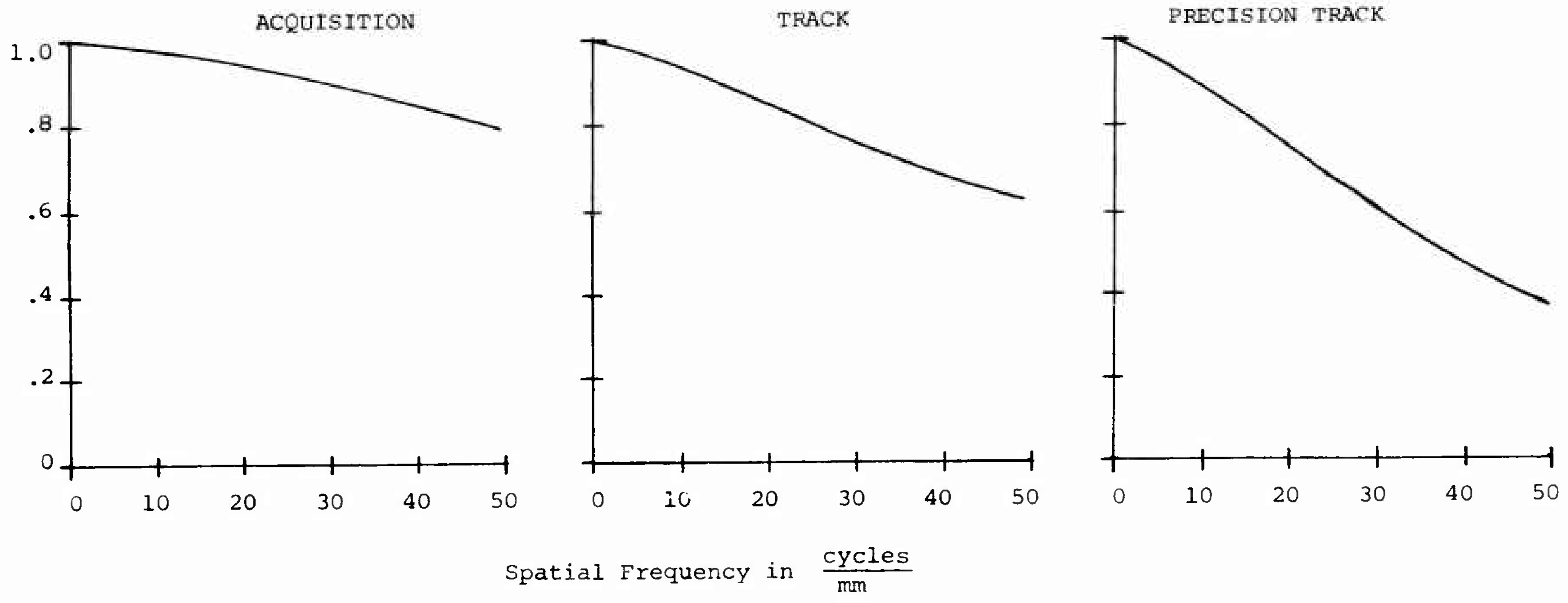

Figure 53. Optics MTF for the Three SLIR Modes

The mm/mrad factor is the reciprocal of this expression, and proper conversion is obtained by multiplying the optical MTF spatial frequency axis values by .3175, .635, and 1.27 mm/mrad respectively, for the Acquisition, Track, and Precision Track modes. The resulting overall receiver MTFs are plotted in Figure 54. The minimum resolution limits of interest are marked by a vertical line on each plot.

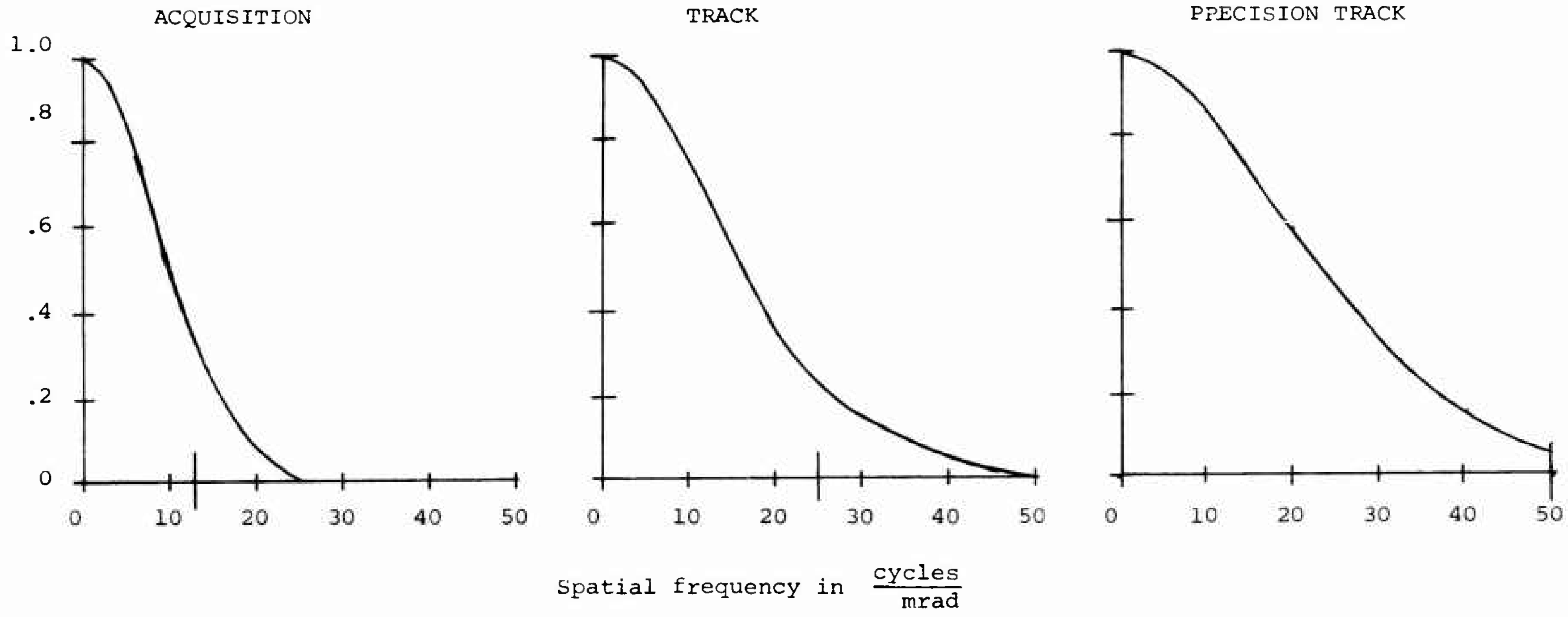

Figure 54. Approximate overall receiver MTF for the three SLIR modes

# SECTION V

# SLIR SYSTEM DESIGN

The design of an operational SLIR system suitable for airborne HEL applications requires the development and integration of a number of technologies, each of which represents an advancement of the present state-of-the-art. Consequently, it is judicious to organize SLIR system design as a phased development effort. This study is representative of the initial phase. The development of a laboratory breadboard SLIR system which would verify the expected system performance through simulation would be a logical second phase goal. This breadboard development would also provide working experience with the SLIR hardware and would serve as a demonstration vehicle for the system concepts involved. A third phase, which integrates the SLIR system into the pointing and tracking gimbal to create an airworthy brassboard, would constitute the next step in the logical progression toward full-up SLIR development.

The following section describes the preliminary design of the Phase II SLIR laboratory breadboard and its associated display and recording interface subsystem. Because this next phase would be the initial hardware development effort for the overall program, system flexibility which permits minor modification and component up-grading is a necessary attribute of the design. Consequently, several options, particularly in the illuminator laser source and the receiver linear detector areas, are envisioned which will expedite the overall system development through parallel subsystem development efforts. This approach allows the breadboard to be rapidly fabricated and tested using existing state-of-the-art componentry and then to be easily up-graded to full-up performance status by the introduction of advanced componentry which is developed in parallel.

The basic characteristics of the SLIR laboratory breadboard are summarized in Table 14. These characteristics are discussed in some detail in the following subsection. Expected range performance of the breadboard system is also detailed and followed by a discussion of the display and recorder interface which is necessary for subsequent system test and evaluation.

TABLE 14

SLIR Laboratory Breadboard System Parameters

| | Acquisition Mode | Track Mode | Precision Track Mode |
|---|---|---|---|
| **Illuminator** | | | |
| Instantaneous Projection Field | 10 mrad x 80 μrad | 5 mrad x 40 μrad | 2.5 mrad x 20 μrad |
| Scan Field | 10 mrad x 10 mrad | 5 mrad x 5 mrad | 2.5 mrad x 2.5 mrad |
| Afocal Power (scan/ortho-scan) | 15X/0.1X | 30X/0.2X | 60X/0.4X |
| Optical Transmission (1.06 μm) | 83% | 83% | 86% |
| Laser PRF | 5 - 10 KHz | 5 - 25 KHz | 5 - 50 KHz |
| **Receiver** | | | |
| Instantaneous FOV | 10 mrad x 40 μrad | 5 mrad x 20 μrad | 2.5 mrad x 10 μrad |
| Scan Field | 10 mrad x 10 mrad | 5 mrad x 5 mrad | 2.5 mrad x 2.5 mrad |
| Linear Detector Array | 250 elements | 250 elements | 250 elements |
| Afocal Power | 10X | 10X | 10X |
| Optical Transmission (1.06 μm) | 48% | 48% | 50% |
| Frame Rate | 10 - 20 Hz | 10 - 80 Hz | 10 - 160 Hz |

## 5.1 SLIR Laboratory Breadboard

Although the SLIR system must eventually be configured for installation on the Airborne Pointing and Tracking (APT) gimbal, it is judicious to postpone detailed consideration of the design complexities which gimballed operation entails until the SLIR concept itself is demonstrably proven. Consequently, the preliminary design of a functional laboratory breadboard model was performed as a first step in the development of the full-up SLIR system. The general configuration of this SLIR laboratory breadboard is illustrated in Figure 55.

The breadboard configuration is based upon SLIR system Concept No. 2, as described in a previous section, with some modification. An oscillating moving-iron galvonometer scanner is at the heart of the system. By means of a two-sided mirror, this scanner provides for the simultaneous and synchronous scan of a fan-beam illuminator and a linear array receiver. A position feed-back servo loop is used to greatly improve the linearity of the scanner and to permit variable scan rate (non-resonant) operation.

A cw-pumped Nd:YAG laser is used as the illuminator source. The output of this laser is modulated by an acousto-optic Q-switch to generate an output pulse train with a programmable PRF over the 5 to 50 kilohertz range. The phase and frequency of the pulse train is electronically synchronized with the galvonometer scanner such that uniform illumination of the scan field in object space will be achieved. A series of anamorphic beam expansion optics is used to shape the illumination beam to the desired fan-beam divergence. This far-field beam divergence is selectable, as required by the chosen operational mode (e.g., acquisition, track, or precision track), by means of an electrically driven lens turret which automatically positions small afocal lens groups of the proper magnification into the illuminator beam path. As shown in Figure 55, the illuminator beam output port is coaxial with the receiver objective so as to eliminate potential boresight alignment difficulties.

The receiver utilizes a ten-power catadioptric telescope with a 9-inch entrance aperture to collect illuminator energy reflected from a target. This energy is scanned by the galvonometer mirror and imaged on a 250-element linear mosaic detector by one of three imaging lens groups.

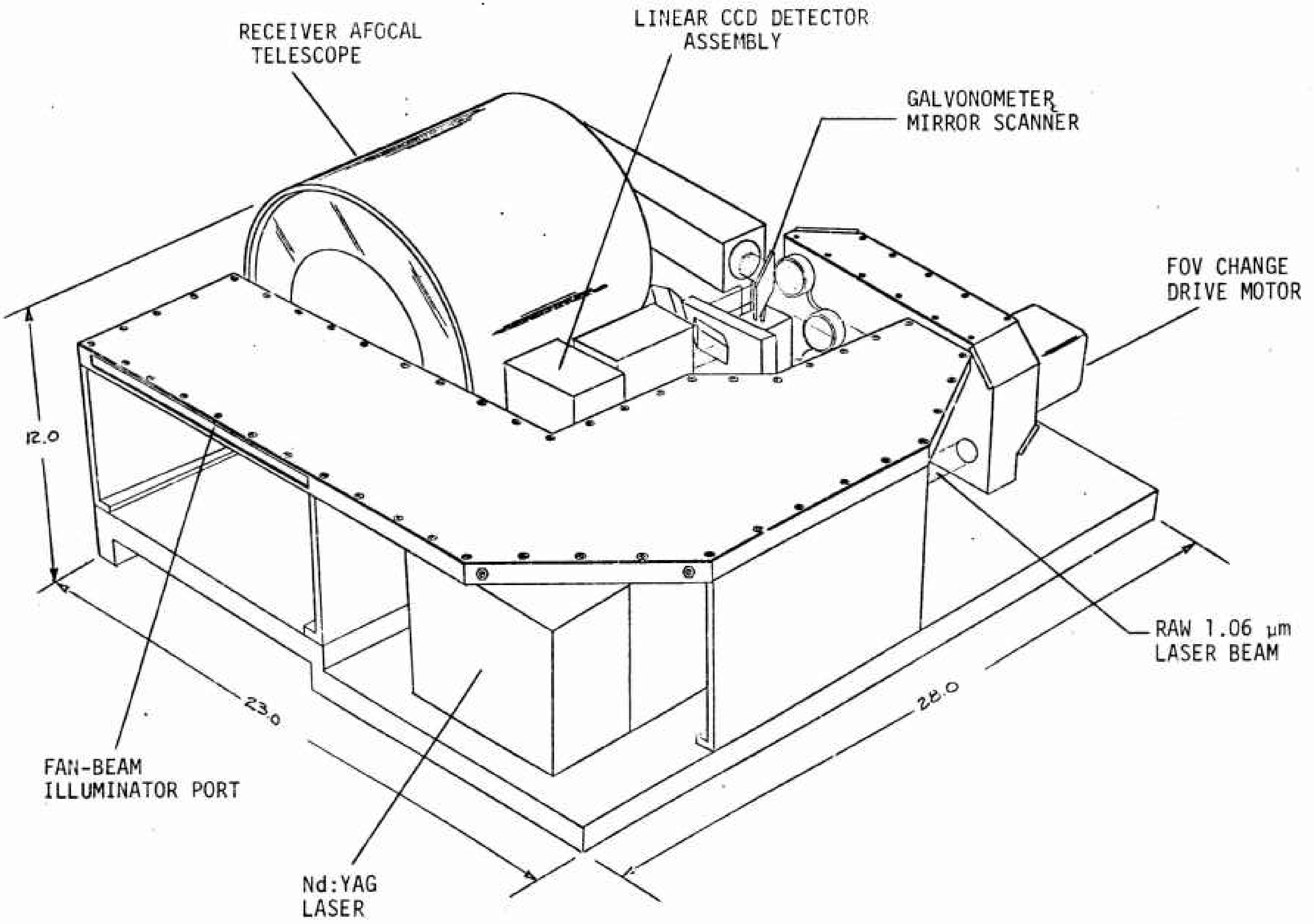

Figure 55. SLIR Laboratory Breadboard Configuration

Each of these lens groups is automatically selected in accordance with the chosen operational mode by mechanical insertion of rhomboid prisms into the optical path. The linear array detector is gated in range-dependent delayed synchronism with the illuminator Q-switch so as to minimize the effects of atmospheric backscatter. The parallel output signals from the detector are then multiplexed by a charge-coupled device (CCD) shift register which generates a serial video bit stream suitable for presentation on a display or interface with tracker logic.

The detail design of the SLIR laboratory breadboard is illustrated in Figures 56 and 57. Modular construction techniques have been employed wherever possible to maximize system flexibility and adaptability to subsequent modification or reconfiguration. This is intended to minimize system development costs while maximizing system development potential. Although little consideration has been given toward integration with the APT gimbal, many modules of this laboratory breadboard should prove to be readily compatible with gimballed installation.

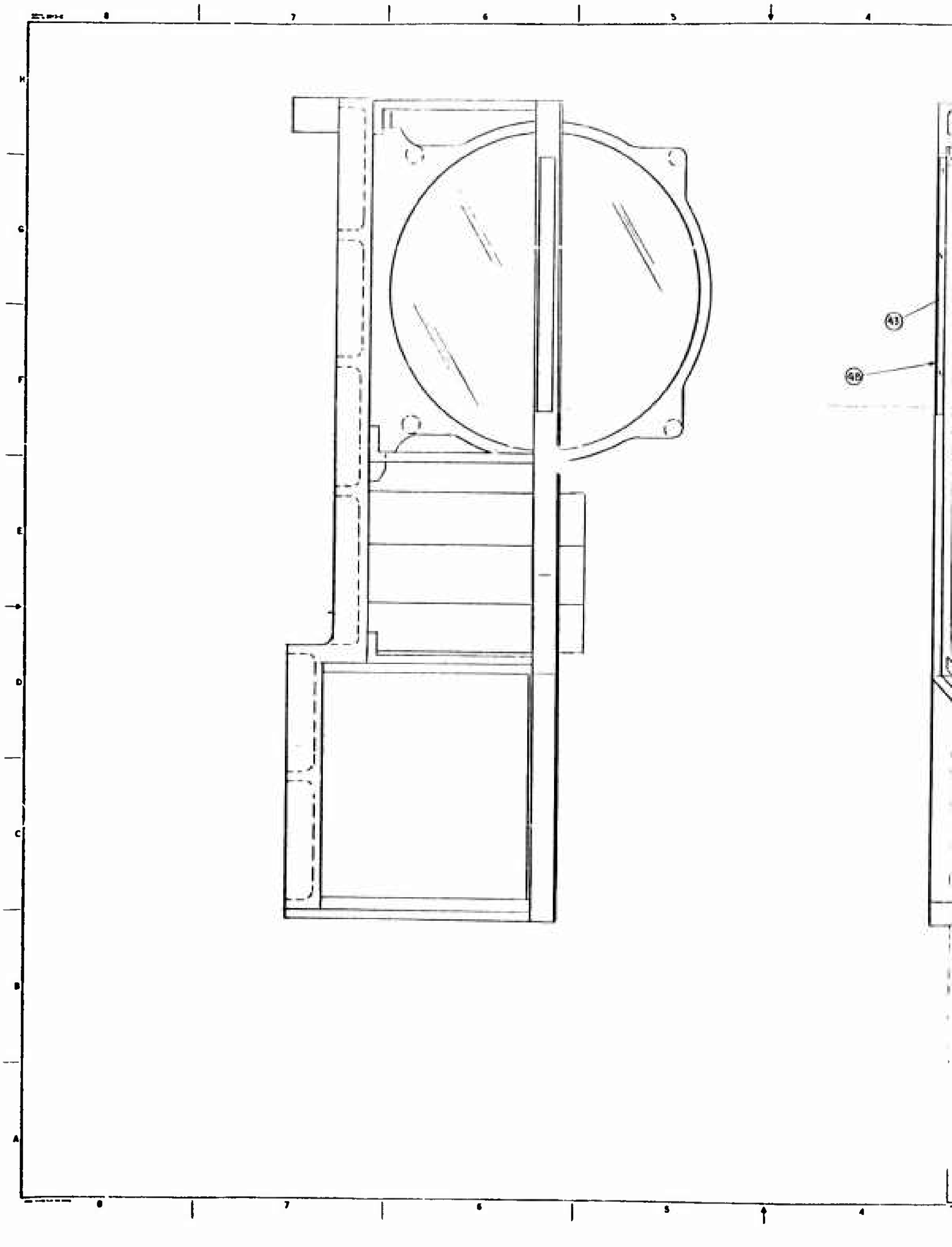

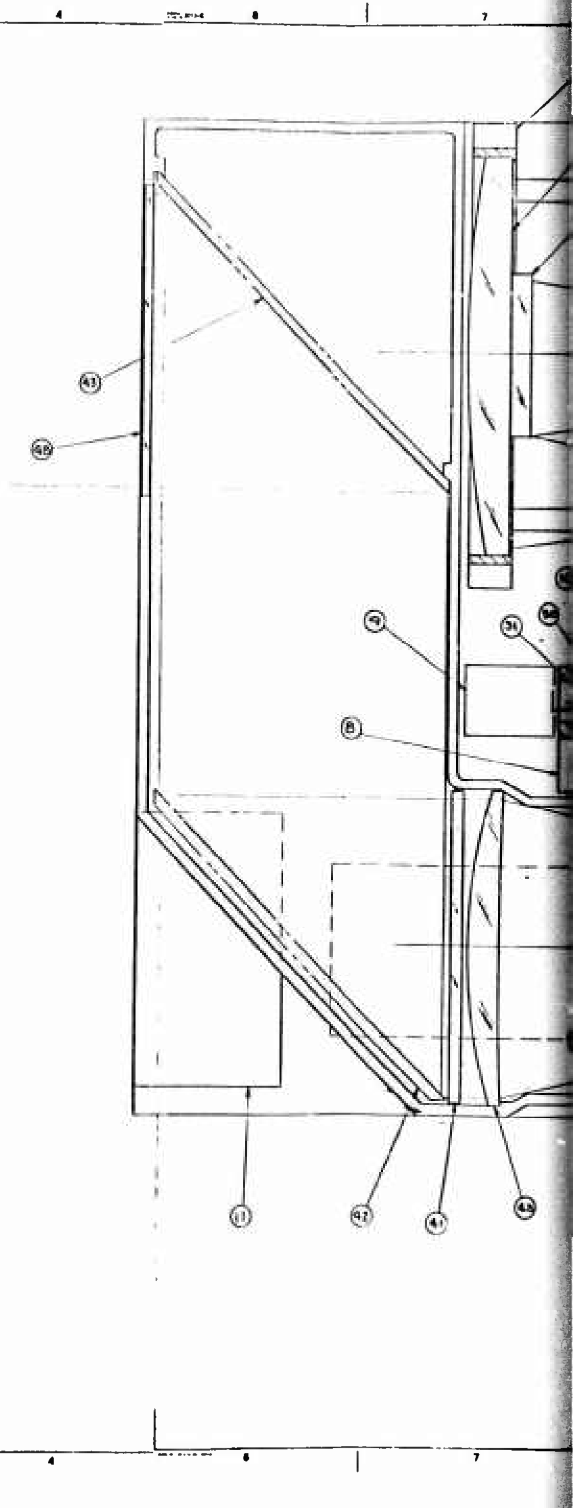

1

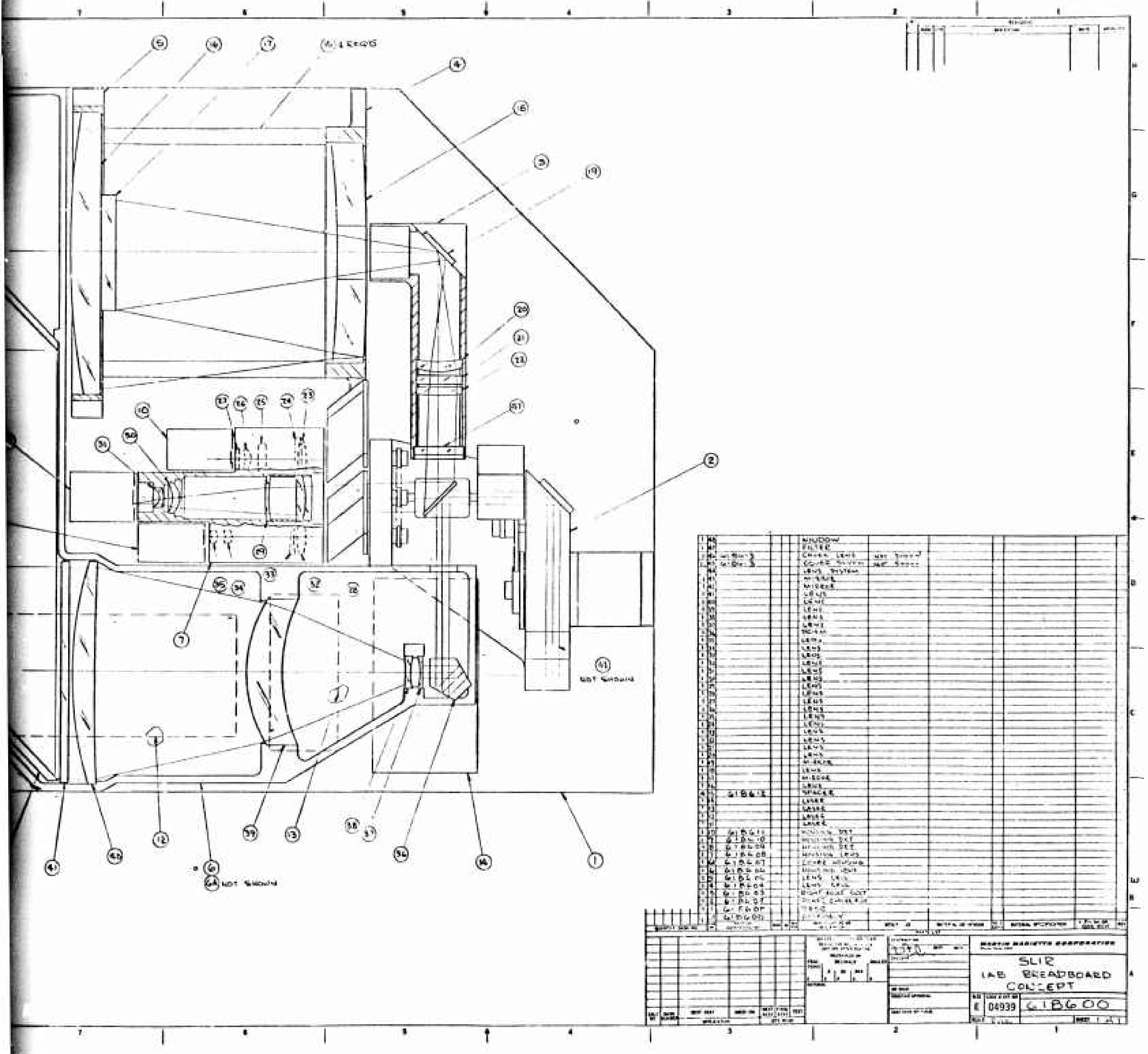

Figure 56. SLIR Laboratory Breadboard Layout

2

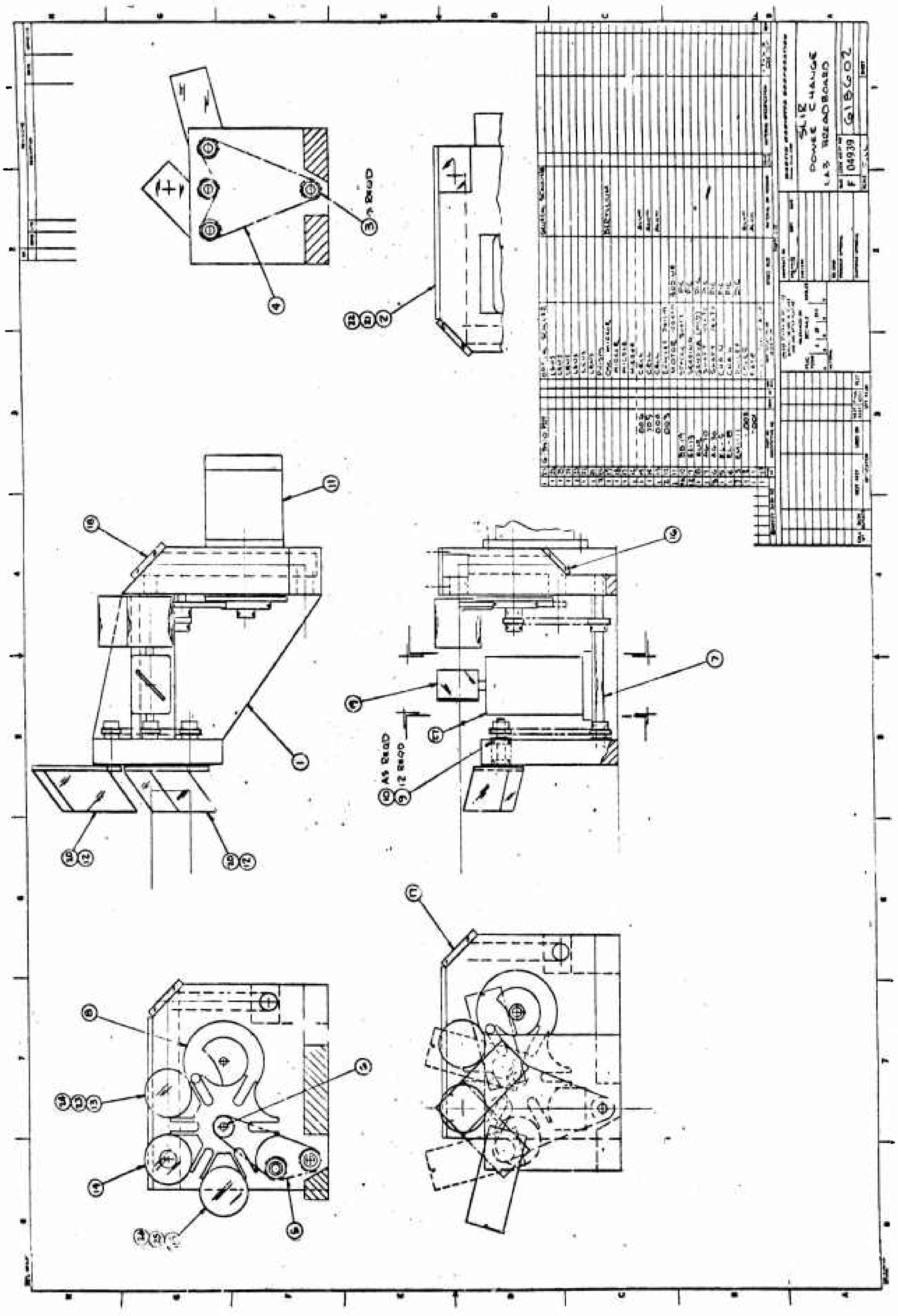

Figure 57. SLIR Breadboard Power Change Layout

### 5.1.1 Optics Design

As illustrated by the optical layout shown in Figure 58, a modular concept was adopted for the design of the SLIR optics. Each optical module was designed to be free of aberrations both by itself and when integrated with the rest of the system. This permits each module to be fabricated and tested independently. Any module which does not perform as it should can then be easily identified and corrected, thereby facilitating the assembly and preliminary testing of the entire optical train.

Laser Illuminator Optics. The transmitted laser energy must be shaped to match the fields of view of the receiver during the acquisition, track and precision track modes of operation. If the laser energy is undersized with respect to the receiver instantaneous field of view (IFOV), the scan pattern may be incomplete. On the other hand, if the scan pattern is spread significantly beyond the receiver IFOV, energy will be wasted and the effective acquisition range of the system will be reduced.

Beam shaping in the SLIR system is accomplished by means of sequential anamorphic lenses which exhibit optical power in one meridian only. This type of optical system will reduce beam divergence in the direction of scan to 80, 40, or 20 μradians (for acquisition, track, or precision track, respectively) while increasing beam divergence to 10, 5, or 2.5 milliradians in the ortho-scan direction.

A 10X anamorphic afocal telescope, which matches the 10X afocal of the receiver, forms the illuminator objective. The power of these afocals must be precisely matched to assure the angular scan motion of the scan mirror yields the same field angle in object space for both the illuminator and receiver. The receiver telescope is a Newtonian telescope which forms a real intermediate image, while the illuminator telescope is of a Galilean form. The Newtonial form is favored for the receiver because it forms a real exit pupil which can be made coincident with the scan mirror, thereby minimizing its size. A Galilean form, however, is desirable in the illuminator path so as to avoid focusing of the high power laser beam. Since the receiver telescope inverts the image but the illuminator telescope does not, an additional inversion is required to

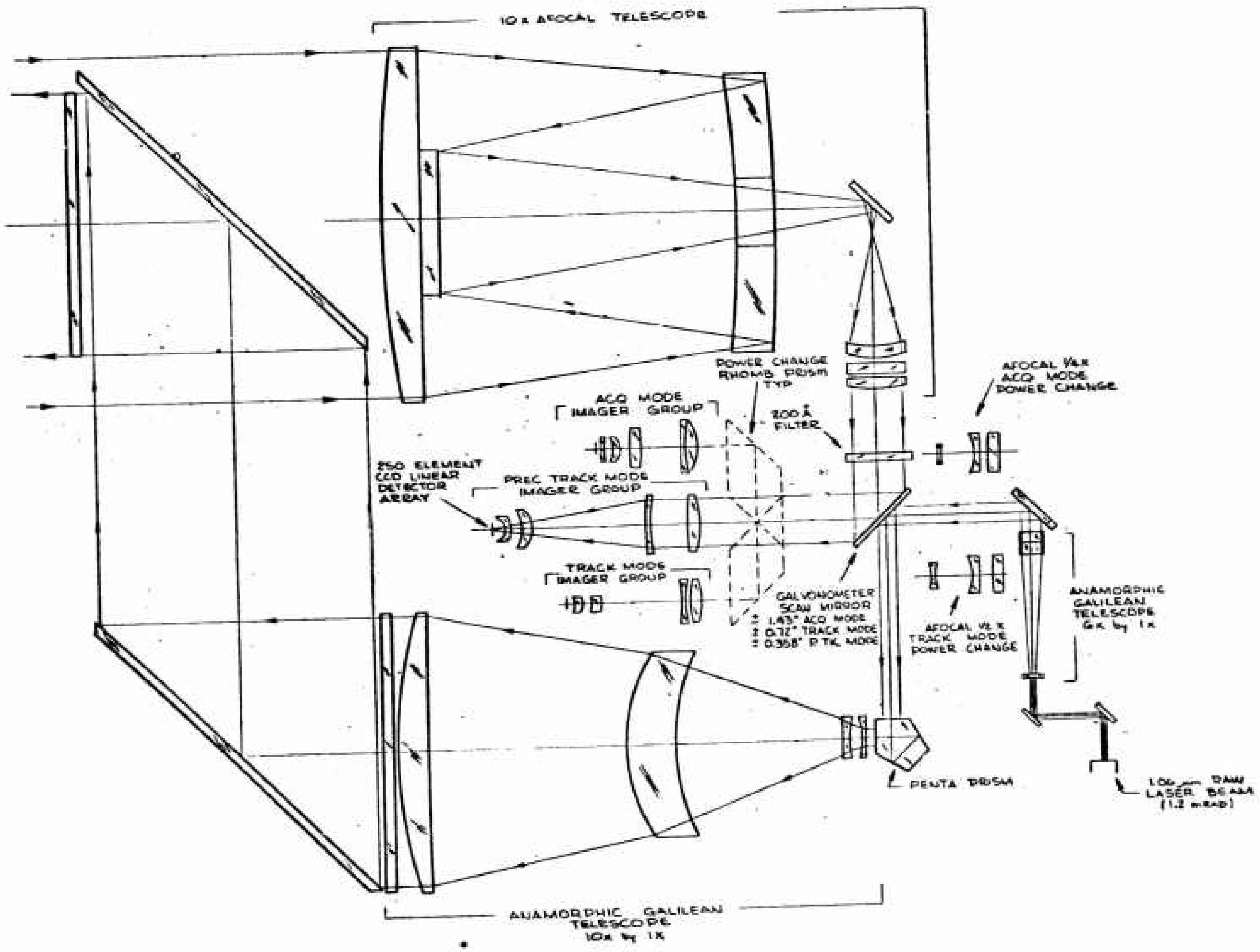

Figure 58. SLIR Laboratory Breadboard Optical Layout

make the scan patterns of the transmitter and receiver coincident. This is accomplished by use of a penta prism in the laser path, as shown in Figure 58. The direct laser path, which has no moving parts, provides the precision track mode illumination beam. A total of 60X in the scan direction is provided by combining two anamorphic telescopes, a 6X Galilean before and a 10X Galilean after the scan mirror. A 0.4X anamorphic Galilean is placed out front to provide the 2.5 milliradian beam divergence in the ortho-scan direction. A power change to provide the required track and acquisition mode beam divergence is accomplished by inserting 1/2X or 1/4X reverse Galilean telescopes, as shown in Figure 58, prior to the scan mirror. These reverse Galileans are of circular (not anamorphic) design so that the power change is accomplished in both meridians simultaneously.

Receiver Optics. The receiver optics consist of a catadioptric objective, a three-element collimating lens (or eyepiece), the scan mirror, and three imaging lens groups. The catadioptric is an f/3.3, 9" diameter lens which serves to collect the reflected laser energy from the target. The folded geometry of this objective yields a relatively compact system in comparison with a refractive lens of the same diameter and focal length. A similar refractive design would be 25 to 30 inches in physical length resulting in a very long and unattractive package. Conversely, the overall length of the catadioptric lens is only 13 inches (from front vertex to focal plane).

The objective is followed by a 3-element collimating lens system. The combination of the catadioptric objective and this eyepiece forms a 10X afocal telescope. The Newtonian form of this combination places the image of the aperture at the scan mirror, thereby minimizing the size of the mirror required.

The focal lengths of the imaging optics following the scan mirror are determined by the required system fields of view and the size of the detector elements. 5", 2.5" and 1.25" EFL imaging lenses, whem combined with the 10X afocal, yield 50", 25" and 12.5" overall system EFL for the precision track, track, and acquisition modes of operation, respectively. The high system resolution required during target tracking dictates that moving components not be used in the precision track mode optical path.

All components for this narrow field of view are, therefore, of stationary design. Power change for the track and acquisition modes of operation is accomplished by interposing rhomboid prisms after the scan mirror, as shown in Figure 58, to separate track and acquisition imaging lens groups. Since each imaging lens group may be designed independently, the performance of each may be easily tailored to optimize the overall performance of the entire optical train for each mode of operation. Computer calculations of the expected MTF of the three optical paths are shown in Figure 59. Note that the expected performance is nearly diffraction-limited for all three modes with little off-axis degradation. The MTF at 20 line pairs/mm is also plotted for each receiver path as a function of focal position in Figure 60. It can be seen that the focal plane is flat and that a reasonable depth of focus is available with each mode. It should be noted that the full 9" collecting aperture is used for each of the three operational modes to maximize system signal-to-noise ratio performance. The f/number of the receiver optics then changes with the field of view and the depth of focus is, therefore, greatest during precision track where the f/number is largest (about ± .01" at f/5.6).

A target that moves to within 700 meters range, however, will shift the focus 0.090" behind the detector focal plane. It will, therefore, be necessary to provide active focusing capability for the tactical system. Sliding glass wedges that move at right angles to the optical axis and are placed near the image, can be used to effect this focusing function because they behave like a variable thickness flat plate and do little to upset boresight alignment. The change in the optical path length provided by these wedges shifts the focal position with range to always keep the target in sharp focus. These focusing wedges have been omitted from the breadboard design since they increase both the cost and complexity of the system and are necessary only at very short range. The feasibility of the SLIR concept can be adequately demonstrated in spite of their omission.

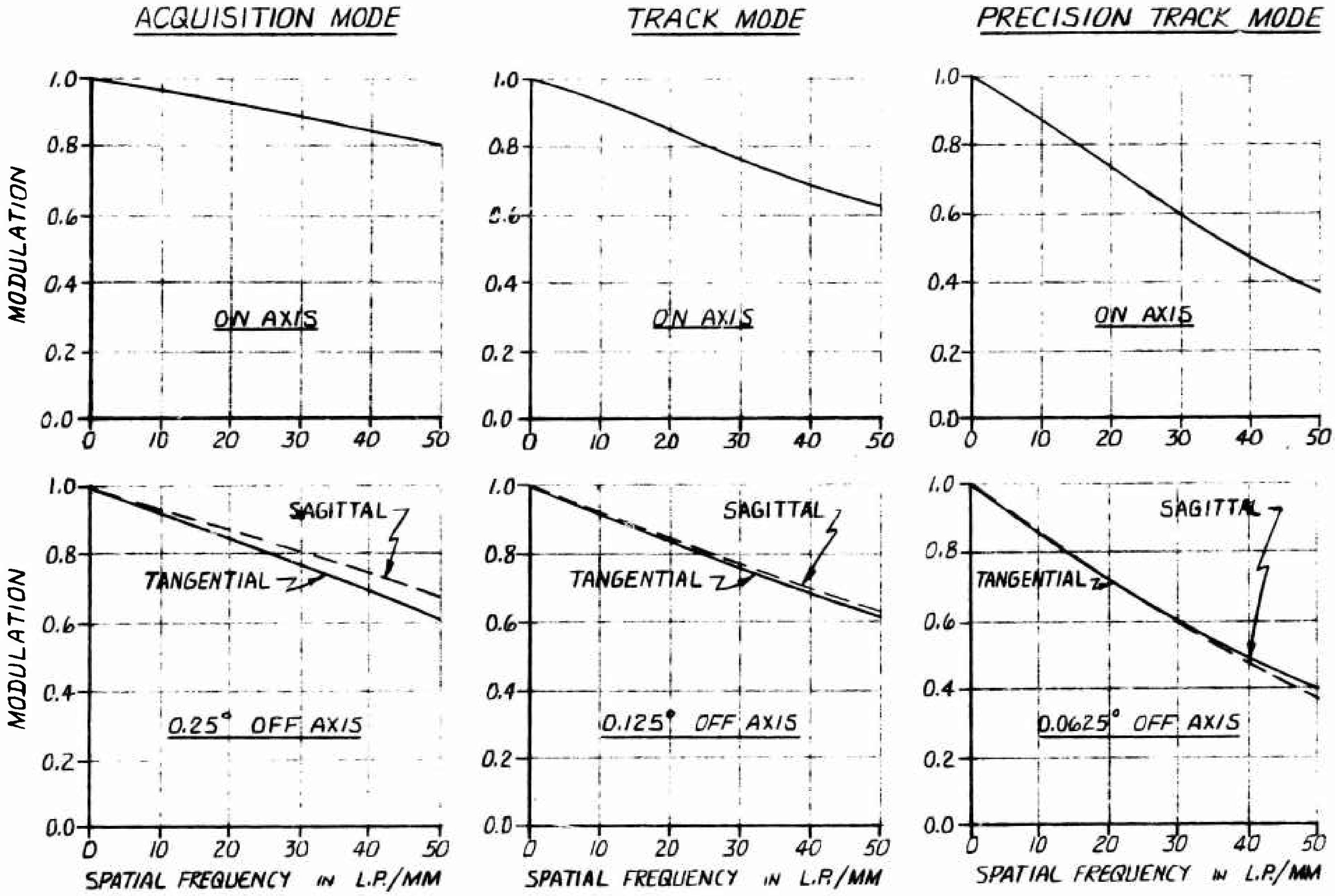

Figure 59. SLIR Laboratory Breadboard Receiver MTF

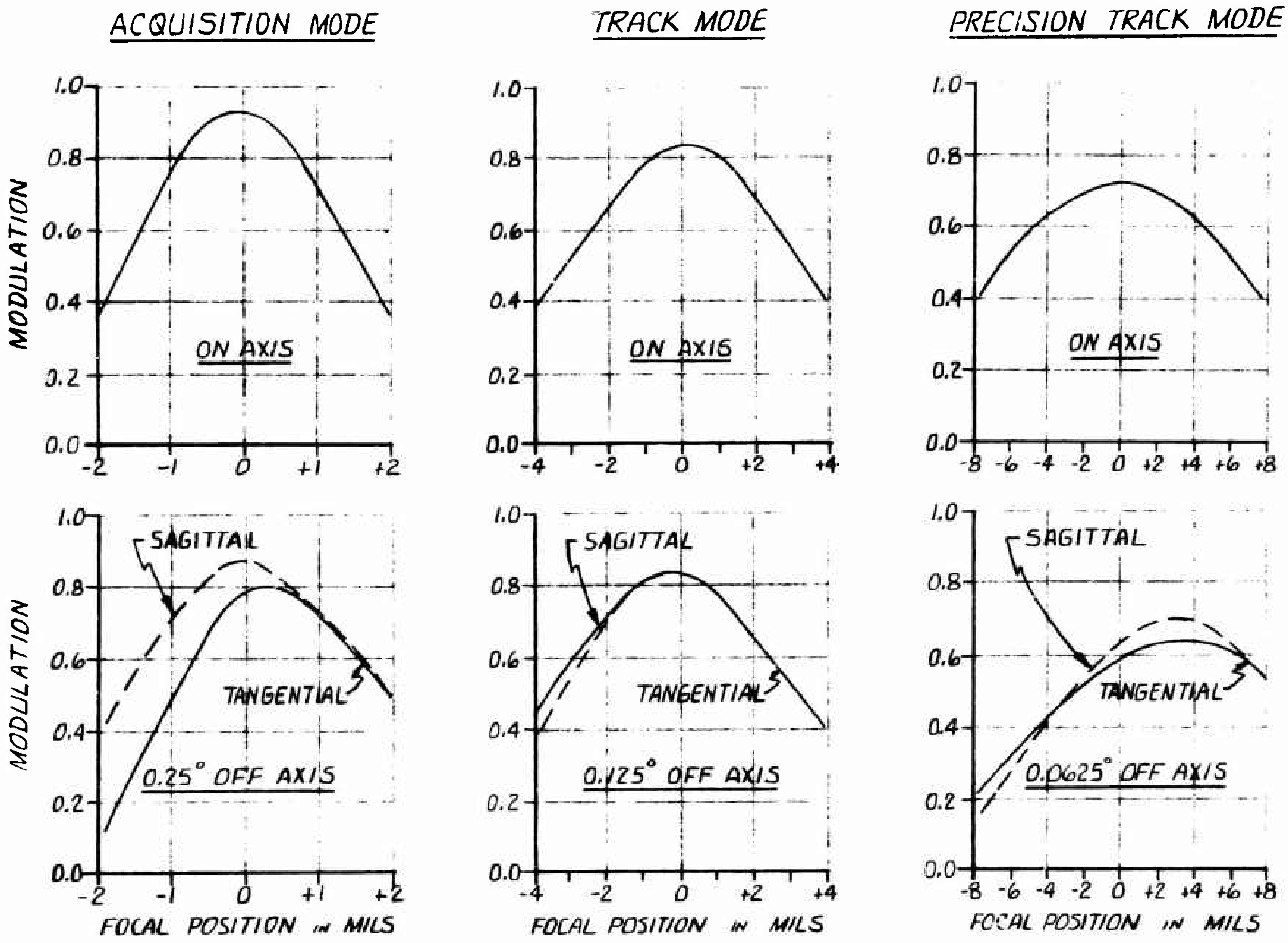

Figure 60. Receiver Focal Position Sensitivity (MTF = 20 l.p./mm)

### 5.1.2 Expected Laboratory Breadboard Performance

The two primary performance factors for a SLIR system are range capability and the quality of the tracking information obtained from the scene. Since the effect of SLIR scene data on tracking performance can be fully evaluated only from a detailed analysis of the tracker system, this factor has been assessed in a general way by deriving modulation transfer functions (MTF's). Since these MTF's (shown in section 4.2) show adequate resolution and good spatial response, it would appear that sufficient track information is available from the SLIR system provided that receiver signal-to-noise (S/N) is adequate. Therefore, the most important parameter which can be examined here is range performance. Although acquisition ranges have been numerically specified, there has not been a detailed specification of the parameters which constitute acquisition or tracking - such as S/N or imaging characteristics. As mentioned previously, a precise derivation of such parameters requires detailed tracker analysis of a scope greater than all work accomplished for this report. Thus range capability is evaluated here for nominal S/N which is sufficient for acquisition in similar systems. S/N as a function or range is also calculated in a following sub-topic. It should be recognized that the S/N required for acquisition with a SLIR system is significantly lower than the S/N typically discussed for a FLIR because of the following factors: a 1.06 micron SLIR has approximately 10 times the scene resolution of an 8-12 micron FLIR of equal aperture, and long-range tracking need only be accurate enough to insure that the target is held approximately in the center of the total field-of-view.

The most important factors to be demonstrated by a near-term breakboard system are:

1. Optical performance in achieving the fanned laser illumination beam
2. Achievement of the mechanical scan
3. Evaluation of signal data in terms of sufficiency of scene information for tracking
4. Achievement of system sensitivity sufficient to meet range requirements.

While it is desirable to demonstrate all of these factors, some relaxation of requirement 4 would result in a simple sensor array which can presently be purchased commercially. This simple alternative is a variant of a recommended baseline system which meets requirement 4, and the other requirements. These considerations have resulted in examination of the following breadboard demonstrator options:

a A CCD sensor

b A PIN diode/CCD hybrid sensor (baseline system)

Since these options differ significantly only in the type of receiver sensor used, they are identified by sensor type.

CCD Sensor

Given the noise equivalent charge developed in sub-section 3.3.1 the noise equivalent energy (NEE) of a CCD photosensor is easily determined. Receiver NEE is:

$$NEE_r = \frac{1}{\tau_o \varepsilon} \sigma e \qquad (22)$$

where $\sigma_e$ is rms charge noise in electrons, $\tau_o$ is effective optical transmission, and $\varepsilon$ is quantum efficiency. $NEE_r$ is in photons/pulse. A 200 Å optical filter is assumed, giving overall $\tau_o = .5$. CCD quantum efficiency for 1.06 micron energy is typically considered to vary from 5 percent to 10 percent. However, quantum efficiency for point source illumination (which approximates the SLIR acquisition range case for the .01 $m^2$ optical cross-section) is less because of diffusion in the CCD structure. This occurs because some photoelectrons are generated deeply into the substrate and migrate to CCD sites adjacent to the site located at the original point of entry of the signal photon. Experimental results at Martin Marietta indicate that 1.06 micron point source quantum efficiency may be as low as 2 percent for a linear CCD. The above equation does not consider background noise or photoelectron generation noise. The background power discussed in Section 3.3.4 is not significant compared to CCD noise. Assuming Poisson statistics, generation noise will be dominated by CCD noise until high signal levels are reached. These parameters give: $NEE_r = 100\ \sigma_e$.

Thus CCD sensor $NEE_r$ for 1.06 micron varies from 3000 to 10000 photons for the $30 \leq \sigma_e \leq 100$ rms electrons derived in subsection 3.3.1. From the range equations and computer program discussed in section 4.1, a number of range performance plots have been run and are illustrated in Figure 61 through 67. Runs 5-1 through 5-7 assume 15W laser power at a 20 hZ (5000 PRF) acquisition frame rate, from a 1.06 micron laser of 20W nominal average power. All distances are in meters. Runs 5-1 and 5-2 are for the 100 $cm^2$ unresolved cross-section target, for $NEE_r = 3000$ and 10000 respectively. Depending on the real physical size of this target, it will be resolved at some range point on the order of 1 or 2 kilometers. For this and closer ranges, the resolved target plots apply. Run 5-3 repeats run 5-1 parameters for $S/N = 10$. Runs 5-4, 5, and 6 repeat the sequence of the first three for a resolved target of .2 reflectivity. Run 5-7 is included to show performance for a high reflectivity target. The same CCD quantum efficiency is assumed for an extended resolved target, although the loss in quantum efficiency due to diffusion is not as great as for a small point source target. These plots indicate probable acquisition and reasonable S/N performance at ranges of several km, even at sea level.

In considering a CCD sensor, a laser operating at a visible wavelength is a very attractive candidate because of the improved quantum efficiency, allowing good receiver sensitivity with a simple and inexpensive sensor. Although there has not been sufficient study of all applicable parameters, it appears that the green copper vapor laser merits some consideration. Assuming 30 percent quantum efficiency at .51 micron, receiver NEE for a copper vapor laser is approximately 400 photons/pulse.

### PIN/CCD Hybrid Sensor

The PIN hybrid is an appealing breadboard sensor candidate because it allows good range performance while being a high confidence approach. It is also inexpensive relative to the development of an exotic sensor array which can give only slightly more range at a given S/N. PIN diode arrays of this type are presently designed and fabricated in-house at Martin Marietta. Section 6.0 will address

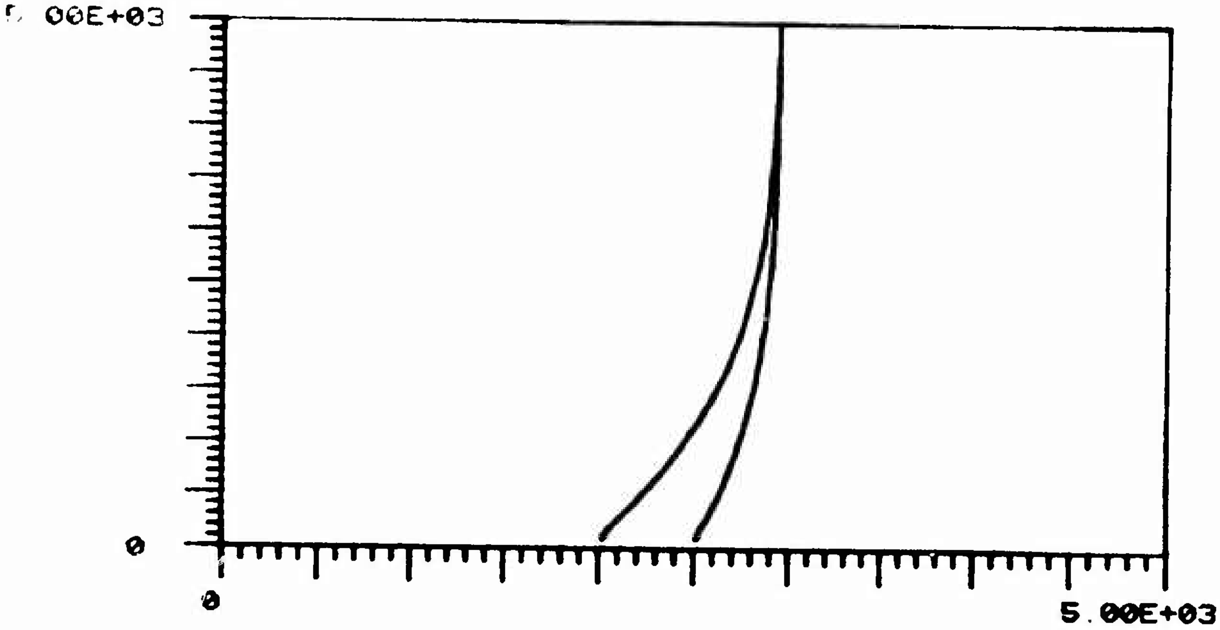

**ALTITUDE VS RANGE FOR FIXED VISIBILITIES**

CURVES FOR 5.00E+03 & 2.00E+04 METER VISIBILITY

PARAMETERS: AVG LASER POWER (W) = 15.0
SIGNAL-TO-NOISE = 3.0
RECEIVER NEE (PHOTONS/PULSE) = 3000.0
FRAME RATE (HZ) = 20.
250 ELEMENT ARRAY OF 40. URAD IFOV

TARGET CROSS-SECTION = 0.010 SQ M

Figure 61. Run 5-1

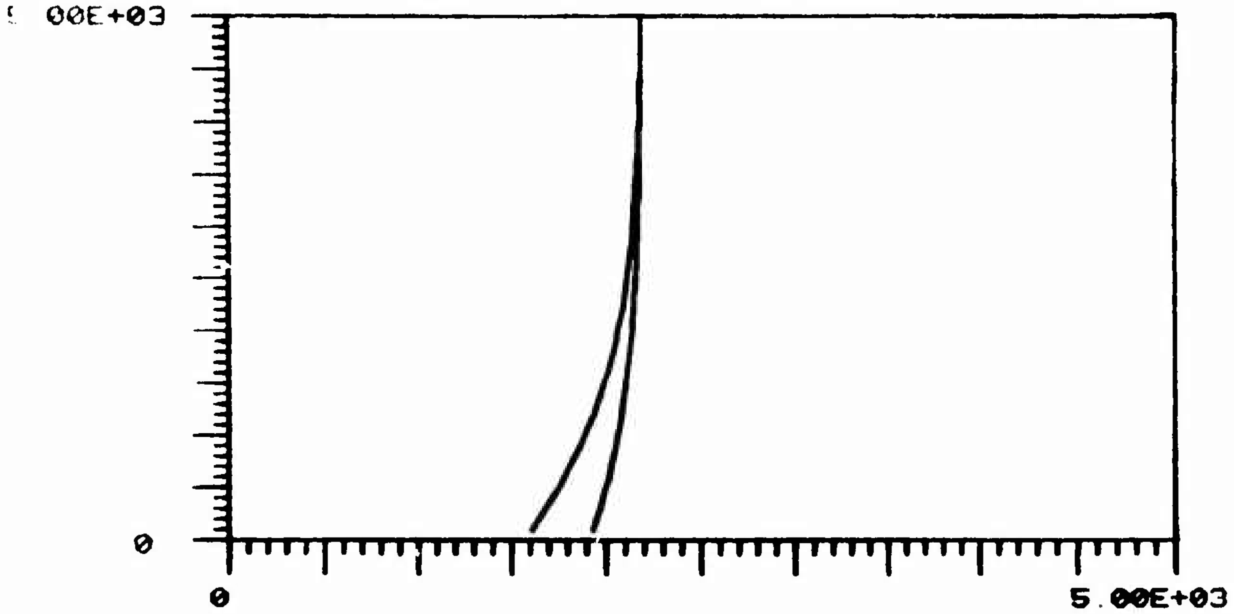

ALTITUDE VS RANGE FOR FIXED VISIBILITIES

CURVES FOR 5.00E+03 & 2.00E+04 METER VISIBILITY

PARAMETERS: AVG LASER POWER (W) = 15.0
SIGNAL-TO-NOISE = 3.0
RECEIVER NEE (PHOTONS/PULSE) = 10000.0
FRAME RATE (HZ) = 20.
250 ELEMENT ARRAY OF 40. URAD IFOV

TARGET CROSS-SECTION = 0.010 SQ M

Figure 62. Run 5-2

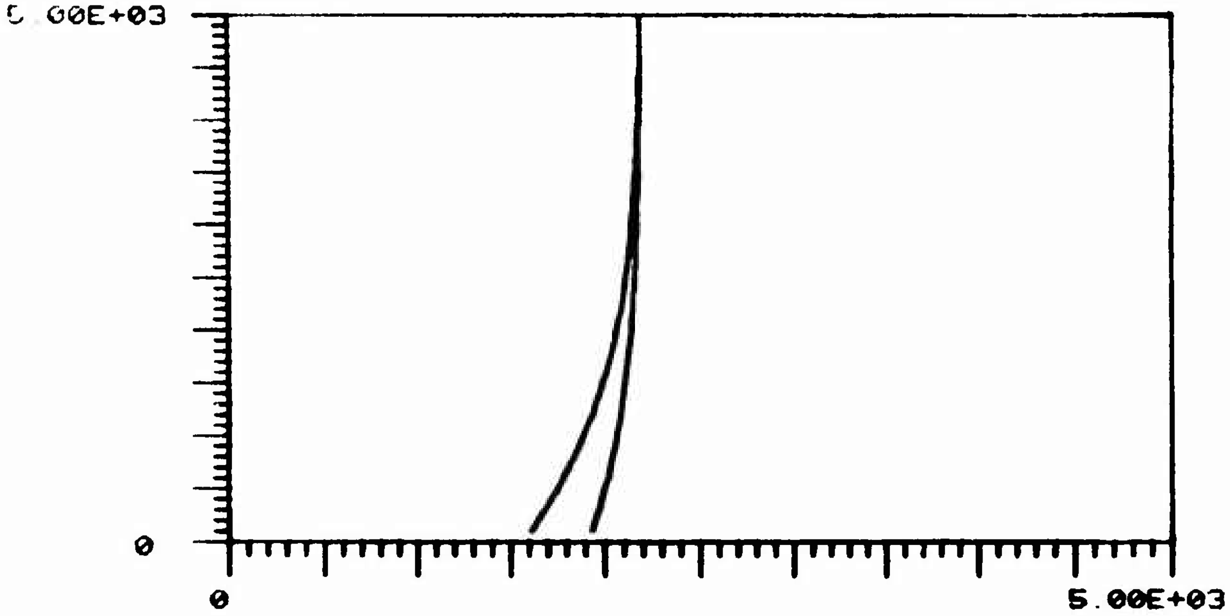

ALTITUDE VS RANGE FOR FIXED VISIBILITIES

CURVES FOR 5.00E+03 & 2.00E+04 METER VISIBILITY

PARAMETERS AVG LASER POWER (W) = 15.0
SIGNAL-TO-NOISE = 10.0
RECEIVER NEE (PHOTONS/PULSE) = 3000.0
FRAME RATE (HZ) = 20.
250 ELEMENT ARRAY OF 40. URAD IFOV

TARGET CROSS-SECTION = 0.010 SQ M

Figure 63. Run 5-3

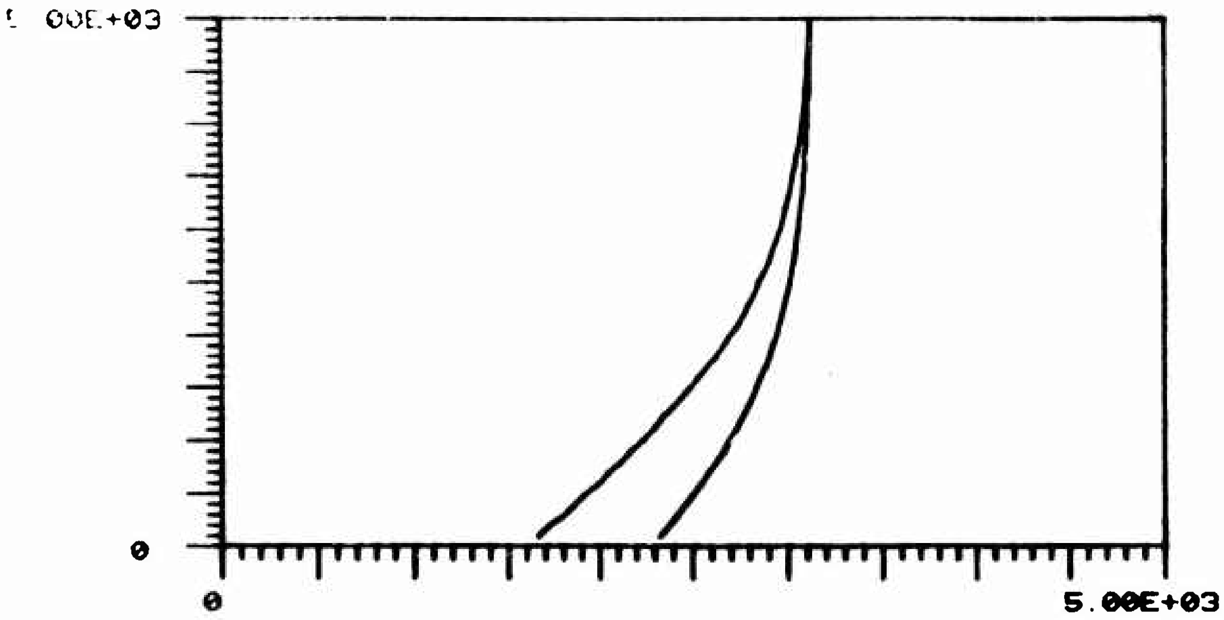

ALTITUDE VS RANGE FOR FIXED VISIBILITIES

CURVES FOR 5.00E+03 & 2.00E+04 METER VISIBILITY

PARAMETERS: AVG LASER POWER (W) = 15.0
SIGNAL-TO-NOISE = 3.0
RECEIVER NEE (PHOTONS/PULSE) = 3000.0
FRAME RATE (HZ) = 20.
250 ELEMENT ARRAY OF 40. URAD IFOV

RESOLVED TARGET OF REFLECTIVITY = 0.20

Figure 64. Run 5-4

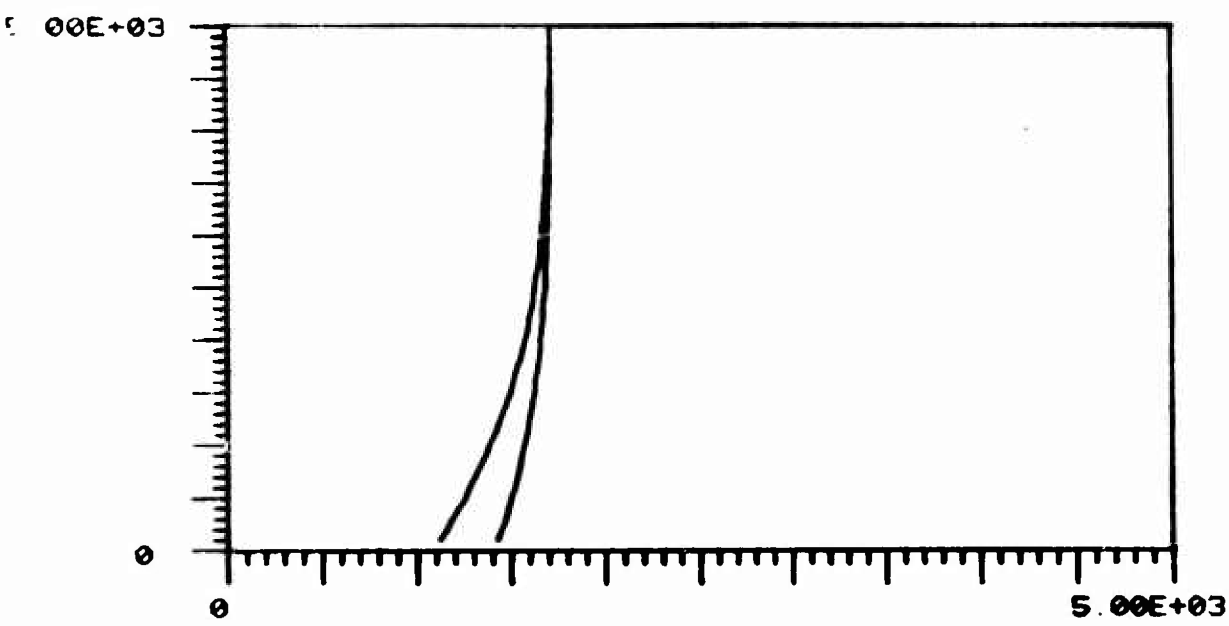

ALTITUDE VS RANGE FOR FIXED VISIBILITIES

```
CURVES FOR  5.00E+03 &  2.00E+04 METER VISIBILITY

PARAMETERS: AVG LASER POWER (W) =    15.0
            SIGNAL-TO-NOISE   =       3.0
            RECEIVER NEE (PHOTONS/PULSE) = 10000.0
            FRAME RATE (HZ)   =      20.
            250  ELEMENT ARRAY OF 40.  URAD IFOV

RESOLVED TARGET OF REFLECTIVITY = 0.20
```

Figure 65. Run 5-5

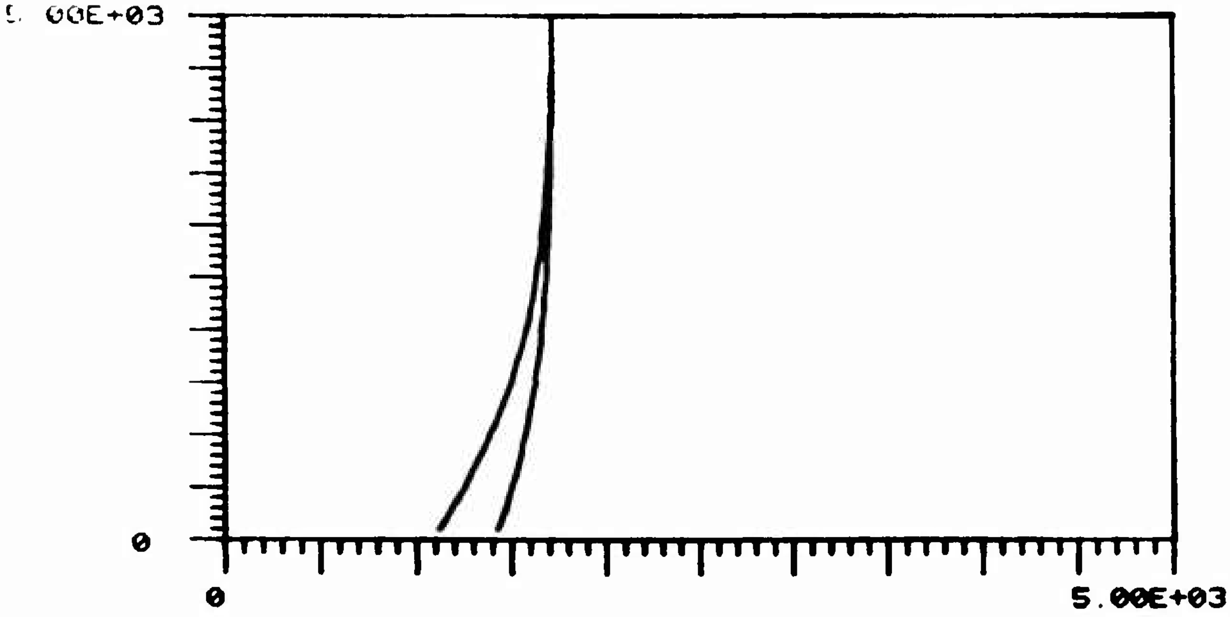

ALTITUDE VS RANGE FOR FIXED VISIBILITIES

CURVES FOR 5.00E+03 & 2.00E+04 METER VISIBILITY

PARAMETERS: AVG LASER POWER (W) = 15.0
SIGNAL-TO-NOISE = 10.0
RECEIVER NEE (PHOTONS/PULSE) = 3000.0
FRAME RATE (HZ) = 20.
250 ELEMENT ARRAY OF 40. URAD IFOV

RESOLVED TARGET OF REFLECTIVITY = 0.20

Figure 66. Run 5-6

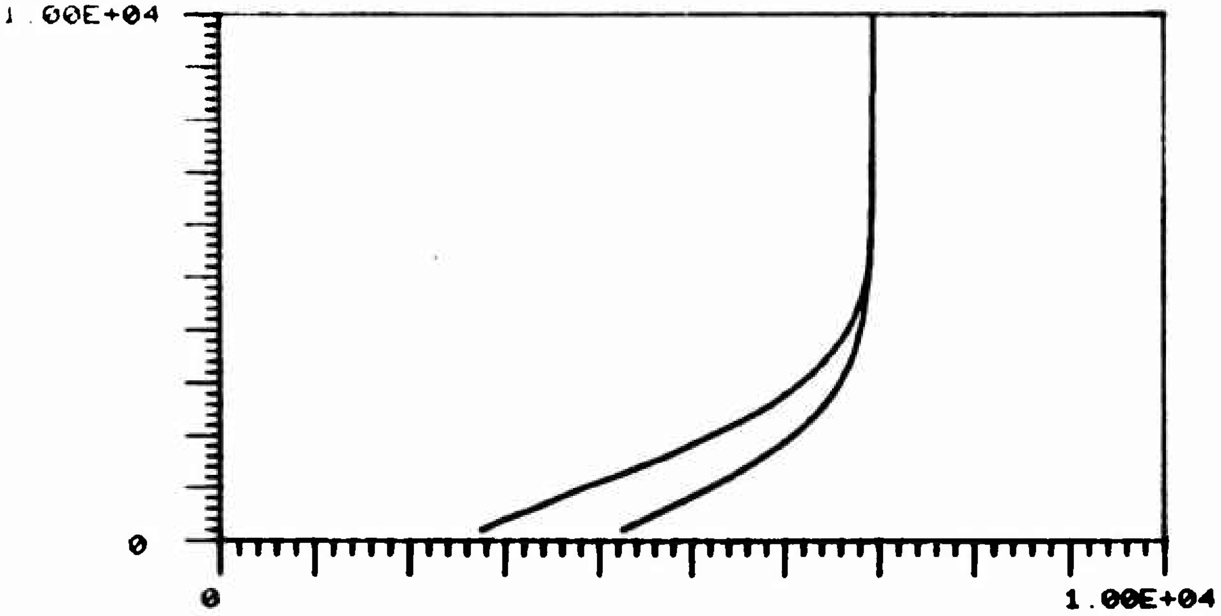

```
ALTITUDE_VS_RANGE_FOR_FIXED_VISIBILITIES
~~~~~~~~~~~~~~~~~~~~~~~~~~~~~~~~~~~~~~~~

CURVES FOR  5.00E+03 &  2.00E+04 METER VISIBILITY

PARAMETERS: AVG LASER POWER (W) =    15.0
            SIGNAL-TO-NOISE    =      3.0
            RECEIVER NEE (PHOTONS/PULSE) =  3000.0
            FRAME RATE (HZ)  =        20.
            250  ELEMENT ARRAY OF 40.  URAD IFOV

RESOLVED TARGET OF REFLECTIVITY = 1.00
```

Figure 67. Run 5-7

schedule and cost considerations for the fabrication of a PIN hybrid sensor. The work in Section 4.1 of this report has derived a PIN hybrid $NEE_r$ of about 300 photons at 1.06 micron. Section 4.1 contains range plots for the PIN sensor, but Runs 5-8 and 5-9 are shown here in Figure 68 and 69 for convenience. The 100W laser is used to give performance compatible with required range performance. Run 5-8 is for the small unresolved cross-section. This run shows a range of 8.4 km for altitude above 4 km, and range at sea level varying from about 4 to 6 km for 5 km to 20 km visibilities. Run 5-9 is for a resolved target of .2 reflectivity, and shows a range of over 24 km at moderate altitude.

S/N variation with target range is of interest for tracking purposes. Figure 70 shows S/N as a function of range (log-linear plot) for the PIN sensor and the two targets addressed by Runs 5-8 and 5-9. The figure assumes an average 100W laser power and takes increased signal shot noise into account as signal level increases. An acquisition PRF of 5000 hZ (20 hZ frame rate) is used at 10 km, and PRF is linearly increased as range decreases to 50000 hZ at 1 km. A 1 micro-second range gate and CCD noise of 30 rms electrons are used. An actual system might follow the curve of Figure 70 in steps if PRF is changed discretely rather than continuously. Since the curves cross at 2 km, the unresolved target would become resolved there if it and the resolved target have similar reflectivities. The figure is for unity atmospheric transmission, and so represents performance at 4 or 5 km altitude and higher.

Breadboard Options

As mentioned previously the PIN/CCD hybrid sensor is an attractive choice for a near-term breadboard. Both the PIN array and the 100W laser will require some fabrication time (discussed further in Section VI). Since it likely that the remaining SLIR hardware could be fabricated several months prior to procurement of the hybrid sensor and large laser, an interim system may be convenient and feasible. A CCD sensor with range-gating capabilities and a 20W 1.06 micron laser can both be purchased commercially at present. This could provide the SLIR performance shown for the CCD sensor in the preceeding sub-topic at low cost, until the procurement of the PIN hybrid and 100W laser.

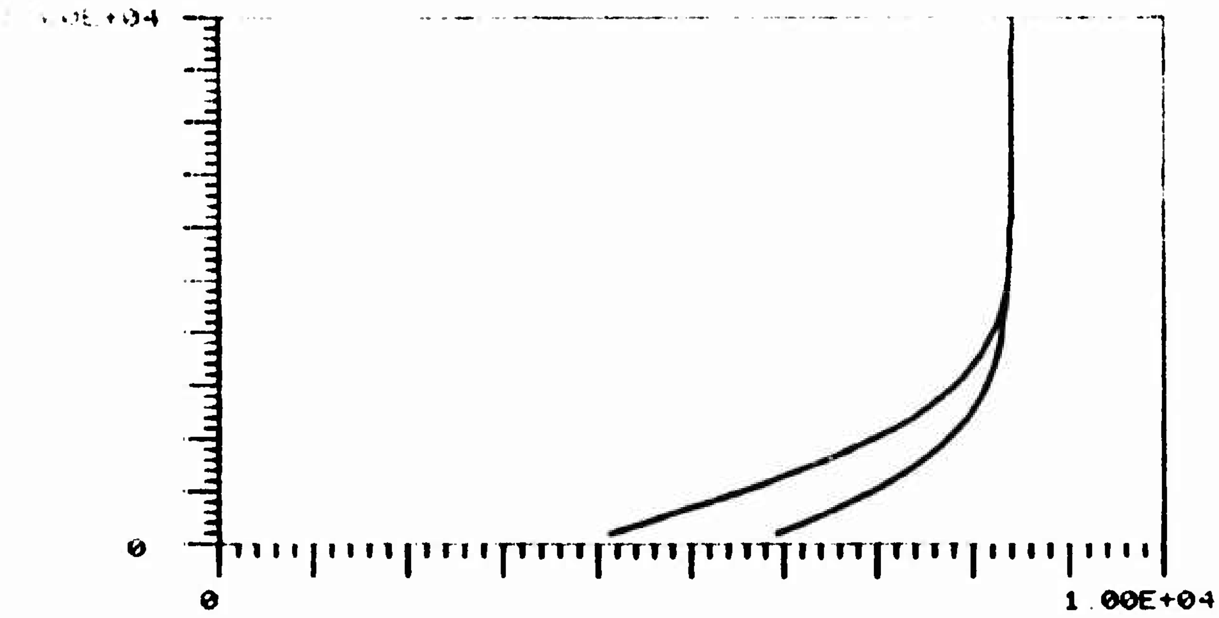

ALTITUDE VS RANGE FOR FIXED VISIBILITIES

CURVES FOR 5.00E+03 & 2.00E+04 METER VISIBILITY

PARAMETERS: AVG LASER POWER (W) = 100.0
SIGNAL-TO-NOISE = 3.0
RECEIVER NEE (PHOTONS/PULSE) = 300.0
FRAME RATE (HZ) = 20.
250 ELEMENT ARRAY OF 40. URAD IFOV

TARGET CROSS-SECTION = 0.010 SQ M

Figure 68. Run 5-8

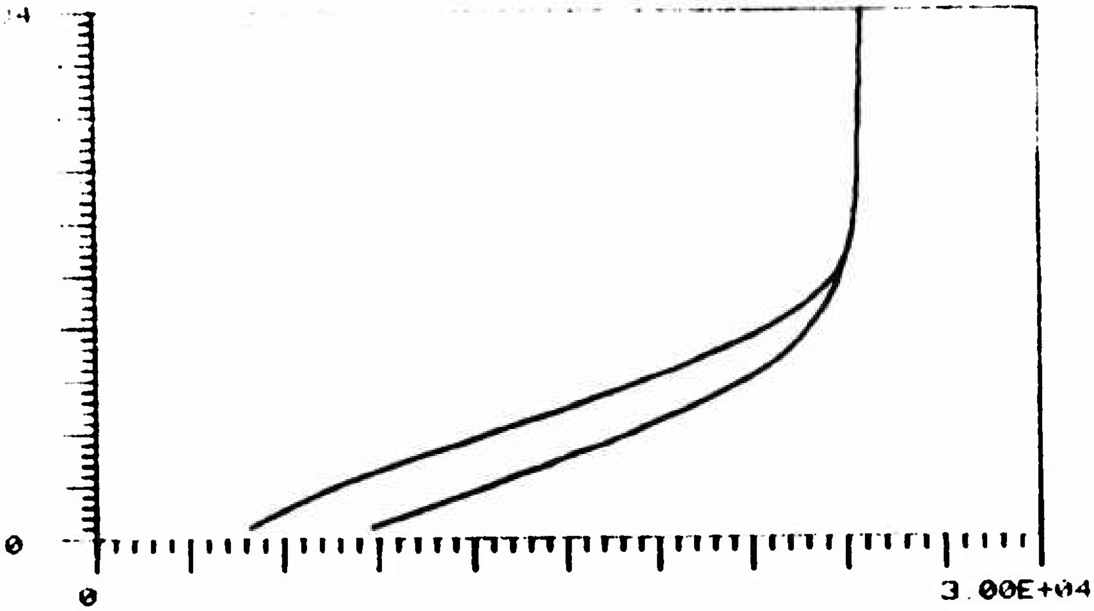

ALTITUDE VS RANGE FOR FIXED VISIBILITIES

CURVES FOR 5.00E+03 & 2.00E+04 METER VISIBILITY

PARAMETERS AVG LASER POWER (W) = 100.0
SIGNAL-TO-NOISE = 3.0
RECEIVER NEE (PHOTONS/PULSE) = 300.0
FRAME RATE (HZ) = 20.
250 ELEMENT ARRAY OF 40. URAD IFOV

RESOLVED TARGET OF REFLECTIVITY = 0.20

Figure 69. Run 5-9

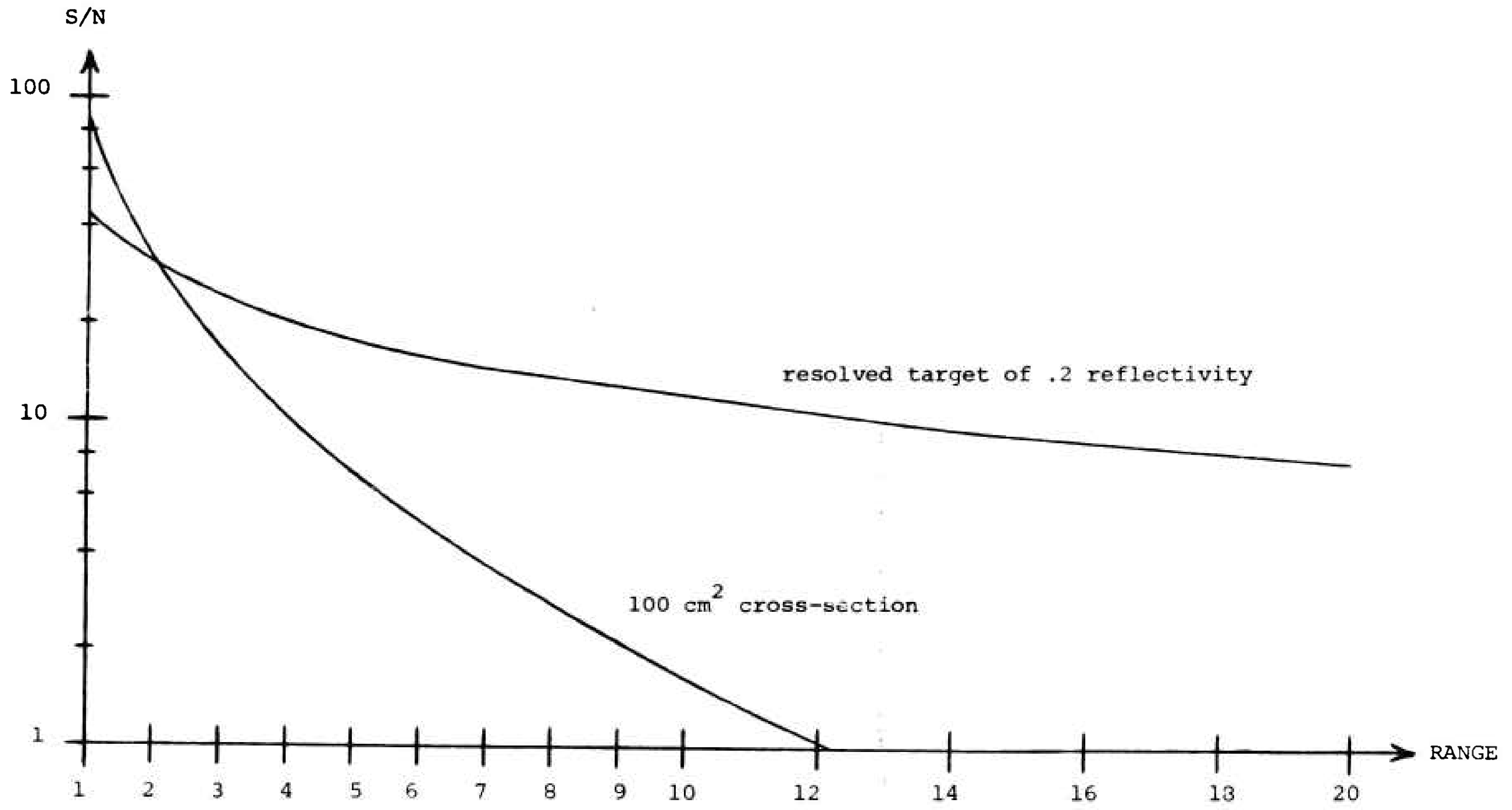

Figure 70. Signal-to-Noise as a Function of Range for SLIR System with Hybrid PIN/CCD Sensor

### 5.1.3 Electronic Circuitry

The SLIR electronics can be implemented with conventional circuitry using standard design techniques. There is perhaps some challenge in achieving a low-noise amplifier following the CCD of sufficient quality to give CCD noise equivalent to 100 or less rms electrons, but this is known to have been previously accomplished. For a presently available CCD photosensor, there are existing designs for signal transfer and amplification. For a specifically fabricated PIN/CCD hybrid sensor, CCD design parameters can be controlled to optimize noise performance.

Figure 71 is an overall block diagram of SLIR breadboard electronics. The SYNC GENERATOR performs system timing functions and receives range and PRF data as inputs. For constant-range testing, these can be switch-selectable. The SENSOR/CCD CONTROL is, in turn, controlled by the SYNC GENERATOR, and performs range-gating and signal transfer functions for the SENSOR/CCD detector unit. Detected signals are amplified and fed to the DISPLAY and RECORDING SUB-SYSTEM. This sub-system is explained further in Section 5.2. A SCAN GENERATOR, which is synchronized by the SYNC GENERATOR, gives input to the OPTICAL SCANNER CONTROL. The scanner sub-system is a purchased unit. The LASER SUB-SYSTEM is also purchased.

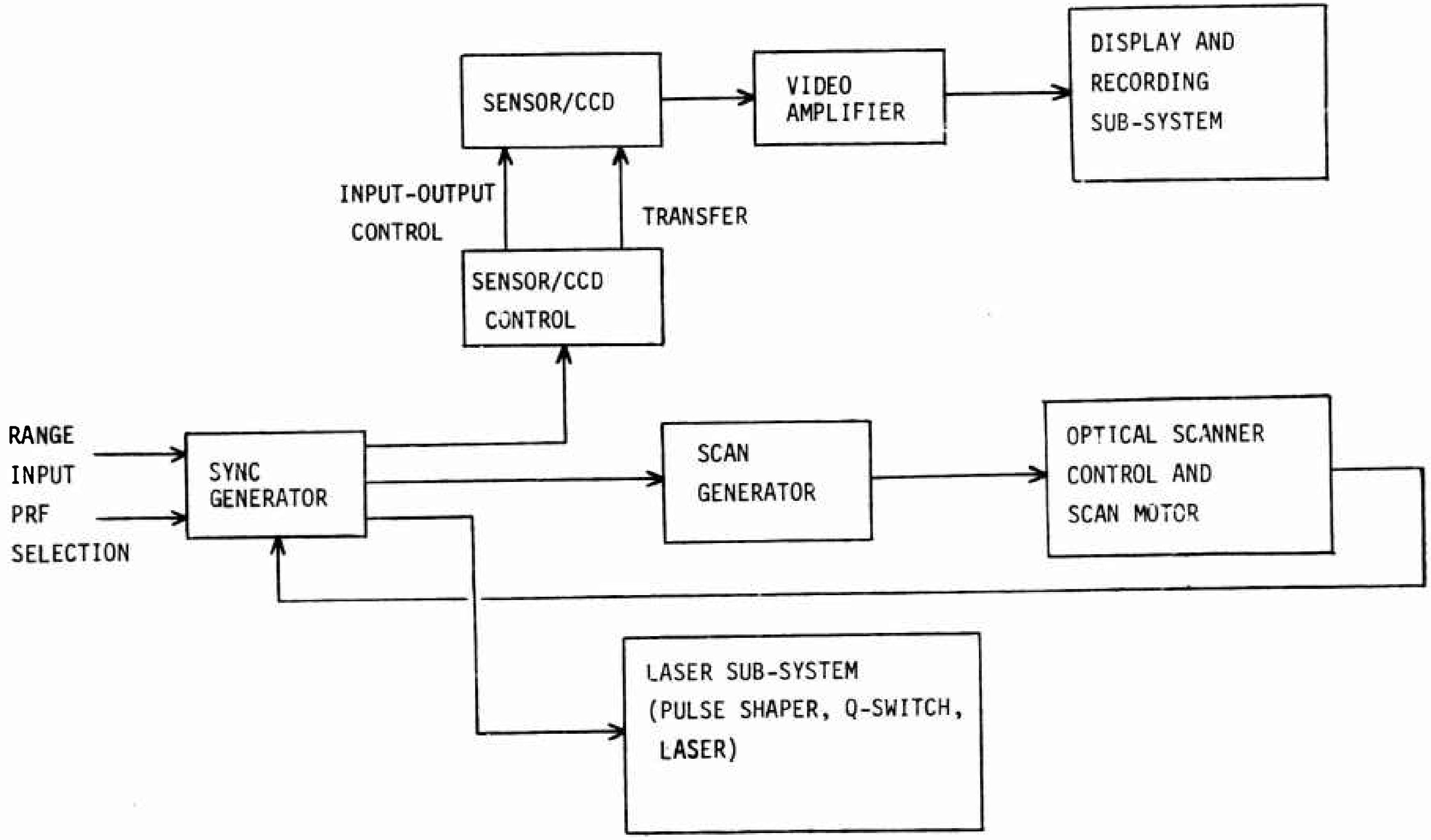

Figure 71. SLIR Overall Electronics Block Diagram

## 5.2 Display and Recorder Interface

The display and recorder interface is that portion of the system which provides a visual imaging display of the return signal and, in addition, provides a means of recording the information for later image reconstruction or analysis. The interface must condition the available signals so that imaging and recording can be achieved. The signals which are used are the video signal from the CCD driver board, a sync pulse from the same source which determines the beginning of a line scan, and a position signal from the mirror scanner.

### 5.2.1 Basic Interface Requirements

A design goal for the frame rates for this system is from 10 Hz to 150 Hz. The number of lines per frame will be 250 at the highest frame rate.

The horizontal scanning is accomplished by a mechanical scanner driving a mirror. Three choices of wave shape are readily available for the scanning. These are sinusoidal, sawtooth, and triangular.

A sinusoidal scan is the easiest to implement in terms of the scanner. Since a pure waveform (with no harmonics) is used, the only corrections necessary for variable frequency drive are amplitude and phase and if a position pickoff is used for the imaging reference instead of the drive, then phase corrections are automatic. In addition, if both left-going and right-going scans are used for image formation, scan efficiency is improved and the scanner frequency is one-half the frame rate. However, even if bi-directional scan is utilized, the scan efficiency of a sinusoidal scan is lower than a linear scan. This is because of the relatively long times spent at the ends of the scan. This also results in a non-uniform picture on the display since the dwell time at the edges is longer than at the center. Sinusoidal scan also requires a greater video bandwidth than a linear scan for the same frame rate because of the high scanning velocity at the center. If bi-directional scanning is used, it is necessary to introduce a correction due to time delays in the video processing. This delay results in a displacement of the left-going image with respect to the right-going image on the display. Since the delay is constant and the sweep is varying in velocity, this requires a non-linear correction which is difficult to achieve.

With a sawtooth scan, it is relatively simple to generate imagery but rather severe requirements are imposed on the scanner. No correction is required for left/right-going scans and scan efficiency can be quite high provided the retrace time is short.

Triangular scan offers a compromise between sinusoidal and sawtooth. For good scanning efficiency, both right-going and left-going scans may be used with the further advantage that the scanner frequency is one-half the frame rate. This requires a correction in the display for the video time delays but, since the scan is linear, this can be corrected for by incorporating a simple displacement of the left-going image with respect to the right-going image.

If an existing CCD is used (Fairchild CCILID 1728), the device will have only a single shift register, making it necessary to transfer and shift alternate detectors. The first transfer moves odd numbered detectors into the shift register. These are then clocked out, following which the even numbered detectors are then transferred and clocked. This requires two interlaced scan lines at the display for each line of optical data. Figure 72 shows the times available for a single half line.

This figure is based on a 150 Hertz frame rate. At 250 complete lines per frame, the half-line (125 detector elements) period will be $1.13 \times 10^{-5}$ seconds resulting in a clock rate of 11 MHz. The video bandwidth required is also 11 MHz. This clock and video rate can be halved, however, with a specifically designed hybrid CCD.

### 5.2.2 Display and Recorder Requirements

Display Requirements. The display should be of reasonable size so that image viewing can be done at comfortable viewing distance. The spot size must be sufficiently small so that a minimum of 250 lines can be resolved

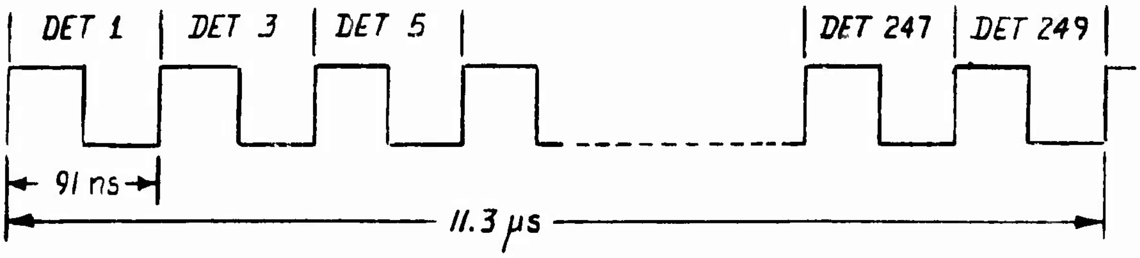

Figure 72. Timing Diagram for Single Half-line of Video Data

in both directions for a square format. The internal amplifiers must have sufficient bandwidth to operate the sweep and video signals. For the worst-case video, this requires a bandwidth of 11.0 MHz. For the horizontal sweep, a maximum frame rate of 150 Hz will be used. Since this is non-sinusoidal, low distortion will require at least ten times this response, or 1500 Hz. Similarly, the maximum vertical rate is 88.5 KHz and for low distortion, the response should extend to .9 MHz.

Recorder Requirements. The recorder should have a response from 10 Hz to 11.0 MHz. It should have at least two channels, one for video and one for voice and sweep information. A 10 KHz bandwidth is adequate for the voice channel. Ideally, it should take standard instrument or video tape.

A recorder with these specifications is very expensive, costing approximately $100K. A more inexpensive solution is to use a high quality standard video recorder. These have bandwidths out to 5 MHz, so that there could be some loss in fidelity for the worst-case clock rate if an existing CCD is used. If the CCD clock rate is changed with the frame rate so as to maintain 250 line resolution, then this loss will be confined to frame rates above 75 Hz for an existing CCD, 150 Hz for the hybrid CCD. For circuit simplicity this could be confined to two clock frequencies for an existing CCD: 5.5 MHz for frame rates from 10 Hz to 75 Hz and 11 MHz for frame rates from 75 Hz to 150 Hz. An additional limitation imposed by using a conventional TV-type recorder is that recording will only be possible for discrete frame rates which are multiples of standard TV frame rates. This is because the drive motors for these recorders are synchronized with the incoming frame rates and only a limited variation about standard rates is possible. Hence, recording could only be done at frame rates of 30, 60, 90, 120, and 150 Hz.

### 5.2.3 Interface, Display, and Recorder Design

The display chosen for this program is the Hewlett-Packard Model 1300A analog display. It has a screen size of 20.3 x 25.4 cm and a spot size of 0.8 mm. This gives a resolution of 254 lines in the narrowest dimension. The X, Y, and Z axis amplifiers all have bandwidths of dc to 20 MHz.

Two tape recorders have been selected as candidates for this program. The first is an IVC model 825A. This is a high quality video recorder with a video bandwidth of 5 MHz and two audio channels with bandwidths of 75 Hz to 10 KHz and 250 Hz to 7.5 KHz. This unit has a cost of approximately $7500.

The second is an RCA Adviser 152. This unit has four channels: a wide band video channel of 10 Hz to 15 MHz, a narrow band video channel of 10 Hz to 5 MHz, a data channel of 100 Hz to 20 KHz, and a second data channel of 600 Hz to 20 KHz. This recorder will handle serial information at these rates so that recording would not be limited to fixed frame rates. Its cost is approximately $100K.

A block diagram of the interface in the record and display mode is shown in Figure 73. In this configuration the video signal from the CCD driver is first amplified and, if necessary, filtered. The signal is then provided with brightness and contrast controls and fed into the display. The CCD driver also generates a line sync pulse which establishes each array scan. This is used to synchronize a sawtooth generator to provide the vertical sweep. This pulse is also combined with the video and the composite fed into the recorder.

The position signal from the scanner is amplified and then mixed with a square wave to produce the correct amount of displacement of the left-going with respect to right-going raster. This compensates for the left/right image displacement caused by the video processing delay. A sync pulse is also generated from the scan position signal and is mixed with the voice signal and then fed into the voice channel of the recorder. This pulse is also operated on by the sync conditioner which will provide a constant 30 Hz pulse rate output for inputs of 30, 60, 90, 120, and 150 Hz. This is necessary to provide a drive sync for the tape recorder.

This system is designed for use with the conventional (IVC-825A) tape recorder. With the Adviser 152 system which can handle straight line information not related to a particular format, the system would be essentially the same except for the elimination of the horizontal sync pulse conditioner.

Figure 74 shows the playback configuration. The sound channel output is passed through low and high pass filters to separate the horizontal sync and the audio information. The audio is amplified and fed to

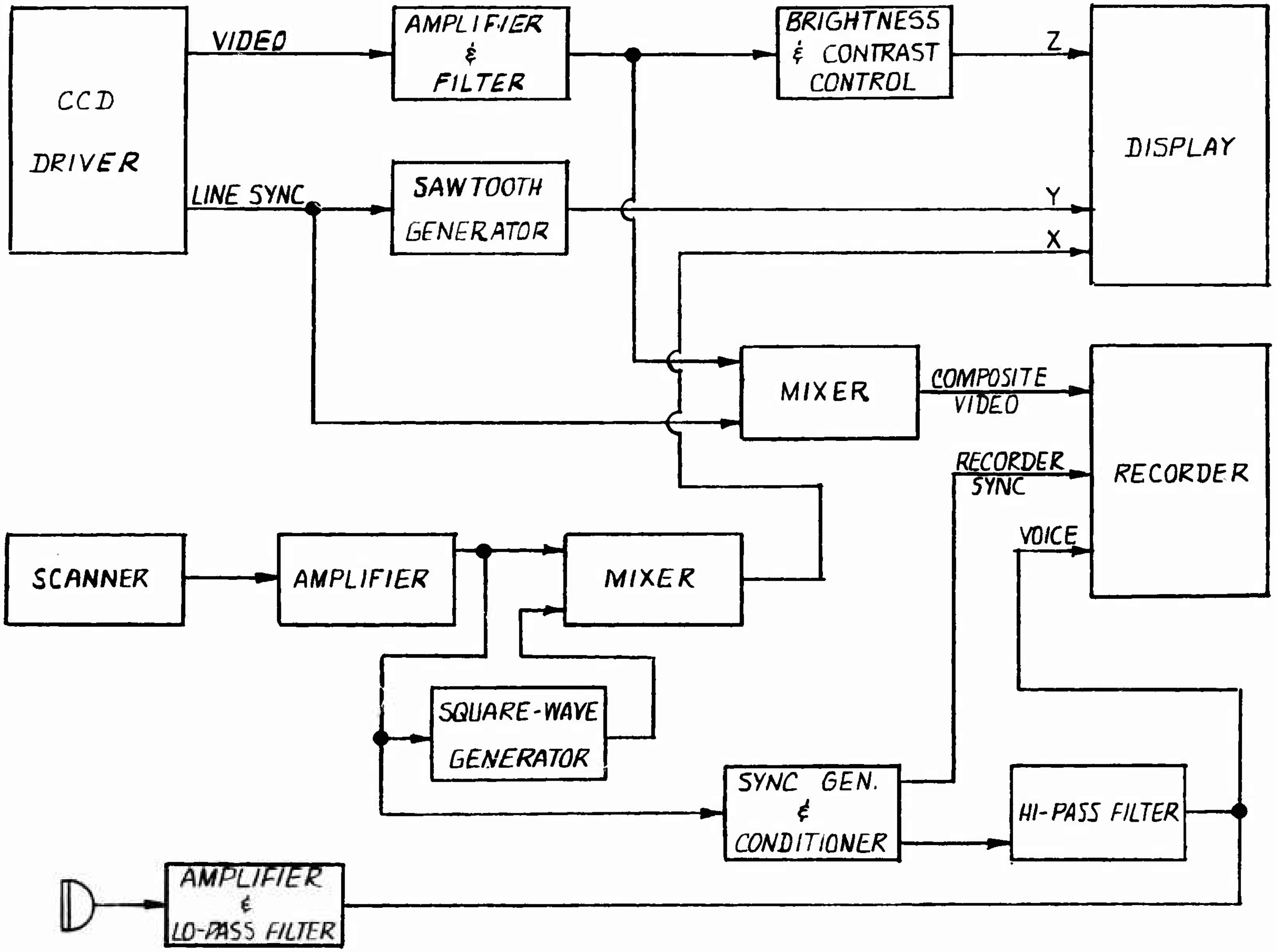

Figure 73. Display and Recorder Interface Block Diagram

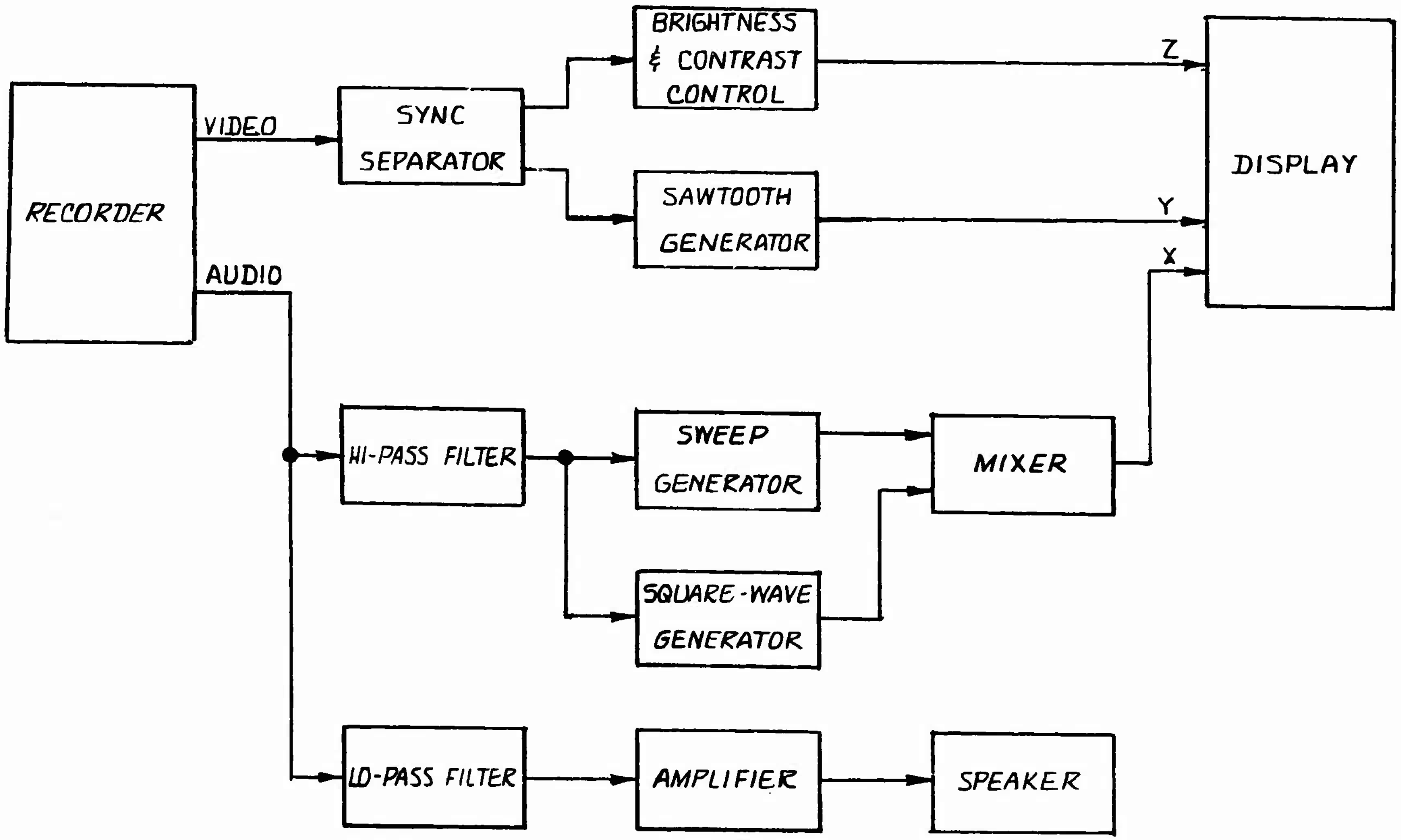

Figure 74. Recorder Playback Block Diagram

a speaker. The sync pulse is used to trigger a sweep generator. This is then mixed with a square wave to provide left/right compensation.

The video signal passes through a sync separator and then through brightness and contrast controls to the display. The sync pulse from the sync separator drives a sawtooth generator to provide the horizontal sweep for the display.

In both the record and playback modes, sweep and video signals can be available for further processing or analysis.

## SECTION VI

## SLIR DEVELOPMENT COST ESTIMATES

Preliminary cost estimates for design and fabrication of a SLIR breadboard system have been accomplished. Although there is no estimate available for a fully developed airborne system, the modular breadboard design accommodates a switch to an air-worthy brassboard without complete redesign and refabrication. The labor and material costs for most phases of breadboard construction are the results of detailed estimates, but costs for sensor array development and the large 100W laser remain approximate at present.

Development Plan. Figure 75 shows the development concept for the recommended baseline approach. The first three blocks along the centerline of the figure represent the detailed design, fabrication, and evaluation of a complete interim SLIR breadboard system. This interim system would use a commercially purchased CCD sensor and 20W laser, allowing system checkout and preliminary evaluation while a more advanced sensor and laser are developed in parallel. The investment in an interim sensor and laser is believed worthwhile because it allows testing before delivery of the advanced components, and does so at very little cost relative to total system cost. Parallel development of both items is expected to take about one year, while the interim system can be produced in 9 months. The cost for a CCD sensor is $10,000 (a minimum of two CCDs at $5,000 each must be purchased), and the 20W laser subsystem can be purchased for $17,900. These costs amount to about 4 per cent of the total expense for the baseline system.

The upper and lower blocks in Figure 75 illustrate parallel development of the PIN diode/CCD sensor hybrid and the 100W laser. Although a detailed cost analysis for procurement of this large laser has not been completed, a preliminary vendor estimate of $170,000 has been obtained. The sensor hybrid will be produced in two steps: fabrication of a 250 element PIN array, and fabrication of a 250 stage CCD to which the array is bonded. PIN diodes and PIN arrays are routinely designed and manufactured in-house at Martin Marietta, and cost figures for the

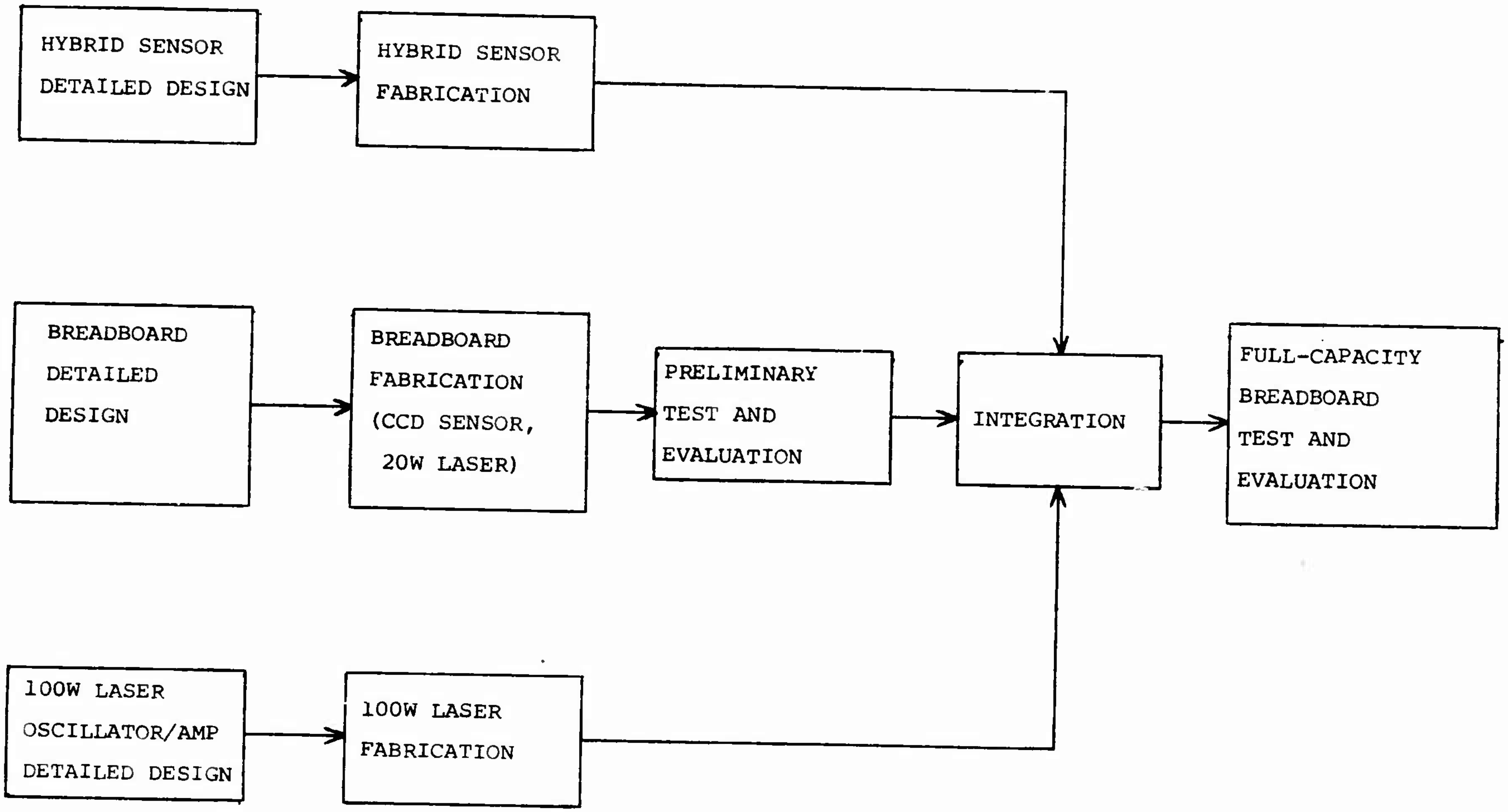

Figure 75. SLIR Baseline Breadboard Development

PIN array have been assessed as $50,000. This amount is for PIN-CCD bonding and the manufacture of about a dozen PIN arrays, from which the best array is selected. The remaining arrays can serve as spares. Present plans call for the CCD portion of the hybrid sensor to be designed at Martin Marietta and fabricated at a custom integrated circuit company. Cost estimates include the possibility of several CCD design and test iterations. Total hybrid sensor costs are summed as follows:

| | LABOR | MATERIAL |
|---|---|---|
| design, fabrication, and testing of CCD | 90,000 | 10,000 |
| design and fabrication of PIN array, marriage of array and CCD | 40,000 | 10,000 |

Total Cost = $150,000

These costs include all necessary computer-aided design. This gives a total cost of procuring the 100W laser and hybrid sensor of approximately $320,000.

Overall Breadboard Cost. Costs for the complete SLIR breadboard system (excluding the 100W laser and hybrid sensor) have been obtained via detailed estimates from the appropriate in-house facilities. Table 15 lists these costs. This pricing includes the interim CCD sensor and 20W laser. Costs for the main breadboard and the Display and Recording System are given separately. Since field testing requirements are unknown at this time, they have been excluded; therefore the table shows costs for final design, fabrication, and check-out of the baseline breadboard. Adding the $320,000 cost for the large laser and hybrid sensor, total cost for manufacture and checkout of the baseline breadboard is approximately $680,000.

## TABLE 15

### SLIR Breadboard Final Design, Fabrication Checkout Costs (All Costs in Thousands of Dollars)

| | LABOR | MATERIAL | OTHER |
|---|---|---|---|
| DESIGN FINALIZATION | | | |
| laboratory breadboard | 43.1 | .5 | 3.0 |
| display and recorder | 15.3 | .5 | |
| FABRICATION AND ASSEMBLY | | | |
| laboratory breadboard | 176.7 | 42.0 | |
| display and recorder | 28.8 | 11.3 | |
| SYSTEM CHECKOUT | 17.0 | | |
| DOCUMENTATION | | | |
| briefings (3) | 3.0 | .5 | 2.0 |
| reports (status & final) | 15.6 | 1.0 | |
| | 299.5 | 55.8 | 5.0 |

Complete Total = $360.3K

## SECTION VII

## CONCLUSIONS AND RECOMMENDATIONS

The work accomplished in compiling this report has established the desirability of imaging the field of regard with a one-dimensional scan of a fan illuminator beam and linear array receiver sensor. Attainment of the fan beam aspect ratio (about 80:1 with a 50 per cent overlap) with anamorphic optics is believed feasible, especially since large aspect ratios have previously been attained at Martin Marietta. Common illuminator/receiver scanning via a galvanometer scanner is a very desirable technique and insures high confidence in scene registration. While a number of illuminator candidates were initially considered, present technology dictates the use of a 1.06 micron Nd:Yag laser. Development of the 100W laser necessary for required range performance is believed credible, particularly since a 20W system of satisfactory beam size and divergence can presently be purchased commercially. The necessary receiver sensitivity is possibly the most demanding requirement placed on the SLIR system. While high sensitivity is possible for exotic sensors such as the GaAsSb avalanche photodiode discussed in this report, there is an undeniable risk in attempting to utilize these sensors in a large linear array. For this reason, a silicon PIN diode array has been recommended as a well known and dependable approach in giving acceptable receiver sensitivity (approximately 300 photons/pulse), when used in a PIN/CCD hybrid. This PIN hybrid sensitivity may be improved if CCD noise contribution is minimized. Present analysis shows acquisition range with the PIN hybrid near or greater than required for the two major target types given in the SOW, although the definition of factors constituting acquisition is perhaps open to some question. The use of a CCD analog shift register is a central advantage for the SLIR receiver. The CCD integration gives much improved noise performance over a similar real-time sensor array, and the parallel-in serial-out CCD capability greatly simplifies electronic design and reduces circuitry.

In view of time frame requirements for SLIR range and imaging capability in the near future, Martin Marietta recommends a near-term breadboard system which can meet the ultimate requirements indicated by the SOW and further assessed and discussed in this report. The development plan calls for parallel development of the 100W laser and PIN hybrid sensor while the remaining hardware is fabricated. The parallel development is estimated to require one year, while remaining hardware can be manufactured in 9 months or less. This has suggested the desirability of providing interim performance with a commercially purchased CCD sensor and 20W laser to enable system checkout and preliminary testing prior to the completion of the parallel development. Cost for this interim capability is only about 4 per cent of total cost of manufacture for the breadboard system, which is approximately $680,000.

The development path beyond an immediate breadboard will, of course, be influenced by performance obtained from the breadboard. In anticipation that the next logical step is an air-worthy brassboard, the existing preliminary breadboard design has been modular so that componentry can be repackaged at minimum cost and design. It is recommended by Martin Marietta that, pending breadboard sensitivity results, the PIN hybrid sensor be maintained in the future as a baseline approach. Although it is presently believed that the SLIR system can provide better than adequate tracking information, this too can be firmly verified by analysis of field test data with a SLIR breadboard.

# REFERENCES

1. Dimmock, J. O., and Keyes, R. J., "Active Imaging Study (U)", MIT Lincoln Laboratory, Technical Status Report No. 55TSR-0001, 2 August 1974.
2. J. E. Negro, "Pointing Variance and Beam Degradation Calculations", <u>Laser Digest</u>, AFWL-TR-74-100, Spring 1974.

4. A. E. Siegman, "Stabilizing Output with Unstable Resonators", Laser Focus, May 1971.

6. A. J. Steckl, "Injection Efficiency in Hybrid IR CCDs", Proceedings, 1975 Conference on the Applications of CCDs, San Diego, Calif., 29-31 October 1975.
7. Brodersen, R. W., and Emmons, S. P., "Noise in Buried Channel Charge-Coupled Devices", IEEE Transactions on Electron Devices, Vol. ED-23, No. 2, February 1976.
8. D. D. Wen, "Design and Operation of a Floating Gate Amplifier", IEEE Journal of Solid-State Circuits, Vol. SC-9, No. 6, December 1974.
9. Buchanan, S., and Schmieder, D., "CCD 121 Performance Data", Doc. No. TRP01300000-001, internal Martin Marietta Test Report, June 1976.
10. R. C. Eden, et al, "High Sensitivity Gigabit Data Rate $GaAs_{1-x}Sb_x$ Avalanche Photodiode 1.06μ Optical Receiver", Proceedings, 1975 International Electron Devices Meeting, Washington, D.C., December 1975.
11. R. C. Eden, "Heterojunction III-V Alloy Photodetectors for High-Sensitivity 1.06 μm Optical Receivers", Proceedings of the IEEE, Vol. 63, No. 1, January 1975.
12. R. C. Eden, "1.06 Micron Avalanche Photodiode", Tech. Rep. AFAL-TR-72-343, Jan. 1973.
13. M. Abramowitz and I. A. Stegun (ed), "Handbook of Mathematical Functions," National Bureau of Standards Mathematics Series 55, March 1965
14. R. A. McClatchey, et al, "Optical Properties of the Atmosphere (Third Edition)", Air Force Cambridge Research Laboratories, Tech. Rep. AFCRL-72-0497, August 1972.

# DISTRIBUTION LIST

| | Copies |
|---|---|
| AFAL/TSR, WPAFB, OH 45433 | 1 |
| 2750ABW/SSL, WPAFB, OH 45433 | 1 |
| Air University Library, Maxwell AFB, AL 36112 | 1 |
| AFSC/IN, Andrews AFB, DC 20334 | 1 |
| AFSC/INA, Andrews AFB, DC 20334 | 1 |
| Hq USAF/SAMID, Washington, DC 20330 | 1 |
| AFEWC/SURP, San Antonio, TX 78243 | 3 |
| DDC/TCA, Cameron Station, Alexandria, VA 22314 | 2 |
| AFAL/RWT (Fitzgibbon), WPAFB, OH 45433 | 1 |
| AFAL/RWT (Dobbins), WPAFB, OH 45433 | 1 |
| AFWL/LRO (Katonak), Kirtland AFB, NM 87117 | 1 |